PHD

An ultrasonic study of refractory hard ceramics

Dodd, Simon Peter

Award date:
2002

Awarding institution:
University of Bath

An Ultrasonic Study of Refractory Hard Ceramics

submitted by
Simon Peter Dodd
for the degree of PhD
of the University of Bath
2002

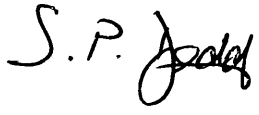

ProQuest LLC
789 East Eisenhower Parkway
P.O. Box 1346
Ann Arbor, MI 48106-1346

"Tursiops Truncatus"

Acknowledgements

I would first like to thank my supervisor Professor George Saunders for his guidance throughout most of my degree. Secondly, the valuable assistance and advice given by both Professor John Davies and Doctor Mehmet Cankurtaran in writing my thesis is greatly appreciated. I also wish to thank Doctor Bryn James for financial support and supplying most of the samples used in this work, and also Professor Mehmet Acet for supplying the cementite samples.

Wendy Lambson, Eddy Lambson, Bob Draper and Barry Chapman have all made my time at the University of Bath very enjoyable; not only have they used their technical expertise and advice to assist me in my work, but their calming influence and ability to turn a moderately serious conversation into a strange or silly one has given me valuable respite from my work.

I thank my parents for their love, encouragement, financial support and putting up with my indecisiveness. Thanks go to my ex-housemates Graeme Boswell and Mark Penney who managed to put up with me for 3 whole years. This achievement also applies to my past and present office colleagues, Tessa Brennan, Mark Acres, Huijin Liu, Richard Martin and Owen Bryant. As for the drinking fraternity of Jim Partridge, Graeme Moore, Adam Armitage, Dave Langridge, Martin Hughes, Stuart Humphreys, Frank Hart and Steve Everitt, I would like to thank them for forcing me to drink moderately large amounts of alcohol, but mainly for their friendship, encouragement and a thoroughly entertaining time while living in Bath. If I had enough (any) money, I would buy you all a life-time supply of beer (no, honestly!). Football is also close to my heart and I would like to thank all the members of past and present physics' seven-a-side teams for their (lack of) vision, commitment and skill on the pitch creating (frustrating but) enjoyable games. Sometime in the far distant future, the physics team will win the league. In addition, I would like to thank Fiona Taylor, Mark Gutteridge and Gillian, Ryan and Sarah Potts, Rich and Clare, Aidan and Lisa Green and Scott Dake for their friendship and also for managing to resist the allure of physics (good choice, except for Aidan).

Abstract

Seven refractory hard ceramics (AlN, β-Si_3N_4, TiB_2, B_4C, TiC, TaC, ZrC) and one ceramic ferromagnetic Invar iron alloy (Fe_3C) have been characterised using a number of standard non-destructive techniques. Pulse-echo overlap measurements of ultrasonic wave velocity have been used to determine the elastic properties of these eight ceramic samples as functions of temperature and hydrostatic pressure. The results obtained for the room temperature elastic moduli of these ceramic samples show that they are stiff materials elastically. Anomalous temperature behaviour in the measured ultrasonic velocities and related elastic properties of the ceramic samples of β-Si_3N_4 and Fe_3C were found. The anomalous temperature behaviour of Young's modulus determined for Fe_3C (cementite) confirms the Elinvar effect for this material. The remaining refractory hard ceramic samples stiffened in the normal way with decreasing temperature. Anomalous hydrostatic pressure induced changes in the shear mode ultrasonic velocity were measured for β-Si_3N_4, which mirrors those changes determined as a function of temperature for this material. With the exception of β-Si_3N_4, ultrasonic velocities measured for these ceramics as a function of hydrostatic pressure increased with increasing pressure, indicating normal behaviour. Consequently, the longitudinal and shear elastic stiffness and bulk modulus hydrostatic pressure derivatives are positive for these ceramics. Assessing the nonlinear acoustic properties of these ceramics by determination of the acoustic mode Grüneisen parameters showed that the thermal properties of these materials are in accord with the low acoustic mode vibrational anharmonicity.

Contents

Chapter 1

General Introduction

The refractory nature of so-called "advanced" ceramics leads to applications where mechanical, chemical and thermal stability are required at high temperatures. Polycrystalline materials that exhibit these qualities are generally labelled as "structural" ceramics. Their refractory nature is related to strong interatomic binding forces. Great hardness is also prevalent in these structural ceramics as a result of this strong bonding. These types of ceramics are promising for a wide variety of applications beyond the reach of conventional materials like metals and alloys. Ceramic alumina and silicon carbide demonstrate these properties and are used extensively in engineering applications. However, one significant drawback in broadening the range of applications for these advanced ceramics is that the strong bonding also promotes brittleness.

In general, the elastic properties are given by the second-order elastic tensor components (*SOECs*), which describe, in a macroscopic way, the resistance of a solid body to strain. Knowledge of the elastic properties of refractory hard ceramics is important for different applications; for example, their elastic properties, which depend on the crystal structure and bonding, are central in determining mechanical behaviour, e.g. strength, hardness and fracture toughness, and also control the response of a material to shock or impact. The microstructure of a ceramic, i.e. size, shape and distribution of grains, number of phases, porosity and impurities, also plays a role in their elastic and mechanical behaviour; microstructure can influence how ceramics respond elastically to temperature and pressure changes.

In fundamental studies, physical properties of solids which are a result of the thermal motion of atoms are governed by the anharmonic behaviour of the crystal lattice; that is, the nonlinearity of the interatomic forces with respect to strain. By determining elastic properties as functions of temperature and hydrostatic pressure, the acoustic mode vibrational anharmonicity can be assessed. In particular, measurements of changes in *SOECs* as a function of hydrostatic pressure provide information on the shift of the acoustic mode energies with strain and characterise the acoustic mode vibrational anharmonicity. The acoustic mode Grüneisen parameters quantify this

strain dependence of normal mode frequencies in the long wavelength limit. The information obtained from these experiments helps in understanding many properties of materials governed by the thermal motion of the atoms, i.e. thermal expansion, mechanical strength and lattice instabilities.

The aim of this study was to assess the elastic and nonlinear acoustic properties of a number of refractory hard ceramics that have recently attracted interest for technological applications and fundamental studies in the areas of materials science and physics. These refractory hard ceramics belong to the carbide (B_4C, TiC, TaC, ZrC), nitride (AlN and β-Si_3N_4) and boride (TiB_2) families. The final sample studied is an iron carbide (Fe_3C), commonly named cementite, which does not have the same degree of refractoriness as these other ceramics, but is hard and brittle and is an important constituent of steels. It is believed that when steels are heavily deformed cementite fractures into fine pieces; in contrast, it also deforms plastically during the processing of steels at elevated temperatures (Li et al. 1998). Li et al. (1998) have pointed out that to design a microstructure of advanced steels, properties of cementite such as hardness, Young's and shear moduli and their temperature dependences are required. Cementite is a ferromagnetic material and below its Curie temperature (T_C) the onset of a positive spontaneous volume magnetostriction produces so-called "Invar" behaviour (an invariant thermal expansion coefficient around room temperature). In previous studies on materials that show Invar behaviour, this magnetic interaction also produced unusual elastic behaviour as functions of temperature and pressure. Therefore, determination of the temperature and hydrostatic pressure dependences of the elastic properties of cementite are important for advanced steel design and fundamental magnetic studies. These measurements may help in understanding both the mechanical behaviour and the thermal properties of cementite. The samples used in this study were fabricated elsewhere.

Brittleness in refractory hard ceramics promotes the use of a non-destructive technique to evaluate their elastic properties. Ultrasonic velocity measurements fit this requirement, since the introduction of infinitesimal small amplitude stress waves into

the samples should not produce irreversible damage. The pulse-echo overlap technique was employed to determine the ultrasonic velocities of propagated stress waves. This technique has the sensitivity to detect small changes in ultrasonic velocity, which makes it ideal for measurements as functions of temperature and hydrostatic pressure. From these measurements, the elastic and nonlinear acoustic properties were then determined. The propagation of ultrasonic waves is also sensitive to the microstructure of a ceramic. Characterisation of each ceramic is important for giving information on the microstructure, and may help to explain unusual behaviour in the ultrasonic velocity measurements, and hence the elastic properties. Non-destructive characterisation techniques were used to determine the physical and chemical information for each ceramic sample. Chemical analysis of the ceramic led to the determination of the number and proportion of phases and any impurities present. From this information, it was possible to find the chemical composition of the ceramic and determine whether the sample was representative of the chemical formula, i.e. TiB_2. An analysis of the physical properties of each ceramic provided information on the shape and distribution of grain sizes and the determination of bulk density, lattice parameters and porosity. X-ray diffraction studies, scanning electron microscopy (SEM), electron microprobe quantitative analysis (EMQA), energy dispersive spectroscopy (EPS) and electrical resistivity measurements were used to gather this information. Ultrasonic velocity measurements at room temperature were also employed to analyse the isotropic nature of each material as part of the characterisation process.

The information given in this report on the elastic behaviour of refractory hard ceramics is presented in the following way. Chapter 2 gives the basic elastic and vibrational anharmonicity theory for isotropic (ceramic) materials. Chapter 3 describes the experimental techniques used to determine ultrasonic velocities and electrical resistivities. The next chapters give the results of the ultrasonic study on these ceramics. Each chapter on the ultrasonic results is set out as follows: firstly, an introduction is given highlighting the main properties and present and potential uses of each ceramic studied, followed by a description of the measurements to date assessing

their elastic and nonlinear acoustic behaviour. Subsequently, the characterisation information is given and where needed is compared with available literature to check for any discrepancies. The results and discussion of the elastic and nonlinear acoustic properties for the ceramics are then presented. In the results and discussion sections of this work, a collation of all the available results of previous studies to assess the elastic and nonlinear acoustic properties are given and compared with those results determined here. This is necessary because, in general, the microstructure of one ceramic tends to differ from that of another, even though they may be represented by the same chemical formula; thus, standardization of the elastic behaviour of ceramic samples is a difficult process. Finally, the conclusions drawn from the results of the ultrasonic study presented in each chapter are brought together in Chapter 8.

Chapter 2

Theory of Elasticity and Lattice Vibrational Anharmonicity for Isotropic Media

2.1 Introduction

In material science and solid state physics, ultrasonic techniques are used as a non-destructive method for measuring the elastic properties of materials. When applied to materials, stress waves can induce three types of motion: linear translation, rotation, local deformation; in pulse-echo ultrasonics, only deformation (strain) is considered. Elastic stiffnesses relate the applied stress to the induced strain of a material. These stiffnesses can be calculated from ultrasonic measurements and in turn the technological elastic properties (Young's modulus, bulk modulus and Poisson's ratio) can be determined.

2.2 Harmonic Approximation

When dealing with stress-strain relationships, at a constant temperature and pressure, the harmonic approximation is sufficient to account for the interatomic interactions under external forces. The harmonic approximation states that atoms in a solid are held at a mean separation from their nearest neighbours by attractive and repulsive forces corresponding to a minimum potential energy; each atom sits in a potential well and has a potential energy (U) proportional to the square of its displacement (x) from the mean separation (x=0). Hence, the constant of proportionality between stress and strain is a second-order elastic coefficient or stiffness tensor component (*SOEC*). A potential well governing the elastic behaviour of an atom is shown below in Figure 2.1.

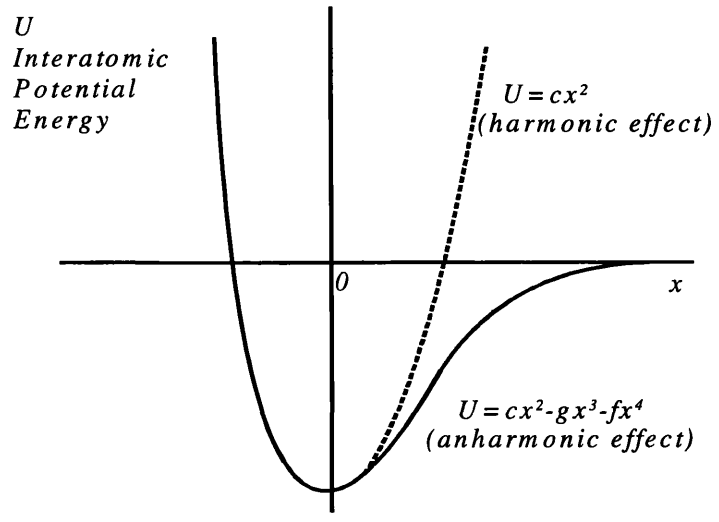

Figure 2.1 Potential wells for both harmonic and anharmonic oscillators.

Properties of a solid that depend upon thermal motion of the atoms are much influenced by anharmonicity (Dodd et al. 2001); the solid line in Figure 2.1 represents this anharmonicity, which can be expressed as extra terms in the potential energy equation (Kittel 1976). These extra terms will be introduced later in the chapter.

2.3 Elasticity Tensors

2.3.1 Stress Tensors

In general, a body in which one part exerts a force on neighbouring parts is said to be in a state of stress. A volume element situated within a stressed body has two kinds of forces acting on it. Firstly, body-forces namely gravity act throughout the body on all volume elements and whose magnitudes are proportional to the volume of the element. Secondly, the material surrounding the volume element exerts forces on the surfaces of that element (Nye 1985). These forces are proportional to the surface area of the element and the force per unit area is the *stress* (σ). Figure 2.2 shows all the components needed to describe the stress.

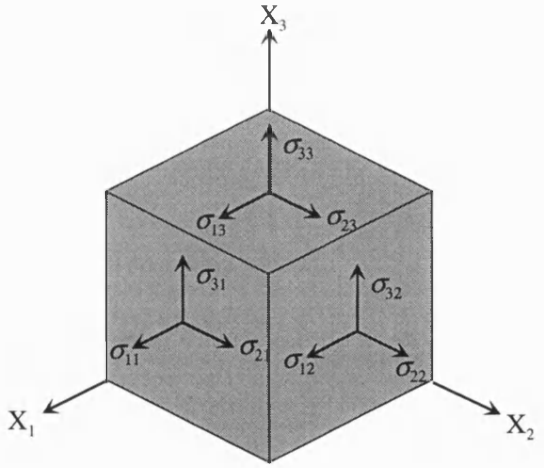

Figure 2.2 The nine components needed to describe the stress on a volume element: three tensile stresses, six shear stresses.

These components make up a second rank tensor (σ_{ij}) that relates the force components (F_i) applied to the surface area with the normal vector (l_j) to that surface. From this definition

$$F_i = \sigma_{ij} l_j \quad (i, j = 1, 2, 3), \tag{2.1}$$

where

$$\sigma_{ij} = \begin{bmatrix} \sigma_{11} & \sigma_{12} & \sigma_{13} \\ \sigma_{21} & \sigma_{22} & \sigma_{23} \\ \sigma_{31} & \sigma_{32} & \sigma_{33} \end{bmatrix}. \tag{2.2}$$

Nye (1985) states that because the element is in static equilibrium the forces on the other three faces of Figure 2.2 must be equal and opposite to those shown. There must also be no net torque on the element, restricting the tensor to six independent components, i.e. the stress tensor is symmetric. A positive value of σ_{ij} when $i=j$ denotes a tensile stress.

2.3.2 Strain Tensors

A simple one-dimensional case will be used, initially, to approach the problem of specifying the state of deformation of a solid body. To demonstrate this deformation, a string which is marked with an origin O and a point P some distance along the string, where $OP = x$, is stretched; under stretching, the point P moves to P' and $OP' = x + u$. Let a point Q, close to P, move to Q' during the stretching and let $PQ = \Delta x$, then $P'Q' = \Delta x + \Delta u$. With strain, only the relative displacements of the two points P and Q are of interest. Therefore, the strain e (fractional change in length) of the section PQ is defined as

$$e = \frac{\Delta u}{\Delta x} \tag{2.3}$$

and the strain at point P is

$$e = \frac{\partial u}{\partial x}. \tag{2.4}$$

In the case of a three-dimensional body, such as a crystal, the displacement u and position x are expanded to three Cartesian axes, then u_i and x_i each have three components; thus Equation (2.4) becomes

$$e_{ij} = \frac{\partial u_i}{\partial x_j} \quad (i, j = 1, 2, 3) \tag{2.5}$$

giving a second-rank tensor with nine independent tensor components.

In ultrasonic measurements, as the translation and rotation of the body are not considered, the strain tensor ε_{ij} is defined as the symmetrical part of e_{ij} (Nye 1985), giving

$$\varepsilon_{ij} = \frac{(e_{ij} + e_{ji})}{2}. \tag{2.6}$$

Since the strain tensor is symmetrical ($\varepsilon_{ij} = \varepsilon_{ji}$), there are only six independent components that define the state of a deformed body; Equation (2.7) shows the full tensor notation of Equation (2.6), which is

$$\varepsilon_{ij} = \begin{bmatrix} \varepsilon_{11} & \varepsilon_{12} & \varepsilon_{13} \\ \varepsilon_{12} & \varepsilon_{22} & \varepsilon_{23} \\ \varepsilon_{13} & \varepsilon_{23} & \varepsilon_{33} \end{bmatrix} = \begin{bmatrix} e_{11} & \frac{(e_{12}+e_{21})}{2} & \frac{(e_{13}+e_{31})}{2} \\ \frac{(e_{12}+e_{21})}{2} & e_{22} & \frac{(e_{23}+e_{32})}{2} \\ \frac{(e_{13}+e_{31})}{2} & \frac{(e_{23}+e_{32})}{2} & e_{33} \end{bmatrix}. \tag{2.7}$$

The diagonal components of ε_{ij} are the stretches or tensile strains and the other components measure the shear strains. Figure 2.3 shows each component represented graphically

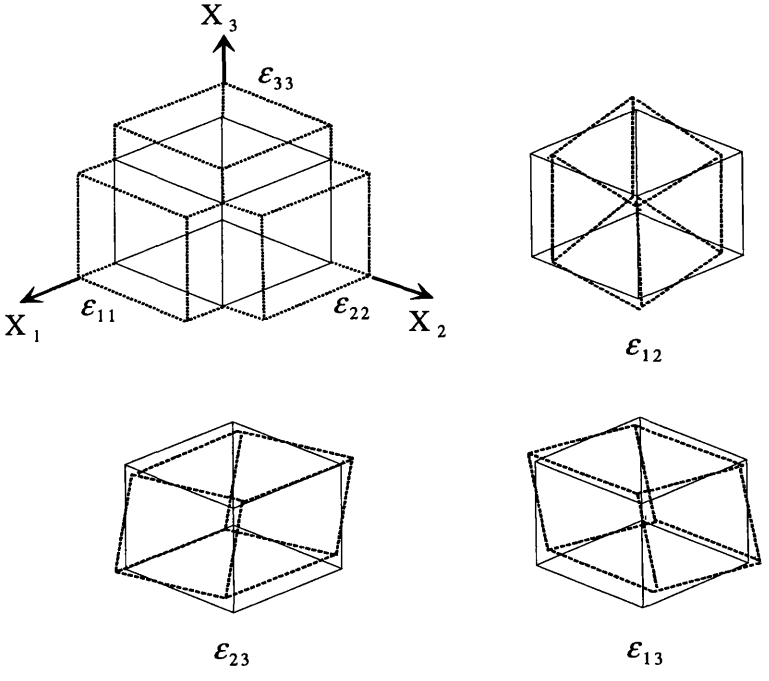

Figure 2.3 The effect of strain on a volume element
(dotted lines show the deformation).

2.3.3 Hooke's Law

Hooke's law states that when a stress is applied to a solid body it is linearly related to the induced strain. Under the stress the body changes shape but will regain its original form once the stress is removed, up to the body's elastic limit. For infinitesimal small deformations, solid bodies behave elastically. The second-order elastic stiffness tensor components for the stress-strain relation are generally written

$$\sigma = C\varepsilon . \tag{2.8}$$

Stress and strain are second-rank tensors; therefore the elastic stiffness tensor is of the fourth-rank. Each stress tensor component can be expressed as a linear combination of the strain components giving

$$\sigma_{ij} = C_{ijkl}\varepsilon_{kl}, \ (i, j, k, l = 1, 2, 3) \tag{2.9}$$

with C_{ijkl} having (in its most general case) 81 components.

Due to stress and strain being symmetric tensors (see Equations (2.2) and (2.7)), the elastic stiffness components are reduced to 36, resulting in

$$C_{ijkl} = C_{jikl} = C_{ijlk} . \tag{2.10}$$

This symmetry allows the stiffness tensor notation to be simplified. In Voigt notation (Nye 1985) the first two suffixes i and j are abbreviated into a single one running from 1 to 6 and similarly for k and l; therefore $ij = n$ and $kl = m$.

Tensor notation	11	22	33	23 32	13 31	12 21
Voigt notation	1	2	3	4	5	6

All 36 tensor components, shown in Voigt notation, are given below

$$C_{mn} = \begin{bmatrix} C_{11} & C_{12} & C_{13} & C_{14} & C_{15} & C_{16} \\ C_{21} & C_{22} & C_{23} & C_{24} & C_{25} & C_{26} \\ C_{31} & C_{32} & C_{33} & C_{34} & C_{35} & C_{36} \\ C_{41} & C_{42} & C_{43} & C_{44} & C_{45} & C_{46} \\ C_{51} & C_{52} & C_{53} & C_{54} & C_{55} & C_{56} \\ C_{61} & C_{62} & C_{63} & C_{64} & C_{65} & C_{66} \end{bmatrix} . \tag{2.11}$$

A further restriction is inserted to reduce the 36 components to 21: the strain energy is only dependent on its final state and not the path taken to reach that state; the

deformation is reversible within the elastic limit of the body (Nye 1985). Now

$$C_{ijkl} = C_{klij} = C_{mn} = C_{nm} \tag{2.12}$$

making the stiffness tensor symmetric.

The stiffness tensor components can be even further reduced because the crystal symmetry also has an effect. Triclinic crystals need all 21 components to define the stress-strain relation and the number decreases as the symmetry increases up to cubic crystals where there are only three components (again see Nye for details). A special case for an isotropic solid body, such as glasses and in principal ceramics, arises because their tensor components do not depend on any axes; their elastic properties are equivalent in all directions. Only two components are needed to define the elastic behaviour, λ and μ, the Lamé constants (Mason 1958). The tensor components now have the form:

$$\lambda = C_{12} = C_{13} = C_{23}, \qquad \mu = C_{44} = C_{55} = C_{66}. \tag{2.13}$$

The anisotropic factor (Truell et al. 1969), which for an isotropic material is

$$C_{11} - C_{12} = 2C_{44} \tag{2.14}$$

is used to generate

$$C_{11} = C_{22} = C_{33} = \lambda + 2\mu \tag{2.15}$$

and all other components are zero.

These values in Equations (2.13) and (2.15) can be substituted into Equation (2.11) giving

$$\begin{bmatrix} \sigma_1 \\ \sigma_2 \\ \sigma_3 \\ \sigma_4 \\ \sigma_5 \\ \sigma_6 \end{bmatrix} = \begin{bmatrix} \lambda+2\mu & \lambda & \lambda & 0 & 0 & 0 \\ & \lambda+2\mu & \lambda & 0 & 0 & 0 \\ & & \lambda+2\mu & 0 & 0 & 0 \\ & & & \mu & 0 & 0 \\ & & & & \mu & 0 \\ & & & & & \mu \end{bmatrix} \begin{bmatrix} \varepsilon_1 \\ \varepsilon_2 \\ \varepsilon_3 \\ \varepsilon_4 \\ \varepsilon_5 \\ \varepsilon_6 \end{bmatrix}. \tag{2.16}$$

The elastic stiffness tensor components, C_{11} (or C_L in isotropic media) and μ, which are commonly referred to as just elastic stiffnesses, can be calculated from ultrasonic velocity measurements; this will be discussed later. From the set of components in Equation (2.16), three useful technological elastic quantities can be computed. Young's modulus (E) is the ratio of a uniaxial stress over the induced strain. Taking a stress in one axis direction only (Mason 1958) yields

$$E = \frac{\sigma_i}{\varepsilon_i} = \frac{\mu(3\lambda+2\mu)}{\lambda+\mu}. \qquad (2.17)$$

Under the same uniaxial condition another quantities can be formulated. Poisson's ratio (σ), not to be confused with stress, is the ratio of the strain parallel (ε_i) and lateral (ε_3) to the applied stress, therefore

$$\sigma = -\frac{\varepsilon_i}{\varepsilon_3} = \frac{\lambda}{2(\lambda+\mu)}, \qquad (2.18)$$

where i is either 1 or 2.

The bulk modulus (B) is the ratio of hydrostatic compression (p) over the fractional volume change (Δ) (Mason 1958), given by

$$B = -V\frac{\partial p}{\partial V} = \frac{p}{\Delta} = \frac{3\lambda+2\mu}{3}. \qquad (2.19)$$

2.4 The Relationship between Ultrasonic Velocities and the Technological Elastic Properties of an Isotropic Solid

The displacement of atoms from their equilibrium position and subsequently the action of the restoring forces, when an external stress is applied, creates the transmission of an elastic wave through the material. These waves can be propagated in any direction in a crystalline medium whether isotropic or not. In each direction, three independent waves whose displacements are mutually orthogonal can be transmitted, one longitudinal and two shear each with a distinct velocity. In general, no waves propagated in a crystal are purely longitudinal or shear in nature. However, there are special directions in any crystal for which the propagation and displacement directions of the wave coincide; this is a longitudinal wave and therefore the two shear waves have orthogonal displacements to the first (Truell et al. 1969). In an isotropic medium both longitudinal and shear modes are pure.

To relate the velocities of these waves to the elastic moduli, the equation of motion derived from Newton's second law is used (Mason 1958); that is: the acceleration of a mass by an external force. For the three directions of motion the equations in an unbounded medium can be written

$$\rho \frac{\partial^2 u_i}{\partial t^2} dxdydz = F_i \quad (i = 1, 2, 3), \tag{2.20}$$

where F_i is the force component and ρ is the mass density.

These force components are defined by the rates of change of the stresses along the edges of the volume element (Figure 2.2), in each direction. Applying the stress-strain relation from Equation (2.16) gives three equations of motion in an isotropic solid. Differentiating the three equations and then adding gives

$$\rho \frac{\partial^2 \Delta}{\partial t^2} = (\lambda + 2\mu)\nabla^2 \Delta, \tag{2.21}$$

where Δ is the dilation $(= \varepsilon_1 + \varepsilon_2 + \varepsilon_3)$.

Using a plane wave solution with the displacement parallel to the propagation direction for the three Cartesian axes yields three equations of motion each giving the velocity related to an elastic stiffness in Equation (2.16), which is simply

$$V_L = \sqrt{\frac{\lambda + 2\mu}{\rho}}. \tag{2.22}$$

A similar method is used for the shear (rotational) wave velocity, and from this the shear velocity is

$$V_S = \sqrt{\frac{\mu}{\rho}}. \tag{2.23}$$

In the long wavelength limit and for infinitesimal small deformations, the velocities (V_L and V_S) are related to the two independent tensor components (C_L and μ) by

$$C_L = \rho V_L^2 \tag{2.24}$$

and

$$\mu = \rho V_S^2. \tag{2.25}$$

The technological elastic moduli, which are measured under adiabatic conditions (high vibrational frequency thus allowing no heat flow in the system), E, B^S and σ are now:

$$E = \frac{\mu(3C_L - 4\mu)}{C_L - \mu}, \tag{2.26}$$

$$B^S = \frac{(3C_L - 4\mu)}{3}, \tag{2.27}$$

$$\sigma = \frac{C_L - 2\mu}{2(C_L - \mu)}. \tag{2.28}$$

2.5 Quasi-Harmonic Approximation

The harmonic approximation falls short of explaining many thermal properties such as: thermal expansion, thermal conductivity, the temperature and pressure dependence of elastic coefficients, adiabatic and isothermal differences in elastic properties, phonon-phonon interaction, deviation from the heat capacity classical limit. Higher order terms are added to the potential energy equation of the harmonic theory which take into account the anharmonic effect. A representation of the potential energy equation including the anharmonic terms is defined in Kittel (1976) as

$$U(x) = cx^2 - gx^3 - fx^4, \tag{2.29}$$

where cx^2 is the harmonic contribution, gx^3 represents the asymmetry of the mutual repulsion of the atoms and fx^4 represents the softening of the vibration at large amplitudes. To quantify the higher order terms in the energy equation the Grüneisen parameter (γ) or gamma is commonly used. The first order anharmonic term can be quantified by ultrasonic velocity measurements as a function of hydrostatic pressure.

2.5.1 Acoustic Mode Grüneisen Parameters

The thermal Grüneisen parameter (γ^{th}) takes into account the contribution of all optic and acoustic phonon modes in the entire first Brillioun zone to the thermal properties of materials. An ultrasonic velocity is a measure of the linear region of the first Brillioun zone centre acoustic phonon dispersion curve; only long wavelength phonons are excited in this region (the continuum model). Ultrasonic velocity measurements as functions of pressure on isotropic materials yield three acoustic mode Grüneisen parameters: longitudinal (γ_L), shear (γ_S), mean (γ^{el}). These represent the contribution of the zone centre acoustic mode Grüneisen parameters to the thermal Grüneisen parameter.

In the quasi-harmonic approximation, the normal mode vibrations are treated as harmonic oscillators but with volume dependence (Barron 1980), i.e. the terms in the interatomic potential energy are only dependent upon atomic separation (strain). Using the Einstein model for normal modes of vibration, statistical mechanics (Born and Huang 1954) and thermodynamic functions, i.e. Helmholtz free energy, since the

system is a function of volume and temperature, Born and Huang (1954), Brugger and Fritz (1967) and Slater (1939) have shown that at constant temperature the dimensionless quantities

$$\gamma_i = -\frac{d \ln \nu_i}{d \ln V}, \tag{2.30}$$

are produced, where ν_i is the frequency of the ith phonon mode. The generalised gamma (γ_i) is the contribution of the ith phonon mode to the thermal expansion. Brüesch (1982) defined the thermal Grüneisen parameter as

$$\gamma^{th} = \sum_i \gamma_i C_i \Big/ \sum_i C_i = \frac{\beta B^S V}{C_P}, \tag{2.31}$$

where C_i, the Einstein specific heat (Born and Huang 1954) for that particular phonon mode, is

$$C_i = k_B \left(\frac{h\nu_i}{k_B T}\right)^2 \frac{\exp(h\nu_i / k_B T)}{[\exp(h\nu_i / k_B T) - 1]^2}. \tag{2.32}$$

Equation (2.31) reflects the weighted contribution of the ith phonon mode to the heat capacity. The second equality in Equation (2.31) is the Grüneisen parameter derived from thermodynamic relations, where C_P is the heat capacity at constant pressure, β is the volume thermal expansion and V is the molar volume.

Barron (1980) has derived an equation relating the pressure derivatives of the *SOEC* to the acoustic mode Grüneisen parameters. Ultrasonic velocity measurements as a function of hydrostatic pressure can be used to evaluate the contribution of zone centre acoustic phonon modes to the thermal expansion from

$$\gamma_L = -\frac{1}{6}\left[1 - \frac{3B^T}{C_L}\left(\frac{\partial C_L}{\partial p}\right)\right] \tag{2.33}$$

and

$$\gamma_S = -\frac{1}{6}\left[1 - \frac{3B^T}{\mu}\left(\frac{\partial \mu}{\partial p}\right)\right]. \tag{2.34}$$

The pressure derivatives are defined in the next section.

At $T \geq \Theta_D$, where Θ_D is the acoustic Debye temperature defined in Section 2.7, all mode heat capacities (C_i) will have the same contribution to the overall heat capacity;

each mode heat capacity will be approximately equal to the Boltzmann constant (k_B) (Sheard 1958). Therefore, using a relation derived by Brugger and Fritz (1967) for the mean acoustic Grüneisen parameter (γ^{el}), a high temperature mean acoustic mode Grüneisen parameter is derived using the equations above giving

$$\gamma^{el} = \frac{1}{3}\left(\gamma_L + 2\gamma_S\right). \tag{2.35}$$

2.6 Hydrostatic Pressure Derivatives of C_L, μ and B^S for an Isotropic Solid

To remove the need to calculate the effective elastic coefficients as a function of pressure, Thurston (1965) developed a way of calculating $(\partial C_{L,\mu} / \partial P)$ without needing to take into account the change in path length and density due to an external pressure. Previously, Thurston and Brugger (1964) introduced a quantity called the "natural" velocity ($W = 2l_0 f$); this being the velocity in ambient pressure conditions at constant temperature. It is possible to use the measured frequency (f) data directly to find the pressure derivatives, with negligible error compared with the effective elastic coefficient pressure derivatives, using the relation

$$\left(\rho_0 W^2\right)'_{P=0} = 2\rho_0 v_0^2 \frac{f'}{f_0}, \tag{2.36}$$

where ρ_0, v_0 and f_0 are density, velocity and overlap frequency at ambient pressure and constant temperature and $(x)' = (\partial x / \partial P)$. Thurston (1965) found for an isotropic solid that

$$\left(\rho v^2\right)'_{P=0} = \rho_0 v_0^2 \left(\frac{2f'}{f_0} + \frac{\chi^T}{3}\right)_{P=0}, \tag{2.37}$$

where $\chi^T (= 1/B^T)$ is the isothermal compressibility and ρv^2 is equal to C_L or μ depending on the ultrasonic velocity used. The pressure derivative of the adiabatic bulk modulus is obtained by using results calculated from Equation (2.37) in

$$\left(\frac{\partial B^S}{\partial P}\right)_{P=0} = \left(\frac{\partial C_L}{\partial P}\right)_{P=0} - \frac{4}{3}\left(\frac{\partial \mu}{\partial P}\right)_{P=0} \tag{2.38}$$

2.7 Acoustic Debye Temperature, Θ_D

Strictly speaking, the Debye temperature is based on an assumption of no dispersion (continuum model), therefore only really valid at low temperatures where the long wavelength acoustic modes are excited. This characteristic temperature is related to the cut-off frequency of the normal modes. The three degrees of freedom for each discrete atom in a lattice create a maximum value for the normal mode frequencies; at this limit all normal modes of vibration are excited. The Debye temperature is a measure of the interatomic bonding and mass of the atoms, i.e. materials with light atoms and very strong interatomic bonding, such as diamond, have high Θ_D values (Rosenberg 1988). Ultrasonic velocity is a measurement of phonon phase velocity in the long wavelength limit and Θ_D can be calculated from the longitudinal and shear velocity values using the formulae

$$\bar{v}_D = \left[\frac{1}{3}\left(\frac{1}{v_L^3}+\frac{2}{v_S^3}\right)\right]^{-\frac{1}{3}}, \tag{2.39}$$

where $\bar{v}_D$ is the average Debye velocity, and an equation derived by Anderson (1963) which is

$$\Theta_D = \frac{h}{k_B}\left(\frac{3\rho An}{4\pi M}\right)^{\frac{1}{3}}.\bar{v}_D. \tag{2.40}$$

In Equation (2.40), n is the number of atoms per formula, M is the molar mass, ρ is the sample density and A is Avogadro's number, while all other parameters are standard constants.

2.8 Model for the Temperature Dependence of Elastic Stiffness

A good representation of a normal elastic stiffness temperature dependence for a given material is useful in detecting and illustrating any deviations from this normal behaviour. Lakkad (1971) has shown that his phenomenological model gives a good approximation to the temperature dependence of the elastic behaviour of a number of materials. His model, incorporating essential parameters: a harmonic oscillator with an applied force term plus a third-order expression representing the anharmonicity of the oscillator, gave

$$M = M_0[1 - KF(T/\Theta_D)], \tag{2.41}$$

where

$$F(T/\Theta_D) = 3(T/\Theta_D)^4 \int_0^{\Theta_D/T} [x^3(\exp(x) - 1)]dx \tag{2.42}$$

and M is the elastic stiffness and M_0 and K are constants.

Fitting this expression to experimental data involves only knowledge of two elastic stiffnesses at their corresponding temperatures and the Debye temperature of the material under study.

2.9 Murnaghan's Equation of State

Murnaghan's equation of state allows pressure versus volume compression data to be extrapolated to moderately high pressure; in other words, one or two orders of magnitude higher than is possible under hydrostatic pressure conditions. This extrapolation allows pressure data measured in small pressure ranges to be compared with data taken in a higher range. The equation of state is based on the assumption that the bulk modulus has a linear relationship with pressure (Anderson 1966), giving

$$B(P) = -V\left(\frac{\partial P}{\partial V}\right)_T = B_0 + B_0' P, \tag{2.43}$$

where $B_0' = (\partial B / \partial p)_{T,P=0}$ and $B_0 = B(P \to 0)$. Murnaghan (1944) integrated Equation (2.43) and yielded

$$P = \frac{B_0}{B_0'}\left[\left(\frac{V_0}{V}\right)^{B_0'} - 1\right]. \tag{2.44}$$

Equation (2.44) is normally used in its logarithmic form:

$$\ln\left(\frac{V_0}{V}\right) = \frac{1}{B_0'}\ln\left[B_0'\left(\frac{P}{B_0}\right) + 1\right]. \tag{2.45}$$

Chapter 3

Experimental Techniques for Ultrasonic and Electrical Measurements

3.1 Introduction

Pulse-echo ultrasonics (May 1958) is a standard method for determining the elastic and nonlinear acoustic behaviour of materials. Its principle is to measure round trip transit times and attenuation of an ultrasonic wave in a material, by transmitting and receiving high frequency pulses. Absolute velocities can be measured with a precision of 1 part in 10^3. The pulse-echo overlap technique devised by Papadakis (1967) is an accurate and sensitive extension of the echo-overlap method. The sensitivity of the pulse-echo measurement for detecting velocity changes is better than 1 part in 10^4; therefore, this technique is ideal for measuring temperature and pressure induced changes in ultrasonic velocity and attenuation.

3.2 Pulse-Echo Overlap System

3.2.1 Ultrasonic Wave Transmission and Detection

The basic principle of the simple pulse echo technique is to transmit an ultrasonic wave pulse through a sample, so that it is reflected back from the opposite face and measure the time difference between the echoes. The ultrasonic wave packet is produced by applying a high frequency, high voltage pulse to a transducer coupled to a sample. For producing a high voltage pulse in these experiments, a Matec 110 oscillator generated a square wave that was fed into a Matec 122B decade divider, lowering the repetition rate of the square wave by a factor of a 1000. A Matec 6600 high voltage, radio frequency, pulse modulator/receiver, triggered by this square wave, generated a driving pulse of approximately 600V peak-to-peak, at a frequency set to the fundamental or higher harmonic of the transducer; thus forcing it to oscillate at maximum amplitude resulting in better transmission of the propagated wave. The stressed transducer transmitted the ultrasonic pulse into the sample. The pulse travelled to the opposite face where it was reflected back towards the transducer and was then detected because the mechanical wave energy re-stressed the piezoelectric transducer; this stress was converted back to electrical energy and the transmitted pulse was amplified and sent to the oscilloscope. The remaining wave energy continued travelling back and forth, periodically stressing the transducer and consequently sending an electrical pulse to the oscilloscope, until the energy had

completely dissipated. As a result, these amplified periodic pulses sent to the oscilloscope formed an attenuated echo train. The equipment was set up such that, when the wave energy had been fully dissipated, the synchronised square wave that triggered the radio frequency pulse introduced the next driving pulse. A typical arrangement of the ultrasonic wave generating equipment is shown below in Figure 3.1. For a graphical representation of the transmission and detection stages, see Figure 3.2 (a) to (d).

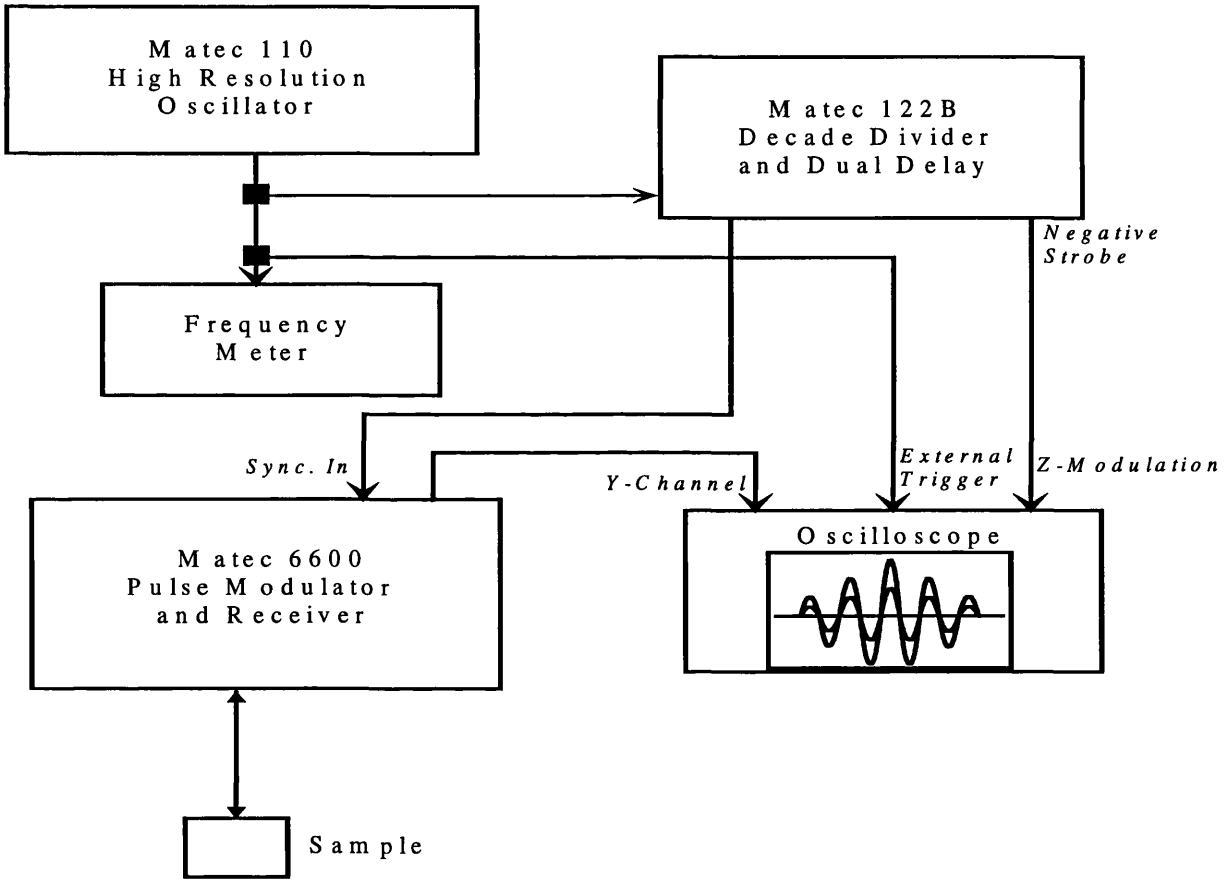

Figure 3.1 A block diagram of the transit time measurement equipment
(arrows denote electrical signal direction and filled squares are electrical junctions).

3.2.2 Displaying and Highlighting the Echo Train

Achieving a precision in measurement of the ultrasonic velocity to 1 part in 10^3 required isolating two ultrasonic pulses from the rest of the echo train, overlapping them and then increasing the resolution of the time base by magnifying the

oscilloscope trace. To reach this point, a pair of strobe pulses generated by the Matec 122B dual delay was sent to the Z-Modulation input of the oscilloscope (shown in Figure 3.1). These pulses were triggered by the dual delay just after the high voltage driving pulse, mentioned in the last paragraph, was triggered. A higher illumination of a section of the trace, with respect to the rest of the trace, could be seen after the strobes were triggered. The time between these two strobe pulses was adjusted manually to equal the time taken for the wave to travel twice the sample thickness, i.e. two consecutive echoes were highly illuminated (Figure 3.2 (e) shows a basic representation of this process). The intensity of the rest of the echo train was lowered, isolating the two echoes on the oscilloscope. The high resolution oscillator output was used to trigger the oscilloscope; an adjustment of the oscillator frequency was made until the isolated echoes appeared to be overlapped and in phase as shown in Figure 3.3. To enable a higher resolution of the oscilloscope, the time base was speeded up to magnify the display.

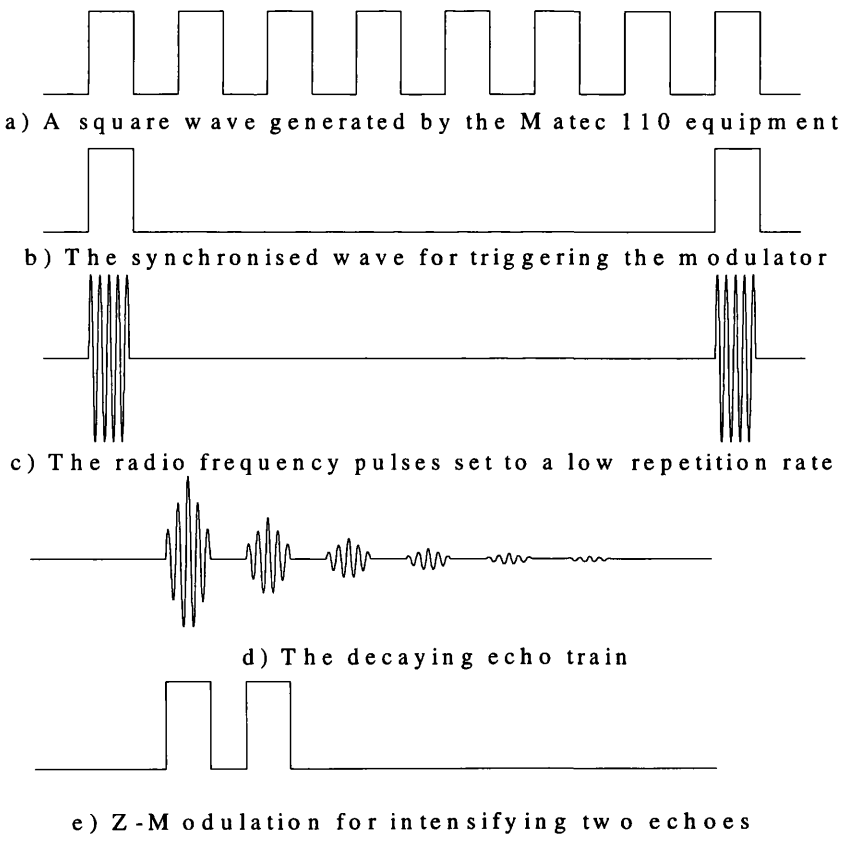

Figure 3.2 The various stages of transmission and detection of ultrasonic waves. The horizontal axis represents time.

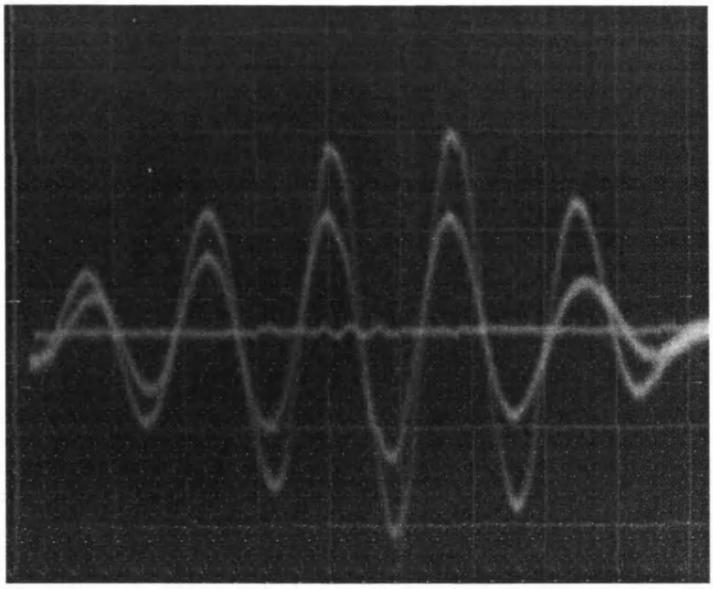

Figure 3.3 Two overlapped echoes at 5 MHz carrier frequency.

3.2.3 Ultrasonic Velocity Calculation

To determine the absolute velocity at a given temperature is not straightforward, as it requires overlapping the correct cycles in the magnified trace; the process of correctly overlapping two echoes becomes more difficult as the frequency increases. At 5 and 10 MHz, the number of cycles in each echo is small (example shown in Figure 3.3) and determining the correct overlap is simple. However, for frequencies of 30 and 50 MHz cycle mismatches can create errors in the absolute velocity values of up to 10%. Two methods were therefore used for determining the correct overlap of the two echoes when frequencies of 30 MHz and above were needed. Firstly, starting at the high amplitude end of the train with two consecutive echoes symmetrically overlapped (Figure 3.3) and then moving the strobe pulse centred on the second echo over to the third and then fourth and so on, a total phase shift was seen through the entire echo train. By altering the overlap frequency, a comparison of phase shifts for different cycle-to-cycle matches was made. Where the smallest total phase shift occurred, this was taken to be the correct overlap. Bonding and phase shifts from reflections in the sample also increased the difficulty in determining the overlap since these time lags caused asymmetrical echoes, therefore, a second method was introduced; this method was outlined by Papadakis (1967). He explained that the phase shift in the pulse at the

transducer-sample interface needed to be addressed to find the correct cycle-to-cycle matching and hence the absolute velocity; the matching of leading edges of each echo was improper. His method, in summary, stated that the right cycle-to-cycle match would be when the carrier frequency was detuned by 10% giving the smallest phase change of any of the compared cycles (assuming a very thin bond). The second method was not used in a quantitative manner, but only as a guide to aid the first method. The correct frequency, when found, was read from the frequency counter and then used to calculate the natural velocity (W) where

$$W = 2l_0 f\,, \tag{3.1}$$

where l_0 is the thickness of the sample under ambient conditions; an average value of l_0 was determined using a digital micrometer.

3.3 Ultrasonic Wave Attenuation Measurements

3.3.1 Introduction

Generally, attenuation is a measure of the absorption and scattering of the ultrasonic wave within the sample. A loss in echo amplitude can be seen on the oscilloscope trace when following the train from left to right; the reason for this loss is each pulse, transmitted through the transducer and converted to an electrical signal, having made one more round trip than its predecessor, has given more energy to the sample. Depending on the frequency of the ultrasonic wave, different wave energy loss processes, such as scattering losses arising from lattice defects and absorption losses related to dislocation damping, phonon-phonon interaction, ferromagnetic resonance interaction effects and so on (Truell et al. 1969), can be determined through attenuation measurements. The method used here to determine the ultrasonic wave attenuation was to find the peak voltage values for two consecutive echoes and then compute the attenuation, in decibels, using

$$\alpha = 20\log_{10}\left[\frac{V_1}{V_2}\right], \tag{3.2}$$

where V_1 and V_2 are the peak voltage values of each selected echo. The attenuation is usually expressed as a coefficient in units of $\mathrm{dBcm^{-1}}$; this is calculated by dividing α by the twice the ultrasonic path length, i.e. the distance between opposite parallel faces of the sample traversed by the ultrasonic wave.

3.3.2 Ultrasonic Wave Attenuation Detection and Automatic Measurement

Detecting and measuring two peak voltage values from the echo train is a similar process to measuring the ultrasonic velocity, whereby two echoes have to be strobed to allow their respective voltages to be measured. No overlap or magnification of any part of the trace is required, allowing the attenuation to be automatically measured. To detect peak voltages anywhere on the echo train, a demodulated echo train from the video output of the Matec pulse modulator was fed into the peak detector and the y-channel input of the second oscilloscope (Figure 3.4). In the peak detector, a section of the echo train passed through a gate, which was triggered externally, and the peak voltage was detected; after a delay, another section of the train was gated and a second peak value was found. Strobe pulses that were fed to the second oscilloscope were used to see the two gated sections of the echo train; the delay time between these strobes was altered by the experimenter, allowing different peaks to be selected. The two detected peak voltages were displayed on the Racal multimeter; the voltages were then available to be read and stored by a computer.

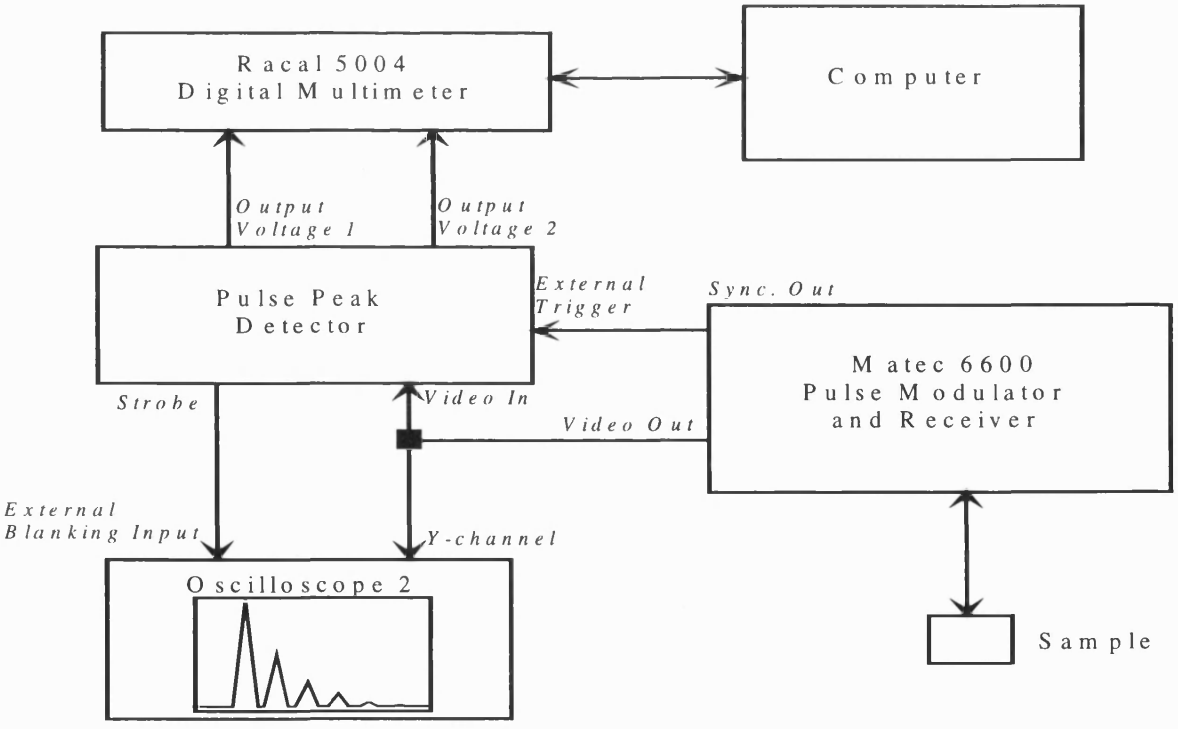

Figure 3.4 The attenuation equipment (arrows denote electrical signal direction and the filled square a electrical junction).

3.4 Hydrostatic Pressure Equipment and Measurements

3.4.1 Introduction

When measuring the pressure dependence of the bulk properties of materials, the application of hydrostatic pressure is a safe and accurate method, even though its pressure range is small (0-0.3 GPa) compared to other available techniques. The principle of the hydrostatic pressure technique is to immerse a sample in fluid and apply a uniform compression to the fluid via a piston-cylinder set up; the pressure is uniformly distributed to all surfaces of the sample by the fluid. Relatively large samples can be compressed using this technique, which is ideal for ultrasonic studies. Since the pressure is applied uniformly and its range is small, experiments could be repeated a number of times without causing irreversible damage to samples.

3.4.2 Pressure Equipment

The main components of the pressure apparatus, illustrated in Figure 3.5, consisted of a pressure cylinder and two end pistons (all made of EN26 nickel alloy carbon steel). Other components involved in the pressure system were: 'O' rings and PTFE delta rings, used for sealing in the pressure transmitting fluid; Dow Corning 200/1000cs silicone oil, the pressure transmitting fluid that operates at a temperature between 300 and 470K; a pre-calibrated manganin resistance coil used as the pressure measuring device which had a four point electrical resistance connection to a Racal-Dana 5004 digital multimeter.

Pressure was converted from ohms to kilobars using Equation (3.3), which relates the resistance of the manganin coil to the applied pressure by

$$P(kbars) = \frac{1}{2.4x10^{-3}}\left(\frac{R}{R_0} - 1\right), \tag{3.3}$$

where R and R_0 are the resistance values at raised and ambient pressures, respectively.

The temperature was controlled by a Eurotherm mini 17-90B controller, electrically connected to a heating jacket surrounding the pressure cylinder; this temperature was

monitored externally on a meter connected to a calibrated NiCr-NiAl thermocouple, positioned close to the sample. An alarm was also fitted to warn the user of seal failure. All the pressuring equipment was contained in a shielding steel case. The ultrasonic wave was transmitted and received by a high voltage electrode, which ran to the Matec 6600 equipment.

3.4.3 Pressure Measurement Technique

A manually operated hydraulic pump forced a large piston, contained within the shielding case, on to the upper piston of the pressure apparatus, shown in Figure 3.5. The resulting pressure increase was transmitted to the sample via the silicone oil. An initial test was performed by putting the system under a pressure of about 1 kbar to make sure the equipment was working properly. From this initial test, the experimenter could determine if there was a good bond between sample and transducer. The first measurement was taken after the pressure was released and the pressure cell returned to ambient conditions. As the sample was compressed to the first pressure value required, the temperature of the cell increased. The value for the overlap frequency was only taken when the temperature fell back to its initial value, i.e. thermal equilibrium was reached. The echo overlap equipment was adjusted to find the new frequency value and the procedure was repeated. Each pressure run was cycled from ambient pressure up to 2 kbars.

3.4.4 Data Acquisition for Pressure Dependent Ultrasonic Wave Attenuation and Velocity Measurements

Several FORTRAN programs, written by Wang (1993), were used to collect and store the measured data. The programs were set out as follows: the resistance at ambient conditions of the manganin coil was logged on the program. At each new pressure and consequently new overlap frequency, a manual input of both resistance and frequency values (read from the multimeter and adjusted frequency counter, respectively) was performed by the experimenter. The computer program then calculated the pressure in kbars using Equation (3.3). Attenuation data, at each pressure, were automatically determined by a computer program, which read a number of voltage values from the

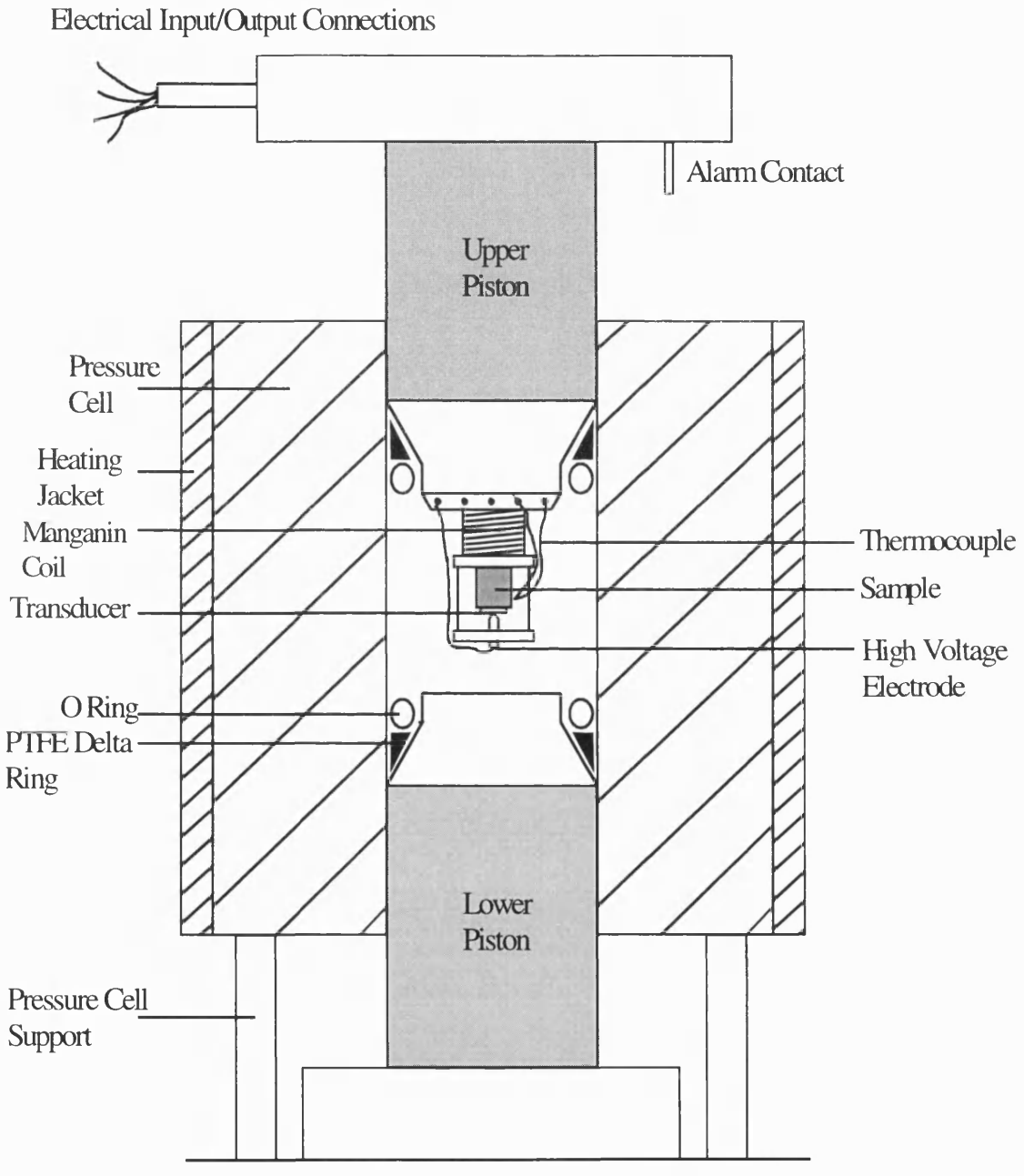

Figure 3.5 The hydrostatic pressure equipment.

digital multimeter; the data were then averaged and used to find α (Equation (3.2)), and finally recorded by the computer.

3.5 Temperature Equipment and Measurements

3.5.1 Introduction

For repeatedly measuring physical properties at low temperatures, the Cryophysics model 22C closed cycle helium cryostat is useful in a number of ways. Like the hydrostatic pressure equipment, the temperature apparatus is suitable for use with ultrasonic measurements because of the relatively large samples that can be cooled from ambient temperatures down to 15K in a vacuum. The cryostat has a capacity to produce small temperature changes (0.1K), which is an advantage for measuring significant property changes over small temperature ranges, e.g. phase transitions. The helium cryostat also has an accurate temperature monitoring and controlling system and can be operated remotely by computers.

3.5.2 Temperature Equipment

In all cases where the elastic properties as functions of temperature have been measured, the Cryophysics model 22C closed cycle helium cryostat was used. Low temperatures were reached inside the aluminium radiation shielded compartment, pictured in Figure 3.6, by helium gas being continuously compressed (compressor) and expanded (cold head assembly) keeping the cold head at a temperature of 10K. The compartment was also kept under a vacuum by a diffusion and rotary pump system; vacuum pressure (<0.02 Torr) was monitored on a high vacuum pressure gauge. A Lakeshore temperature controller stabilised the temperature through a heating coil and sensor, which were mounted under the sample (see Figure 3.6). A spring-mounted electrode, which also held the sample in place, was used to transmit and receive the ultrasonic signal.

3.5.3 Temperature Measurement Technique

Ultrasonic pulse-echo overlap frequencies and attenuation data as functions of temperature were taken in the same manner as the pressure dependent data. At each temperature of measurement, which was controlled and recorded by a computer

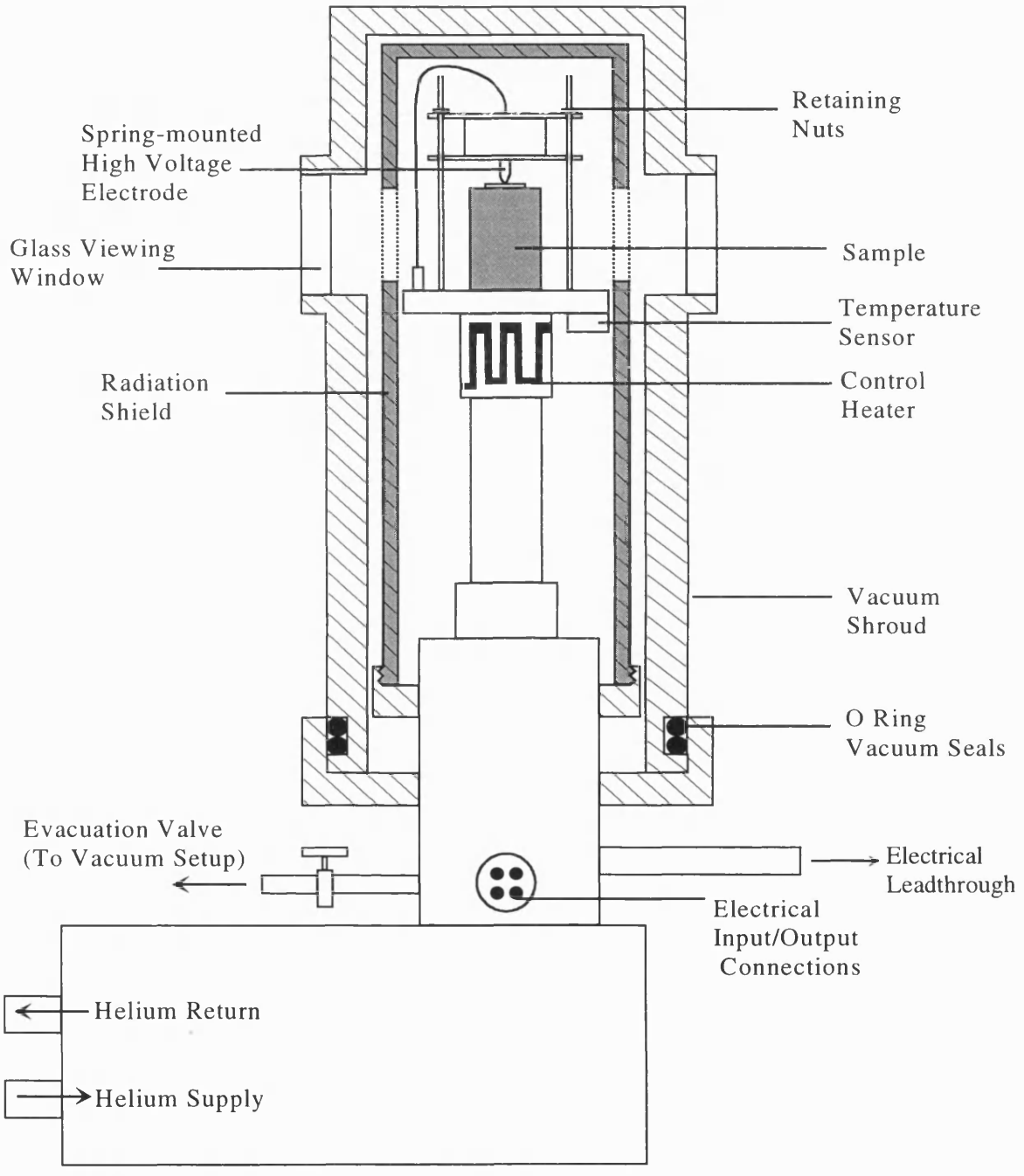

Figure 3.6 The cryogenic cold head assembly (only an electrical connection to the high voltage electrode has been shown; other electrical connections exist within the assembly, but have been omitted).

program remotely operating the Lakeshore temperature controller, the sample was allowed to reach thermal equilibrium before an overlap frequency was recorded and the attenuation automatically measured. Data were recorded by the same method as that described in Section 3.4.4.

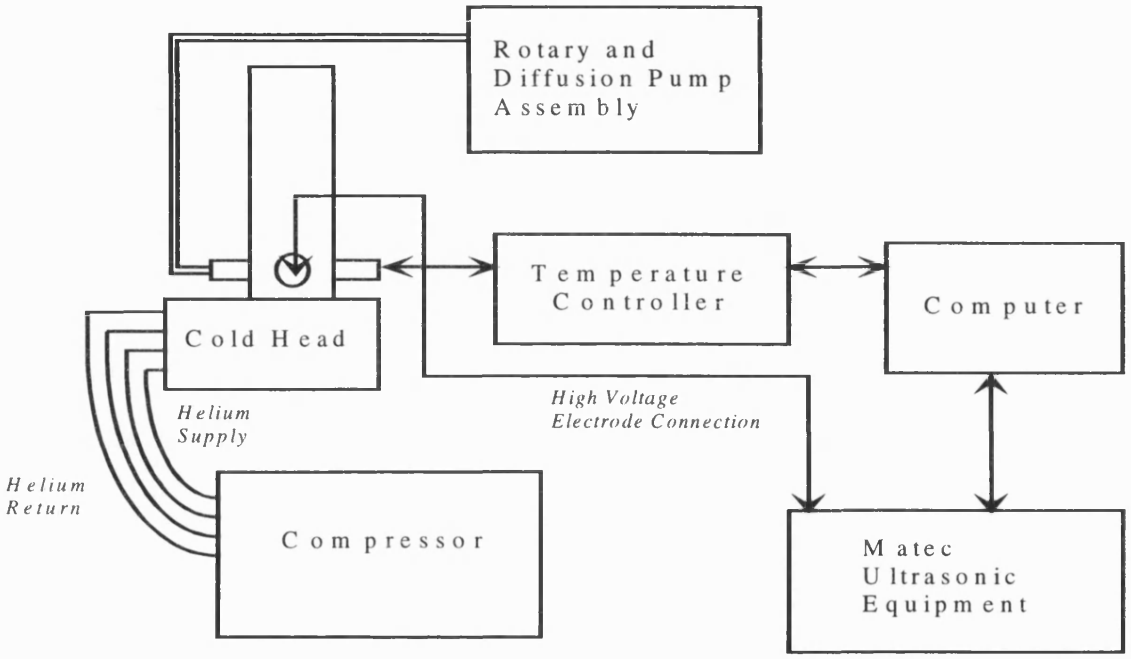

Figure 3.7 Block diagram of low temperature equipment
(arrows denote electrical signal direction).

3.6 Piezoelectric Transducers

Quartz piezoelectric transducers are used to transmit and receive mechanical vibrations. Piezoelectric transducers are devices that produce a mechanical displacement proportional to an applied electric field; the principle used is the converse piezoelectric effect. For signal acquisition the reversible process, the direct piezoelectric effect, is employed. For a compound to be piezoelectric, it must not possess a centre of symmetry. This crystal property occurs naturally, to a marked degree, in some crystalline materials such as quartz, tourmaline, ammonium dihydrogen phosphate (ADP), Rochelle salt, cadmium sulphide, diamine tartrate (EDT), dipotassium tartrate (DKT) and lithium sulphate (LH) (Mason 1958; Goldman 1962). In pulse-echo ultrasonics, quartz transducers are used because of the following

properties: a high Curie temperature, which has an advantage over piezoelectric ceramics when using a bonding agent such as indium, a low coefficient of thermal expansion, low internal friction, high mechanical strength, a capacity for obtaining highly polished surfaces for good wave direction.

Manufacturing suitable quartz transducers for use in ultrasonics takes the following route: they are cut from a quartz crystal in such a way as to allow for longitudinal and shear mode vibrations to be generated. X-cut (longitudinal) transducers are cut with their thickness parallel with the *x*-axis crystal direction, the electric axis. Similarly for Y-cut (shear) transducers, their thickness lies along the *y*-axis direction, the mechanical axis (shown in Figures 3.8 (a) and (b)).

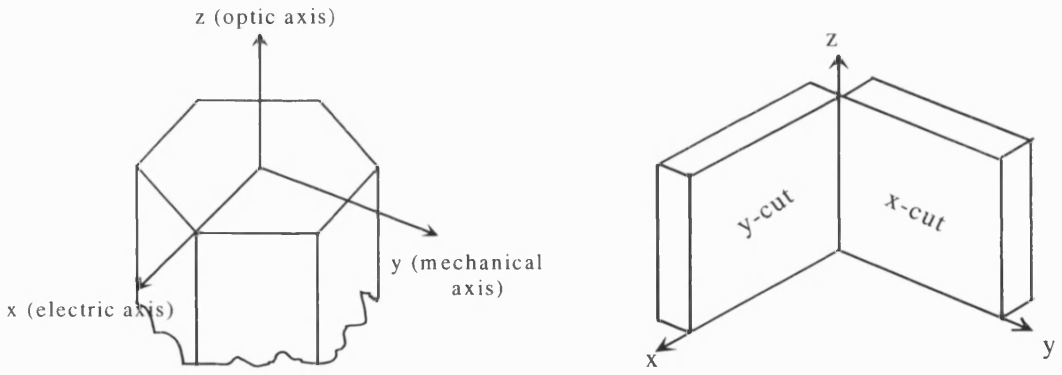

(a) (b)

Figures 3.8 (a) and (b) A representation of the axes of a quartz crystal and the transducer cuts, respectively.

The transducers are processed as circular discs and coated with a thin layer of gold; a small insulating ring is left on the upper surface to separate the gold into two electrodes. The gold is then used to apply an electric field to induce a mechanical displacement. The fundamental frequency of a quartz transducer is dependent on its thickness (L) according to the equation

$$L = \lambda / 2, \tag{3.4}$$

where λ is the wavelength corresponding to a fundamental frequency.

To produce mechanical vibrations from the transducer requires it to be operated at odd harmonics, since when an electric field is applied the strain changes sign every half wavelength and causes cancellation of even harmonics. The frequency of these odd harmonics is given by

$$f_n = f_0(2n-1). \tag{3.5}$$

$n = 1, 2, 3,.....$ and f_0 is the fundamental frequency.

The mechanical vibration of the transducer is piston like and will transmit an essentially plane wave into a sample coupled to it; but beyond a distance (d) from the piston source the wave starts to diverge and becomes spherical (Mason 1958). Limited divergence occurs up to distance (Mason 1958) defined by

$$d \approx a^2 / \lambda, \tag{3.6}$$

and a is the radius of the piston source.

3.7 Bonding Agents

To transmit sound energy into a sample requires a transducer bonding agent. At the transducer-bond boundary, energy will be lost. How much energy depends on the matching of acoustic impedances (Z) of the materials, where

$$Z = \rho c \tag{3.7}$$

and ρ and c are the material density and the sound velocity generated in the material, respectively. The reflection coefficient (R) that defines the amount of acoustic energy reflected at the boundary between two materials is related to the impedances by

$$R = (Z_1 - Z_2) / (Z_1 + Z_2). \tag{3.8}$$

Z_1 and Z_2 are the impedances in the transducer and sample, respectively. A suitable bonding agent should have the following qualities:

(1) an acoustic impedance close to that of the bond and sample, which creates a low reflection coefficient and high energy coupling;

(2) be non-toxic and non-corrosive to both the sample and transducer;

(3) be capable of producing and maintaining a thin, parallel and uniform bond under the temperature and pressure conditions required;

(4) be easily removable after use.

Bateman (1967) and Schreiber et al. (1977) listed a number of bonding agents appropriate for cryogenic temperatures: Nonaq stopcock grease, Natural Gas, Dow-Corning silicone fluid. Nonaq stopcock grease and Apiezon-N vacuum grease (Cankurtaran et al. 1993) were chosen for low temperature ultrasonic measurements. Dow-Corning resin was used for pressure and room temperature work, as suggested by Schreiber et al. (1977). Different methods, mainly dependent on the properties of the samples, can be applied to create a good bond between transducer and sample; a thin and uniform bond was achieved by wringing the transducer while coupled to the sample.

3.8 Ceramic Sample Preparation and Standard Non-Destructive Characterisation Techniques

3.8.1 Grinding and Polishing Procedure

All hard ceramics studied here were ground using a Logitech PP5 polishing jig on a PM5 Logitech polishing machine. These ceramics are amongst the hardest known materials, so care was taken to select the right grinding powder for each material, i.e. often grinding powders with a similar hardness to the ceramic sample had to be used. To produce typically 0.5 μm flatness and 2 seconds of arc (10^{-6} radians) parallelism, a combination of a 14 μm and then a 6 μm diamond paste was used.

3.8.2 Sample Density Measurements

Archimedes' rule was employed to measure the density of each ceramic for two reasons. Firstly, bulk ceramics are prone to developing pores, so mass and volume measurements would give incorrect densities. Secondly, in some cases the shape of the sample did not permit accurate volume measurements anyway. Calculation of the sample density (ρ) involved an average measurement of the weight in air (W_A) and then in the appropriate flotation liquid (W_L), acetone or distilled water, and then using

$$\rho = \frac{W_A}{W_A - W_L} \rho_L, \tag{3.9}$$

where ρ_L is the density of the flotation liquid.

3.8.3 X-ray Diffraction Studies

X-ray diffraction has been used here to characterise the sample by gathering data on the number of phases present in each sample. Initially the aim of X-ray analysis was to discover the dominant phase in the material. The diffraction measurements were performed, using a 4kW Philips PW1730 assembly, on three approximately orthogonal faces of the hard ceramics, as in most cases these samples possessed an almost parallelepiped shape. Where possible alongside the detection of primary phases, secondary phases were qualitatively determined. X-ray data standards, which were used for comparison with measured ceramic X-ray data, were taken from the International Centre for Diffraction Data (ICDD) powder diffraction database.

3.8.4 Electron Microprobe Analysis

To further characterise the samples, a JEOL model 8600 electron microprobe analyser was used for quantitative phase analysis in conjunction with the X-ray analysis. Using the analyser it was possible to find percentages of the constituent elements; following on from this, a determination of which elements contributed to secondary phases and impurities was carried out. Wavelength dispersive analysis was used for the quantitative determinations; the principles of this method are described by Reed (1993).

3.9 Equipment and Data Errors and Their Corrections

Below is a list of errors incurred, and in some cases how they were reduced or eliminated, in: measuring and calculating ultrasonic velocities and attenuations, determining elastic and nonlinear acoustic properties, temperature and pressure measurements.

3.9.1 Absolute Velocity

To produce a precision of 1 part in 10^3 in the absolute ultrasonic velocity of any given material, the overlap frequency and sample length measurements at room temperature were repeated at least three times. The sample lengths were determined using a digital micrometer with a resolution of one micron.

3.9.2 Ultrasonic Wave Diffraction

The divergence of a stress wave in solid bodies causes small changes in the velocity calculation. Corrections to velocity for diffraction have been calculated using equations given by Papadakis (1967) and are no more than 0.02% for the longitudinal mode and 0.018% for the shear mode. These corrections are smaller than the precision errors determined for the velocities and have not therefore been included.

3.9.3 Transducer Time Lag Error and Correction

A time lag occurred at the transducer-sample boundary when the incident pulse from the sample had its transmitted amplitude reflected back and forth in the transducer (Kittinger 1977). Kittinger (1977) attributes this time lag to a superposition of partial pulses in the transducer medium being created; each partial pulse having a time lag equivalent to the reciprocal of the fundamental frequency, created a delayed response time and altered the measured frequency of the ultrasonic wave. The time lag can create a velocity change of 1-2% depending on the material properties. Therefore, a correction for this time lag was made on every velocity calculation. To apply this correction, a previously written computer program, using correction factors determined by Kittinger (1977), was employed.

3.9.4 Attenuation Errors

Measurement of absolute attenuation using the pulse echo overlap method is difficult because the parameters involved need to be precise to produce useful results. The two main types of error are those from non-parallelism of the two faces in the ultrasonic propagation direction, called wedging, and those from sidewall diffraction (Truell et al. 1969). Errors concerning non-parallelism arise because of the difficulty of producing perfectly plane, parallel surfaces. Since the transducer is phase sensitive, waves arriving back at the transducer at an angle cause a modulation effect (an example of this effect is seen in Figure 3.9). Higher frequencies enhance the modulation effect. A derivation of the analytical approach to this problem is found in Truell et al. (1969). The outcome of this parallelism problem is that the faces need to be parallel to around 10^{-6} radians to produce a good exponential decay (in highly

attenuated materials). Ultrasonic velocities are also affected by wedging but the changes are small. Diffraction effects on attenuation can cause very large errors at low frequencies and small transducer diameters because mode conversion from sidewall reflections causes interference and maxima and minima appear in the observed echo train. A maximum in the echo pattern will occur around a distance equivalent to a^2/λ from the transducer (a and λ are the transducer diameter and wavelength of the propagated wave, respectively). Increasing the frequency will increase the parameter d (Equation (3.6)) and lower the beam divergence; thus reducing the diffraction effects, but as mentioned earlier, enhancing the wedging effect. These problems were reduced by good sample preparation and employing the appropriate carrier frequencies. If the absolute attenuation of the wave due to losses in the sample is low (i.e. so that the received echo train does not have an exponential decay), then large errors are associated with the measured absolute attenuation; this is due to the diffraction and wedging effects masking the losses produced in the sample. The diffraction and coupling effects make the measurement of absolute attenuation very difficult as they always contribute to it. Therefore, attenuation measurements were utilised for comparison purposes only.

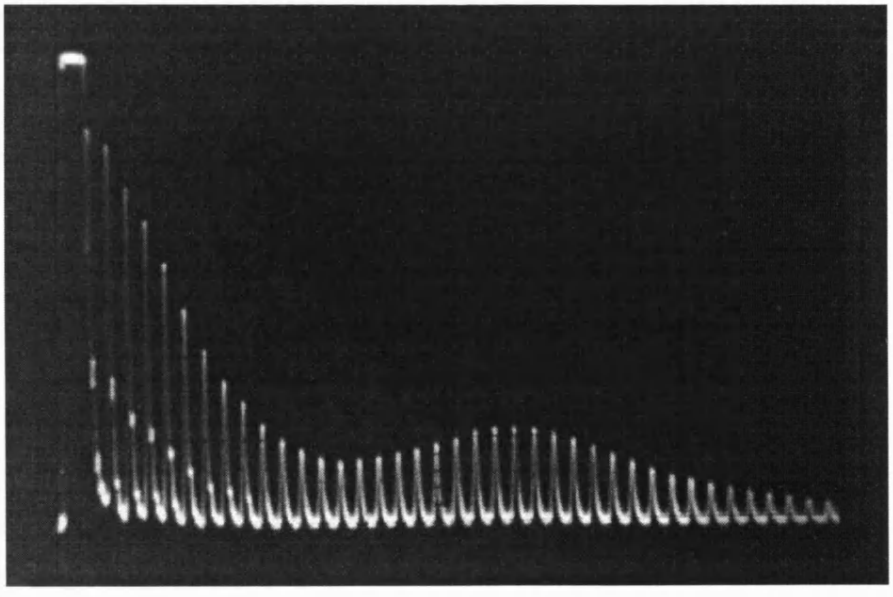

Figure 3.9 Oscilloscope trace of the non-parallelism effect for silicon carbide at 50 MHz.

3.9.5 Temperature Measuring Devices

Equipment for monitoring temperature variations such as the NiCr-NiAl thermocouple and the cryostat temperature controller had precision errors. For the controller, the precision in temperature readings above 40K is 75mK which amounted to a precision error of 0.1%; therefore this small error was not included in any calculations involving temperature. A calibrated NiCr-NiAl thermocouple is precise to within 0.5°C; but as this temperature gauge was used to determine when thermal equilibrium was achieved in pressure measurements, it did not have a bearing on any calculations performed.

3.9.6 Temperature Coefficient of the Manganin Pressure Gauge

Manganin pressure gauges fill many of the criteria for reliable measurements, such as: a high pressure coefficient, low temperature coefficient, a linear resistance-pressure relationship, high resistivity. Samara and Giardini (1964) discovered that the manganin gauge gave a linear pressure response at relatively high temperature, thus making it a reliable gauge. In addition, by using multi-calibrants against the manganin gauge, a coefficient of pressure around 2.4×10^{-3} $kbar^{-1}$ was produced; this value was used in the electrical resistance-hydrostatic pressure conversion (Equation (3.3)). For a compression range of 0-0.2 GPa, the gauge gives a linear response to pressure and the temperature coefficient has no influence on any calculations. As the manganin gauge had been pre-calibrated, errors in pressure measurements were attributed to the digital multimeter resolution. In the pressure range 0-2 kbars, the resistance of the manganin coil was between 70 and 80 ohms with a resolution of 1 milliohms.

3.9.7 Pressure and Temperature Dependence of the Quartz Transducer Carrier Frequency

According to Davies and O'Connell (1977), the pressure coefficient of the quartz transducer carrier frequency for both longitudinal and shear modes is the order of 10^{-11} Pa^{-1}. Changes in carrier frequency for the pressure range 0-0.2 GPa amounted to an error of approximately 0.1%. The pressure induced transducer errors were found to be small compared with the precision errors produced in calculating the ultrasonic

velocity pressure derivatives. Similarly, the coefficient of thermal expansion of quartz is around 10^{-6} K^{-1} (Barron 1982). Over the temperature range used in these studies, the effects of thermal expansion on the carrier frequency result in changes of around 0.1%. Since the carrier frequency is used in the time lag correction in Section 3.9.3, the changes in time lag corrected velocity as a result of the carrier frequency changing with temperature is small compared with the calculated precision errors in velocity at a given temperature.

3.9.8 Differences in Natural and Actual Velocity

The linear coefficient of thermal expansion is very small for the hard ceramics studied here; a number of typical values have been tabulated (Table 3.1) below. The dimensional changes in these materials brought about by thermal expansion are negligible when measuring samples with ultrasonic path lengths around a centimetre. A correction for the change in path length and density due to pressure is neatly built into Equation (2.38) for the pressure derivative of the elastic stiffnesses, derived by Thurston (1965). A value for bulk modulus (B) at ambient pressure, used in the calculation of the these pressure derivatives, compared with that at 0.2 GPa gives a negligible error, so the former value was taken for B.

Table 3.1 Linear thermal expansion coefficient (α) in different temperature ranges for a number of refractory materials.

Material	Linear Thermal Expansion Coefficient α ($x10^{-6}$ K^{-1})	Reference
AlN	2.56 (300K)	Slack and Bartram (1975)
β–Si_3N_4	4.0 (40-1000°C)	Miyauchi and Kobayashi (1985)
TiB_2	7.67 (20-1000 °C)	Bellosi et al. (1992)
B_4C	5.73 (300-1950K)	Tsagareishvili et al. (1986)
Fe_3C	4.63 (20-100 °C)	Belikov and Saumskaya (1962)
TiC	7.39 (20-700 °C)	Stuart and Ridley (1970)
TaC	6.15 (20-700 °C)	
ZrC	6.03 (20-700 °C)	

3.9.9 Use of the Adiabatic Instead of Isothermal Bulk Modulus

Adiabatic (B^S) and isothermal (B^T) bulk moduli are thermodynamically related (Cankurtaran et al. 1993) by

$$B^T = B^S / (1 + \gamma^{th} \beta T). \tag{3.10}$$

Ultrasonic measurements generated adiabatic elastic moduli values and calculations of B^T from B^S required values for each material of γ^{th} (thermal Grüneisen parameter) and β (volume thermal expansion); in some cases these values are sparse. In the temperature range for the ultrasonic measurements in this study, the difference between the two bulk moduli is small and within the calculated precision errors. For example, typical room temperature values of the parameters in Equation (3.10) for the compound AlN are γ^{th}=0.65 (Dodd et al. 2001), β (=3α)=7.6x10^{-6} K^{-1} and T=300 K which result in a B^S:B^T ratio of 1.001. Therefore the adiabatic bulk modulus is used.

3.9.10 Errors in Calculation of Elastic Properties and Grüneisen Parameters

Measurement errors from quantities such as density, overlap frequency, carrier frequency and sample thickness all contribute to errors in the calculated elastic moduli, acoustic Debye temperature and Grüneisen parameters. For this type of calculation the root mean square errors were used. These errors for independent variables such that $z = F(x_1, x_2, x_3, ...)$ were computed using

$$\Delta z = \left[\sum_i \left(\frac{\partial F}{\partial x_i} \Delta x_i \right)^2 \right]^{\frac{1}{2}}. \tag{3.11}$$

3.10 Temperature Dependent Electrical Resistivity Measurements

3.10.1 Introduction

The electrical resistivity and its temperature dependence are fundamental measurements for any solid, since the electron plays a significant role in the characteristic properties of materials. For materials behaving in a metallic manner, the electrical resistivity as a function of temperature is an important parameter in physics, as it sheds light on the degree of electron-phonon and other interactions. In engineering and materials science, the effects of electron-phonon coupling, or lack of

in some cases, is important for design purposes. Therefore, alongside the measurement of the elastic properties of these hard ceramics, the electrical resistivity as a function of temperature above 300K was also measured on thin ceramic bars, using the collinear direct current four-point probe method. These measurements were performed using apparatus, newly designed by the author of this study, which was capable of reaching temperatures around 1400K.

3.10.2 Four-Point Probe Electrical Resistance Measurement

The principle of a standard four-point probe resistance measurement, generally used on a wide variation of sample shapes, is to apply a constant direct current to a sample surface through two outer electrical point-contact probes and measure the voltage drop across two inner probes, with the four probes collinearly arranged. Using a high impedance input, high resolution voltmeter ensures that the voltage measured is only that developed across the sample and not an "apparent" voltage, which would include EMFs from ohmic contacts and connecting electrical cables (Wieder 1979).

3.10.3 Electrical Resistance Measurement Equipment

The following description of the apparatus has been split into three sections: the components of the electrical circuitry, the temperature source and monitoring equipment and the high temperature shielding equipment. The electrical circuit consisted of four 1mm diameter tungsten rods, each with a point contact to the sample surface (illustrated in Figures 3.10 and 3.11), the sample itself, a Time Electronics current calibrator with a range 1 μA–1 A (accuracy <0.05%) and a Keithley digital multimeter (DMM) with a resolution of 1 μV (accuracy 1%). To retain contact between probes and sample, a "spring effect" was employed throughout each experiment. In accordance with the four point probe measuring method, the two outer probes (rods labelled 1 and 4 in Figure 3.11) had electrical connections to the current source and the two inner probes to the DMM (rods labelled 2 and 3). Raising the temperature of the sample was achieved by using an alumina tube furnace coupled to a Eurotherm temperature controller, which monitored the temperature inside the furnace using a platinum/rhodium thermocouple (shown in Figure 3.12). For an accurate

measurement of the sample temperature, a calibrated NiCr-NiAl thermocouple was positioned next to the sample (Figure 3.10). The shielding equipment consisting of an alumina rod and outer shield was chosen for two reasons: alumina is an electrical insulator with a resistivity at 1000°C of around 10^6 Ωcm (Gitzen 1970), and its use ensured that there was no current leakage to the material supporting the sample. Secondly, alumina possesses refractory properties, i.e. good mechanical stability at high temperatures, so was ideal in this temperature environment.

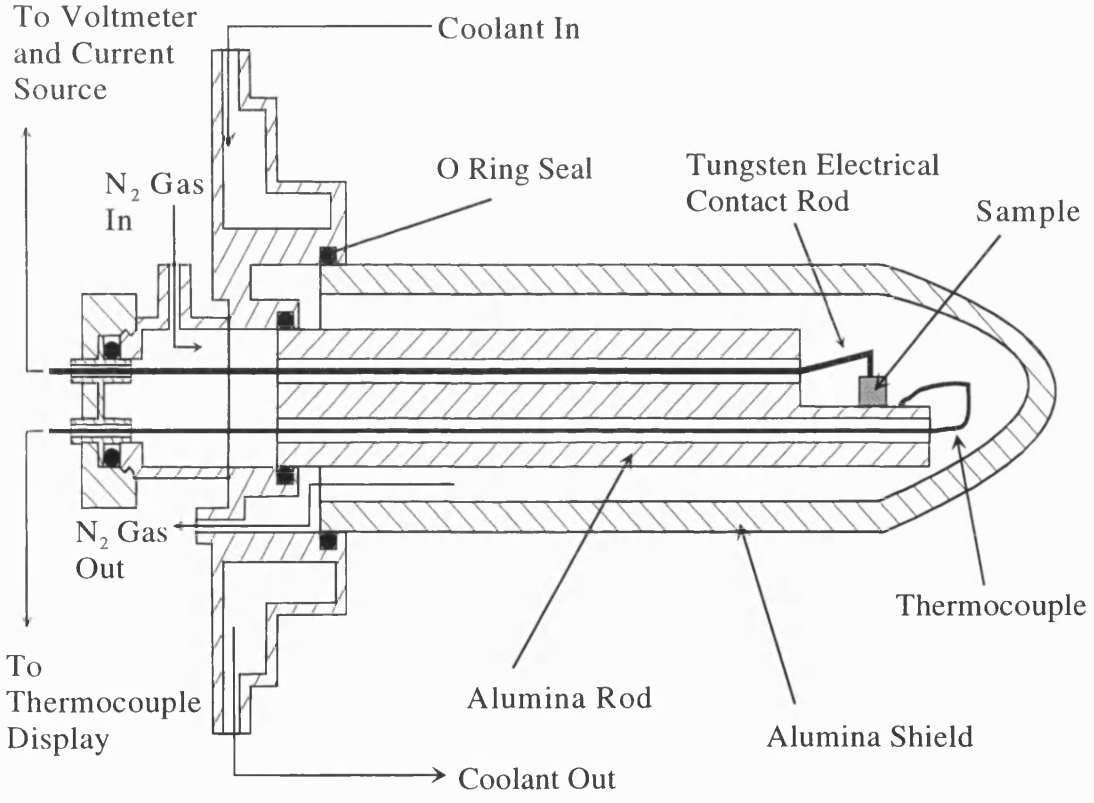

Figure 3.10 A cross-sectional side view of the resistance measurement equipment.

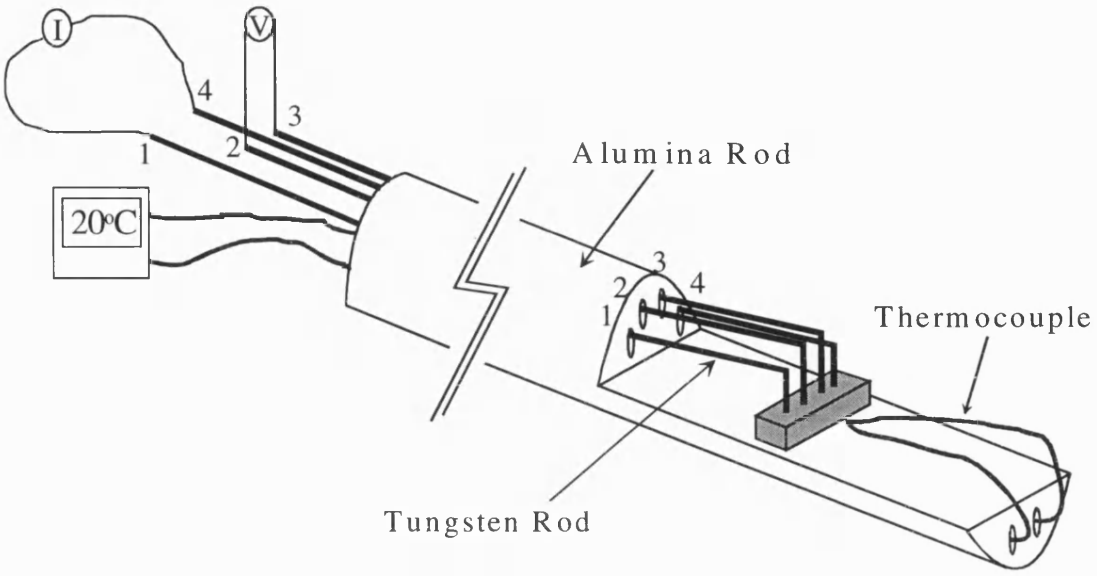

Figure 3.11 An enlarged section of both ends of the alumina rod, in Figure 3.10, showing the thermocouple, sample and four tungsten electrical rods.

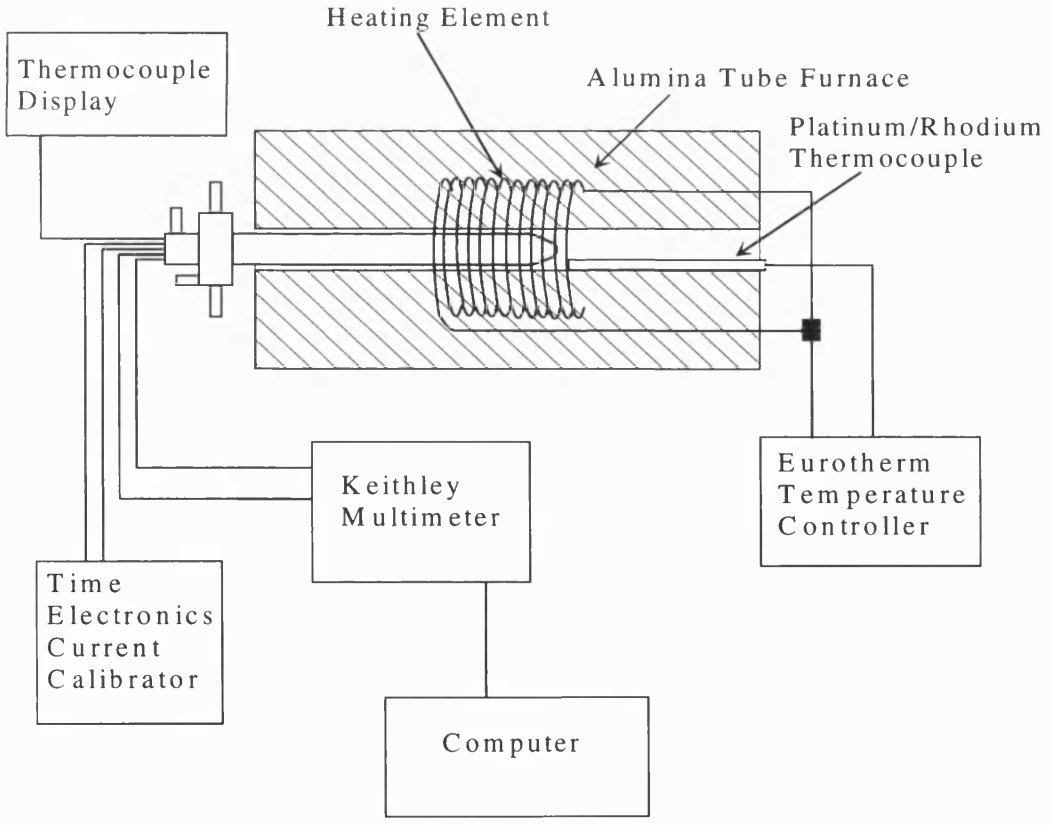

Figure 3.12 A block diagram of the electrical connections for the temperature equipment.

3.10.4 Electrical Resistance Measurement Technique

Since the ceramics were prone to oxidation at elevated temperatures (Wang et al. 1995a), throughout each experiment, a slow continuous flow of dry nitrogen was passed through the O-ring sealed chamber of the apparatus shown in Figure 3.10; the nitrogen was bubbled through water after exiting the compartment so as to monitor and maintain the flow rate. The region outside the furnace, i.e. the junction between the alumina rod and external electrical connections, shown in Figure 3.12, was cooled by a fast flow of water around that junction. This extraction of heat helped to keep all electrical junctions in the circuit at constant temperature and therefore reduced or steadied the thermal EMFs (reasons for the existence of thermal EMFs are found in Section 3.10.6).

A simple procedure was employed to measure the resistance at each temperature: a constant forward and then reverse current was applied to each sample for the duration of each measurement; an average voltage was recorded for each current direction. The two averaged voltages were added and averaged to remove the thermal EMFs and the resistance was calculated using Ohm's law and then stored. At elevated temperatures, resistance measurements may not have been performed in true isothermal condition; so to compensate for this, an overall average resistance calculation was performed by repeating the procedure mentioned above three times. At different high temperatures during the each experiment, the contacts were tested to see if they retained ohmic behaviour by applying forward and reverse currents with magnitudes spanning three decades and recording the corresponding voltages. A Quickbasic program specifically written for this experiment performed all these tasks. Finally, the resistivity (ρ) was calculated using the standard relation

$$\rho = RA / l, \tag{3.12}$$

where R is the resistance, A is the cross-sectional area perpendicular to current flow and l is the separation of the two voltage contact probes; an average measurement of the contact separation was performed using digital callipers.

3.10.5 Sample Density Measurements

Archimedes' principle, described in Section 3.8.2, was also employed to determine the density of each thin ceramic bar.

3.10.6 Sample Preparation

At the surface of the sample where current was applied, ohmic contacts were readily formed on metallic-like materials by lightly grinding off any oxide or unwanted surface compounds. This leaves a clean area for the hard tungsten point-contact probes to penetrate in to the bulk material. In contrast to forming ohmic contacts on metals, semiconductors require ohmic pads to be deposited on to their surface due to the rectifying behaviour of semiconductor/metal electrical junctions (Sze 1985). In the case where a sample possessed semiconducting behaviour, the following process was used to form pads: a Shipley S1813 resist was spun onto the sample using a photomask and Karl-Suss MJB-3 mask aligner. The ohmic layers were deposited in an Edwards 306 thermal evaporator. A lift-off process defined the ohmic pads and these were alloyed at 400°C for one minute in the presence of forming gas (90% nitrogen, 10% hydrogen).

3.10.7 Errors in Electrical Resistance Measurements and Electrical Resistivity Calculations

1. Thermal EMFs

Unwanted thermal EMFs arise in an electric circuit from two sources: electrical connections between dissimilar metals and thermal gradients inducing electric fields, the Seebeck effect (Wieder 1979). The EMFs attributed to dissimilar metals were reduced by keeping the number of connecting junctions to a minimum and where possible the electrical cables and junctions were made of the same conducting material. The other EMFs that were incurred when performing the high temperature measurements were minimised by a number of methods. The first method was cooling the apparatus with flowing water, for reasons explained in Section 3.10.4. The second, resistance measurements were taken in approximate isothermal conditions and finally the size of the applied current was purposely chosen so as not to cause Joule heating in the sample.

2. Probe Contact Placement and Sample Dimensions

Errors in measuring the correct voltage are also influenced by contact placement; certain conditions are placed on the separation of the collinear contact probes in relation to the sample dimensions. One of these conditions is that the diameter of the contacts must be small compared to their separation distance (Wieder 1979); this was achieved in these experiments by using point-contact probes. The second is that the probes are considered to be far from any of the sample edges, so that the sample surface may be considered as an infinite area of uniform resistivity. Another factor is the sample thickness that is also taken into account for corrections to measured resistances. For samples measured in this study, some of these conditions were not satisfied, so a correction factor developed by Yamashita (1987) based on Poisson's equation was applied to each resistivity calculation to test the shape effects; these effects were found to be negligible.

3. Thermal Expansion Coefficients

Since the thermal expansion coefficients for these hard ceramics are small (described in Section 3.6), their influence on the calculation of resistivity for each material was negligible.

4. Temperature Measuring Devices

Both thermocouples used in these experiments had been calibrated against a standard thermometer. Over the experimental temperature range, the maximum difference found between these two thermocouples was about 2°C, giving a less than 1% discrepancy. The NiCr-NiAl thermocouple used to measure the temperature of the sample had a precision within 0.5°C of the display reading.

5. Sample Density and Dimension Measurements

Similarly to the errors incurred in calculating the elastic properties, also described in Section 3.6, resistivity calculations contained errors from the determination of cross-sectional areas and contact probe separations; Equation (3.11) was also used here to determine such errors.

Chapter 4

Ceramic Aluminium Nitride (AlN), Titanium Diboride (TiB_2) and Boron Carbide (B_4C)

4.1 Introduction

The compounds aluminium nitride (AlN), titanium diboride (TiB_2) and boron carbide (B_4C) in their polycrystalline forms are important in industrial applications primarily because of their refractory nature: high melting point, high mechanical, chemical and thermal stability, and also their great hardness and resistance to both corrosion and wear (Carlotti et al. 1995; McNeil et al. 1993; Bellosi et al. 1992; Tennery et al. 1983; Thévenot 1990; Thompson 1990). In particular, by utilising their refractory properties and relatively low densities, both TiB_2 and B_4C ceramics are attracting interest for use in high temperature and corrosive environments, e.g. light body armour, cutting tools, jet engine components, sand blast nozzles and wear parts (Thévenot 1990; Wang et al. 1994; Schwetz and Grellner 1981). In addition, the electrical properties of these compounds span the electrical spectrum. Aluminium nitride can be classed as an insulator or wide band-gap semiconductor with an often reported direct band-gap of 6.2eV (Monemar 1999) and is already utilised as a substrate for integrated circuits (Gerlich et al. 1986; Ruiz et al. 1994; Xia et al. 1993) and in high power, high temperature transistors applications (Deger et al. 1998). Recently, the large band-gap of AlN coupled with its thermal and mechanical stability has led Monemar (1999) and Mohammad and Morkoç (1996) to believe that these properties may be used to realise the fabrication of LEDs and lasers capable of emitting light in the blue-ultraviolet region. Boron carbide is a p-type semiconductor, which results from the ideal stoichiometry of four boron atoms to one carbon being seldomly reached. The replacement of carbon atoms for boron atoms removes bonding electrons and leaves hole-like charge carriers of density ~10^{21} cm^{-3} (Aselage et al. 2001). Emin (1987) has suggested that B_4C has the potential to be used in high temperature semiconductor technology. The metallic-like high electrical conductivity of TiB_2 ceramics (Williams 1999; McLeod et al. 1984) coupled with their capacity to resist molten metals has led to its use as electrodes in Hall-Heroult cells (Kang and Kim 1990)

Other properties which are not common to all three compounds also show promise for practical applications. For example, utilising the piezoelectricity of AlN may lead to surface acoustic wave applications (Deger et al. 1998), and due to the large neutron

absorption cross-section of B_4C, neutron control rods in fast breeder reactors (Murgatroyd and Kelly 1977).

The results of the ultrasonic study to determine the elastic behaviour below room temperature and under hydrostatic compression of these three refractory ceramic compounds are presented together in this chapter for two main reasons. Firstly, these ceramics constitute "normal" materials, in the sense that they show normal temperature and hydrostatic pressure dependences in their ultrasonic velocities (and hence elastic properties) and wave attenuation. Therefore, their behaviour can be compared with the materials in later chapters that may deviate from this normality, due to such effects as magnetism and porosity. In addition, essential physical and chemical information about the ceramics under study is given through the characterisation of each compound. Details of the characterisation techniques, other than those mentioned in Chapter 3, and any calculations performed using information from these techniques will be given in this chapter and referred to in subsequent chapters. Secondly, many of the elastic (and other physical) properties of these three compounds are well known, and have been studied extensively at elevated temperatures because of their refractory nature. Since these ceramics are important for industrial applications, knowledge of their response to temperature and pressure changes is important for design purposes. In particular, the available literature on the elastic behaviour under compression and hence the nonlinear acoustic properties for these ceramics is either contradictory or sparse, so the determination of the ultrasonic velocities as a function of hydrostatic pressure on these three ceramics is an important contribution to that area of study.

4.2 Crystal Structures

A separate description of the crystal structure of each compound, which makes up the primary phase of each ceramic used in this study, is given below. Even though their respective crystal structures are different, they can all be expressed in terms of a hexagonal lattice. Some typical values for the two lattice parameters (*a* and *c*) which describe a hexagonal lattice are given in Table 4.1. Alongside a description of each structure, the graphical representations of these structures (taken from the literature) have been given to help visualise the atomic arrangements.

4.2.1 Aluminium Nitride

At ambient conditions, AlN crystallizes in the hexagonal wurtzite structure; this structure consists of two interpenetrating hexagonal close packed (HCP) sublattices, each with one type of atom offset along the *c*-axis by approximately 0.625 of the unit cell height, shown in Figure 4.1 (a) (Mohammad and Morkoç 1996). There are four atoms per unit cell; each aluminium atom is tetrahedrally coordinated by four nitrogen atoms and vice versa, with the bonding said to be partially ionic and partially covalent (Ueno et al. 1992). AlN is considered to deviate from the "ideal" wurtzite structure because the unit cell *c/a* ratio is 1.601 instead of 1.633 (Ruiz et al. 1994).

4.2.2 Titanium Diboride

Titanium diboride has a hexagonal structure of the AlB_2 type with interatomic bonding mainly of a covalent nature (Castaing and Costa 1977; Castaing et al. 1969; Samsonov and Kovenskaya 1977; Lie et al. 1999). The crystal structure is usually described as a simple stacking of graphite-like parallel sheets of boron intercalated with a simple hexagonal lattice of titanium, positioned in such a way that each titanium atom is surrounded by 12 boron atoms and each boron is coordinated by six titanium atoms (Figure 4.1 (b)). Each unit cell contains three atoms (Perottoni et al. 2000).

4.2.3 Boron Carbide

The crystal structure of boron carbide consists of distorted $B_{11}C$ icosahedra located at the corners of a rhombohedral unit cell. Details of this unique structure can be found from many sources, for examples see any of the following: Thévenot 1990; Schwetz and Grellner 1981; Nelmes et al. 1995; Vast et al. 2000. In the ideal stoichiometric B_4C structure (Figure 4.1 (c)), a chain of three atoms (C-B-C), shown as larger spheres in Figure 4.1 (c), links the icosahedra along the [111] direction of the rhombohedral unit cell, which is parallel to the *c*-axis of the hexagonal lattice (Lundström 1997). The carbides of boron ($B_{12+x}C_{3-x}$) exist as single-phase materials over a wide range of compositions: $0.06<x<1.7$ (Aselage et al. 2000); B_4C represents the carbon rich single-phase limit.

Table 4.1 The lattice parameters of AlN, B_4C and TiB_2, obtained from different sources.

Form of sample	*a* (Å)	*c* (Å)	Reference
aluminium nitride			
powder	3.1105±0.0005	4.9788±0.0008	Slack and Bartram (1975)
-	3.110	4.980	Van Camp et al. (1991)
titanium diboride			
ceramic	3.033	3.229	Tyan et al. (1969)
-	3.026-3.038	3.213-3.233	Castaing and Costa (1977)
boron carbide			
powder	5.601±0.0002	12.070±0.001	Champagne and Angers (1979)
-	5.616±0.0001	12.087±0.0002	Telle (1990)

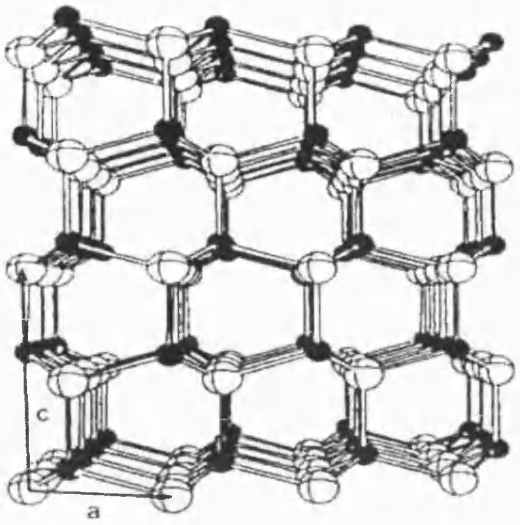

(a)

The wurtzite structure of AlN (Ruiz et al. 1994). Black balls represent aluminium atoms, white ones nitrogen atoms.

(b)

The crystal structure of TiB_2 (Perottoni et al. 2000), with large (small) spheres representing titanium (boron) atoms.

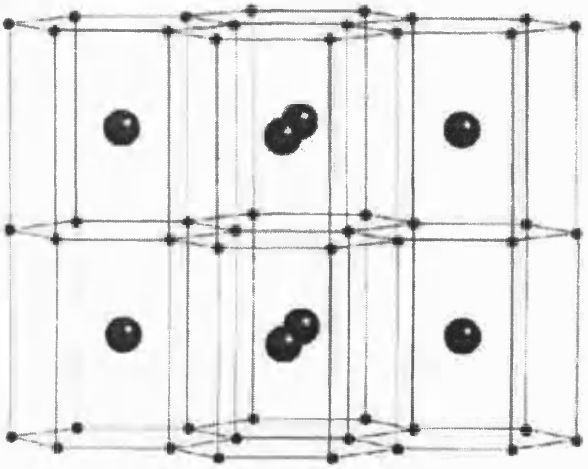

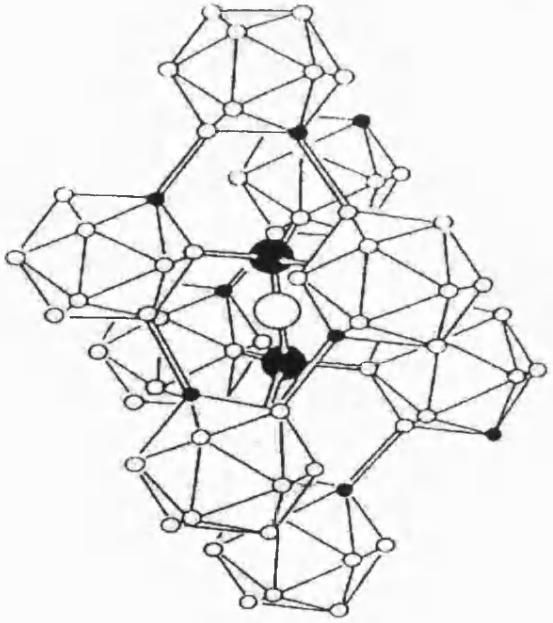

(c)

Ideal B_4C crystal structure (Aselage et al. 1993), with open (closed) circles representing boron (carbon) atoms.

Figures 4.1 (a), (b) and (c) Representations of the crystal structures for AlN, B_4C and TiB_2, respectively.

4.3 Characterisation of Ceramic Samples

The prime objective of the work presented in this section was to obtain as much information about the ceramics as possible from standard non-destructive characterisation techniques. Essential physical and chemical information has been obtained, for each ceramic used in the ultrasonic studies, from numerous characterisation techniques. Apart from the sample density and ultrasonic path length (distance between the two opposite parallel faces traversed by the ultrasonic wave) measurements, which are both necessary to calculate the elastic stiffnesses from the measured ultrasonic velocities, a list of the remaining non-destructive characterising methods is given below:

(1) X-ray diffraction analysis;

(2) a test for elastic isotropic behaviour in each ceramic by measurements of shear mode velocities with different polarisation directions;

(3) scanning electron microscope (SEM) analysis;

(4) electron microprobe analysis (EMA);

(5) electrical resistivity measurements (from 290-1000K).

Although each of these analysis methods was used to obtain information on the ceramics subjected to the ultrasonic measurements, characterisation method (5) was performed on other smaller samples. Since the samples used in method (5) were cut from the same block as their ultrasonic counterparts, their results were considered representative of the electrical behaviour of the larger ultrasonic samples.

Firstly, the results of measurements to determine: sample densities, ultrasonic wave path lengths, lattice parameters and sample phase content (X-ray diffraction analysis), elastic isotropy of the ultrasonic samples are presented in Section 4.3.1. Subsequently, in Sections 4.3.2 and 4.3.3 information obtained from the SEM images and the results of the EMA study are given, respectively. Finally, in Section 4.3.4, the results of electrical resistivity measurements on the smaller bar samples are discussed.

4.3.1 Ultrasonic Samples

The densities of the aluminium nitride, titanium diboride and boron carbide ultrasonic samples were measured using two flotation fluids, water and then acetone, to ensure

that the measured values were reproducible. Since porosity in ceramics can make the determination of their bulk densities an uncertain procedure these measured values will be lower limits. To make the results of room temperature shear mode velocity measurements with different polarisation directions (elastic isotropy test) and the X-ray diffraction studies (described in Section 3.8.3) meaningful, the reader will need to understand which results correspond to which directions in each sample. Therefore, a coordinate system has been introduced, graphically represented in Figure 4.2, to enable easy description of quantities associated with a certain direction in each sample. For convenience, face *X* (Figure 4.2) has been chosen to represent the surface perpendicular to the ultrasonic wave propagation direction for each ceramic (N.B. the shape of each ultrasonic sample was not a uniform cube and only one pair of faces were sufficiently parallel to perform ultrasonic experiments). Similarly, shear mode polarisation directions are defined as being parallel to a particular face of the sample (illustrated in Figure 4.2 for a polarisation parallel to *Y*-face). In practice, the actual surface area, corresponding to the *X*-face, and the path length magnitudes of each ceramic sample constituted the best conditions for precision ultrasonic velocity measurements. The data obtained from three X-ray diffraction studies on three approximately orthogonal faces of each sample will also be presented with respect to the coordinate system (Figure 4.2). This coordinate system used for associating direction with measured quantities has been used throughout the remaining chapters. Table 4.2 gives the results of these different measurements.

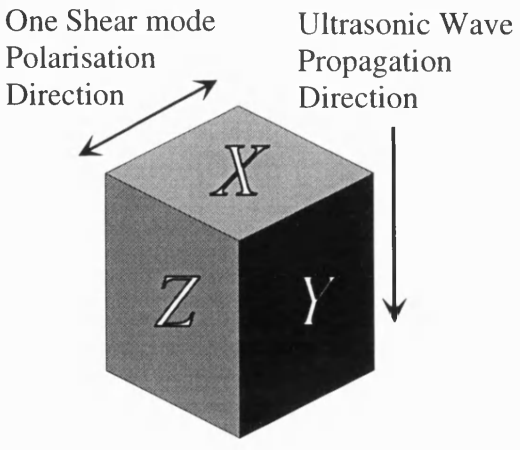

Figure 4.2 A coordinate system to represent the ultrasonic samples.

X-ray densities (given in the International Centre Diffraction Database, ICDD), which are larger than the single crystal values, are used to show in Table 4.2 that the measured densities are close to those of pure AlN, TiB_2 and B_4C compounds. The lattice parameters (Table 4.2) were obtained from the X-ray diffraction data in Figures 4.3 (a) to (c) for the three different directions. These calculations were achieved by finding the average of the three 2Θ angles, corresponding to certain diffraction peaks with appropriate Miller indices, and converting those to lattice parameters using the condition of constructive interference (Bragg's law). The appropriate diffraction peaks for calculating the lattice parameters in these ceramics have been labelled with their corresponding Miller indices and are shown in Figures 4.3 (a) to (c). A legend, which is used in every X-ray spectra graph, has also been provided in Figure 4.3 (a) to show which colours correspond to which faces studied. The lattice parameters agree well with those previously measured (Table 4.1).

Table 4.2 The sample density, X-ray density, lattice parameters, ultrasonic path length and room temperature shear mode velocities polarised parallel (or at 45°) to different faces of AlN, TiB_2 and B_4C ceramics.

Material		AlN	TiB_2	B_4C
Density (kgm^{-3})		3260±10	4510±10	2514±15
X-ray density (kgm^{-3})		3260±2	4495±1	2515±4
Lattice parameters (Å)	*a*	3.098±0.03	3.016±0.03	5.594±0.011
	c	4.961±0.03	3.209±0.03	12.059±0.048
Path length (mm)		9.699±0.002	9.440±0.015	10.250±0.009
Room temperature shear mode ultrasonic velocities, V_S ±10 (ms^{-1})				
Polarisation direction				
Y		6307	7469	8766
45°		6308	-	-
Z		6309	7637	8736

The difference in X-ray and measured density for the TiB_2 ceramic is possibly a consequence of the impurities, tungsten and carbon, which were discovered in the EMQA work and are shown in Table 4.3. However, Abbate et al. (1993) and Gurin and Sinelnikova (1977) have given values for the single crystal TiB_2 density of

4510kgm^{-3} and 4502 kgm^{-3} which suggests that the X-ray density used in Table 4.2 is too small.

Comparisons of the resulting X-ray diffraction spectra lines with the X-ray standard data (dotted lines) in Figures 4.3 (a) to (c) shows that each ceramic is essentially single phase; additional peaks are also present, but these could not be identified with any known secondary phases quoted in the literature. These quoted phases were Al_2O_3, Y_2O_3 and $Y_3Al_5O_{12}$ (and other Y-Al-O phases) for AlN ceramics (Gerlich et al. 1986), TiO_2, C, B_4C and B_2O_3 for TiB_2 ceramics (Tennery et al. 1983) and Al and Al_2O_3 for B_4C ceramics (Thévenot 1990). Also considered as potential secondary phases, to interpret the EMQA data in Table 4.3, were tungsten and its compounds for TiB_2 and any combination of Al-O-B compounds for B_4C.

The results of the elastic isotropy tests (Table 4.2), through the shear mode velocity measurements, show that the AlN ceramic is isotropic, but TiB_2 and B_4C have differences in their shear mode velocities. These differences can be associated with texture (preferred grain orientation) in the samples brought about by the fabrication process. Evidence of this texture can be seen in the measured X-ray diffraction patterns for TiB_2 and B_4C, which are shown in Figures 4.3 (b) and (c), respectively. If a sample is truly isotropic, the ratio in intensity of any X-ray line compared to an adjacent one should be approximately constant for any face of a ceramic studied. In Figures 4.3 (b) and (c), it can be seen that this ratio is not constant for faces *X*, *Y* and *Z*, particularly in Figure 4.3 (b).

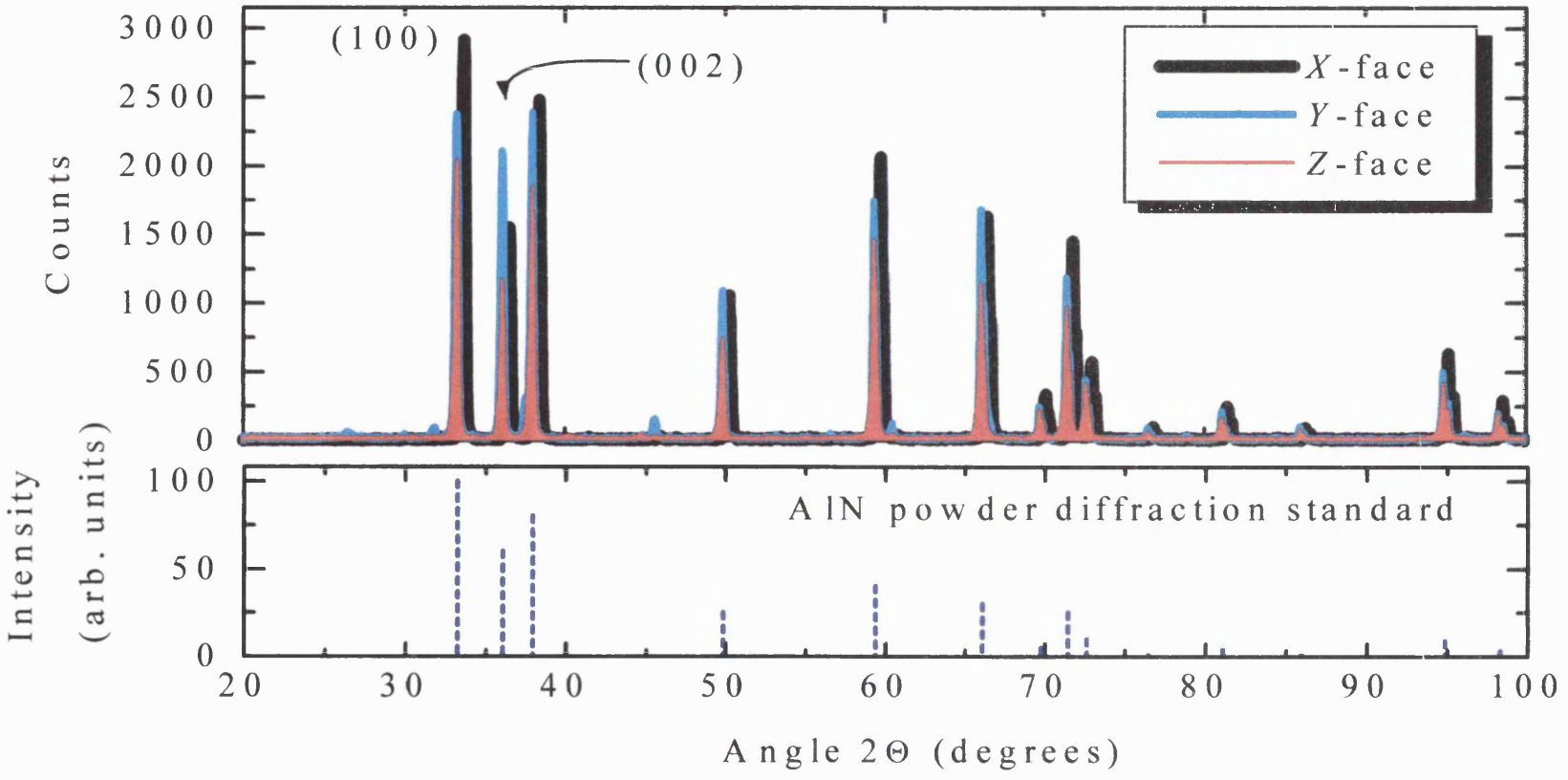

Figure 4.3 (a) X-ray diffraction spectra for three orthogonal faces of aluminium nitride ceramic.

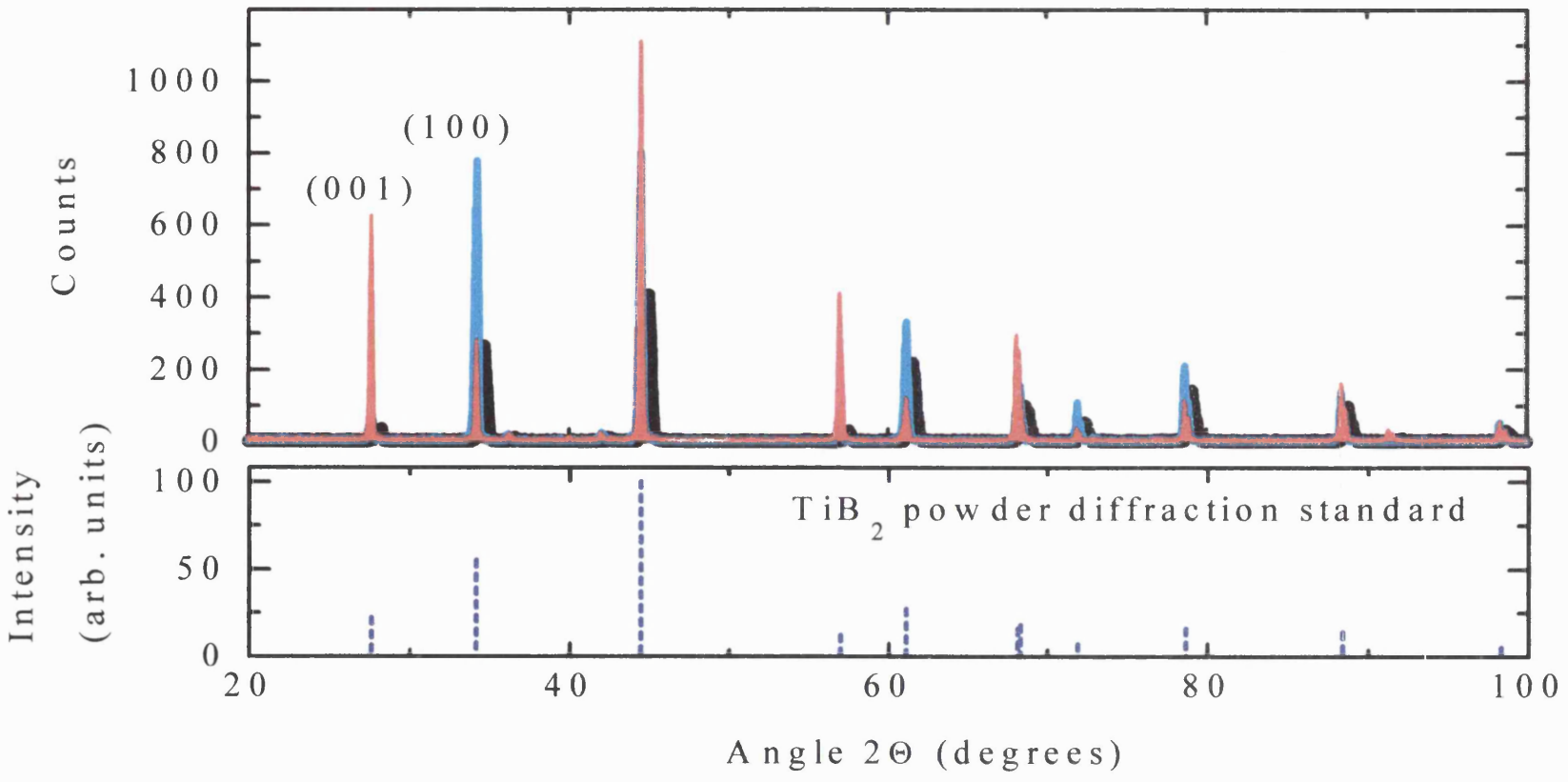

Figure 4.3 (b) X-ray diffraction spectra for three orthogonal faces of titanium diboride ceramic.

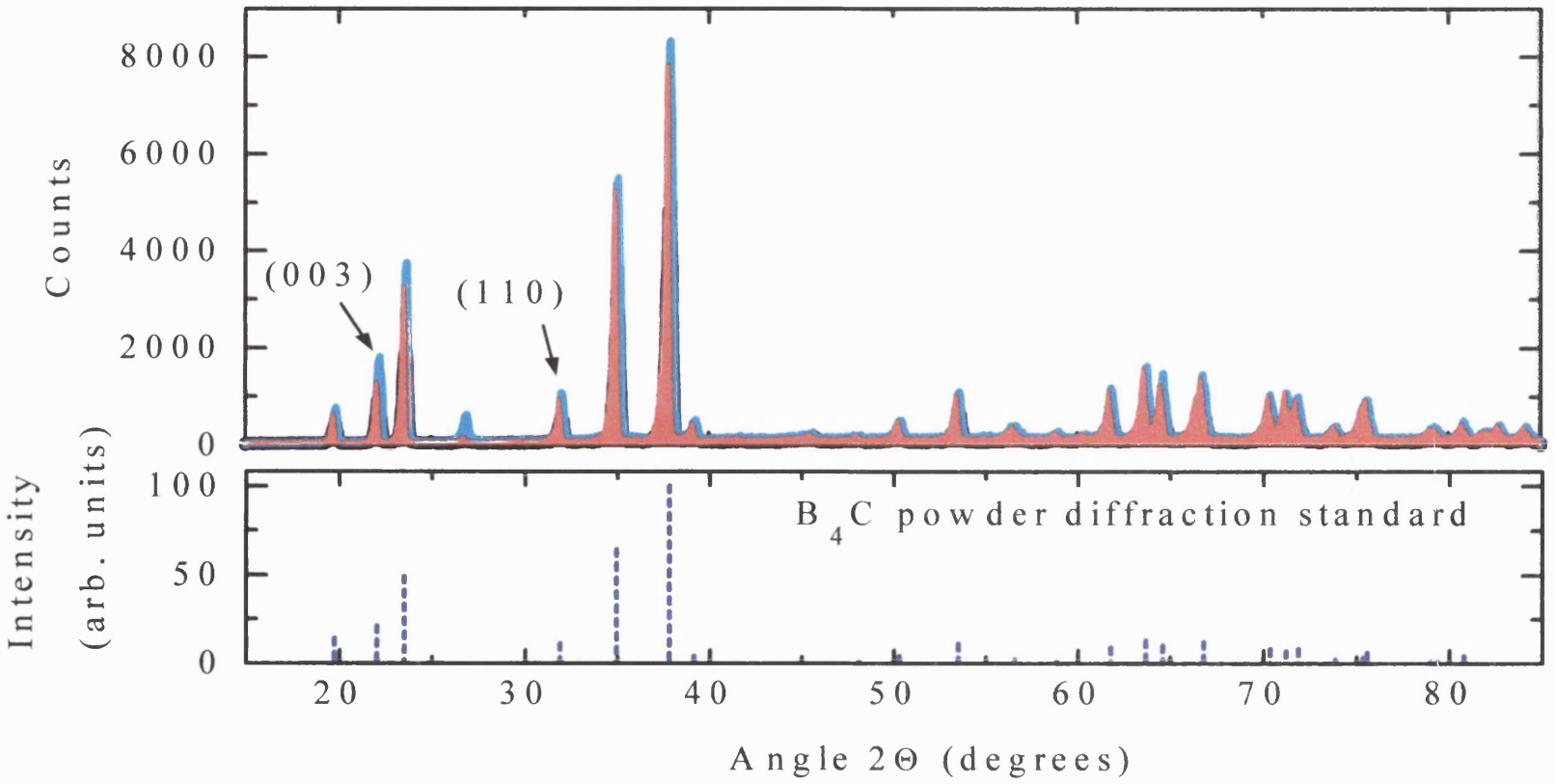

Figure 4.3 (c) X-ray diffraction spectra for three orthogonal faces of boron carbide ceramic.

4.3.2 SEM Analysis

SEM images of ceramic grain structures were taken by DSTL on suitably polished and thermally etched samples of AlN and TiB_2. SEM image contrast problems were encountered for the B_4C ceramic, so those SEM images have been omitted. The grain size distributions and average grain sizes of both AlN and TiB_2 ceramics were determined by DSTL using a lineal intercept: the intercept length for 1000 grains was measured. Actual grain sizes (d) were calculated using the expression

$$d = 1.56(L/m_f), \tag{4.1}$$

where L is the measured lineal intercept length and m_f is the magnification factor used in the scanning electron microscope. The factor 1.56 is an effective correction factor derived by Mendelson (1969) for random slices through a model system consisting of space filling tetrakaidecahedrally shaped grains (truncated octahedrons) with a log-normal size distribution. SEM images and grain size distributions are shown in Figures 4.4 (a) and (b) for AlN and Figures 4.4 (c) and (d) for TiB_2; the grains are randomly orientated and have a range of sizes. Average grain sizes for AlN and TiB_2 ceramics were: 4.18±2.75 and 8.2±5.3 microns, respectively.

4.3.3 Electron Microprobe Analysis

Electron microprobe quantitative analysis (EMQA) was used to determine the weight percentage (wt%), and hence atomic percentage (at%), of each element present in the TiB_2 and B_4C ceramics. The lack of EMQA data for AlN ceramic was due to an oversight by the author. The results of a number of surface scans are presented in Table 4.3 as normalised atomic percentages calculated from averaged weight percentages and averaged errors. The total weight percentage of the TiB_2 ceramic is 100%, within error. From these results, the calculated proportion of Ti atoms to B atoms was almost 1:2. In contrast, the underestimated total weight percentage produced for boron carbide resulted in a boron to carbon ratio of around 4:1.4. The causes of this underestimate lie in the fact that the sample is mainly composed of elements with low atomic numbers ($Z<9$). Lifshin (1994) has listed the causes of these significant errors (some of which can be minimized or corrected), when electron microprobing samples with low atomic number elements, which are:

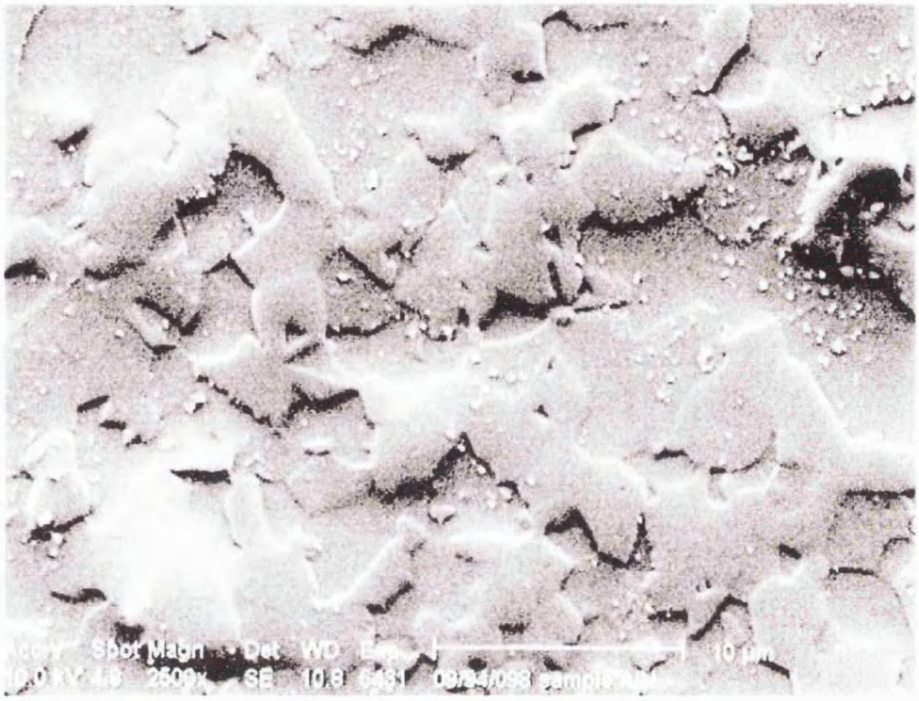

Figure 4.4 (a) Scanning electron microscope image for AlN ceramic.

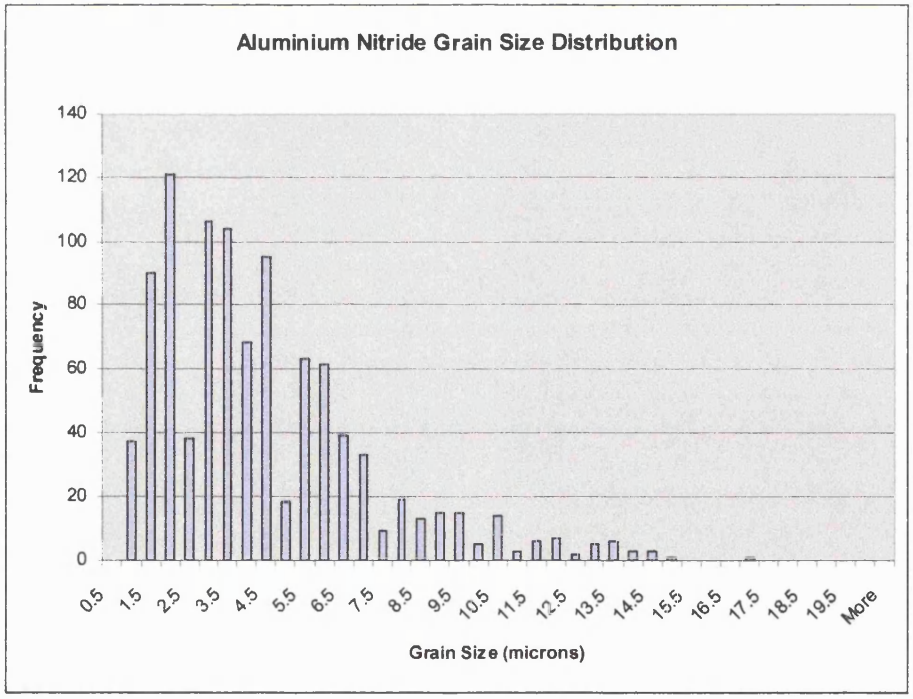

Figure 4.4 (b) Grain size distribution for AlN ceramic.

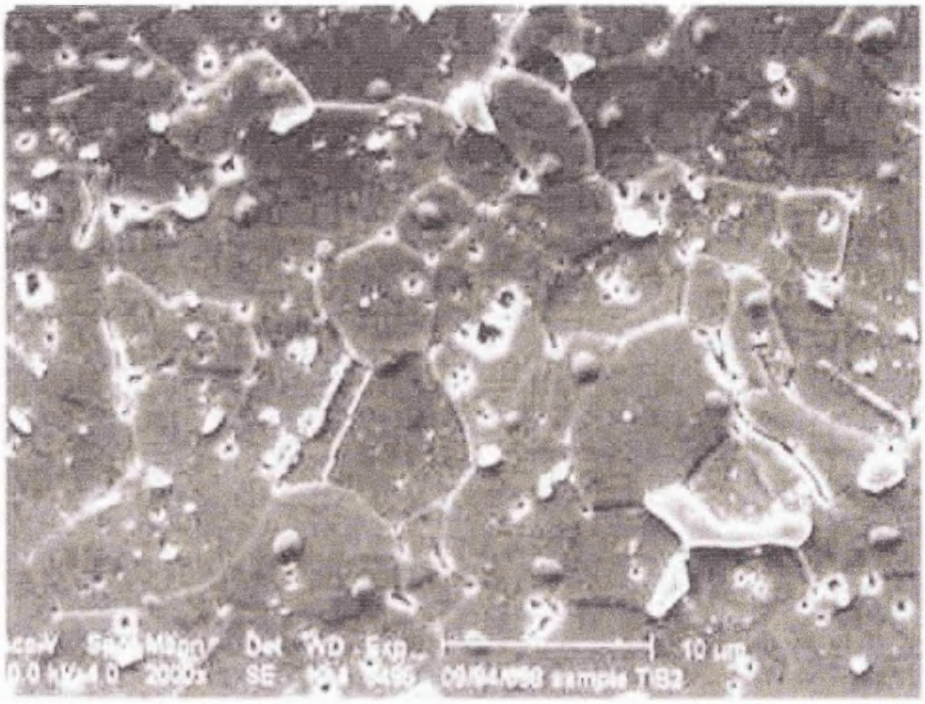

Figure 4.4 (c) Scanning electron microscope image for TiB_2 ceramic.

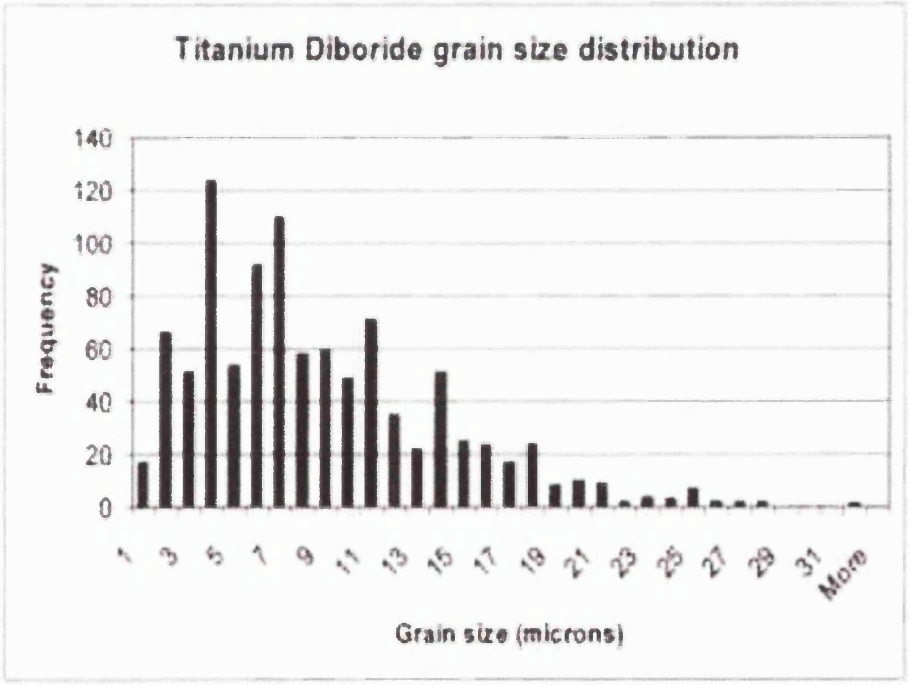

Figure 4.4 (d) Grain size distribution for TiB_2 ceramic.

(1) large X-ray wavelengths cause strong absorption in the sample and detector and the mass absorption coefficient tends to be large and sometimes inaccurate for such lines;
(2) their fluorescent yields, which are the fraction of electronic relaxations which result in X-ray photo emission, are much lower than for higher Z elements;
(3) interference of a number of M and L lines from higher Z elements at low energies with low Z element K lines. This is particularly significant in energy dispersive analysis;
(4) carbon build up at the point of impact of the electron beam with the sample, resulting in spurious or enhanced carbon signals that build up over time;
(5) the electrons in low Z elements may be involved in chemical bonding which results in shifted or broadened peaks.

Table 4.3 Results of the electron microprobe analysis showing the weight and atomic percentages of elements present in TiB_2 and B_4C ceramic samples.

	Material			
	TiB_2		B_4C	
Element	wt%	at%	wt%	at%
Ti	69.59±0.90	32.8±0.43	-	-
W	0.74±0.48	0.40±0.26	-	-
C	2.45±1.69	4.60±3.18	26.13±0.40	25.84±0.40
B	29.97±1.30	62.5±2.7	65.35±0.84	71.75±0.92
O	-	-	2.36±0.04	1.76±0.03
Al	-	-	1.60±0.01	0.70±0.01
Total	102.8±2.4	100.3±4.2	95.4±0.9	100±1

As well as the standard *ZAF* corrections that are applied to any quantitative EMQA measurements, the data for B_4C were corrected for mass absorption (1) and bonding effects (5) by using theoretical calculations (Lifshin 1994). The errors quoted in Table 4.3 are the random errors.

By using the data provided in Table 4.3, the percentages by weight of the major impurities in the two ceramic samples: TiB_2 and B_4C, were calculated to be between

3-4%, thus leaving approximately 96-97% of each ceramic composed of the primary phase.

4.3.4 Electrical Resistivity Measurements for TiB_2 and B_4C Ceramics

Electrical resistivity measurements were performed on two ceramic samples of both TiB_2 and B_4C, as the final characterisation procedure. The room temperature resistivity measurements were performed as described in Section 3.10, and the results obtained are given below in Table 4.4.

Table 4.4 The sample densities and room temperature resistivities obtained for ceramic bar samples of TiB_2 and B_4C ceramics.

Material		TiB_2	B_4C
Density (kgm^{-3})	sample 1	4526±128	2548±53
	sample 2	4593±98	2432±13
Resistivity (Ωcm)	sample 1	$(8.1\pm0.3) \times 10^{-6}$	0.94±0.01
	sample 2	$(8.04\pm0.12) \times 10^{-6}$	0.92±0.02

The results of the room temperature electrical measurements on TiB_2, shown in Table 4.4, are slightly lower than the range (=8.7-26 μΩcm) of values found for polycrystalline samples of TiB_2 produced by McLeod et al (1984); other results of electrical studies by Vahldiek (1967), Rahman et al. (1995) and Li et al. (1996) also fall into this range. The temperature dependence of the resistivity for the TiB_2 samples (Figure 4.5 (a)) shows a linear response to temperature increase. The temperature derivatives of electrical resistivity (shown as dotted lines in Figure 4.5 (a)) calculated for samples 1 and 2 are: 36.6±0.4 and 35.9±0.4 $n\Omega cmK^{-1}$, respectively. This linear resistivity-temperature behaviour is in accord with studies collated by McLeod et al. (1984) and those measurements by Rahman et al. (1995) from 293 up to 1535K, which resulted in a temperature derivative of 36 $n\Omega cmK^{-1}$.

For the resistivity measurements on B_4C ceramic samples, a different type of contact was applied to each material surface, using the contact defining process described in Section 3.10.6. High purity (99.99%) aluminium metal was deposited on to sample 1

and annealed at 500°C for 10 minutes in dry flowing nitrogen; this annealing was in accordance with processes described by Card (1975). Contacts deposited on the other sample were composed of, in order of deposition: germanium, gold, titanium and gold, and were annealed at 350°C for 2 minutes in forming gas. The current-voltage characteristics of the two different sets of contacts, tested on a model Tektronix 577 curve tracer, showed ohmic behaviour. Results obtained in the present study for the room temperature resistivity of B_4C (Table 4.4) agree well with each other, but are slightly higher than published data on this parameter (Aselage 1990; Shaffer 1964; Bouchacourt and Thévenot 1985), which had a range from 0.3-0.8 Ωcm. Impurity levels can often raise the absolute electrical resistivity of a semiconductor and the higher value determined here for the room temperature resistivity is possibly a consequence of the oxygen and aluminium impurities present in the ceramics (Table 4.3).

Electrical conduction in boron carbide is believed to proceed by a small bipolaron: $(B_{11}C)^+$ icosahedrons, hopping mechanism (Aselage et al. 2001). This electrical conduction as a function of temperature is commonly described by an Arrhenius-type equation (Wang et al. 1995a)

$$\sigma(T) = CT^{\eta} \exp(-Q/kT), \qquad (4.2)$$

where C is a constant, η depends on the conduction mechanism and Q is the activation energy of conduction. Previous measurements of this activation energy have resulted in a range: 0.14-0.18 eV (Bouchacourt and Thévenot 1985; Wood and Emin 1984; Samara et al. 1985; Aselage et al. 2001). By using the results of the temperature dependence of electrical resistivity measured in the present study (shown in Figure 4.5 (b)), the logarithmic version of Equation (4.2) and setting η=-1 (in accordance with the literature), the activation energies have been calculated to be 0.160±0.001 eV and 0.160±0.002 eV for samples 1 and 2, respectively. Figure 4.5 (c) shows the generated data, in accordance the Arrhenius-type equation, needed to calculate these activation energies from the data in Figure 4.5 (b).

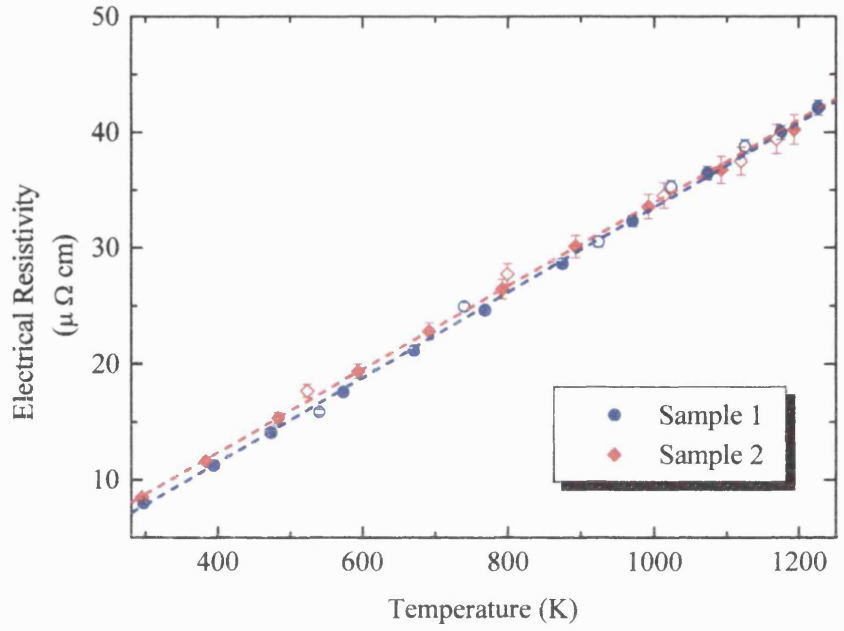

Figure 4.5 (a) The electrical resistivity as a function of temperature for TiB_2 ceramics. Filled (open) symbols correspond to increasing (decreasing) temperature. Dotted lines correspond to the temperature derivatives.

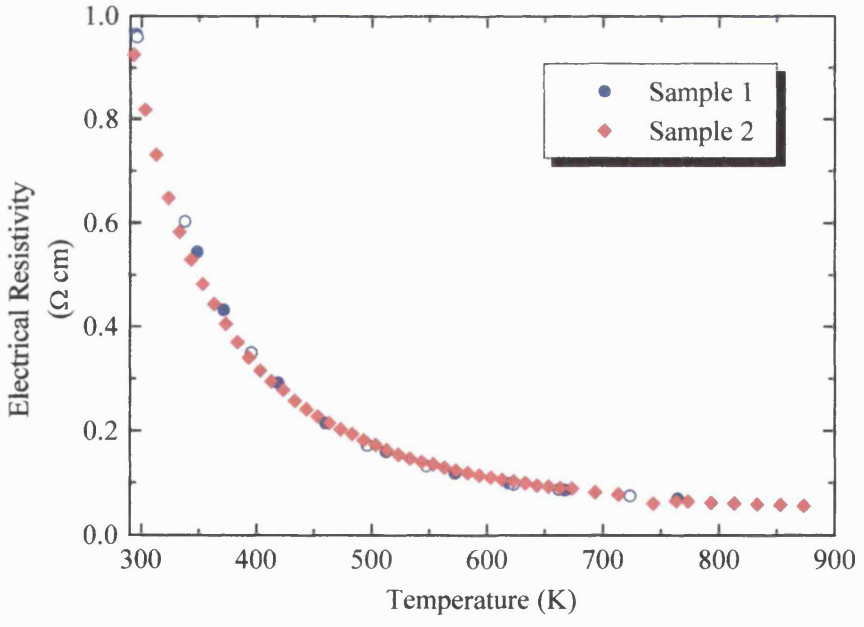

Figure 4.5 (b) The electrical resistivity as a function of temperature for B_4C ceramics. Filled and open symbols have same meaning as Figure 4.5 (a).

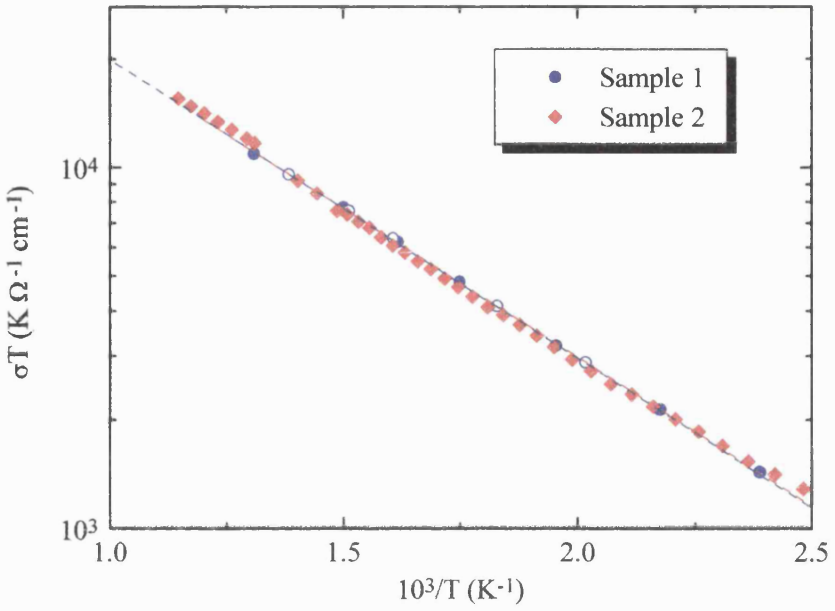

Figure 4.5 (c) The Arrhenius-type plot of data in Figure 4.5 (b). Filled and open symbols have same meaning as Figure 4.5 (a). Dotted lines correspond to slopes used to calculate activation energies.

In conclusion, no discrepancies have been found between the sample properties determined here using different characterising methods and those in the literature; therefore, each ceramic can be classed as representative of the three different compounds.

4.4 Ultrasonic Results and Discussion

4.4.1 Room Temperature Elastic Moduli for AlN, TiB_2 and B_4C Ceramics

The results of propagating longitudinal (V_L) and shear (V_S) ultrasonic waves in the ceramic forms of AlN, TiB_2 and B_4C are given in Table 4.5. Carrier frequencies were equal for both ultrasonic modes propagated in each ceramic: AlN (30MHz), TiB_2 and B_4C (50MHz). These high frequencies were chosen to reduce diffraction effects and produce a good resolution for the echo pattern. Using the appropriate equations in Chapter 2, calculations of elastic stiffness moduli (C_L and μ), the adiabatic bulk modulus (B^S), Young's modulus (E), Poisson's ratio (σ), and the acoustic Debye temperature (Θ_D) were made from these ultrasonic velocities; Table 4.5 gives the results of these elastic moduli calculations. Hereforth the term "elastic moduli" is defined as referring to all above elastic parameters including acoustic Debye temperature.

To determine whether the elastic moduli measured using this pulse-echo overlap method are representative of these ceramics, ultrasonic velocities (and hence calculated elastic moduli) are compared, where possible, with existing data. Firstly, comparisons are made in Table 4.5 with other workers who have measured room temperature longitudinal and shear mode velocities on polycrystalline samples with similar densities to those used here; the sources of these comparison data are given below Table 4.5. Subsequently, other techniques used to determine one or more of these elastic moduli will be considered. On comparing both longitudinal and shear mode velocities (and hence the elastic moduli) determined in the present work for AlN with those quoted by other sources, good agreement is found with data given by Rosenberg et al. (1991) and Subhash and Ravichandran (1998) on commercial AlN ceramic samples (Dow Chemical Co, MI). Although the density of the AlN ceramic used by Gerlich et al. (1986) is similar to that of the material used in the present work, the value of the longitudinal wave velocity measured by them is about 5% smaller than that determined here; this accounts for the differences found between the values of the room temperature elastic moduli (Table 4.5).

Table 4.5 The sample densities, ultrasonic wave velocities, adiabatic elastic moduli and their hydrostatic pressure derivatives, and the acoustic mode Grüneisen parameters of ceramic AlN, TiB_2 and B_4C at 295 K. The sound velocities quoted in Gust et al. (1973) and Gust and Royce (1971) were stated to have been accurate to within about 2%.

Material	AlN				TiB_2			B_4C			
Reference	This Work	(1)	(2)	(3)	This work	(4)	(5)	This work	(6)	(7)	(8)
ρ (kgm^{-3})	3260±10	3270	3226	3250	4510±10	4510	4490±10	2514±15	2500	2550	2510
V_L (ms^{-1})	10700±10	10127	10720	10700	11650±10	11210	11230±210	14086±12	13780	14166-14205	
V_S (ms^{-1})	6307±10	6333	6270	6300	7470±10	7250	7410±130	8766±7	8540	8851	
C_L (GPa)	373±2	334.3			612±2	567		498±4	475		
μ (GPa)	130±1	130.8	127	129	252±1	237	246±9	193±1	182	200	
B^S (GPa)	200±2	159.9	201	203	276±2	251	237±16	240±3	232	247	
E (GPa)	320± 3	308.3	314	320	579±3	541		456±4	434	472	461
σ	0.234±0.002	0.179	0.238	0.237	0.151±0.002	0.141	0.114	0.180±0.004	0.188	0.18	0.178
Θ_D (K)	952±5				1190±5			1480±3			
$(\partial C_L / \partial P)_{P=0}$	4.64±0.17	5.5±0.7			7.29±0.10		(14)	5.63±0.20			
$(\partial \mu / \partial P)_{P=0}$	0.28±0.03	0.2±2			2.54±0.10		(8.98±0.42)	0.78±0.03			
$(\partial B^S / \partial P)_{P=0}$	4.30±0.18	5.2±4			3.91±0.10		2.02±0.18	4.59±0.17	4.2±50%		
γ_L	1.08±0.05	1.16			1.48±0.01			1.19±0.04			
γ_S	0.046±0.024	-0.01			1.23±0.03			0.32±0.02			
γ^{el}	0.39±0.02	0.38			1.31±0.02			0.61±0.02			

References: (1) Gerlich et al. (1986); (2) Rosenberg et al. (1991); (3) Subhash and Ravichandran (1998); (4) Gust et al. (1973); (5) Abbate et al. (1992) and Dandekar and Benfanti (1993); (6) Gust and Royce (1971); (7) Aselage et al. (1990) and Gieske et al. (1991); (8) De With (1984)

Although not given in Table 4.5, Nipko and Loong (1998) have determined the longitudinal and shear wave velocities to be V_L=10700 ms^{-1} and V_S =6200 ms^{-1} from time-of-flight neutron spectroscopy measurements on a polycrystalline AlN sample; these velocities agree well with those given in Table 4.5.

For TiB_2, those results given in Table 4.5 determined by Abbate et al. (1992) and Gust et al. (1973) for hot-pressed TiB_2 ceramic samples are in general smaller than found here. Finally for hot-pressed samples of B_4C measured by Aselage et al. (1990), Gust and Royce (1971), De With (1984) and Gieske et al. (1991), the presented results are comparable to the sample studied here.

In most other cases apart from data given by Gerlich et al. (1986), small discrepancies in elastic moduli associated with polycrystalline materials can be put down to sample effects such as: microstructure (microcracking, porosity, grain sizes, texture) and purity (secondary phases, impurities). For example, Ferber et al. (1983) and Baumgartner and Steiger (1984) have pointed out that TiB_2 has a substantial anisotropy in thermal expansion: that along the *c*-axis being considerably larger than that along the *a*-axis. According to Evans (1978) and Case et al. (1980), this anisotropy produces considerable internal stress during post-fabrication cooling and generates microcracking, relieving the localized residual stresses, when the grain size is larger than a critical size (~15-20 μm). The microcracking occurs in the grains and at the grain boundaries, and results in degradation of macroscopic mechanical properties (Ferber et al. 1983; Tennery et al. 1983; Becher et al. 1986). The scanning electron microscope image (Figure 4.4(c)) revealed very little evidence of microcracking in the hot-pressed TiB_2 ceramic used in the present work. The average grain size is lower than the critical value and hence its elastic moduli correspond to that of a high density, uncracked ceramic. The lack of microcracks for this TiB_2 ceramic may explain the higher elastic moduli found here in comparison to those determined by Abbate et al. (1992) and Gust et al. (1973) on other ceramics, which may have contained cracks.

Materials scientists are mainly concerned with measuring the elastic (or mechanical) properties of ceramics, due to the appeal of using cheap high quality ceramics oversingle crystals for technological applications. In particular, the technological elastic property Young's modulus (E) is very important for engineering design purposes, especially at elevated temperatures; hence, numerous studies have been devoted to the measurement of Young's modulus for these technologically important ceramics and there are a number of different methods developed to determine this elastic property.

Experimental techniques used to obtain Young's modulus for B_4C were strain gauge (Champagne and Angers 1979), resonance frequency technique (Liebling 1967), composite piezoelectric oscillator method (Murthy 1985) and sonic method (Lang 1960). Other workers who did not mention the technique used to determine Young's modulus for polycrystalline B_4C were: Murgatroyd and Kelly (1977), Schwetz and Grellner (1981), Hollenberg and Walther (1980), Arenberg (1958), Bairamashvili et al. (1979) and Katz and Brantley (1971). Due to these different measurement techniques and the intrinsic ceramic properties such as porosity, composition and purity, a range was found for the Young's modulus of B_4C (432-480 GPa), within which lies the value determined here. Similarly, a range was found from a collation of Young's modulus values (=503-580 GPa) for TiB_2. Measurement techniques similar to those used on B_4C were also used by Ferber et al. (1983), Tennery et al. (1983), Becher et al. (1986), Wiley et al. (1969), Baumgartner and Steiger (1984), Green et al. (1996) and Pan et al. (1997) to obtain the values which resulted in this range for TiB_2. The lower bound of this Young's modulus range for TiB_2 resulted from a sample with a mean grain size over the critical size for microcracking (Ferber et al. 1983), hence the low value. Although many papers have concentrated on measuring or calculating *SOECs* for AlN from which Young's modulus could be obtained, surprisingly, previously measured data on AlN polycrystalline samples for this elastic property are sparse, with the exception of those shown in Table 4.5; the focus has been directed towards bulk modulus determinations and hence this important parameter will now be discussed.

In general the bulk modulus (B) is widely used as a parameter to examine interatomic binding forces in solids. For this reason, a large number of both theoretical and experimental investigations have been performed on these compounds. Tables 4.6 (AlN) and 4.7 (TiB_2 and B_4C) shows bulk moduli obtained from various methods. By inspecting the values for AlN in Table 4.6, in general the theory and experiment agree fairly well on the bulk modulus with the average value just over 200 GPa. Calculations of bulk modulus (B), shown in Tables 4.6 and 4.7, from *SOECs* were computed in the literature using

$$B = \frac{(C_{11} + C_{12})C_{33} - 2C_{13}^2}{C_{11} + C_{12} + 2C_{33} - 4C_{13}}. \tag{4.3}$$

The bulk modulus of B_4C and TiB_2 have been less well studied than AlN, and these studies have produced contrasting results, in particular for TiB_2. In comparison with the other values shown in Table 4.7, those found by Dandekar and Benfanti (1992), calculated from shockwave loading data measured by Gust et al. (1973) and Marsh (1980), have larger magnitudes. In these shockwave loading experiments, the slope of the shock velocity versus particle velocity data was used to determine the bulk modulus of TiB_2. In general these slopes are linear and positive, but in the case of TiB_2 a V-shape was recorded. According to Gust et al. (1973), a V-shape is indicative of a phase transition. However, since there was an absence of other shockwave loading data characteristic of a phase transition, Gust et al. (1973) suggest that the V-shape measured for TiB_2 is a manifestation of kinetic limitations in the compression. Thus, the large bulk modulus values obtained from the shockwave experiments maybe a result of these kinetic limitations. Experimental methods used by Spoor et al. (1997) and Abbate et al. (1993) give smaller bulk moduli for TiB_2 than that measured in the present study. In contrast to these smaller values, theoretical methods tend towards higher bulk moduli, close to 276 GPa measured here. Van Camp and Van Doren (1995) and Milman and Warren (2001) have calculated values comparable with 276 GPa. Experiments performed on B_4C to determine B agree fairly well for both sets of data shown in Tables 4.5 and 4.7, which range from 220-247 GPa. A value of 240 GPa determined by Vast et al. (2000) for B_4C using density functional perturbation theory is

Table 4.6 A comparison between the adiabatic bulk modulus B^S and its hydrostatic-pressure derivative $(\partial B^S / \partial P)_{P=0}$ determined for AlN ceramic at room temperature and the results of previous ultrasonic experiments under uniaxial pressure, very-high pressure X-ray diffraction measurements and theoretical calculations. (LCAO: linear combination of atomic orbitals; LDA: local density approximation; OLCAO: orthogonalized linear combination of atomic orbitals; LMTO: linear muffin-tin orbitals). The symbol (*) denotes bulk modulus calculated from experimentally or theoretically determined single-crystal elastic coefficients.

B (GPa)	$(\partial B / \partial P)$	Method	Reference
Experiment			
200±2	4.3±0.1	Pulse-echo overlap ultrasonic	Present work
159.9	5.2±4	Ultrasonic, cw resonance	Gerlich et al. (1986)
207.9±6.3	6.3±0.9	X-ray diffraction	Ueno et al. (1992)
185.0±5.0	5.7±1.0	X-ray diffraction	Xia et al. (1993)
201*	-	Surface acoustic waves	Tsubouchi et al. (1981)
210*	-	Brillouin scattering	McNeil et al. (1993)
193, 206*	-	Brillouin scattering	Carlotti et al. (1995)
209	-	Surface acoustic waves	Deger et al. (1998)
Theory			
209	3.7	Pseudopotential-LDA	Serrano et al. (2000)
209	5.58	Pseudopotential-LDA	Stampfl and Van der Walle (1999)
207	3.98	LCAO	Ching and Harmon (1986)
195	3.74	Pseudopotential-LDA	Van Camp et al. (1991)
207	5.60	OLCAO-LDA	Xu and Ching (1993)
237-243	3.77-4.45	Hartree-Fock	Ruiz et al. (1994)
202	3.8	LMTO-FP	Kim et al. (1996)
198	4.764	Empirical interatomic potentials	Ito (1998)
205	-	LMTO-FP	Christensen and Gorczyca (1993)
194	-	Pseudopotential-LDA	Miwa and Fukumoto (1993)
207*	-	Pseudopotential-LDA	Kato and Hama (1994)
207	-	Pseudopotential-LDA	Wright (1997)
212	-	First principles-total energy	Shimada et al. (1998)

Table 4.7 A comparison between the adiabatic bulk modulus B^S and its hydrostatic-pressure derivative $(\partial B^S / \partial P)_{P=0}$ determined for TiB_2 and B_4C ceramics at room temperature and the results of previous ultrasonic experiments under hydrostatic pressure, shock wave loading experiments, very-high pressure neutron diffraction measurements, mechanical resonance, and theoretical calculations. (DFPT: density functional perturbation theory; NCP: norm-conserving pseudopotentials LDA: local density approximation; GGA: generalised gradient approximation; OLCAO: orthogonalized linear combination of atomic orbitals; LMTO: linear muffin-tin orbitals). The symbol (*) denotes bulk modulus calculated from experimentally or theoretically determined single-crystal elastic coefficients.

B (GPa)	$(\partial B / \partial P)$	Method	Reference
Experiment			
TiB_2			
276±2	3.91±0.1	Pulse-echo overlap ultrasonics	Present work
237±16	2.02±0.18	Ultrasonics	Abbate et al. (1993)
346±8	1.89±0.29	Shock wave	Dandekar and Benfanti (1992)
323.0±8	2.39±0.19	Shock wave	Dandekar and Benfanti (1992)
240*	-	Mechanical resonance method	Spoor et al. (1997)
B_4C			
240±3	4.67±0.3	Pulse-echo overlap ultrasonics	Present work
232	4.2±50%	Shock wave	Gust and Royce (1971)
220	1 ± 2	Neutron diffraction	Nelmes et al. (1995)
247	-	Pulse-echo overlap ultrasonics	Gieske et al. (1991)
Theory			
TiB_2			
292±1	3.34±0.03	*Ab initio* calculations	Perottoni et al. (2000)
213	2.1	TB-LMTO-LDA	Vajeeston et al. (2001)
250.6	3.86	Pseudopotential-GGA	Milman and Warren (2001)
277.2	3.84	Pseudopotential-LDA	Milman and Warren (2001)
271*	-	NCP-LDA	Van Camp and Van Doren (1995)
B_4C			
240	3.5	DFPT/Raman spectra	Vast et al. (2000)
234*	-	Stress-strain relations	Lee et al. (1992)
273	-	OLCAO	Li and Ching (1995)

in excellent agreement with that determined here. The large bulk moduli determined for these three ceramics are evidence of the strong binding forces present and also the good bonding between grains in the ceramics.

Shear stiffness (or modulus) is a measure of the resistance to bond bending, i.e. rigidity. All three ceramics have high rigidity (Table 4.5), with TiB_2 showing the largest resistance to shearing; this result has been further strengthened by thesuggestion that the graphite-like boron layers in the TiB_2 crystal structure have a direct interaction in the *c*-axis crystallographic direction and this should contribute significantly to the rigidity (Perottoni et al. 2000). Other workers, mainly those who calculated Young's modulus for the three ceramics, also determined the shear stiffness and the comparisons are good where they exist.

The magnitude of Poisson's ratio found for TiB_2 ceramic (Table 4.5) is significantly larger than those determined previously (Ferber et al. 1983; Becher et al. 1986) using ultrasonic methods and that (=0.097) obtained by Baumgartner and Steiger (1984) using strain gauges. The results of the ultrasonic studies shown in Table 4.5 for B_4C all give values of σ around 0.18, with other workers' values covering a range from 0.14-0.21 (Murgatroyd and Kelly 1977; Schwetz and Grellner 1981; Liebling 1967). Aselage et al. (1990) calculated Poisson's ratio as a function of composition for B_4C; at the low end of the carbon composition range Poisson's ratio increased to 0.22, which may suggest that the elastic stiffnesses are influenced by non-central forces at the carbon rich limit (Shirai 1997). With the exception of Gerlich et al. (1986), in general good agreement can be seen to exist in Table 4.5 between Poisson's ratio measured here and those given elsewhere.

Large values determined for the acoustic Debye temperature are in accord with the relatively low densities and strong bonding (large stiffness) of these three ceramics. Even though TiB_2 has the largest set of elastic moduli for these three ceramics, B_4C possesses the largest acoustic Debye temperature; this can be attributed to the lighter

atoms in B_4C: light atoms coupled with strong bonds producing high frequency lattice vibrations (phonons). The acoustic Debye temperature (952±5 K) for AlN determined in the present work is in accord with 950 K (at zero K) quoted by Slack and Bartram (1975) and lower than that (≅983 K at room temperature) deduced from lattice specific heat of AlN given by Nipko and Loong (1998). Previous measurements of elastic constants on TiB_2 produced values of 952-1130 K (Vahldiek 1967), 1140 K (Wiley et al. 1969) and 1170 K (Andrievski and Asanov 1991) and 960 K, determined by Miksic (1963) using an X-ray technique. Due to the lack of published material on Debye temperature for B_4C, values were calculated for Θ_D from ultrasonic velocities given by references (6) and (7) in Table 4.5. These calculations were made using Equations (2.39) and (2.40) and produced values of 1442K and 1503K, which lie either side of Θ_D determined in the present study.

4.4.2 Temperature Dependences of the Elastic Moduli for AlN, TiB_2 and B_4C Ceramics

The behaviour of the elastic moduli upon cooling for these ceramic compounds are shown in Figures 4.6 (a) to (c). Since the results for these three ceramics are presented together, the graphs have been displayed as the change in a given property $\Delta M(=M(T)-M(290K))$ with respect to temperature (T). In addition, a legend has been provided in Figure 4.6 (a) to distinguish between these results: each sample corresponds to a colour on the graphs and this legend is used throughout the rest of the chapter. The ultrasonic velocities as a function of temperature have not been included, since the elastic stiffnesses are calculated from these velocities and give no additional information. No thermal hysteresis or irreversible effects were found for the ultrasonic velocity temperature runs, which is reflected in the corresponding elastic moduli data. At low temperatures, ultrasonic signal loss occurred due to thermal expansion differences between sample, bond and transducer.

All three materials show normal elastic behaviour below room temperature: the longitudinal and shear elastic stiffnesses stiffen upon cooling; this normal behaviour is

emphasized by fitting a conventional vibrational anharmonicity model (Section 2.8) to the measured data (shown as dotted lines in Figure 4.6 (a)). These ceramics follow the approximated model for anharmonicity quite well, but deviations from the dotted line are possibly a consequence of the preferred grain orientation in the ceramic. The increase in shear stiffness (or modulus) and Young's modulus with decreasing temperature (Figure 4.6 (b)) reflects those results found in the literature. Previously measured TiB_2 ceramics showed the same temperature dependence in shear and Young's modulus to the results found here, but at 290K and above (Wiley et al. 1969; Baumgartner and Steiger 1984; Andrievski and Asanov 1991; Green et al. 1996; Pan et al. 1997). This is also true for measurements on B_4C by Murthy (1985) and Hollenberg (1980). However, only recently has $E(T)$ been measured for a polycrystalline AlN sample from 293 to 973K (Bruls et al. 2001a); an increase in Young's modulus with decreasing temperature measured by Bruls et al. (2001a) is in accord with the temperature dependence of Young's modulus found in the present study. In the temperature range studied, Poisson's ratio decreases approximately linearly with decreasing temperature for B_4C and TiB_2 ceramics by 0.05%, while for AlN it increases by roughly the same percentage (Figure 4.6 (c)). It is therefore considered to be constant over the measured temperature range for these materials. Also shown in Figure 4.6 (c) is the change in acoustic Debye temperature upon cooling which, as a result of the longitudinal and shear stiffnesses increasing as temperature decreases, also increases.

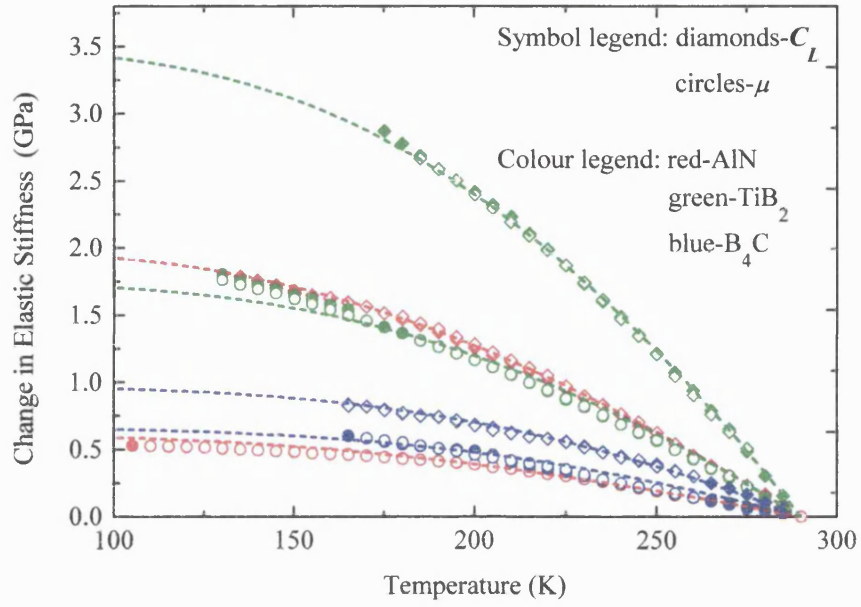

Figure 4.6 (a) Change in longitudinal and shear elastic stiffnesses as a function of temperature. Filled (open) symbols correspond to decreasing (increasing) temperature. Dotted line corresponds to fit of lattice vibrational anharmonicity model.

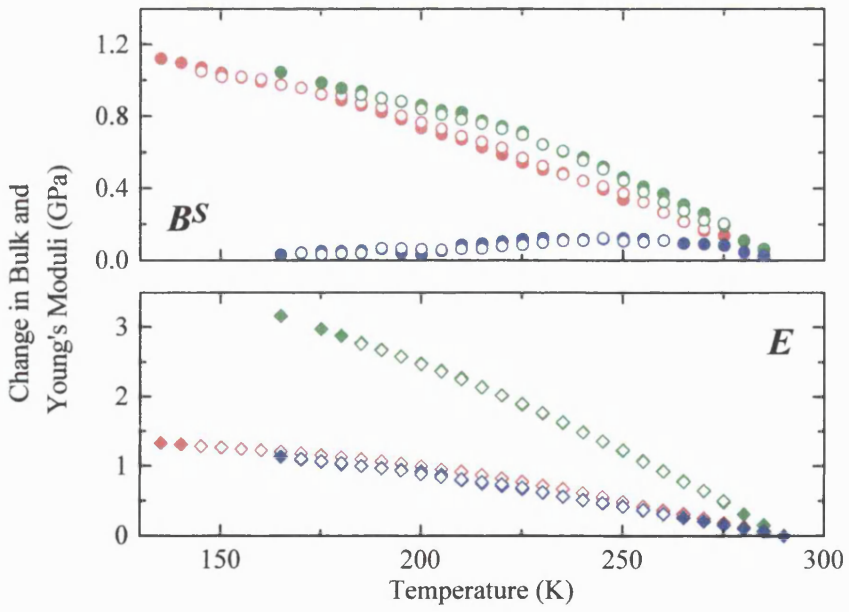

Figure 4.6 (b) Change in bulk and Young's moduli as a function of temperature. Filled and open symbols have same meaning as Figure 4.6 (a).

4.4.3 Temperature Dependences of the Ultrasonic Wave Attenuation Coefficients for AlN, TiB_2 and B_4C Ceramics

Measurements of the attenuation of the ultrasonic waves as a function of temperature in these ceramics were all taken at 30MHz and on separate temperature runs to the ultrasonic velocities. The results of these measurements are shown in Figure 4.6 (d). The kinks seen in the shear mode attenuation coefficients are a result of the bond freezing around 250-200K. Non-parallelism of the opposite faces perpendicular to the direction of ultrasonic propagation in these ceramics caused the longitudinal and shear mode attenuated echo patterns of these ceramics to show similar behaviour to that displayed by the SiC sample at 50MHz (Figure 3.9). Therefore, the absolute attenuation values include "apparent losses" and will have large errors associated with them, so only the change in attenuation with temperature is considered.

In normal polycrystalline materials, the predominant wave energy loss mechanisms contributing to the attenuation of the ultrasonic waves in the temperature range measured will be from thermoelastic damping (which is not present when propagating pure shear waves) and scattering of the wave energy from grain boundaries (and secondary phases), pores and the elastic anisotropy of the grains (Bhatia 1967). The scattering from pores and secondary phases in these ceramics should be negligible. The results shown in Figure 4.6 (d) are practically constant over the temperature range measured and show no anomalous behaviour. Contributions to the attenuation will be a combination of thermoelastic effects (longitudinal mode only) and the elastic anisotropy of the individual grains (Bhatia 1967).

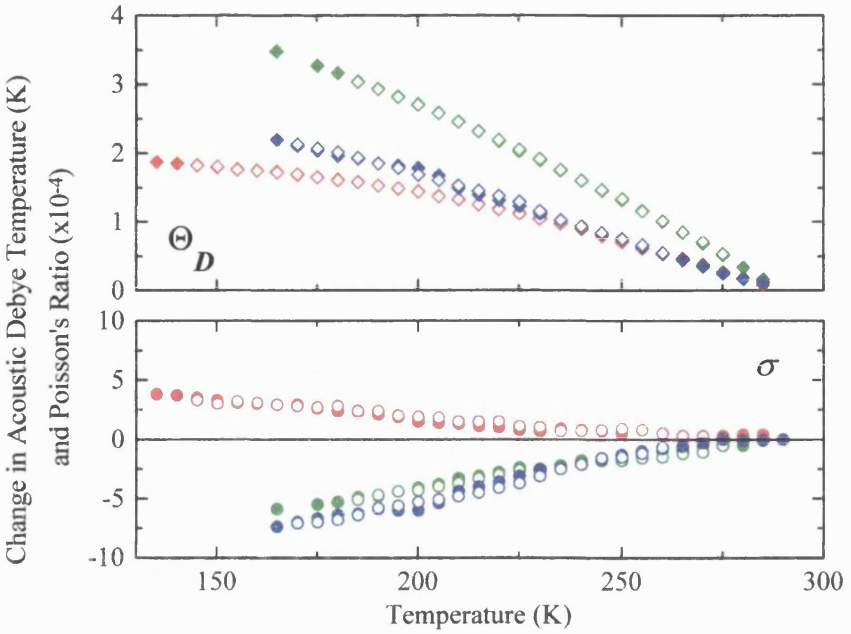

Figure 4.6 (c) Change in acoustic Debye temperature and Poisson's ratio as a function of temperature. Filled (open) symbols correspond to decreasing (increasing) temperature.

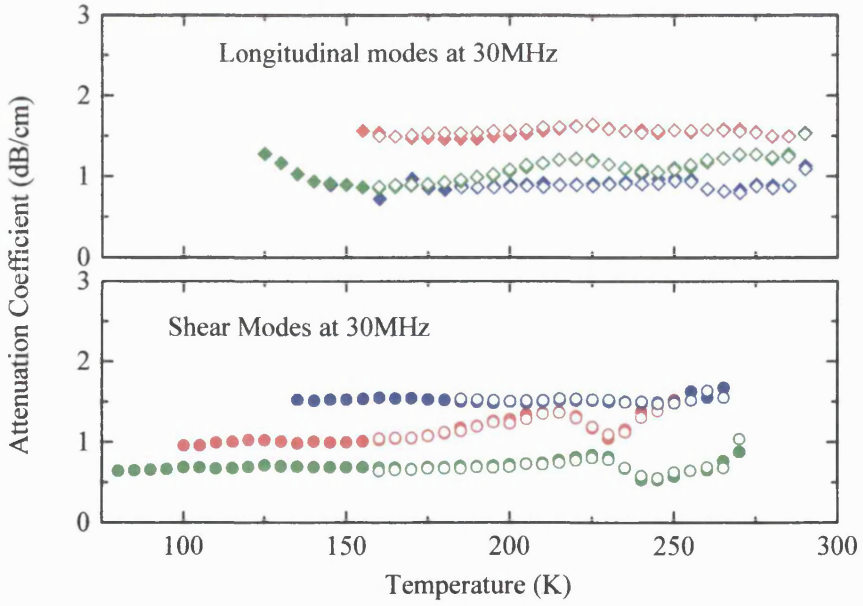

Figure 4.6 (d) Attenuation coefficients as a function of temperature. Filled and open symbols have same meaning as Figure 4.6 (c).

4.4.4 Hydrostatic Pressure Dependences of Ultrasonic Wave Velocities and Elastic Stiffness Moduli for AlN, TiB_2 and B_4C Ceramics

The effects of hydrostatic pressure on ultrasonic wave velocities in these three ceramics are small (Figures 4.7 (a) and (b)). The data for the pressure dependence of the velocities of both longitudinal and shear ultrasonic waves are reproducible under pressure cycling and show no measurable hysteresis effects. This observation indicates that these ceramics do not alter in morphology under pressure cycling up to 0.2 GPa and that there is no relaxation of any residual stress, which is in accord with the temperature dependent data.

The velocities of both longitudinal and shear ultrasonic waves increase approximately linearly with pressure in all three materials (Figures 4.7 (a) and (b)). This is normal behaviour: both the long wavelength longitudinal and shear acoustic modes stiffen under pressure, the effect on the longitudinal mode being larger. The longitudinal mode velocity is more pressure dependent than that of the shear mode for both AlN and B_4C ceramics, but the shear mode in the TiB_2 ceramic has quite a large pressure dependence approaching that of its longitudinal mode. Due to the very small shear mode velocity pressure dependence for AlN, one pressure run was performed with a differently orientated shear mode polarisation (at 90^o) to the other two; the fact that the three pressure runs are indistinguishable in Figure 4.7 (b) is a demonstration of the isotropic nature of the sample.

The results of previous pressure work on these ceramics shown in Table 4.5 were presented as elastic stiffness pressure derivatives: $(\partial C_L / \partial P)_{P=0}$ and $(\partial \mu / \partial P)_{P=0}$. In the present study, the pressure derivatives were calculated from the ultrasonic velocity pressure derivatives $(\partial W_L / \partial P)_{P=0}$ and $(\partial W_S / \partial P)_{P=0}$ using Equation (2.37). The resulting values for $(\partial C_L / \partial P)_{P=0}$ and $(\partial \mu / \partial P)_{P=0}$ calculated here are in line with those results in Table 4.5 given by Gerlich et al. (1986). In stark contrast to this comparison, measurements by Dandekar et al. (1994) of sound velocity in AlN under pressures up to 0.7 GPa revealed surprisingly that the shear wave velocity is more dependent than that of the longitudinal wave. Dandekar et al. (1994) calculated a value

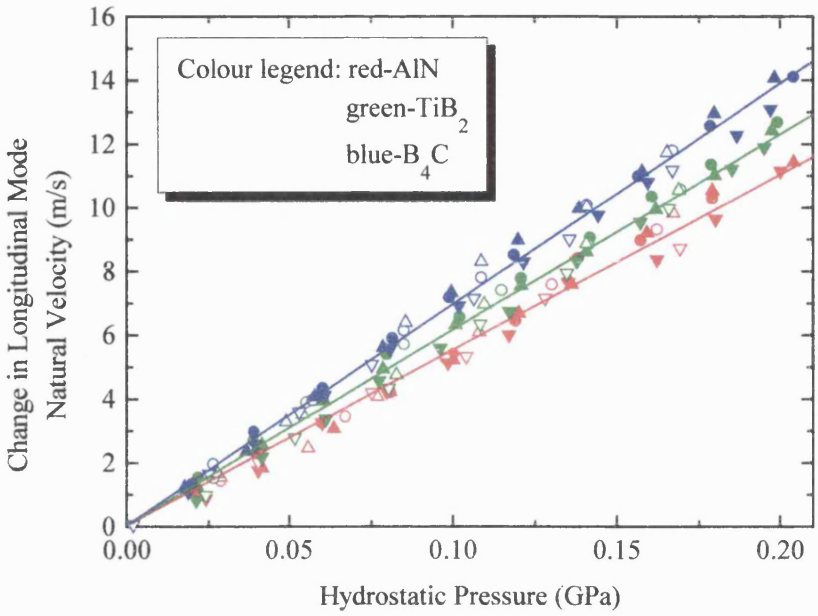

Figure 4.7 (a) Change in longitudinal mode natural velocities as a function of hydrostatic pressure, at 295K. Filled (open) symbols are increasing (decreasing) pressure and different symbol shapes correspond to different runs. Solid lines are for visual guidance only.

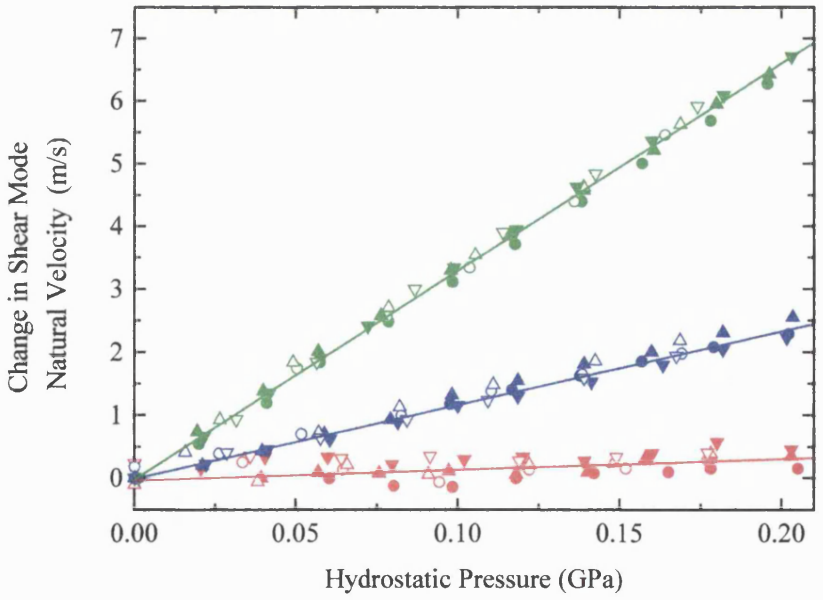

Figure 4.7 (b) Change in shear mode natural velocities as a function of hydrostatic pressure, at 295K. Filled and open symbols have same meaning as Figure 4.7 (a).

of 4.24±0.78 for $(\partial\mu / \partial P)_{P=0}$. Abbate et al. (1992) measured the pressure derivatives of the ultrasonic velocities for a TiB_2 ceramic sample and found very large pressuredependences for the two modes (Table 4.5) which are inconsistent with the present study; in fact, they appear to be much too large for a hard ceramic. Other studies on isotropic elastic stiffness pressure derivatives of B_4C ceramics appear to be sparse.

The bulk modulus pressure derivative $(\partial B^S / \partial P)_{P=0}$ can be calculated from knowledge of the elastic stiffness pressure derivatives by using Equation (2.38). The results of these calculations for each ceramic studied here are given in Tables 4.6 (AlN) and 4.7 (TiB_2 and B_4C); previous experimental and theoretical calculations of $(\partial B^S / \partial P)_{P=0}$ for these ceramic compounds are also shown. In Table 4.6 (AlN), the agreement is quite good for different experimental and theoretical calculations of $(\partial B^S / \partial P)_{P=0}$. However, this agreement does not follow for TiB_2 and B_4C. Dandekar and Benfanti (1992) used compression data from uniaxial shock wave loading on TiB_2, reported in Gust et al. (1973) and Marsh (1980), to generate 2.02±0.18 and 1.89±0.29 for $(\partial B^S / \partial P)_{P=0}$, respectively. These bulk modulus pressure derivatives were determined together with the bulk modulus from the same shock velocity versus particle velocity data mentioned in Section 4.4.1. The same reason for the discrepancy between the shock wave and present bulk modulus results described in that section will therefore also apply to the $(\partial B^S / \partial P)_{P=0}$ data. Abbate et al. (1993) gave a similar value for $(\partial B^S / \partial P)_{P=0}$ to those produced from shock wave loading, but this number was calculated from the very large elastic stiffness pressure derivatives shown in Table 4.5, which appears to be unrealistic for what seems to be a highly incompressible material, given the large bulk modulus. Most of the theoretical determinations of $(\partial B^S / \partial P)_{P=0}$ for TiB_2 agrees well with the value stated here, especially that calculated by Milman and Warren (2001). In contrast, Vajeeston et al. (2001) agrees with the shock wave loading experimental data. This division of both theoretical and experimental studies makes the correct value of $(\partial B^S / \partial P)_{P=0}$ inconclusive. Similarly for B_4C, a much larger number of studies on its

pressure behaviour need to be performed before any reasonable conclusion can be made.

By using the bulk modulus and its pressure derivative and Murnaghan's equation of state (Section 2.9), the volume compression ($V(P)/V(0)$) for each ceramic can be extrapolated to high pressures and compared with previous very high pressure studies on the same compound. Figures 4.8 (a) to (c) show the results of these comparisons for the volume compression of AlN, TiB_2 and B_4C, respectively. Where possible, volume compression data were extracted from the literature, but for other pressure studies, such as that by Gerlich et al. (1986), the volume compression data was also extrapolated to very high pressure using Murnaghan's equation of state. The calculation of volume compression for AlN has not been extended above 24 GPa, since there exists an irreversible transition from the wurtzite to the cubic rocksalt structure which begins at 14 GPa (Ueno et al. 1992; Xia et al. 1993) and ends around 23 GPa. No structural phase transition has been found for the other two materials, so for TiB_2 the extrapolation has been extended to 150 GPa to tie in with shock wave loading data. However, to compare existing volume compression data for B_4C, this has led to the pressure range being confined to a limit of 12 GPa. Volume compression data determined from theoretical methods have not been included in these plots, mostly for clarity.

Good agreement can be found in Figures 4.8 (a) and (b) between extrapolated data and measured volume compression data for both AlN and TiB_2, respectively. Both the previous ultrasonic studies on AlN and TiB_2 ceramics by Gerlich et al. (1986) and Abbate et al.(1991), respectively, have also been included as extrapolation from low pressures and show a larger volume compression than the rest of the data; this can be attributed to different values of $(\partial B^S / \partial P)_{P=0}$ and bulk modulus and not sample effects.

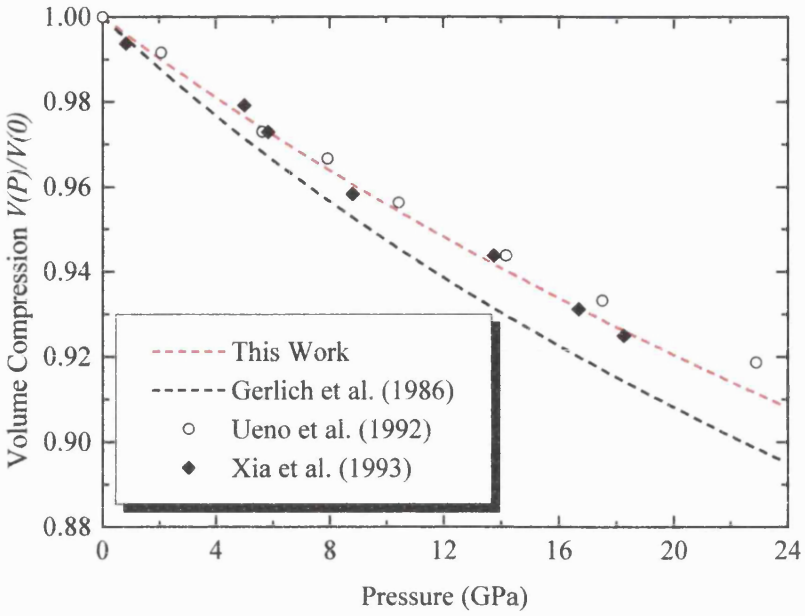

Figures 4.8 (a) Volume compression for AlN ceramic, compared with data extracted from studies by Ueno et al. (1992) and Xia et al. (1993) using X-ray diffraction methods and extrapolated data obtained by Gerlich et al. (1986).

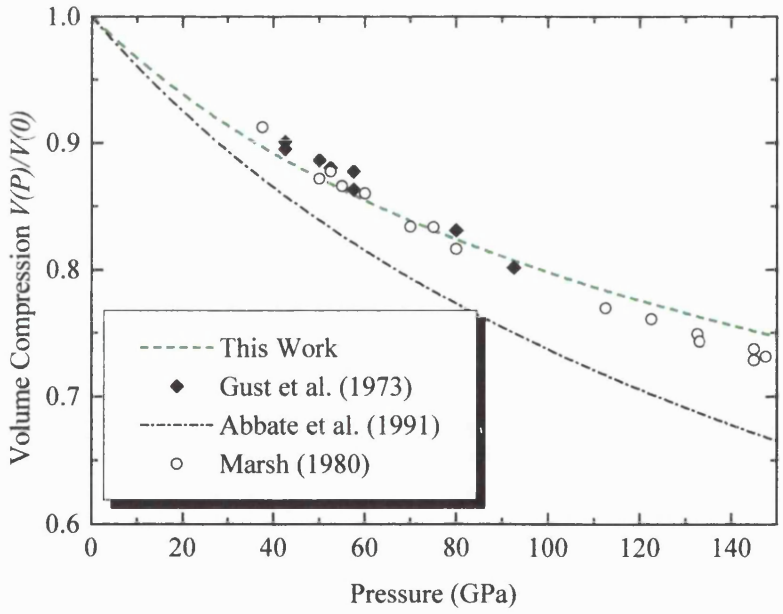

Figure 4.8 (b) Volume compression for TiB_2 ceramic, along with extracted shock wave loading data produced by Gust et al. (1973) and Marsh (1980) and extrapolation of ultrasonic compression data given by Abbate et al.(1991).

In Figure 4.8 (c), the compression data for the B_4C ceramic has been compared with an extrapolation of data estimated from shock wave measurements (Gust and Royce 1971) and neutron diffraction versus pressure data (Nelmes et al. 1995). A comparable result to that determined here was found by Gust and Royce (1971), but work by Nelmes et al. (1995) suggests that B_4C is more compressible. It is interesting to note that due to the nature of the bonding and the unique structure associated with boron carbide, Aselage (1990) and Nelmes et al. (1995) have proposed that the icosahedra themselves could be more compressible than the structure between them. Whereas Vast et al. (2000) have suggested that the high bulk modulus of B_4C (and alpha boron, α-B_{12}) is mainly determined by stiff intramolecular bonding within the icosahedra.

A comparison between the volume compression of the three ceramics used in the present study (Figure 4.8 (d)) shows that TiB_2 is the least compressible ceramic in the group.

4.4.5 Grüneisen Parameters and Acoustic Mode Vibrational Anharmonicity for AlN, TiB_2 and B_4C Ceramics

One aim in measuring the ultrasonic velocities as a function of hydrostatic pressure was to determine the degree of vibrational anharmonicity associated with a material. The thermal motion of atoms in a solid are largely influenced by the anharmonic nature of the interatomic bonding. Quantifying the anharmonic effects, in the quasi-harmonic approximation, is achieved by determining the mode Grüneisen parameters. Generally, the greater the anharmonicity in normal solids the larger the mode Grüneisen parameters. Equations (2.33-2.35) have been used to determine the Grüneisen parameters which are appropriate to elastically isotropic materials such as these ceramics, i.e. γ_L, γ_S and γ^{el} the longitudinal, shear and mean acoustic mode Grüneisen parameters, respectively. All acoustic mode Grüneisen parameters shown in Table 4.5 are positive, this fact means that these samples show normal behaviour. Values of γ_L and γ^{el} for AlN calculated in the present study are similar to those determined by Gerlich et al. (1986); however, γ_S is slightly positive compared with their small negative value.

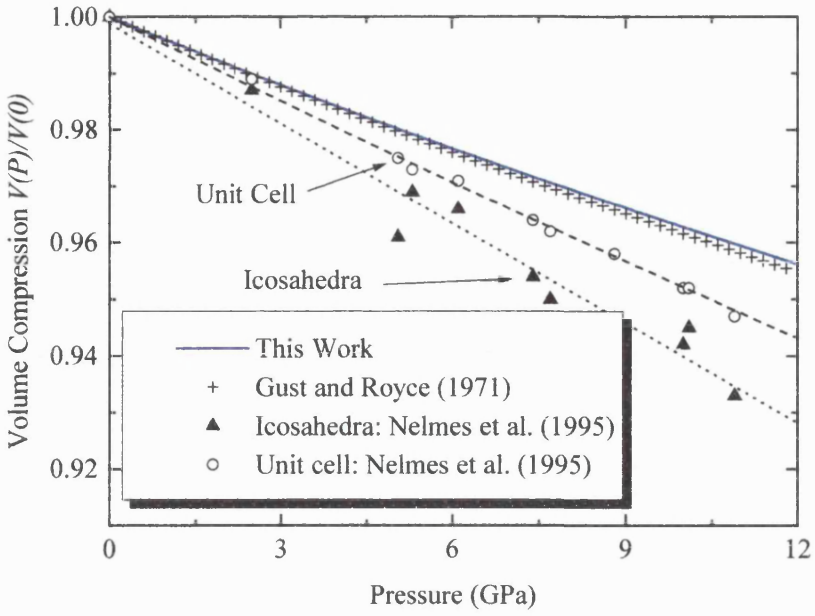

Figure 4.8 (c) Volume compression for B_4C ceramic, compared with an extrapolation of compression data found by Gust and Royce (1971) using shock wave methods and a combination of unit cell and icosahedra compression determined by Nelmes et al.(1995). The dotted line is a least squares fit to the deduced icosahedra compression.

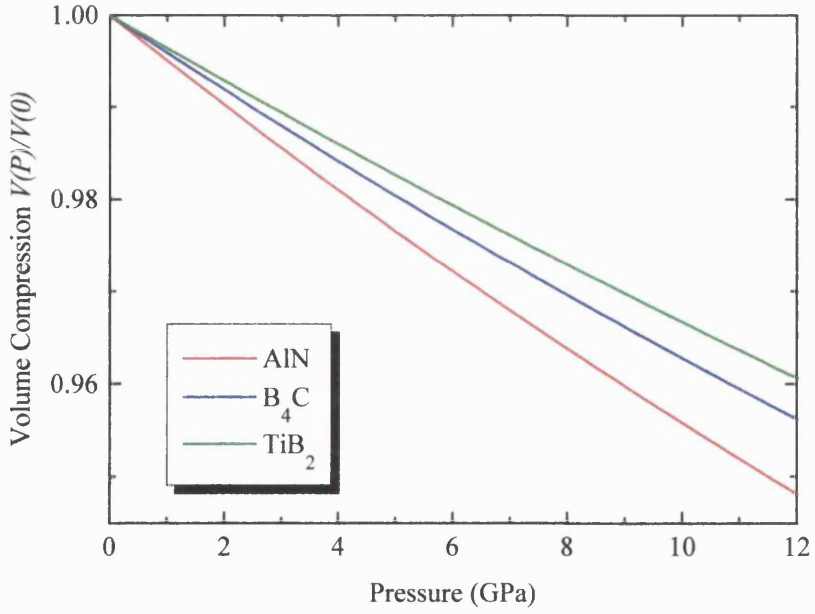

Figure 4.8 (d) Volume compression for AlN, TiB_2 and B_4C ceramics used in present study.

At first glance the small value of γ^{el} for AlN indicates that the effects of acoustic mode vibrational anharmonicity are quite small. However, the almost zero shear acoustic mode Grüneisen parameter measured here, coupled with the results by Gerlich et al. (1986), indicates a possible soft shear mode. Experiments by Goñi et al. (2001) and Perlin et al. (1993) on the pressure dependence of Raman active phonon modes of hexagonal AlN also found that a low frequency mode associated with a zone centre transverse acoustic mode had a zero or slightly negative Grüneisen parameter. No direct link has been made between this apparent soft mode and the structural phase change determined experimentally, only that it may be caused by a balancing of central and non-central elastic forces (Goñi et al. 2001). Since the origin of this shear mode behaviour under compression for AlN is inconclusive, the value of the mean acoustic Grüneisen parameter (=0.39 ± 0.02), calculated using γ_S, may not be determined solely by the anharmonic nature of the interatomic potential. The relative sizes of the two γ^{el} values in Table 4.5 for TiB_2 and B_4C suggest that TiB_2 is more anharmonic than B_4C, which is in accord with the temperature dependence of their elastic stiffnesses: the TiB_2 ceramic has larger temperature dependences than B_4C.

The thermal Grüneisen parameter (γ^{th}) includes the effects of all phonons in the Brillouin zone, but contributions from optic phonons are expected to be negligible at room temperature. The shear acoustic mode Grüneisen parameter γ_S(=0.046) is much smaller than the longitudinal acoustic mode Grüneisen parameter γ_L(=1.08) for the AlN ceramic used in the present study, accounting for the low thermal Grüneisen parameter γ^{th}(=0.69) determined by Bruls et al. (2001b) for a AlN ceramic. A value of 1.39 was found by Steinberg (1991) for the thermal Grüneisen parameter of a hot-pressed TiB_2 ceramic, which is comparable to 1.31 determined here for the mean acoustic mode Grüneisen parameter. A larger estimated thermal Grüneisen parameter for B_4C of 1.76 was calculated using thermal expansion coefficient value given in Table 3.1 by Tsagareishvili et al. (1986) and the specific heat data presented by Thévenot (1990). This larger value obtained for γ^{th} compared with 0.61 for γ^{el} implies that the optic phonons have the relatively larger Grüneisen parameters. Since the

acoustic Debye temperatures calculated for AlN, TiB_2 and B_4C are very high, long wavelength acoustic phonons can be expected to dominate properties determined by vibrational anharmonicity even at room temperature. Shear acoustic modes play a more important role than longitudinal acoustic modes in the acoustic phonon population at room temperature. This enhances their contribution to thermal expansion and specific heat, lowering the thermal expansion and hence the thermal Grüneisen parameter.

Chapter 5

Ceramic Beta-Silicon Nitride (β-Si_3N_4)

5.1 Introduction

Silicon nitride (Si_3N_4) is an important structural ceramic due to its high thermal resistance, strength and chemical stability, and a relatively low density. These properties have led to a variety of technological applications, especially in high-temperature and corrosive environments, as well as considerable scientific interest (Riley 1983; Kelly and Macmillan 1986). A recent paper by Riley (2000) lists a large number of these technological applications in which silicon nitride ceramics have been used, some of which are: high efficiency gas turbine engines; bearings, used in abrasive environments such as oil drilling, vacuum pumps and unlubricated dental drills; cutting tools; and because of its high strength, high electrical resistance and good thermal shock resistance, has been used as threaded shroud nozzles for inert-gas welding. In addition, Buljan et al. (1987) has stated that by combining different percentages of Si_3N_4 ceramics with one or more other refractory materials (composites) to increase their fracture toughness and strength will considerably expand their application range; a popular composite is composed of Si_3N_4 with different percentages of SiC whiskers (Buljan et al. 1987; Fisher et al. 1992; Pezzotti et al. 1989).

The elastic stiffness moduli of Si_3N_4 ceramics have been measured previously at room temperature by ultrasonic techniques (Yeheskel et al. 1984; Yeheskel and Gefen 1985; Singh et al. 1988; Fisher et al. 1992; De Arellano-Lopez 1998), and in a temperature range from room temperature to about 1270 K at atmospheric pressure (Fate 1975). The elastic behaviour of silicon nitride below room temperature is unknown. Previous pressure studies on silicon nitride amounted to determination of the volume compression of β-Si_3N_4 from high pressure X-ray (Li et al. 1997) and neutron diffraction (Cartz and Jorgensen 1981) techniques; apart from these studies, the effects of pressure on the elastic behaviour of Si_3N_4 are unknown. Therefore, in this chapter an investigation into the elastic and nonlinear acoustic properties of a β-Si_3N_4 ceramic, prepared by hot pressing, is presented.

5.2 Crystal Structures of Silicon Nitride

There are two stable polymorphs of Si_3N_4 with trigonal (α-phase) and hexagonal (β-phase) lattice structures. The α-Si_3N_4 phase has 28 atoms in the unit cell, whereas the β-Si_3N_4 phase has 14 atoms per unit cell (Ching et al. 1998). The unit cell dimensions for these two structures can be described by a hexagonal lattice, and have two lattice parameters (a and c). These two structures are also closely related: α-Si_3N_4 consists of basal planes of β-Si_3N_4 and a mirror image (Riley 2000), which results in the unit cell c-axis dimension of α-Si_3N_4 being approximately twice that of β-Si_3N_4. The material used in the present study is β-Si_3N_4, which is commonly formed from the α-phase through a liquid phase formation above 1400°C; this phase transformation is irreversible and changes the morphology of the grains from equiaxed to elongated (De Arellano-Lopez 1998). The crystal structure of β-Si_3N_4 is built up of SiN_4 tetrahedra joined in a three-dimensional network by sharing corners, where each nitrogen corner is common to three tetrahedra; the S-N bond is said to be approximately 70% covalent and 30% ionic (Wang et al. 1996). Figures 5.1 (a) and (b) show the α- and β-phases, respectively, given by Ching et al. (1998).

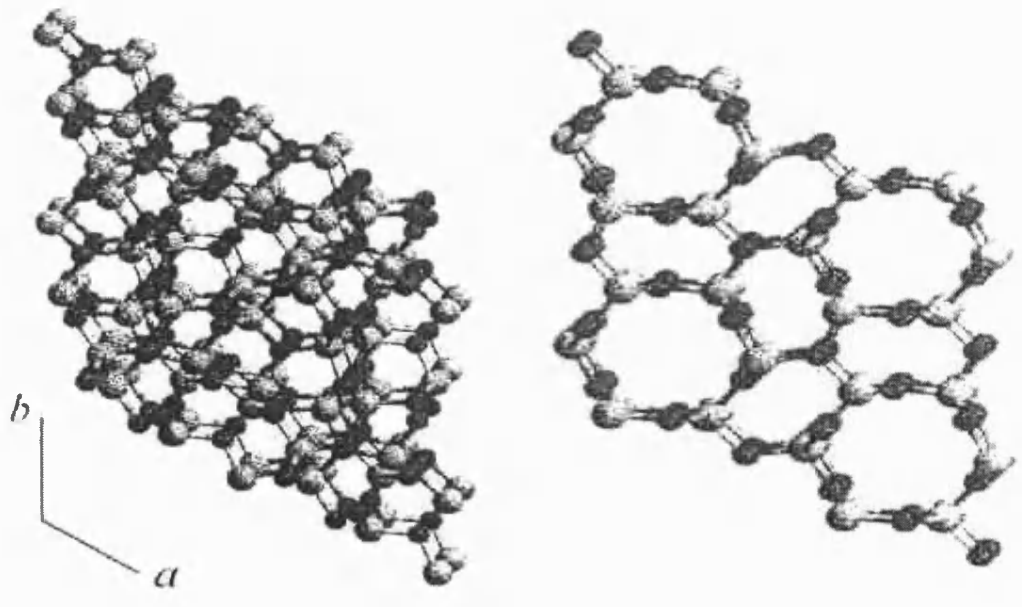

(a) (b)

Figures 5.1 (a) and (b) Crystal structures of α- and β-Si_3N_4, respectively (Ching et al. 1998). Grey (black) spheres correspond to silicon (nitrogen) atoms. a and b crystallographic axes are given with the c-axis direction pointing towards the reader.

5.3 Characterisation of Beta-Silicon Nitride Ceramic

By using the same techniques and calculations described in Chapter 4, the important physical and chemical properties of the β-Si_3N_4 sample studied here have been obtained. The manufacturers (Cercom, USA) of this β-Si_3N_4 ceramic gave some information on the fabrication process: the compound was formed from silicon which was converted to silicon nitride and then hot pressed. Data gathered from the characterisation are presented in the same manner as in Chapter 4. The results of the determination of sample density, ultrasonic path length, lattice parameters (by X-ray analysis) and the elastic isotropy have been presented in Table 5.1. A comparison between the sample and X-ray densities in Table 5.1 shows that the ceramic sample is close to that of pure β-Si_3N_4. The two room temperature 30MHz shear mode velocities propagated with orthogonal polarisation directions (Table 5.1) only differ by around 2%; the ceramic sample is essentially isotropic in its elastic behaviour.

Table 5.1 The sample density, ultrasonic path length, lattice parameters and the results of the elastic isotropy test of β-Si_3N_4 ceramic.

Material		β-Si_3N_4
Density (kgm^{-3})		3290±10
X-ray density (kgm^{-3})		3200±1
Lattice parameters (Å)	*a*	7.618±0.022
	c	2.911±0.003
Path length (mm)		7.942±0.002
Room temperature 30MHz shear mode velocities, V_S±10 (ms^{-1})		
Polarisation direction		
Y		6117
Z		6009

5.3.1 X-ray Diffraction Analysis

The results of the X-ray diffraction study (Figures 5.2 (a) and (b)) on the ceramic were compared with diffraction standards for both the α and β phases. The diffraction pattern in Figure 5.2 (a) did not match that of the α-phase; the material is found to be β-phase except for a secondary phase. Yeheskel et al. (1984) had previously listed a number of secondary phases produced in the processes of ceramic silicon nitride fabrication. To determine the correct secondary phase in this ceramic, the X-ray pattern of each secondary phase given by Yeheskel et al. (1984) was matched against the strongest X-ray lines in Figure 5.2 (a) not corresponding to the β-phase. The closest possible X-ray spectrum match to the additional peaks observed in Figure 5.2 (a) was from the binding agent: $Y_{20}N_4Si_{12}O_{48}$ ($10Y_2O_3$-$9SiO_2$-Si_3N_4), whose X-ray diffraction pattern has been shown in Figure 5.2 (b) as blue lines. Calculations of the lattice parameters of both the primary and secondary phases in this ceramic were performed using the same method as that in Chapter 4. Table 5.1 gives the results for the lattice parameters of the β-phase of Si_3N_4; these lattice parameters agree well with the range of values quoted by Wang et al. (1996): a=7.595-7.608 Å and c=2.900-2.911 Å. For the secondary phase (binding agent), whose structure can be expressed in a hexagonal lattice, the results of lattice parameter calculations were: a=9.417±0.020 Å and c=6.795±0.030 Å. Within the errors, these lattice parameters for the binding agent are in good agreement with values given by Yeheskel et al. (1984), which were a=9.436 Å and c=6.822 Å. The good agreement between the lattice parameters calculated here and those quoted by Yeheskel et al. (1984) for the binding agent, justifies the choice of this particular compound to represent the secondary phase.

5.3.2 SEM Analysis

Scanning electron microscope images of the grain structure for β-Si_3N_4 ceramic were taken by DSTL, with one image shown in Figure 5.3 (a). Determination of the grain size distribution (Figure 5.3 (b)), using the same method described in Chapter 4, resulted in the average grain size for this Si_3N_4 ceramic of 0.98±0.71 μm. The characteristic elongated grains of β-Si_3N_4, as mentioned in Section 5.3, whose long axis is parallel to the c-axis of the hexagonal lattice (Lee and Bowman 1992), can

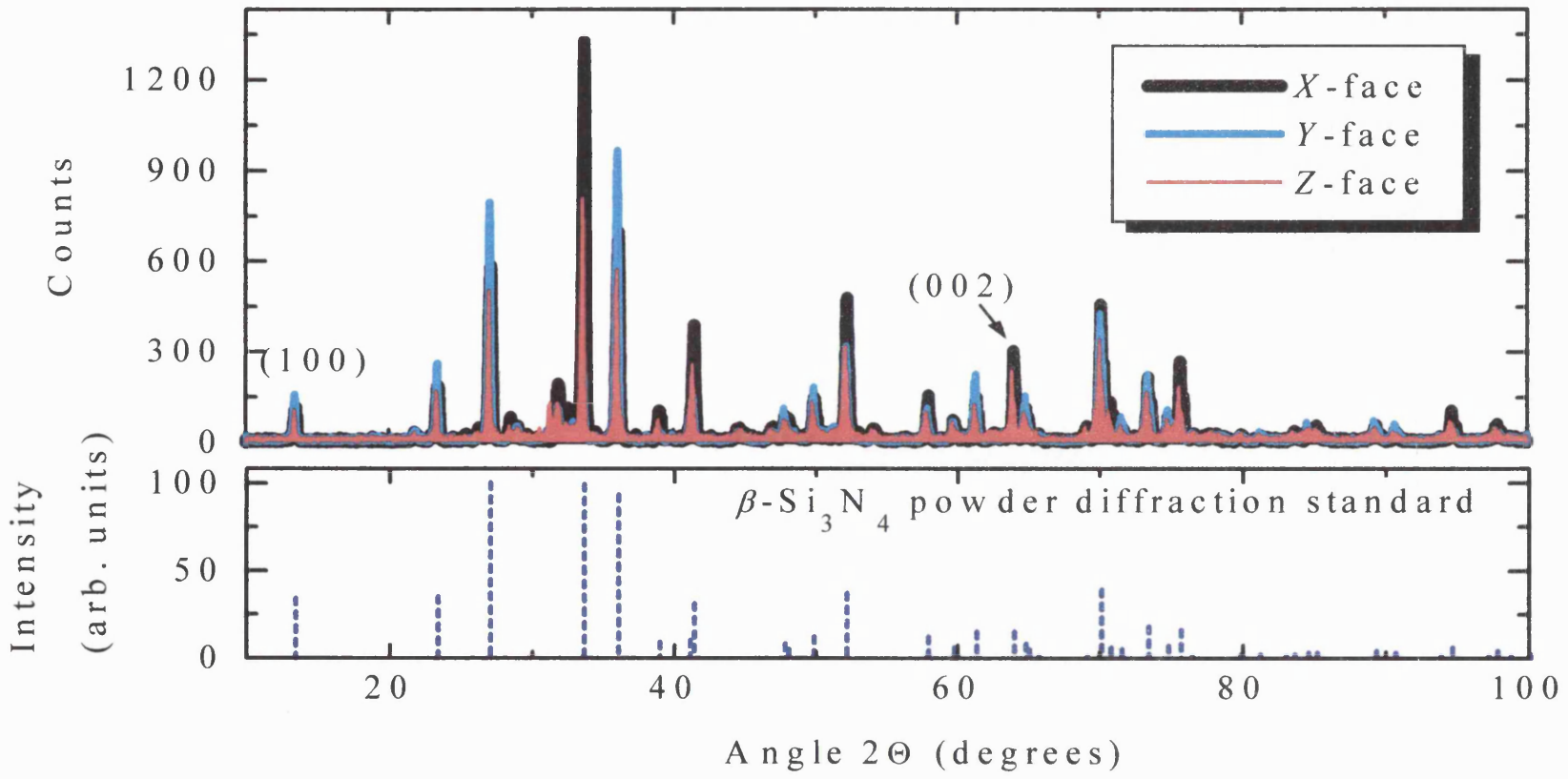

Figure 5.2 (a) X-ray diffraction spectra for three orthogonal faces of β-Si_3N_4 ceramic.

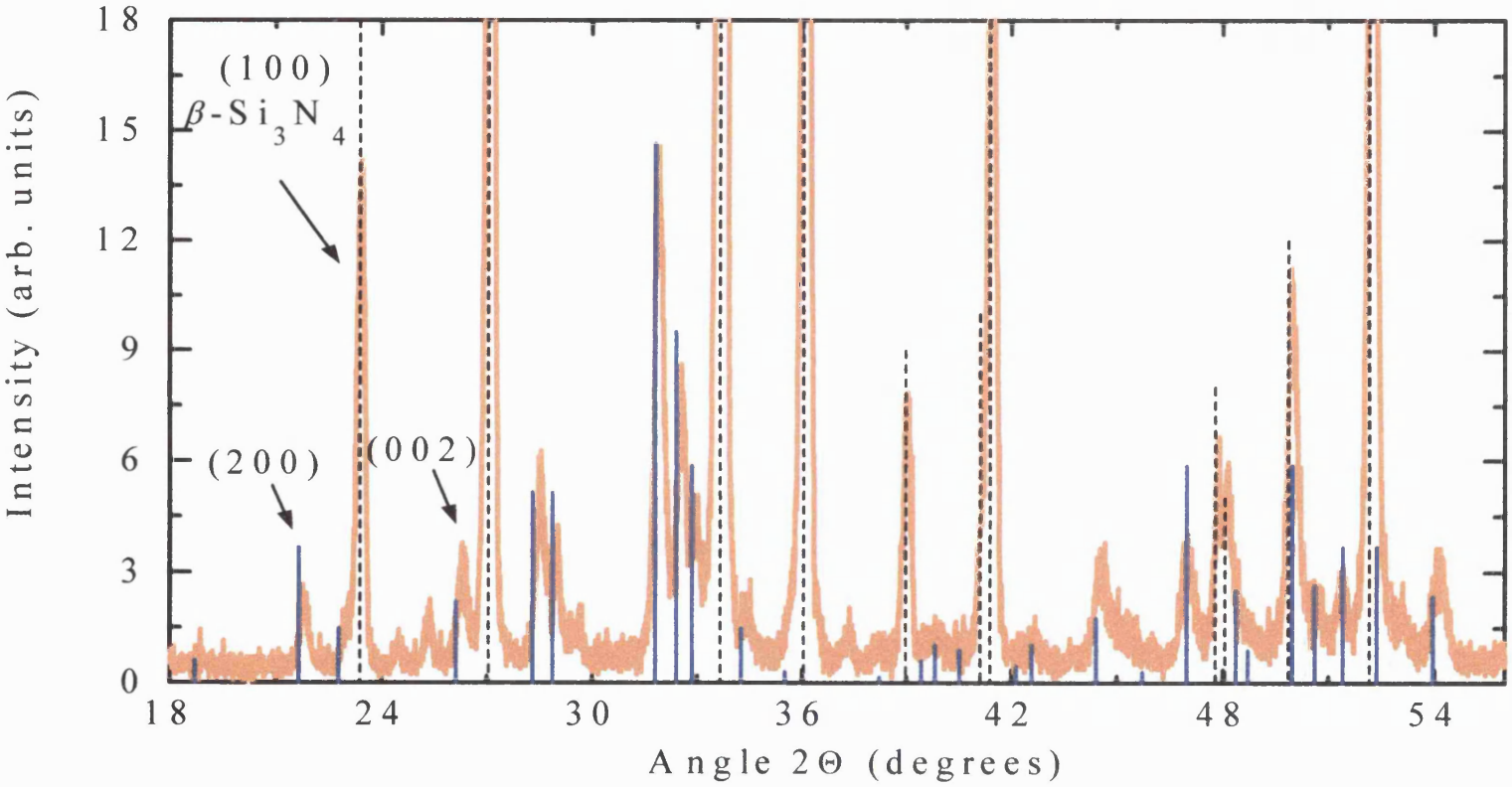

Figure 5.2 (b) X-ray diffraction spectrum of secondary phase ($Y_{20}N_4Si_{12}O_{48}$) resulting from densification agents. Blue (dotted) lines correspond to the secondary (β-Si_3N_4) phase.

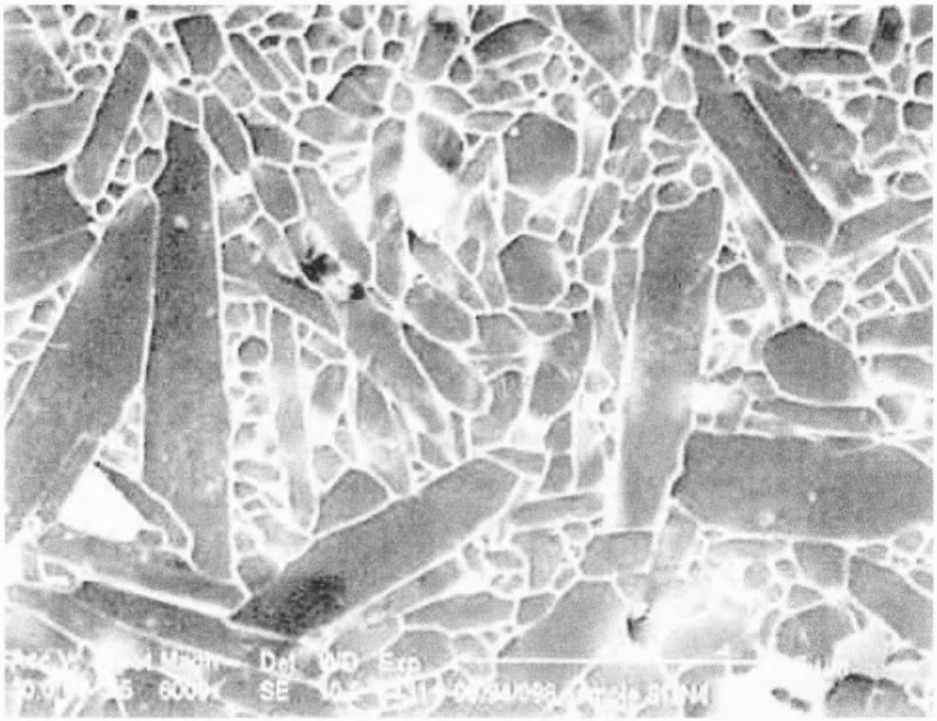

Figure 5.3 (a) Scanning electron microscope image for β-Si_3N_4 ceramic, showing the binding agent as the lighter area bordering the elongated β-Si_3N_4 grains.

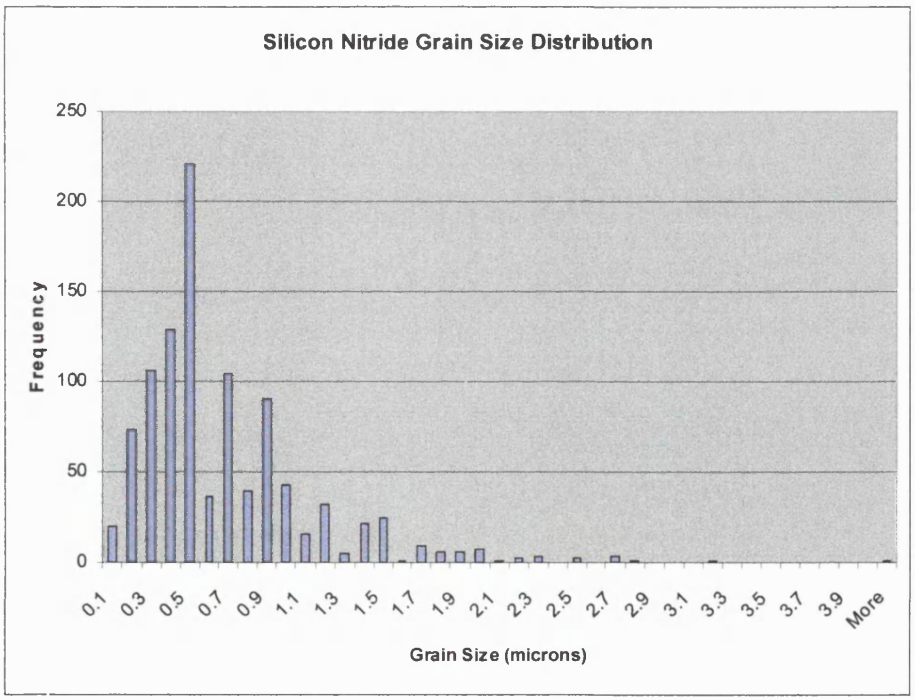

Figure 5.3 (b) Grain size distribution for β-Si_3N_4 ceramic.

clearly be seen in Figure 5.3 (a). Also evident in the SEM image is the binding agent, which appears as the light regions surrounding the silicon nitride grains.

5.3.3 Electron Microprobe Analysis

After discovery of the binding agent through the X-ray analysis, an electron microprobe analysis was performed on eight different sites of the sample surface to quantitatively determine the weight percentages of the elements present. The weight percentage of each element determined from the analysis was used to find the atomic percentage (at%); the results of these calculations are shown in Table 5.2. From knowledge of the composition of the binding agent, it was possible to estimate the proportion of Si to N atoms of the β-Si_3N_4 phase in this ceramic; this was achieved by approximating the number of atoms for the binding agent and then subtracting this from the total number of atoms and finding the ratio of the remaining silicon and nitrogen atoms. This estimation resulted in a silicon-to-nitrogen ratio of around 3:4.2 for this β-Si_3N_4 ceramic. Impurities are also present in this sample; these are iron, aluminium and carbon. According to Riley (2000), the presence of iron in the fabrication of β-Si_3N_4 acts as a catalyst to the material production mechanisms; this would account for its presence in the results of the electron microprobe analysis. Aluminium may also have been used in the fabrication process (in the form of alumina) as a densification agent (Riley 2000; De Arellano-Lopez et al. 1998). A likely source of carbon in this ceramic is accounted for by reason (4) given in Section 4.1.3, which is carbon build up generated at the sample surface while performing the electron microprobe analysis. Using the data in Table 5.2, the ceramic sample was calculated to be, by weight, 95% β-phase, 3.78% binding agent and 1.22% other impurities.

Table 5.2 Results of electron microprobe analysis showing the weight and atomic percentage of elements in the β-Si_3N_4 ceramic.

Element	wt%	at%
Y	6.44±0.74	1.49±0.17
Si	52.39±0.4	38.33±0.3
N	35.67±2.80	52.32±4.11
C	2.22±0.55	3.80±0.95
Fe	0.144±0.08	0.053±0.027
Al	0.77±0.02	0.58±0.02
O	2.67±0.22	3.43±0.08
Total	100±3	100

5.4 Ultrasonic Results and Discussion

5.4.1 Room Temperature Elastic Moduli for β-Si_3N_4 Ceramic

The velocities of 30 MHz longitudinal (V_L) and shear (V_S) ultrasonic waves propagated in the β-Si_3N_4 ceramic at 295 K are given in Table 5.3. In calculations of the room temperature elastic moduli, the shear wave velocity measured with polarisation parallel to the *Z*-face was used. Errors of 2% for the elastic moduli of the ceramic compound have been quoted in Table 5.3; these errors cover the difference of 2% in the shear wave velocities shown in Table 5.1. Comparisons of data in Table 5.3 are with those values determined by other workers using ultrasonic techniques. Most of the data compiled in Table 5.3 are those measured for high-purity, dense β-Si_3N_4 produced by hot pressing. There is general agreement between the present and previous data where it exists; in particular, those values determined by Yeheskel and Gefen (1985), from an extrapolation of ultrasonic velocity measurements on Si_3N_4 with varying amounts of porosity and α/β ratios.

The Young's modulus of Si_3N_4 has also been investigated extensively using various experimental methods. Apart from ultrasonic velocity measurements, other methods have been employed such as a strain gauge technique (Lange 1973, Choi and Salem 1994), vibration resonance methods (Himsolt et al. 1979; Pezzotti et al. 1989; Tanaka et al. 1992), nano-indentation (Hay et al. 1998) and depth sensing indentation (Gubicza

Table 5.3 The sample density, ultrasonic wave velocities, adiabatic elastic moduli and their hydrostatic pressure derivatives, and the acoustic mode Grüneisen parameters of ceramic β-Si_3N_4 at 295 K, in comparison with data taken from the literature. The values quoted in brackets for $(\partial\mu / \partial P)_{P=0}$ and γ_S refer to the high pressure region, above 0.12 GPa.

Reference	This work	Fate (1975)	Yeheskel and Gefen (1985)	Fisher et al. (1992)	De Arellano-Lopez et al. (1998)
ρ (kgm^{-3})	3290±10	3180	Fully dense	3154	99 % dense
V_L (ms^{-1})	10971±10				
V_S (ms^{-1})	6009±120				
C_L(GPa)	396±7	330		383.6	
μ (GPa)	119±3	118	122±1	126.1	128
B^S (GPa)	238±5		234±5	215.4	
E (GPa)	306±6	290	312±1	316.5	324
σ	0.285±0.005	0.220	0.280	0.255	0.269
Θ_D (K)	923±20				
$(\partial C_L / \partial P)_{P=0}$	4.5±0.1				
$(\partial\mu / \partial P)_{P=0}$	0.19±0.04 (-0.040±0.002)				
$(\partial B^S / \partial P)_{P=0}$	4.35±0.11				
γ_L	1.18±0.03				
γ_S	0.018±0.002 (-0.21±0.08)				
γ^{el}	0.35±0.02				

et al. 1999) techniques. The polycrystalline Young's moduli typically fall in the range of 300-330 GPa, with the exact value depending on porosity, intergranular phase content, texture, and the relative amounts of α and β phases present in the specimen. Only a small anisotropy in Young's modulus has been observed in hot-pressed β-Si_3N_4 ceramic samples (see for instance Buljan et al. 1987; Lee and Bowman 1992). Nevertheless, Hay et al. (1998) found a significant anisotropy in Young's modulus of whisker-like grains of β-Si_3N_4.

The bulk modulus of Si_3N_4 has been the subject of several experimental and theoretical investigations. A high pressure neutron diffraction study up to 3 GPa of the compression of β-Si_3N_4 yielded a bulk modulus of 256 GPa. X-ray diffraction measurements by Li et al. (1997) on β-Si_3N_4 under pressure up to 34 GPa at room temperature gave the values 273±14 GPa and 266±1 GPa for the bulk modulus by fitting the data to the Birch-Murnaghan equation of state and a "universal" equation of state, respectively. Considerable effort has been devoted to determination of the bulk modulus of β-Si_3N_4 from model calculations; for a recent overview see Ching et al. (1998). The range of bulk modulus values obtained from these theoretical studies is ~258-282 GPa, and the results were obtained by using such techniques as the orthogonalized linear combination of atomic orbitals (OLCAO) (Xu and Ching 1988), a method based on Hartree-Fock theory (Wendel and Goddard III 1992) and a phenomenological model (Mirgorodsky et al. 1993). These calculated results obtained for the bulk modulus of β-Si_3N_4 are comparable with (at most 18 % larger than) that found in the present ultrasonic study (Table 5.3), and support the proposition by Cartz and Jorgensen (1981) that a high value of the bulk modulus of silicon nitride is mainly due to its rigid framework structure.

5.4.2 Temperature Dependences of the Elastic Moduli and Ultrasonic Wave Attenuation Coefficients for β-Si_3N_4 Ceramic

The temperature dependences of the ultrasonic velocities have been used to determine the behaviour of the elastic moduli below room temperature for the β-Si_3N_4 ceramic sample (Figures 5.4 (a) to (c)). Bond breakage between sample and transducer and

subsequently ultrasonic signal loss occurred below 150K, due to thermal expansion differences between sample, bond and transducer; thus, giving a limiting temperature range of measurement (290-150K). When the sample was cycled between room temperature and 150 K, there was no thermal hysteresis in the ultrasonic wave velocities and no irreversible effects were observed; consequently this is mirrored in the presented temperature dependent data.

The longitudinal stiffness (Figure 5.4 (a)) increases with decreasing temperature and shows the unusual feature of a change in slope at about 235 K where there is a knee. A number of temperature runs were performed which confirmed this unusual behaviour. Below this knee, an apparent softening occurs. In Figure 5.4 (a), the longitudinal stiffness temperature data has been plotted along with the conventional model for vibrational anharmonicity (dotted line) described in Section 2.8. A "softening" is observed at temperatures below 235 K as previously mentioned, i.e. the gradient is not as large as that calculated on the basis of this model which, for example, holds for the ceramics described in Chapter 4. The temperature behaviour of the longitudinal elastic stiffness above 235K is consistent with high temperature longitudinal modulus measurements made by Fate (1975).

The shear stiffness also shows unusual behaviour with temperature (Figure 5.4 (a)): it softens anomalously upon cooling from room temperature. Due to this unusual behaviour in the shear stiffness, the shear mode velocity, used to calculate the shear stiffness in the present work, was measured with two different polarisation directions: parallel to the *Y*- and *Z*-faces, as a function of temperature (Figure 5.4 (a)). The temperature coefficients of these two shear mode velocities are very small, being: 3.28 x 10^{-6} and 1.69 x 10^{-6} K^{-1}, respectively; the shear mode velocity (and hence the shear elastic stiffness) is practically temperature independent. This is in accord with measurements by Fate (1975) on the elastic properties of a number of β-Si_3N_4 ceramics at elevated temperatures. Fate (1975) witnessed the beginning of a softening of the shear stiffness at ~625 K for β-Si_3N_4 samples with density 3180 kgm^{-3} and 3050 kgm^{-3}.

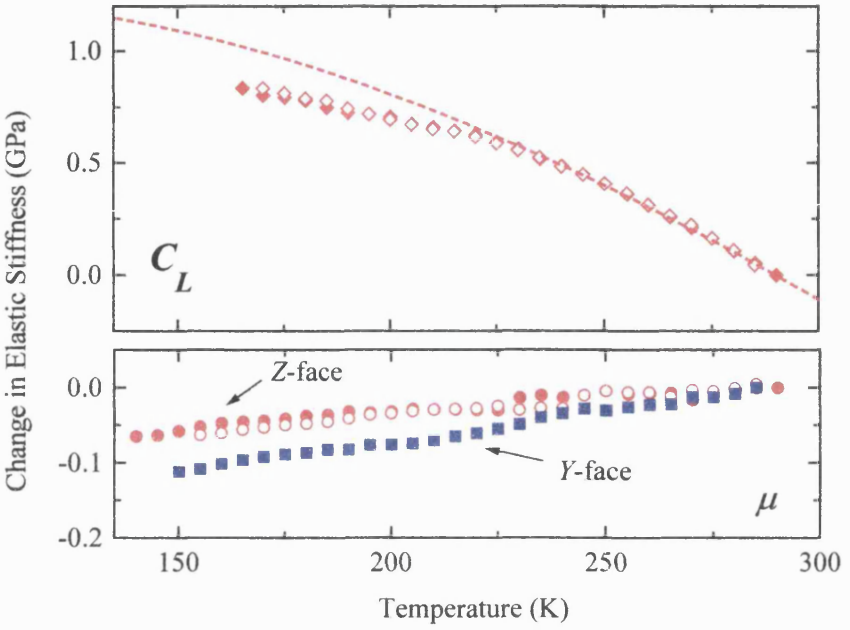

Figure 5.4 (a) Change in longitudinal and shear elastic stiffnesses as a function of temperature for β-Si_3N_4 ceramic. Filled (open) symbols correspond to decreasing (increasing) temperature. Dotted line corresponds to fit of lattice vibrational anharmonicity model.

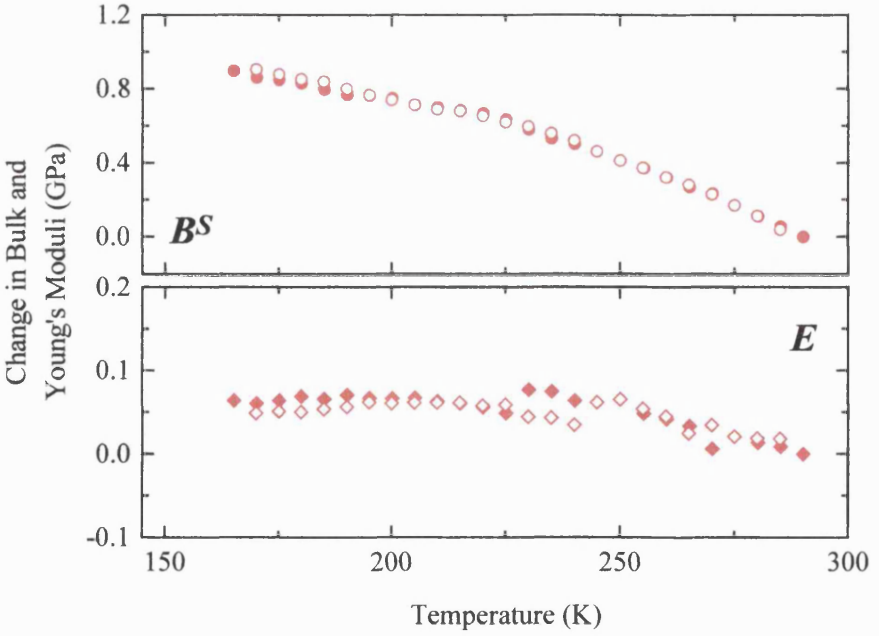

Figure 5.4 (b) Change in bulk and Young's moduli as a function of temperature for β-Si_3N_4 ceramic. Filled and open symbols have same meaning as Figure 5.4 (a).

The temperature behaviour of the longitudinal and shear stiffnesses is reflected in the data for the bulk and Young's moduli versus temperature (Figure 5.4 (b)). The bulk modulus increases by around 0.4%, while Young's modulus shows a very small increase (~0.02%) over the temperature range measured. Small Young's modulus temperature dependences were reported by Sato et al. (1993) in two beta-silicon nitride samples sintered with Y_2O_3-based additives in the range 20-1050°C. Above 800°C and 1050°C, the Young's moduli of these two samples significantly decreased. Sato et al. (1993) attributed these anomalies to polycrystalline anelasticity that involved grain boundary sliding. The acoustic Debye temperature exhibits similar features to those observed in the shear stiffness (Figure 5.4 (c)) by decreasing slightly with temperature. Poisson's ratio only changing by 0.3% over the temperature range of measurement (Figure 5.4 (c)), so is taken to be practically constant. No anomalous data was recorded for the attenuation coefficients of 30MHz ultrasonic waves propagated in the ceramic as a function of temperature (Figure 5.4 (d)); they show similar behaviour to the ceramics studied in Chapter 4. That is, the wave energy loss as the material is cooled is similar to that observed for a normal ceramic.

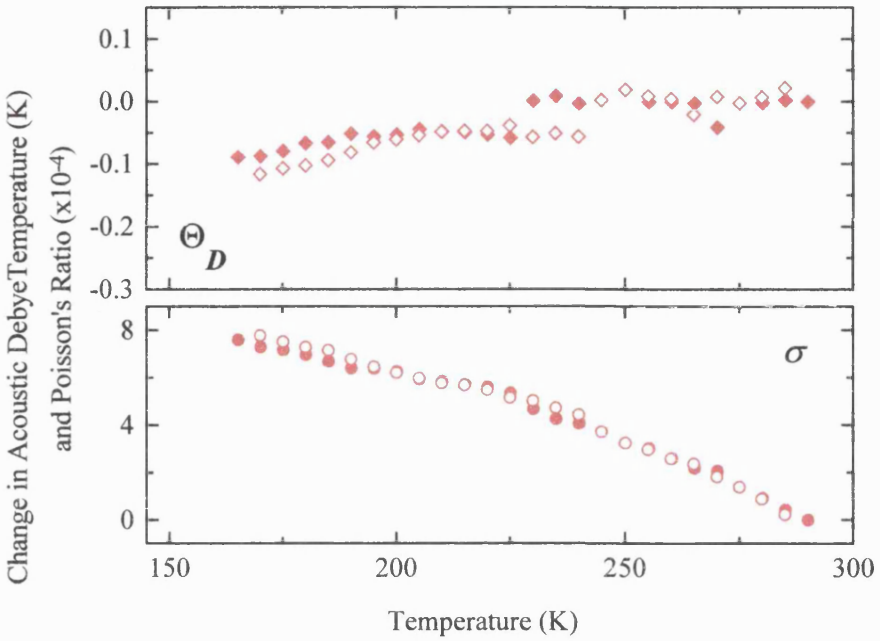

Figure 5.4 (c) Change in acoustic Debye temperature and Poisson's ratio as a function of temperature for β-Si_3N_4 ceramic. Filled (open) symbols correspond to decreasing (increasing) temperature.

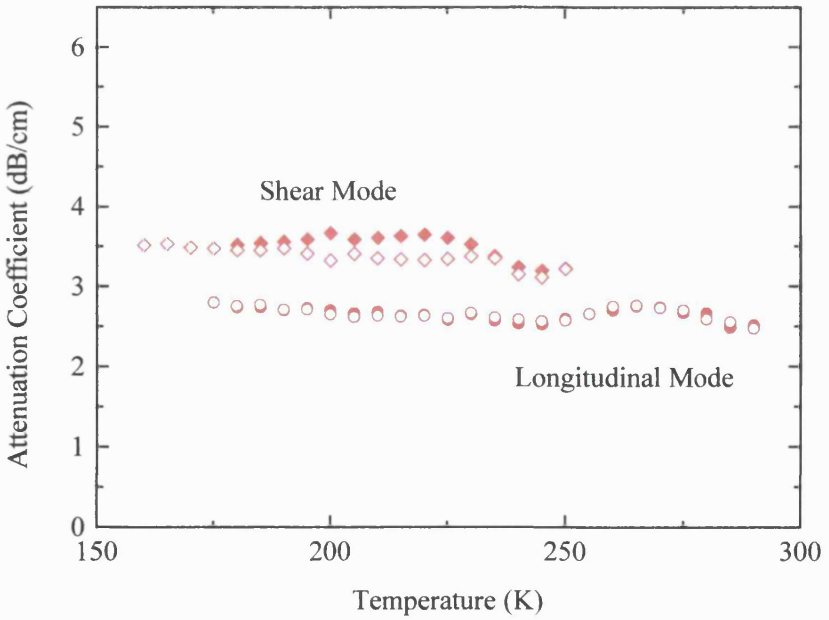

Figure 5.4 (d) Ultrasonic wave attenuation coefficients as a function of temperature for β-Si_3N_4 ceramic. Filled and open symbols have same meaning as Figure 5.4 (a).

5.4.3 Hydrostatic Pressure Dependences of Ultrasonic Wave Velocities and Attenuation Coefficients and Elastic Stiffness Moduli for β-Si_3N_4 Ceramic

The effects of hydrostatic pressure on ultrasonic wave velocity in β-Si_3N_4 ceramic are small, particularly for the shear wave velocity shown in Figure 5.5. The data for the pressure dependence of the velocities of both longitudinal and shear ultrasonic waves are reproducible under pressure cycling and show no measurable hysteresis effects. This observation indicates that the β-Si_3N_4 ceramic does not alter under pressure cycling up to 0.2 GPa and that there is no relaxation of any residual stress.

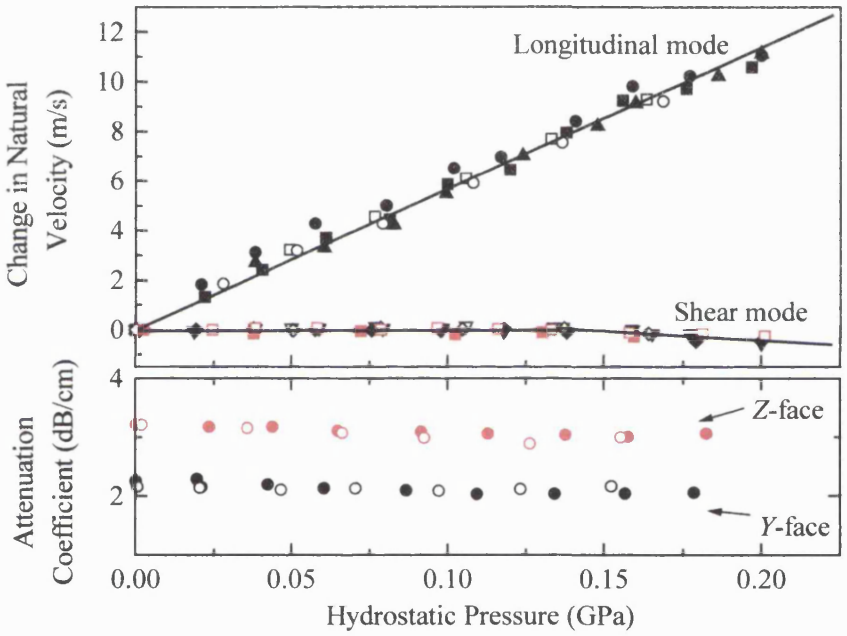

Figure 5.5 Change in longitudinal and shear mode natural velocities and shear mode ultrasonic wave attenuation coefficients (for two orthogonal polarisations) as a function of hydrostatic pressure, at 295K. Filled (open) symbols correspond to increasing (decreasing) pressure. Red data in the velocity plot corresponds to shear mode polarisation parallel to *Z*-face.

The velocity of the longitudinal ultrasonic waves increases approximately linearly with pressure. This is a normal behaviour: the long wavelength longitudinal acoustic modes stiffen under pressure. However, the behaviour under pressure of the velocity of shear ultrasonic waves is unlike that of the longitudinal mode. As the pressure increases up to around 0.12 GPa, the shear wave velocity is practically constant and above this

pressure region it decreases slightly. Increasing pressure has generally analogous effects on elastic stiffness to decreasing temperature. Thus, the shear acoustic mode softening observed at low temperatures (Figure 5.4 (a)) may well be correlated to that found at high pressures: they may have the same origin. In the work of Sato et al. (1993) the observed dependence of the Young's modulus with temperature was analogous to that shown in Figure 5.4 and was attributed to anelastic behaviour caused by grain boundary sliding. The ceramic sample studied here contains a significant amount of a secondary phase (binding agent). This phase is similar to those discovered by Sato et al. (1993) which suggests that the behaviour of the elastic stiffnesses shown in Figures 5.4 (a), e.g. the deviation at low temperatures of the longitudinal elastic stiffness from the anharmonic approximation, is caused by the same effect.

Shear wave attenuation measurements as a function of pressure were performed to see if any anomalous absorption or scattering effects accompanied this apparent shear acoustic mode softening; the results of these measurements are shown in Figure 5.5, for two different polarisation directions. No anomalous behaviour under compression is evident from these data, which is in accord with the wave attenuation as a function of temperature.

By using a phenomenological model to study the lattice dynamics of β-Si_3N_4, Mirgorodsky et al. (1993) predicted a lattice instability under high pressure, namely, a pressure induced softening of some low frequency vibrational modes originating from out-of-plane motions of nitrogen atoms in silicon-nitrogen triangles. The interatomic forces arising in the material as a response to application of high pressure would soften certain vibrational modes of the lattice. This prediction may be applicable here, but inelastic neutron diffraction measurements to determine the pressure dependence of the long wavelength acoustic phonon mode dispersion curves for β-Si_3N_4 should be performed to confirm this prediction.

The hydrostatic pressure derivative $(\partial C_L / \partial P)_{P=0}$ determined for the β-Si_3N_4 ceramic has a positive, normal value (Table 5.3). The longitudinal elastic stiffness and thus the

slope of the corresponding acoustic mode dispersion curve, at the long-wavelength limit, increase with pressure in the normal way. At low pressures, $(\partial\mu / \partial P)_{P=0}$ has a small positive value, while at higher pressures it is slightly negative due to the negative slope of the shear mode velocity. The shear wave velocity data over the whole pressure range do not fit to a single straight line (see Figure 5.5), therefore the average of the two values of $(\partial\mu / \partial P)_{P=0}$ in Table 5.3 has been used in the calculation of $(\partial B^S / \partial P)_{P=0}$. Since the technique used in the present pressure study can determine the adiabatic bulk modulus pressure derivative in a more direct manner than other methods, it is instructive to compare the $(\partial B^S / \partial P)_{P=0}$ value of ceramic β-Si_3N_4 with those determined by other researchers using other methods. Li et al. (1997) performed X-ray diffraction measurements on β-Si_3N_4 under pressure up to 34 GPa at room temperature and analysed the data on the pressure dependence of unit cell volume in terms of the Birch-Murnaghan equation of state and a "universal" equation of state: the former yielded 3.8±1.6 for the pressure derivative of bulk modulus at zero pressure and the latter gave 4.3±2.1 for the same parameter. From *ab-initio* total energy calculations, Ching et al. (1998) derived a value of 3.99 for the pressure dependence of the bulk modulus of β-Si_3N_4. The value 4.35±0.11 found for the pressure derivative of the adiabatic bulk modulus of ceramic β-Si_3N_4 in the present high pressure ultrasonic study is in good agreement with the results of these recent high pressure X-ray measurements (Li et al. 1997) and theoretical calculations (Ching et al. 1998).

The measurements of the bulk modulus and its hydrostatic-pressure derivative have been used to calculate the volume compression $V(P)/V(0)$ of ceramic β-Si_3N_4 up to very high pressures, using Equation (2.45). The calculation was performed at room temperature and results are shown below in Figure 5.6. The comparatively small magnitude of the volume compression for ceramic β-Si_3N_4 is typical of that found for silicon nitrides, in which the rigid framework reduces the compressibility coefficients and hence increases the bulk modulus (Cartz and Jorgensen 1981; Li et al. 1997). A comparison has been made in Figure 5.6 between the volume compression of ceramic β-Si_3N_4, determined in the present work, with data extracted from Cartz and Jorgensen (1981) and Li et al. (1997), α-quartz data (SiO_2) by Wang et al. (1992) and the three

ceramics studied in Chapter 4. The remarkably incompressible behaviour of β-Si_3N_4 is consistent with its basic structure: irregular networks of SiN_4 tetrahedra which are unable to undergo cooperative reorientations. The SiN_4 tetrahedra are linked such that only distortions of the tetrahedra are permitted, hindering angle and bond length deformations. Neutron diffraction measurements by Cartz and Jorgensen (1981) showed no change in the Si-N bond length and less than a 2° change in the N-Si-N angle upon applying pressures up to 3 GPa to a β-Si_3N_4 crystal. This is in contrast with α-quartz SiO_2 in which the SiO_4 tetrahedra can easily undergo cooperative reorientations leading to a considerably larger compression, as shown in Figure 5.6.

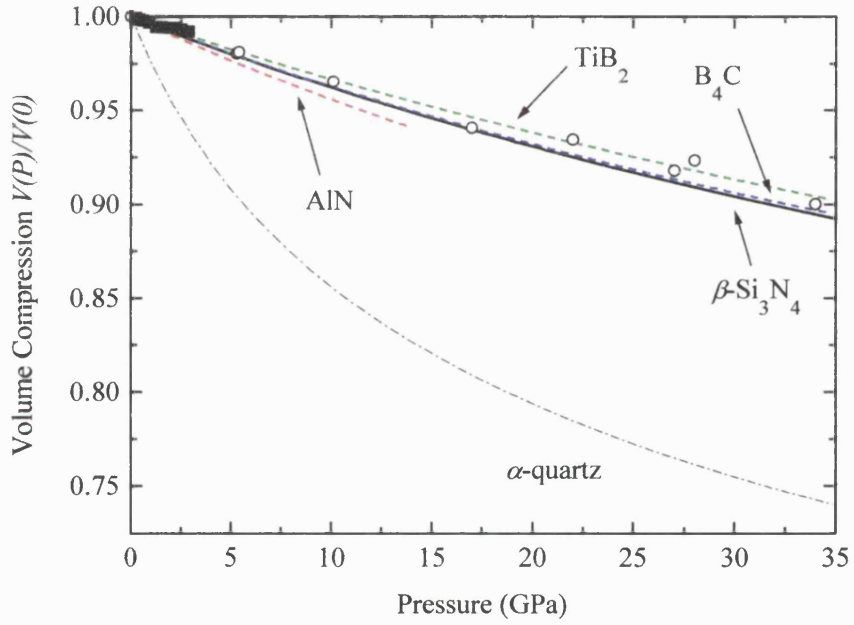

Figure 5.6 Volume compression for β-Si_3N_4 ceramic, compared with data taken from Cartz and Jorgensen (1981)-filled squares, Li et al. (1997)-open circles, Wang et al. (1992)-dot-dashed line and the AlN, TiB_2 and B_4C ceramics studied in Chapter 4.

5.4.4 Grüneisen Parameters and Acoustic Mode Vibrational Anharmonicity for β-Si_3N_4 Ceramic

The results obtained for γ_L, γ_S and γ^{el} of ceramic β-Si_3N_4 at room temperature are included in Table 5.3. Both γ_L and γ^{el} are positive. The shear mode Grüneisen parameter is very small and positive in the low pressure region; however, it is slightly negative in the high pressure region indicating shear acoustic mode softening. For the same reasons expressed in Chapter 4, the high acoustic Debye temperature Θ_D (=923±5 K) suggests that the longer wavelength acoustic phonons can be expected to dominate properties determined by vibrational anharmonicity even at room temperature. Although the thermal Grüneisen parameter (γ^{th}) includes the effects of all phonons in the Brillouin zone, contributions from optical phonons are expected to be negligible at room temperature. Comparing the mean acoustic mode Grüneisen parameter (=0.35) taken from Table 5.3 with a value of 0.39 for the thermal Grüneisen parameter estimated by Bruls et al. (2001b) indicates that the contribution of the acoustic phonon modes to the thermal Grüneisen parameter is larger than that of the optic modes at room temperature. Small values for the acoustic mode Grüneisen parameters and hence low vibrational anharmonicity are compatible with the low thermal expansion of β-Si_3N_4. Shear modes have a higher population density than the longitudinal modes. The shear acoustic mode Grüneisen parameter γ_S (=0.018, at low pressures) is much smaller than the longitudinal acoustic mode Grüneisen parameter (=1.18); this coupled with their higher density accounts for the low thermal Grüneisen parameter estimated for this ceramic compound. Thus the higher population density of shear acoustic phonons at room temperature enhances their contribution to thermal expansion and specific heat, lowering the thermal expansion and hence the thermal Grüneisen parameter. The low anharmonicity of long wavelength acoustic modes of β-Si_3N_4 as quantified by the relatively small value of γ^{el}, which in part is due to the apparent soft shear modes, is compatible with the small thermal expansion. A typical value of the thermal expansion for β-Si_3N_4 is shown in Table 3.1.

Chapter 6

Ceramic Transition Metal-Carbides: TiC, TaC and ZrC

6.1 Introduction

Transition-metal carbides (TMCs) are interesting for both fundamental studies and technological applications. The carbides studied here: TiC, TaC and ZrC, have a range of properties which are utilised for technological purposes; these are great hardness, high melting point (TaC has the highest melting point of any known material at 3983°C), good mechanical stability and brittle-to-ductile transitions at high temperatures (Toth 1971). These carbides are extensively used as hard constituents in metal matrix composites (hard-metals) and in the forming of layers (coatings) on cutting tools (Kral et al. 1998). Fundamental properties of these carbides such as metallic behaviour in their electrical, magnetic and optical properties, superconducting transitions (TaC) and defect structures have also been found (Toth 1971). According to Williams (1997), a potential electrical application for these carbides is for interconnects in very large-scale integrated circuits.

In a critical review, Kral et al. (1998) listed a large number of room temperature Young's modulus and Poisson's ratio values for transition-metal carbides with varying compositions and porosity, but the data scatter was large. Some data exists for the measurements of technological elastic moduli (E, B and σ) extended to high temperatures (20-1600°C), but very little has been studied on the low temperature behaviour. A small number of experimental and theoretical studies have been performed to determine the elastic response of these transition-metal carbides to compression. This study was motivated by the lack of knowledge of the elastic behaviour of transition-metal carbides at room temperature and below and under high pressure.

6.2 Crystal Structure of TiC, TaC and ZrC

Each carbide (or monocarbide) used in the present ultrasonic study crystallize in a NaCl (*B*-1) structure, with 2 atoms per unit cell. One way to visualise this *B*-1 structure is a face-centred cubic (FCC) metal lattice with all the octahedral interstitial sites filled by carbon atoms (Figure 6.1); when all the octahedral sites are filled the transition-metal to carbon ratio is one-to-one, and the compound is classed as "stoichiometric". In practice, this stoichiometry is seldom reached and the carbides are then classed as "sub-stoichiometric" and retain their NaCl structure over a wide range of carbon concentrations (Toth 1971), which results in carbon vacancies at the interstitial sites. The corresponding concentration of carbon vacancies ranges from 2-3% to 50% in these monocarbides (Williams 1988). One consequence of this defect structure, stated by Williams (1988), is that the carbon vacancies are randomly distributed in the carbon sublattice of these monocarbides and are recognised as scattering centres for electrons and phonons. It has also been suggested by Williams (1988) that disordered-to-ordered phase transitions, which occur in some monocarbides at different metal/non-metal ratios, means that the structures are metastable. Due to a mixture of metallic, covalent and ionic bonding in transition-metal carbides, Williams (1999) has described these compounds as "metallic ceramics".

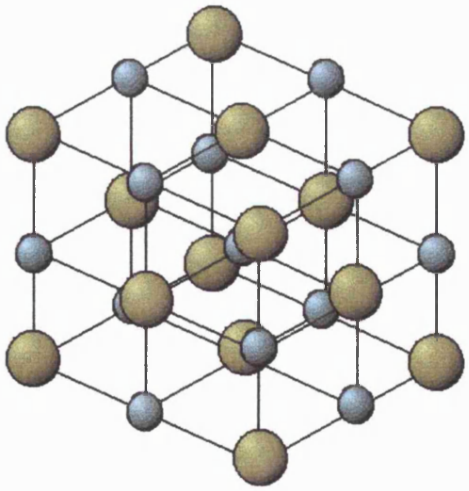

Figure 6.1 Representation of the crystal structure of cubic *B*-1 carbides, green (blue) spheres correspond to transition-metal (carbon) atoms.

6.3 Characterisation of Transition-Metal Carbide Ceramic Samples

Toth (1971) has stipulated that, in general, there is a need for good characterisation of these transition-metal carbides because their elastic properties depend upon many factors, which are:

(1) the crystal structure and lattice parameters;

(2) the chemical composition, including carbon-to-metal ratio, combined and free carbon concentrations and impurity concentration, especially oxygen;

(3) the defect structure including vacancy concentration, porosity and pore distribution;

(4) sample homogeneity.

To obtain these important physical and chemical properties, listed above, for each ceramic sample, the standard characterising techniques have been employed.

6.3.1 Ultrasonic Samples

The ceramic samples, manufactured in the USA using a hot pressing technique, were all parallelepipeds with approximate dimensions: 10x8x8 mm. Sample densities, lattice parameters, ultrasonic path lengths and results of the elastic isotropy test are presented in Table 6.1. In previous chapters, the measurements of shear mode velocities with different polarisations for one propagation direction only were used to test for the elastic isotropy of a ceramic sample. To examine the elastically isotropic nature of these carbide ceramics, the same technique was applied to the ultrasonic sample, but in three orthogonal directions, which provided a better overall picture for the isotropic nature of each sample. The results of these room temperature velocity measurements (Table 6.1) are represented in terms of the coordinate system defined in Chapter 4 (Figure 4.2), and show that the ceramics behaved in an elastically isotropic way. Out of the three samples, the ceramic ZrC sample had the largest discrepancies in the measured set of longitudinal and shear ultrasonic velocities; but these discrepancies only amounted to differences of 2% in the longitudinal mode velocities and around 3% in the shear mode.

X-ray studies performed on each ceramic used for ultrasonic measurements (Figures 6.2 (a) to (c)) revealed that all samples were single phase, and that there was no

Table 6.1 The sample densities, lattice parameters and longitudinal and shear mode ultrasonic velocities propagated in different directions and with different polarisations for TiC, TaC and ZrC ceramic samples. The ultrasonic wave carrier frequency is the figure in parenthesis next to the ultrasonic velocities; where a value is absent this signifies that the velocity was measured at a frequency equal to the value shown in the row above.

Material		TiC	TaC	ZrC
Density (kgm^{-3})		4495±4	12788±50	5153±20
Lattice Parameter (Å)		4.323±0.004	4.448±0.003	4.678±0.004
Room temperature longitudinal mode velocities, $V_L \pm 10$ (ms^{-1})				
Propagation direction				
X		9385 (50MHz)	6238 (30MHz)	6468 (10MHz)
Y		9459 (30MHz)	6230 (10MHz)	6341
Z		9444	6229	6400
Room temperature shear mode velocities, $V_S \pm 10$ (ms^{-1})				
Propagation direction	Polarisation direction			
X	*Y*	5888 (30MHz)	3741 (10MHz)	3876 (10MHz)
	Z	5886	3743	3873
Y	*X*	5846	3730	3931
	Z	5849	3755	3967
Z	*X*	5835	3731	3917
	Y	5834	3762	3969

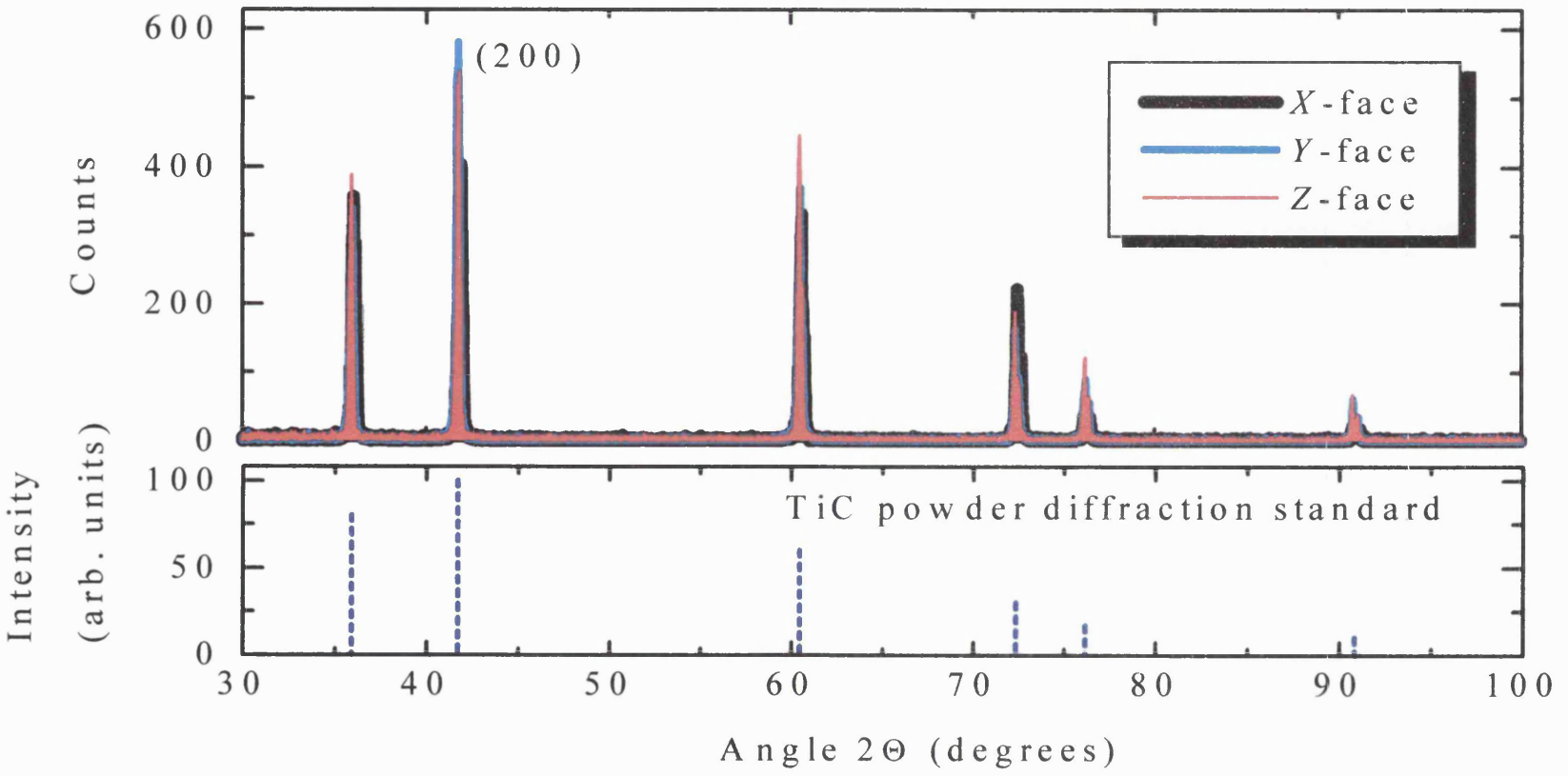

Figure 6.2 (a) X-ray diffraction spectra for three orthogonal faces of TiC ceramic.

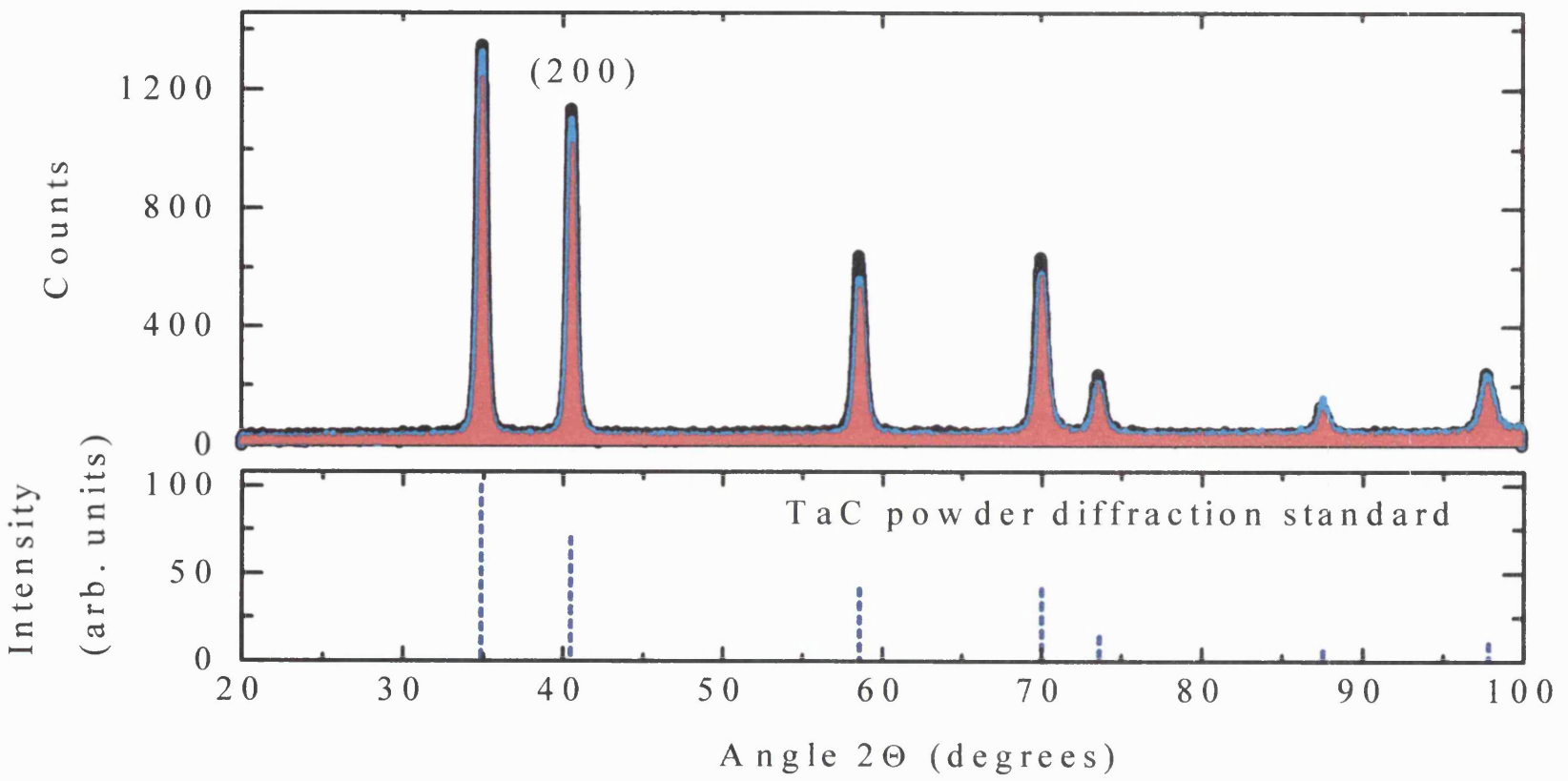

Figure 6.2 (b) X-ray diffraction spectra for three orthogonal faces of TaC ceramic.

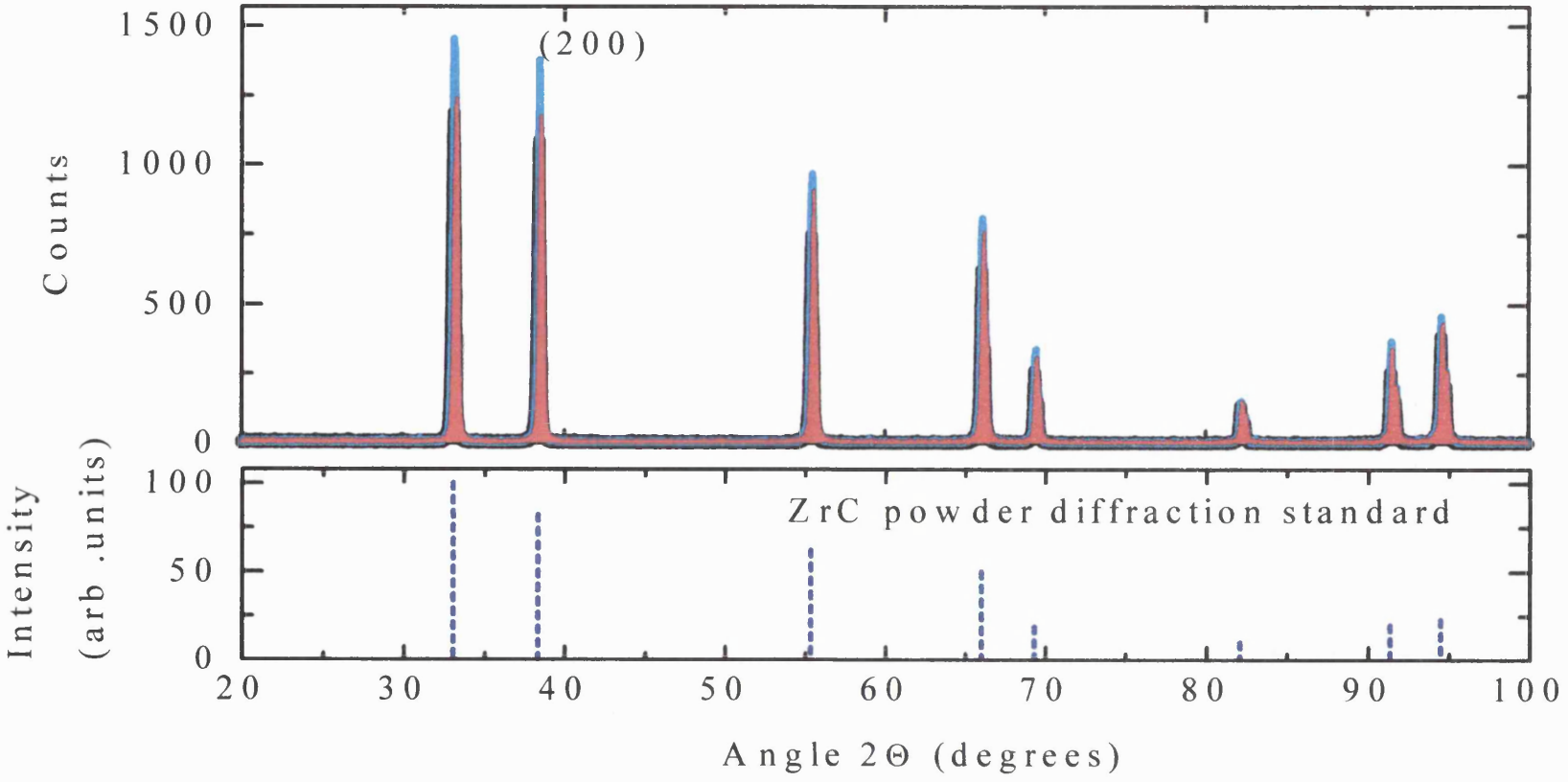

Figure 6.2 (c) X-ray diffraction spectra for three orthogonal faces of ZrC ceramic.

evidence of secondary phases. Values for the lattice parameters (Table 6.1) werecalculated using the (200) plane angles determined from the X-ray diffraction spectra of each ceramic; these particular planes are labelled in Figures 6.2 (a), (b) and (c).

Storms (1968) showed that the lattice parameters of transition-metal carbides (TMCs) depend on their defect structure, i.e. carbon concentration. This dependence was found by taking previous characterisation data on TMCs from the literature and plotting the carbon concentration against lattice parameters for each TMC, which included the three monocarbides studied here. By taking into account the influence of impurities such as oxygen on the lattice parameters, Storms (1968) plotted best-fit curves to his collected data for each TMC. These plots provide a method for determining the carbon concentrations of each TMC used in the present study by comparing the lattice parameters from Table 6.1 with the data plotted by Storms (1968); this comparison produced sub-stoichiometries of $TiC_{0.68}$, $TaC_{0.93}$ and $ZrC_{0.45}$ for the ceramic samples. Since this comparison method at best estimates the carbon concentrations in these ceramics, more conventional methods have been used to obtain more accurate information for the chemical compositions in these ceramics; this will be discussed further in the next section.

6.3.2 Techniques Used to Determine the Actual Carbon Concentrations of the Ultrasonic Samples

Nondestructive techniques were used to determine the actual carbon concentrations in each ceramic sample. Electron microprobe quantitative analysis (EMQA) was initially used to provide an accurate determination of the composition of these carbides. The averaged results of a number of scans on one surface of each ultrasonic ceramic sample are shown in Table 6.2; also shown is an independent spectrographic analysis of the starting powders used to produce these ceramics, but this does not include the metal compound used in the fabrication process. Each ceramic is essentially composed of carbon and transition metal with small amounts of oxygen impurities (Table 6.2). Carbon-to-metal ratios have been calculated from the normalised atomic percentage for each carbide sample; the normalisation was performed with respect to the weight

Table 6.2 Spectrographic analysis of starting powders used in fabrication of ultrasonic and bar carbide samples and the results of electron microprobe analysis performed to estimate the carbon-to-metal ratio of the ultrasonic samples. The symbol (*) signifies a normalisation with respect to transition-metal atoms.

Material	TiC	TaC	ZrC
Spectrographic analysis of starting powders (wt%)			
Al	-	0.005	<0.03
Ca	<0.01	<0.001	<0.01
Fe	<0.03	0.01	-
Nb	-	0.02	-
Hf	-	-	0.003
Si	-	0.01	-
Ti	-	-	-
Carbon	19.29	6.23	11.68
Electron microprobe analysis of ultrasonic samples			
Measured weight percentage (wt%)			
Metal (wt%)	86.11±0.84	96.326±0.66	86.34±0.44
Carbon (wt%)	16.15±0.77	4.543±0.127	15.20±0.17
Oxygen (wt%)	0.94±0.25	0.171±0.051	3.035±0.093
Total	103.20±1.86	101.04±0.84	104.58±0.70
Normalised atomic percentage (atom%)			
Metal (atom%)	*61.21±0.59	57.80±0.40	*46.49±0.24
Carbon (atom%)	37.17±1.77	41.08±0.01	46.58±0.52
Oxygen (atom%)	1.62±0.43	0.011±0.003	0.070±0.002
Carbon/Metal Ratio	0.61±0.03	0.71±0.005	1.00±0.012

percentage of each transition metal element, since oxygen and carbon are likely to be affected by factors listed in Section 4.1.3 of Chapter 4, for low atomic number elements. An indication of the spurious compositional data determined from this analysis is evident when the carbon weight percentage in Table 6.2 for the ceramic ZrC sample is larger than the original spectrographic carbon weight percentage, even after a number of correction methods were employed.

The carbon-to-metal ratio calculations shown in Table 6.2 were compared with the estimated carbon-to-metal ratios in Section 6.4.1 to check for any inconsistencies. This comparison revealed inconsistencies for the carbon concentrations of both TaC and ZrC ceramics: the results from Section 6.4.1 gave $TaC_{0.71}$ and $ZrC_{0.45}$, while the EMQA produced $TaC_{0.93}$ and $ZrC_{1.00}$. In contrast to these inconsistencies, fairly good agreement on the carbon-to-metal ratio for TiC was found using these two methods: $TiC_{0.61}$ and $TiC_{0.68}$.

These inconsistencies were investigated further by using the electrical resistivity measurements as a function of temperature, in the range 300-1400K, for these ceramic samples. This investigation was possible due to the fact that electrical resistivity temperature dependences for these transition-metal carbides show strong dependences on sample composition (Wang et al. 1995a). The same technique applied in Section 4.4 has been used here to determine the electrical resistivity measurements at room and elevated temperatures; that is, the results produced from measurements on smaller samples (dimensions: 10x1.5x1.5 mm) cut from the same block as their ultrasonic counterparts are used to represent the electrical behaviour of the larger samples. The temperature dependence of electrical resistivity has been plotted in Figure 6.3 (a) to (c) for the ceramic bars of TiC, TaC and ZrC, respectively. A number of temperature runs were performed for each carbide bar sample and in some cases a certain degree of hysteresis was observed on cooling, especially when the samples were subjected to temperatures greater than 1000K; this hysteresis is strongest in Figure 6.3 (c). In most cases, when the upper limit of the temperature range was lower than 1000K the hysteresis on cooling disappeared. It is not clear whether this hysteresis is from sample effects or a consequence of measurements in non-isothermal conditions.

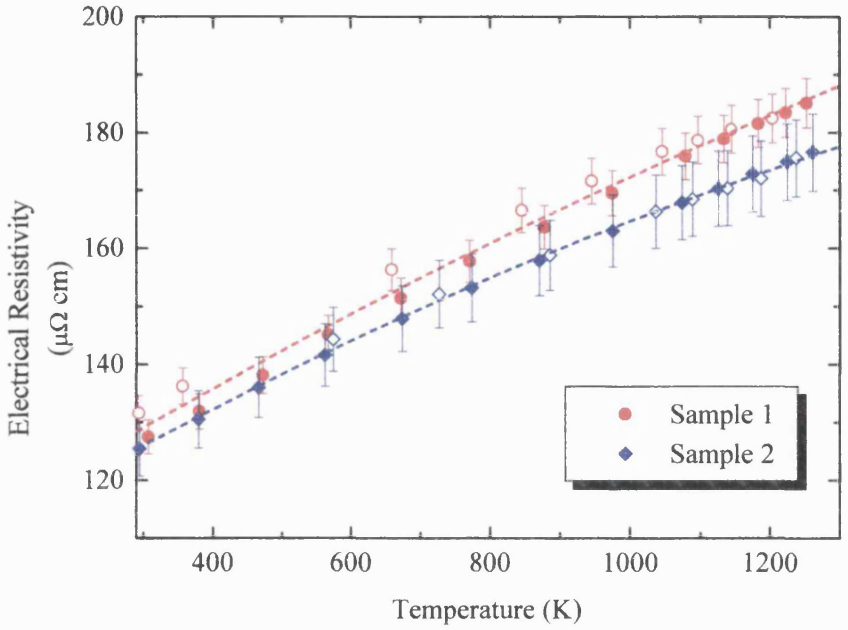

Figure 6.3 (a) The electrical resistivity as a function of temperature for TiC ceramics. Filled (open) symbols correspond to decreasing (increasing) temperature. Dotted lines are second-order polynomial fits to data.

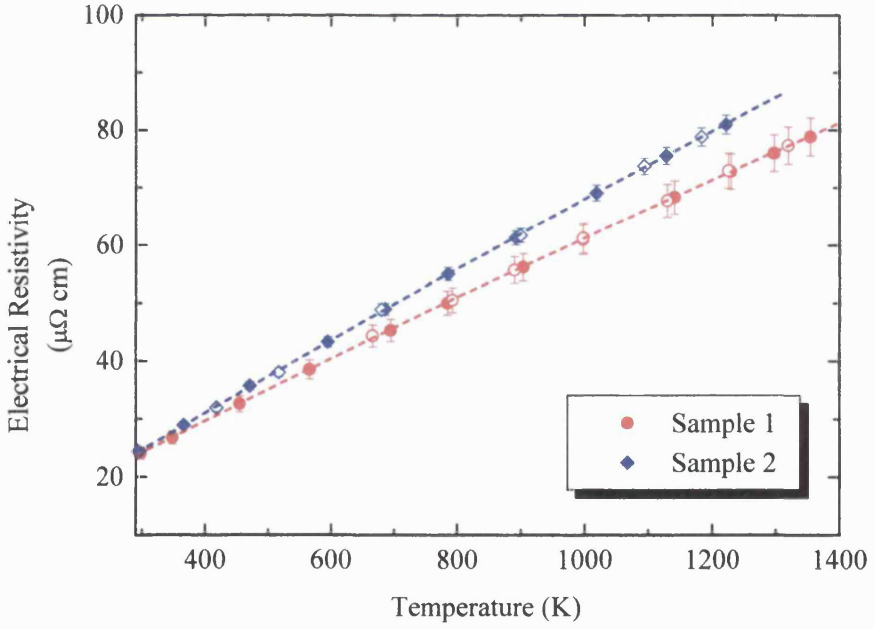

Figure 6.3 (b) The electrical resistivity as a function of temperature for TaC ceramics. Filled and open symbols have same meaning as Figure 6.3 (a). Dotted lines are second-order polynomial fits to data.

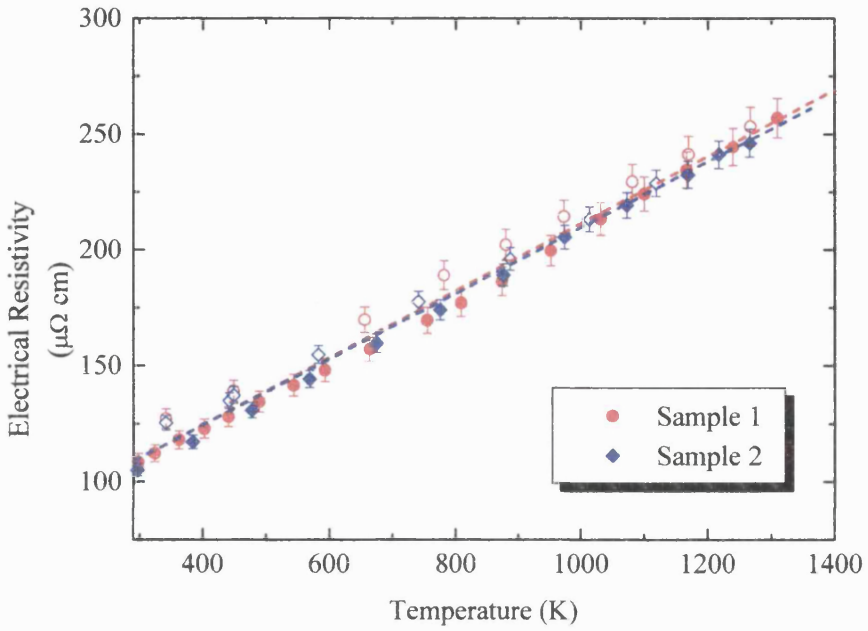

Figure 6.3 (c) The electrical resistivity as a function of temperature for ZrC ceramics. Filled and open symbols have same meaning as Figure 6.3 (a). Dotted lines correspond to the temperature derivatives.

A very slight curvature in the temperature dependence of electrical resistivity was produced for the TaC ceramics and is shown in Figure 6.3 (b); this curvature has been observed elsewhere for different carbon compositions of TaC (Williams 1999). Steinitz and Resnick (1966) calculated the temperature coefficient of resistivity (TCR) for TaC samples with different carbon compositions in a range of -196-160°C; at the stoichiometric end (TaC), Steinitz and Resnick (1966) found the TCR was around $25x10^{-4}$ $^{o}C^{-1}$ and decreased rapidly to $0.5x10^{-4}$ $^{o}C^{-1}$ at $TaC_{0.82}$. From experimental data reported by Allison et al. (1988) on the low temperature resistivity of a $TaC_{0.99}$ sample, a similar value to that produced by Steinitz and Resnick (1966) of ~$20x10^{-4}$ K^{-1} was calculated here. With this trend in mind, the average TCR at 300K for the two TaC samples used in the present study was calculated to be around $24x10^{-4}$ K^{-1}; this average TCR was determined from the measured room temperature resistivities and their temperature derivatives given in Table 6.3 for TaC. The result of $24x10^{-4}$ K^{-1} suggests that the carbon composition of the TaC ceramics are close to the stoichiometric end.

This finding backs up the result found using the lattice parameter comparison method already mentioned above.

Table 6.3 The sample densities, room temperature electrical resistivities and their temperature derivatives for TiC, TaC and ZrC samples.

Material	TiC	TaC	ZrC
sample 1			
Density (kgm^{-3})	4419±34	12658±75	5214±127
Resistivity (μΩcm)	127±3	24.1±1	108±4
$(\partial\rho / \partial T)_{300K}$ ($n\Omega cmK^{-1}$)	68±13	55±2	145±3
sample 2			
Density (kgm^{-3})	4524±102	12661±74	5126±80
Resistivity (μΩcm)	125±3	24.4±1	105±3
$(\partial\rho / \partial T)_{300K}$ ($n\Omega cmK^{-1}$)	64.2±14	64±1	142±4

In contrast to these findings for TaC samples, a recent paper by Lipatnikov and Gusev (1999) on the temperature dependence of electrical resistivity of a number of substoichiometric TiC samples showed remarkably different temperature behaviour than was observed here (Figure 6.3 (a)). One of their TiC samples had a very similar carbon composition to that estimated for the ultrasonic sample ($TiC_{0.62}$), but an order-disorder transition was found at 950K by Lipatnikov and Gusev (1999), which resulted in a pronounced step to a higher resistivity on increasing temperature. This anomaly is not present in Figure 6.3 (a) and suggests that the estimated carbon concentration of the TiC ultrasonic sample is incorrect. From the literature, there appears to be no evidence of a compositional dependence for the resistivity-temperature data on ZrC samples. However, the linear temperature behaviour measured in the study presented here (Figure 6.3 (c)) mirrors previous measurements in the same temperature range for nearly stoichiometric hot-pressed (Grossman 1965), single crystal (Hinrichs et al. 1990) and thin film (Okimura and Brittain 1990) samples of ZrC.

Since the analysis by nondestructive techniques provided a largely inconsistent picture for the determination of carbon concentrations in these carbides, a different approach was needed; this involved a destructive technique, which was outlined by Toth (1971), and is based on the weight gain produced by converting the carbides to oxides. Although this oxidation process did not allow a distinction between any free carbon in the ceramic sample and that which formed the carbide, it gave more realistic carbon concentrations values than EMQA. Ceramic off-cuts were supplied with the small bar samples, which were used for electrical resistivity measurements. Bulk density measurements on these off-cuts revealed that within error their densities compared well with those of both the ultrasonic and bar samples. The ceramic off-cuts were pulverised to produce the powders used in these oxidation experiments.

Initial weight measurements of each carbide powder were taken. Subsequently, the oxidation experiments were performed in still air with each powdered sample placed on a platinum foil lined alumina boat inside a tube furnace, capable of reaching 1200°C; the weight changes were monitored periodically until no further change was witnessed. The results of these experiments including the predicted oxidation reactions, oxidation temperatures and duration times for full oxidation of these three carbides are given in Table 6.4. Initial and final weights of the alumina boat and platinum foil were compared after each oxidation experiment. If the final and initial weights were not equivalent for the boat and foil, these discrepancies were incorporated into the final carbide/oxide powder weight; this procedure produced larger errors in some results. A carbon concentration (x) for each carbide was estimated from the weight change information in Table 6.4 using

$$x = \left[M_{Oxide} (W_C / W_{Oxide}) - M_{TM} \right] / M_{Cbn}, \qquad (6.1)$$

where M_{Oxide}, M_{TM} and M_{Cbn} are the molar (or atomic) masses of the transition-metal oxide compound, transition metal and carbon, respectively, and W_C and W_{Oxide} are the measured weights of the carbide powders before and after oxidation, respectively. Some assumptions were made to arrive at these estimations, such as: the weight influences due to impurities were negligible; no transition-metal oxide was present in the powder before oxidation; no transition metal or metal oxide was lost during the

oxidation experiments; the final oxide compounds corresponded to those suggested in the literature. The assumption that no transition metal or metal oxide was lost during the reaction is valid because the vapour pressures are negligible at the reaction temperatures given in table 6.4 e.g. the pressures are $3x10^{-9}$, $3x10^{-27}$ and $9x10^{-29}$ Pa for Ti, Ta and Zr respectively (Lide 1994). The vapour pressures are 1 Pa at 1780°C for TiO_2, 1 Pa at 2000°C for Ta_2O_5 and 0.1 Pa at 2110°C for ZrO_2 (data taken from http://www.jubochina.com), values that will be significantly lower at the temperatures used in this study. The last assumption was strengthened by the results of an X-ray study on powder 1 of each carbide; these results are given in Appendix A and show that the predicted oxide compounds were in fact produced.

This study of the methods used to determine the carbon composition of transition metal carbides has highlighted the difficulties involved in this type of analysis. The reasons for the failure of the first three methods used to determine the carbon concentration of the three transition metal carbide samples are summarised as follows. The first method of using relations between lattice parameters and carbon concentration can only give an estimate of the concentration because the scatter in lattice parameters versus carbon concentration data is high. This scatter is a direct result of the role impurities play in altering the lattice parameters, in particular the presence of oxygen. Secondly, for accurate EMQA results, samples with non-porous surfaces are desirable and it is preferable if the constituent elements have high atomic numbers, i.e. $Z>9$. Both these conditions were not satisfied for these transition metal carbide ceramics and hence the results were inaccurate. Finally, the temperature versus electrical resistivity behaviour with varying carbon composition is not a reliable test of the carbon content since impurities and porosity play an important role. Overall, these three methods may provide better results for highly pure, nonporous transition metal carbide samples, but in the case of samples that do not possess these qualities the most accurate determination of carbon composition is provided by the oxidation method.

Table 6.4 The experimental parameters for the oxidation experiments: predicted oxide compounds produced in the oxidation reactions, oxidation temperatures and experiment durations. Oxidation reactions and temperatures were taken from the references given. Results of the oxidation of TiC, TaC and ZrC powders are given as carbide powder weights before and after oxidation. Subsequently, the estimated carbon concentrations calculated using Equation (6.1) are given .

Material	TiC	TaC	ZrC
Experimental parameters			
Oxidation reaction	$TiC \Rightarrow TiO_2$	$TaC \Rightarrow Ta_2O_5$	$ZrC \Rightarrow ZrO_2$
Temperature	900°C	800 °C	500 °C
Duration	~4 days	~2 days	~3 hours
Reference	Storms (1968)	Desmaison-Brut et al. (1997)	Storms (1968)
Results			
Weight of carbide powders (grams)			
Powder 1	0.0400±0.0002	0.0789±0.0002	0.0969±0.0002
Powder 2	0.0315±0.0003	0.0407±0.0003	-
Measured weight after oxidation (grams)			
Powder 1	0.0540±0.0006	0.0906±0.0003	0.1169±0.0003
Powder 2	0.0419±0.0003	0.0466±0.0003	-
Estimated carbon concentration (x)			
Powder 1	0.94±0.06	0.95±0.07	0.90±0.03
Powder 2	1.01±0.06	1.00±0.16	-
Average	0.98±0.06	0.98±0.12	0.90±0.03

6.3.3 SEM Analysis

Scanning electron microscope (SEM) images of polished surfaces of these carbide samples are given in Figures 6.4 (a) to (c); these images show that each sample has a degree of porosity and that the $ZrC_{0.90}$ ultrasonic sample has a more open pore structure than either $TiC_{0.98}$ or $TaC_{0.98}$. From the estimated values for the carbon concentrations of these ceramics, porosity percentages were determined. A "theoretical" density from which to determine the porosity was needed. To generate the "theoretical" density for each carbide, data by Storms (1968) on the lattice parameters as a function of carbon composition were again used. Only this time, the correct lattice parameters corresponding to the averaged carbon concentrations (Table 6.4) were used to calculate the unit cell volumes, which in turn enabled the theoretical densities to be computed. The results of these calculations to determine the theoretical densities, and hence porosity percentages, are shown in Table 6.5, in the following section.

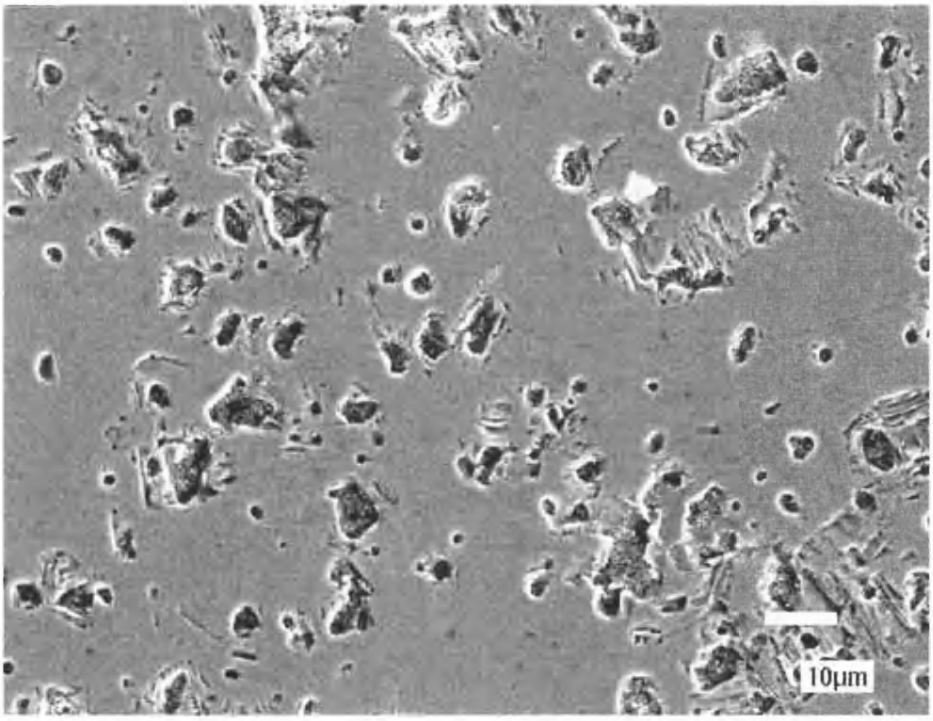

Figure 6.4 (a) Scanning electron microscope image for TiC ceramic.

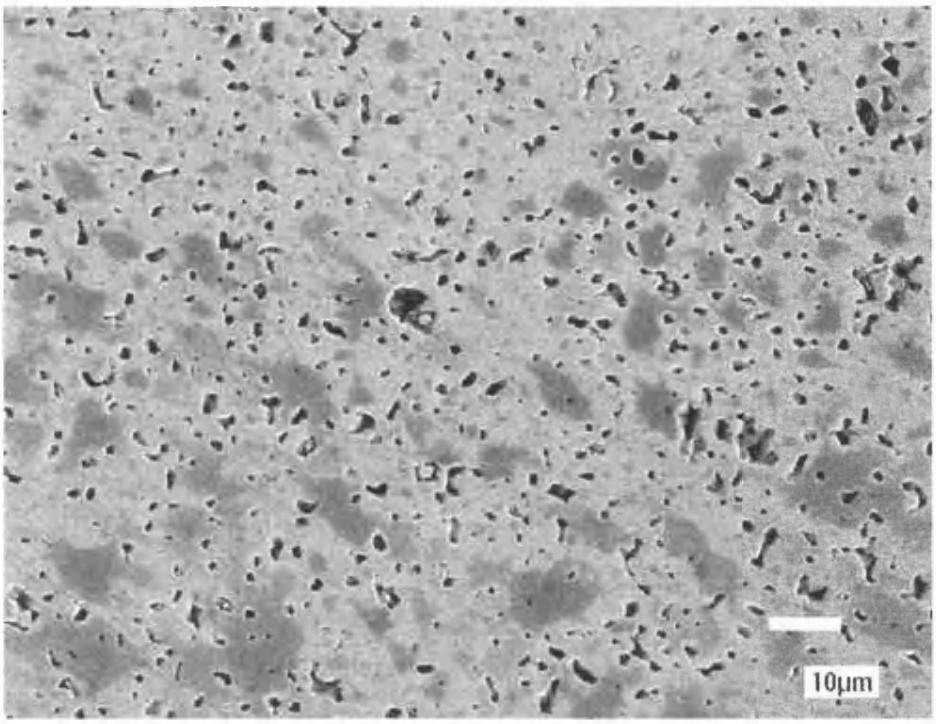

Figure 6.4 (b) Scanning electron microscope image for TaC ceramic.

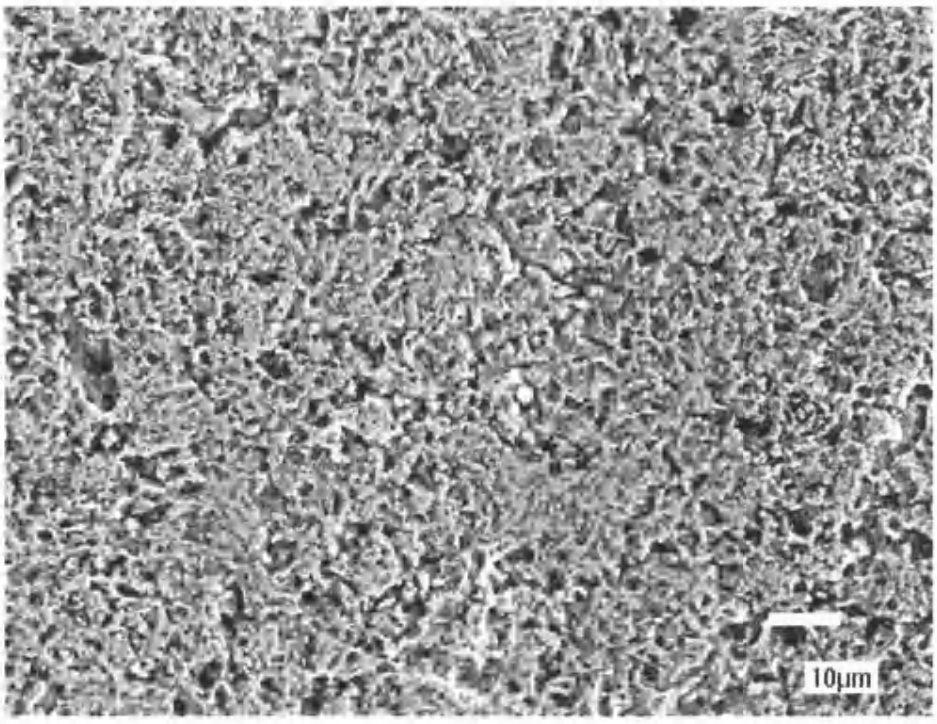

Figure 6.4 (c) Scanning electron microscope image for ZrC ceramic.

6.4 Ultrasonic Results and Discussion

6.4.1 Room Temperature Elastic Moduli for the Transition-Metal Carbide Ceramics

Table 6.5 shows the results of the room temperature ultrasonic study on the carbide ceramics. The average longitudinal and shear mode velocities, obtained from data in Table 6.1 measured to determine the elastic isotropy of the ceramics, have been used to calculate the elastic moduli of each ceramic shown in Table 6.5. The porosity of these samples has affected the absolute magnitudes of the ultrasonic velocities and hence the elastic stiffnesses and technological elastic moduli, in particular those relating to $ZrC_{0.90}$. The problem of porosity in polycrystalline forms of these carbides and its effect on the elastic properties has previously been encountered in studies on samples of TiC (Yang et al. 2000; Frantsevich et al. 1967), TaC (Jun and Shaffer 1971; Bukatov et al. 1975) and ZrC (Ordan'yan and Fishchev 1976). The elastic properties measured in these studies were corrected to zero porosity by extrapolation of porosity dependent data.

The ultrasonic results for ceramics such as AlN and TiB_2 (Chapter 4) were unaffected by porosity and reliable comparisons of these data with those in other studies using similar samples were possible. In contrast, a compilation of the elastic moduli data for TiC, TaC and ZrC ceramics presented in other studies, which were determined through different porosity correction procedures, has led to somewhat scattered results; these results are shown in Table 6.6. To compare these scattered results with the elastic moduli results determined from the present study (Table 6.5), a well known self-consistent porosity correction model produced by Sayers and Smith (1982) was applied to the elastic data in Table 6.5 and thus produced the values shown in Table 6.6.

Table 6.5 The sample densities, "theoretical" densities, porosity percentages, averaged wave velocities, adiabatic elastic moduli and their hydrostatic pressure derivatives, and the acoustic mode Grüneisen parameters for the ceramic transition-metal carbides at 295 K. The wave velocities and elastic moduli have not been corrected for porosity.

Material	$TiC_{0.98}$	$TaC_{0.98}$	$ZrC_{0.90}$
Density (kgm^{-3})	4495±4	12788±50	5153±20
Theoretical density (kgm^{-3})	4886±293	14478±1737	6476±194
Porosity (%)	8.0±0.5	11.7±1.4	20.4±0.6
V_L (ms^{-1})	9429±40	6232±10	6403±63
V_S (ms^{-1})	5856±24	3744±13	3922±42
C_L (GPa)	399±2	496±2	211±2
μ(GPa)	154±1	179±1	79±1
B^S (GPa)	193±2	257±2	105±2
E (GPa)	365±4	435±3	189±4
σ	0.186±0.002	0.218±0.002	0.201±0.004
Θ_D (K)	862±6	531±3	505±9
$(\partial C_L / \partial P)_{P=0}$	6.32±0.26	7.12±0.24	18.9±2.3
$(\partial \mu / \partial P)_{P=0}$	1.83±0.20	1.61±0.06	1.66±0.08
$(\partial B^S / \partial P)_{P=0}$	3.88±0.35	4.97±0.25	16.7±2.3
γ_L	1.37±0.07	1.68±0.07	4.56±0.61
γ_S	0.98±0.11	0.99±0.04	0.94±0.07
γ^{el}	1.11±0.08	1.22±0.04	2.15±0.21

Table 6.6 Comparison of the available elastic data on nearly stoichiometric TiC, TaC and ZrC ceramics and single-crystals with the porosity corrected values found in the present study. The symbol (*) denotes Hill averages for (s) single crystal elastic constants, (hp) and (sint) denotes porosity corrected elastic properties of hot-pressed and sintered ceramic samples, respectively, and (-) means sample preparation method not given.

Material		Type	E (GPa)	μ (GPa)	B (GPa)	σ	Θ_D (K)	Reference
titanium carbide	$TiC_{0.98}$,	hp	436±26	184±11	233±14	0.187±0.010	929±56	This work
	$TiC_{0.84}$	-	400	164	233	0.25	884	Hannink and Murray (1974)
	$TiC_{0.91}$	s,*	449	188	242	0.191		Chang and Graham (1966)
	$TiC_{0.94}$	s	448±40					Williams and Schaal (1961)
	$TiC_{0.95}$	s,*	462	193	253			Pintschovius et al. (1978)
	$TiC_{\sim 1.0}$	sint	460	190	232	0.17	946	Frantsevich et al. (1967)
tantalum carbide	$TaC_{0.98}$	hp	567±68	234±27	332±39	0.215±0.020	593±71	This work
	$TaC_{0.97}$	s,*	539	217	343			Rowcliffe and Hollox (1971)
	$TaC_{0.99}$	sint	552	227	317	0.21		Bukatov et al. (1975)
	$TaC_{0.99}$	hp	546	226		0.21		Jun and Shaffer (1970)
	$TaC_{0.994}$	-	537	216	344	0.24		Brown et al. (1966)
zirconium carbide	$ZrC_{0.90}$	hp	321±14	134±6	178±8	0.200±0.08	631±25	This work
	$ZrC_{0.95}$	-	392	150	337	0.306		Ordan'yan and Fishchev (1976)
	$ZrC_{0.94}$	s,*	406	166	223	0.196	713.8	Chang and Graham (1966)
	$ZrC_{0.91}$	-	381	147	307	0.293		Ordan'yan and Fishchev (1976)
	$ZrC_{0.964}$	hp	387	162	209	0.191		Brown and Kempter (1966)

Due to the scatter in results for the ceramics shown in Table 6.6, brought about by these porosity correction procedures, the Hill averages of the Voigt and Reuss polycrystalline approximations calculated from the independent elastic stiffness tensor coefficients (C_{11}, C_{12} and C_{44}) of transition-metal carbide single crystals are also included in Table 6.6. The Hill average is simply the average of the Voigt (upper) and Reuss (lower) approximations found from the independent *SOECs* using standard equations. This technique of approximating *SOECs* to the technological elastic moduli of isotropic polycrystalline materials is commonly used to compare the measured technological elastic moduli data of ceramics with those of single crystals. The Hill averages of Voigt and Reuss polycrystalline approximations as given in Table 6.6 are calculated using standard equations given by Wolf et al (1999); these equations for the upper (μ_V, *Voigt*) and lower (μ_R, *Reuss*) bounds of the shear stiffness and bulk modulus take the form:

$$\mu_V = (C_{11} - C_{12} + 3C_{44})/5, \tag{6.2}$$

$$\mu_R = \frac{5(C_{11} - C_{12})C_{44}}{4C_{44} + 3(C_{11} - C_{12})}, \tag{6.3}$$

$$B_V = B_R = (C_{11} + 2C_{12})/3. \tag{6.4}$$

The Young's modulus bounds can be calculated from these equations using

$$E_{V,R} = \frac{9B_{V,R}\mu_{V,R}}{3B_{V,R} + \mu_{V,R}}. \tag{6.5}$$

Even though there exists a scatter in the data in Table 6.6, the results suggest that generally TaC samples are the stiffest elastically with TiC and ZrC having similar elastic moduli values. The porosity corrected acoustic Debye temperatures for the ceramics used in the present study fall in the ranges quoted by Chang et al. (1971): 845-950K for TiC, 573-616K for TaC and 619-714K for ZrC.

6.4.2 Temperature Dependences of the Elastic Moduli for the Transition-Metal Carbide Ceramics

The temperature dependences of the elastic stiffness moduli (Figure 6.5 (a)) show that no thermal hysteresis or irreversible effects were present and that the longitudinal and shear elastic stiffnesses stiffen in a normal way from room temperature to around

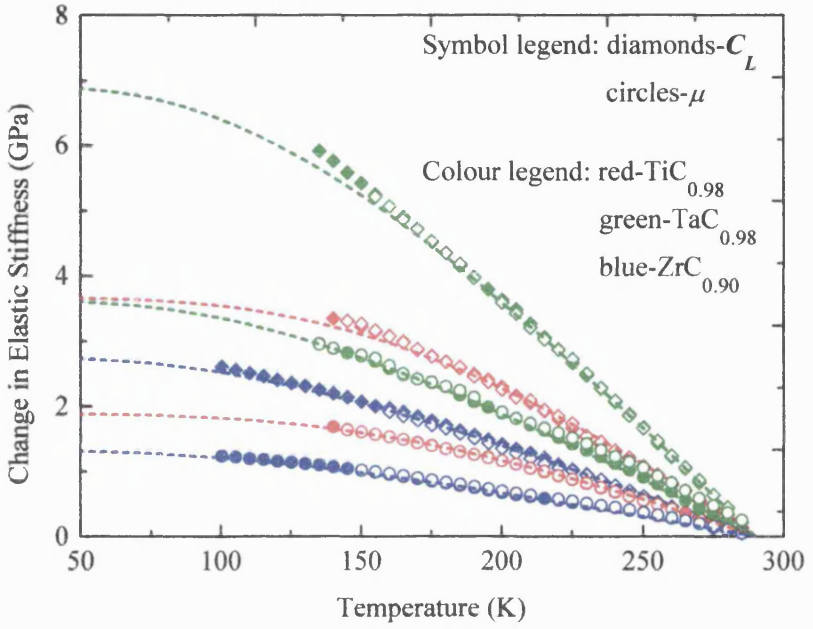

Figure 6.5 (a) Change in longitudinal and shear elastic stiffnesses as a function of temperature. Filled (open) symbols correspond to decreasing (increasing) temperature. Dotted line corresponds to fit of lattice vibrational anharmonicity model.

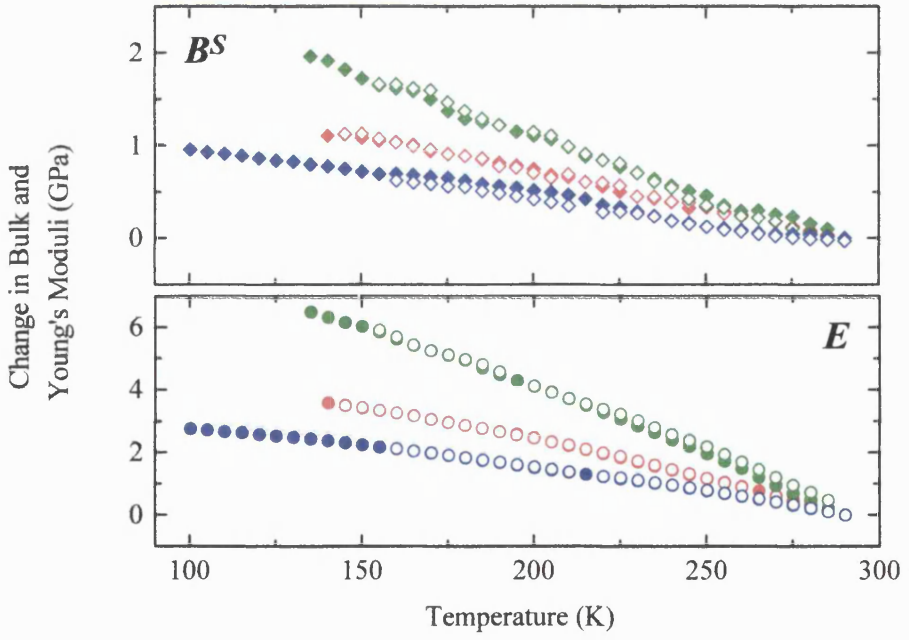

Figure 6.5 (b) Change in bulk and Young's moduli as a function of temperature. Filled and open symbols have same meaning as Figure 6.5 (a).

100K. The conventional vibrational anharmonicity model (dotted lines in Figure 6.5 (a)) has been used to emphasize this behaviour.

For $TiC_{0.98}$ and $ZrC_{0.90}$, the behaviour of the elastic stiffness with temperature decrease is in accord with single crystal elastic stiffness coefficient data plotted in the range of ~0-300K by Chang and Graham (1966), i.e. elastic stiffness moduli increase upon cooling.

The variation of Young's modulus with temperature for each ceramic is shown in Figure 6.5 (b). The Young's modulus of these carbide ceramics increase with decreasing temperature: this behaviour is in accord with those found previously in the range 20-1600°C for TiC (Hannink and Murray 1974) and 300-2300K for TaC (Jun and Shaffer 1971; Bukatov et al. 1975). To determine whether the porosity is affecting the temperature dependence of the elastic moduli, a comparison between previously determined temperature coefficients of Young's modulus (TCYM) and those calculated from this study is made. The coefficients determined for this study were calculated using the single crystal Young's moduli in Table 6.6. Hannink and Murray (1974) calculated a temperature coefficient of Young's modulus (TCYM) from their measurements on TiC to be -1.06×10^{-4} K^{-1}. In the same paper, a value of -1.0×10^{-4} K^{-1} for both $TiC_{0.91}$ and $ZrC_{0.94}$ single crystals was also calculated from the work of Chang and Graham (1966). From data provided by Jun and Shaffer (1971) for a polycrystalline $TaC_{0.99}$ sample, a temperature coefficient of -0.95×10^{-4} K^{-1}, which is close to that quoted by Hannink and Murray (1974), was calculated here. The previously determined temperature coefficient for $TaC_{0.99}$ compares quite well with the TCYM of -0.85×10^{-4} K^{-1} for $TaC_{0.98}$. However, $TiC_{0.98}$ and $ZrC_{0.90}$ have TCYMs of $-0.6 \times 10^{-4} K^{-1}$ and -0.3×10^{-4} K^{-1}, respectively, which are much lower than those values quoted in the literature. These reductions in TCYMs suggest that the porosity is affecting the temperature dependence of the elastic moduli for these two samples. The differences in TCYMs between the values calculated here and those from the literature are around 10% for $TaC_{0.98}$, 40% for $TiC_{0.98}$ and 70% for $ZrC_{0.90}$. These differences do not follow the order of increasing porosity for these materials, i.e. from $TiC_{0.98}$ to $TaC_{0.98}$ and then $ZrC_{0.90}$ (Table 6.5). Hence, the differences appear not to be a function

of the degree of porosity, but rather the type of porosity, i.e. size and shape of pores and whether they are interconnected.

Figure 6.5 (b) shows the temperature dependences of the bulk moduli for the carbides. A linear increase in bulk modulus with decreasing temperature was observed previously by Jun and Shaffer (1971) for a $TaC_{0.99}$ sample; this linear increase is in accord with that found here for the $TaC_{0.98}$ ceramic. Poisson's ratio decreases slightly with decreasing temperature for all carbide samples and the Debye temperature increases on decreasing temperature, which is in accord with the elastic stiffening under temperature decrease (Figure 6.5 (c)).

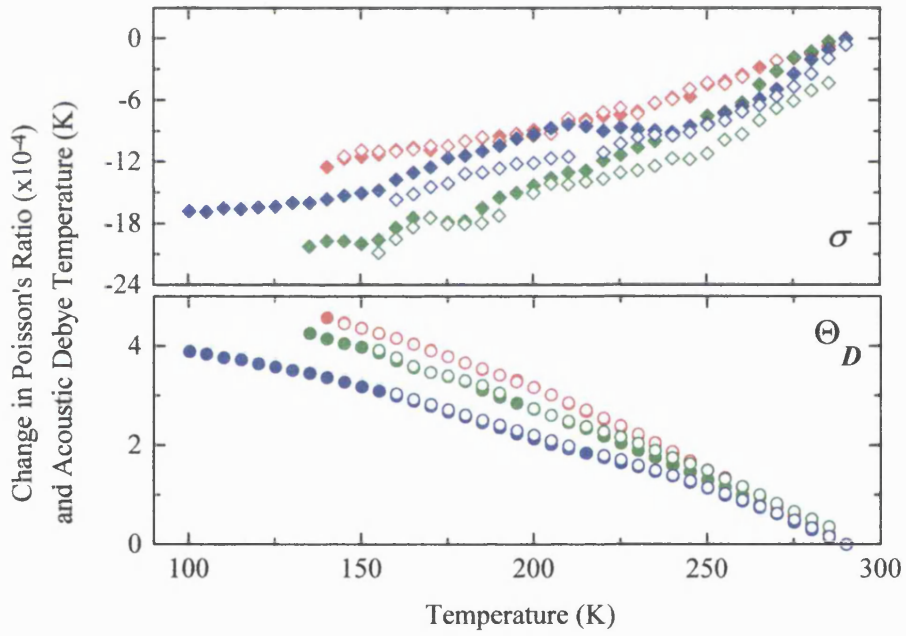

Figure 6.5 (c) Change in Poisson's ratio and acoustic Debye temperature as a function of temperature. Filled (open) symbols correspond to decreasing (increasing) temperature.

6.4.3 Hydrostatic Pressure Dependences of the Ultrasonic Wave Velocities and Elastic Stiffness Moduli for the Transition-Metal Carbide Ceramics

The hydrostatic pressure dependences of the longitudinal and shear mode natural velocities for each ceramic carbide are shown in Figures 6.6 (a) and (b), respectively.

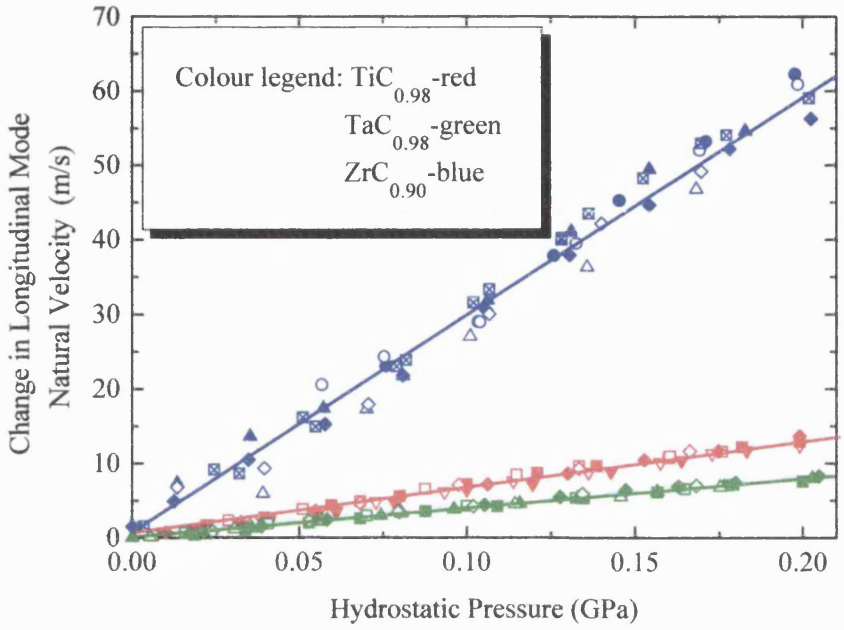

Figure 6.6 (a) Change in longitudinal mode natural velocities as a function of hydrostatic pressure, at 295K. Filled (open) symbols are increasing (decreasing) pressure and the different symbol shapes correspond to different runs. Solid lines are least squares fits to measured data.

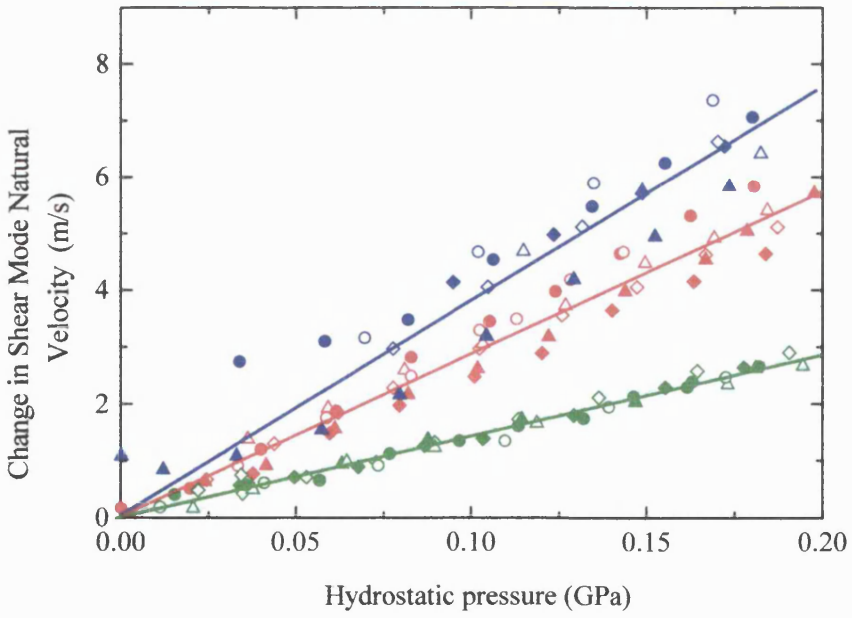

Figure 6.6 (a) Change in shear mode natural velocities as a function of hydrostatic pressure, at 295K. Filled and open symbols have same meaning as Figure 6.6 (b).

Three different pressure runs for each ultrasonic mode were performed on each ceramic and were reproducible under pressure cycling and showed no measurable hysteresis effects. The pressure dependence of the shear wave velocities for eachceramic is small, which is typical for a stiff material, and increases approximately linearly with increasing pressure. This behaviour typifies a normal solid: the long wavelength acoustic modes stiffen under pressure. No indication of mode softening in the measured pressure range was found. $TaC_{0.98}$ has the smallest shear wave velocity hydrostatic pressure dependence, followed by $TiC_{0.98}$ and then $ZrC_{0.90}$. The pressureeffects on the longitudinal wave velocities in these samples (Figure 6.6 (a)) are also typical of a normal solid: increasing with compression. However, an unusually large longitudinal velocity change was measured as the $ZrC_{0.90}$ ceramic was compressed; the calculated longitudinal velocity pressure derivative was approximately 6 times larger than the pressure derivatives determined for the other two samples.

These unusually large ultrasonic velocity pressure dependences in porous ceramics have been observed previously. Wang et al. (1995b) collated the ultrasonic velocity hydrostatic pressure dependences of a large number of high T_C superconducting ceramics with similar compositions but different porosities. The outcome of this comparison conducted by Wang et al. (1995b) was that on increasing porosity, the hydrostatic pressure dependences of both ultrasonic mode velocities also increased, with the longitudinal mode change being much larger than the shear. Consequently, $(\partial B^S / \partial P)_{P=0}$ for these superconducting ceramics increased with porosity and reached a large value (=31.9) at high porosity (28%); thus, suggesting that the porous nature of the microstructure in ceramics influences the hydrostatic pressure induced changes in ultrasonic velocities. Similar pressure effects have been found here with the $ZrC_{0.90}$ carbide ceramic possessing the highest pore fraction (20.4±0.6%) in these three carbides and also producing an unusually large adiabatic bulk modulus pressure derivative (=16.7±2.3). However, calculations of $(\partial B^S / \partial P)_{P=0}$ for $TiC_{0.98}$ and $TaC_{0.98}$, shown in Table 6.5, do not seem to be greatly influenced by the porous nature of the microstructures.

The results of a number of previous experimental and theoretical studies on the bulk modulus pressure derivatives for these carbides also suggest that the pressure induced changes in velocity found in the present study for $ZrC_{0.90}$ are not mainly a consequenceof vibrational anharmonicity. Dubrovinskaia et al. (1999) performed high pressure X-ray powder diffraction measurements on TiC, and used the Birch-Murnaghan equation of state to calculate the bulk modulus and its pressure derivative: values found were 235 GPa and 6.5±3, respectively; these values are similar to 233±14 GPa and 3.88±0.35 found in the present pressure study for $TiC_{0.98}$. This indicates that porosity has only a small influence on the pressure behaviour of this ceramic. In addition, theoretical calculations of $(\partial B / \partial P)$ for TiC agree well with the value determined here, even though it is a porous ceramic: Méçabih et al. (2000) used the FP-LAPW method and found a value of 4.30 for $(\partial B / \partial P)$, while an estimation, by using calculations of theoretical data given by Wolf et al. (1999) yielded around 4.0. Using the same theoretical method, Méçabih et al. (2000) also calculated $(\partial B / \partial P)$ for ZrC and produced a value of 4.01. Since the theoretical study performed by Méçabih et al. (2000) to determine $(\partial B / \partial P)$ for TiC is comparable with the value determined here, their method used to generate 4.01 for ZrC should be a reasonably accurate value for $(\partial B / \partial P)$; thus, the $(\partial B^S / \partial P)_{P=0}$ value of 16.7±2.3 for the $ZrC_{0.90}$ ceramic measured here appears not to be mainly an anharmonic effect, but is also determined by the porous microstructure of the sample.

It is difficult on the basis of the present results to clearly correlate $(\partial B^S / \partial P)_{P=0}$ with the sample porosity. For example, $(\partial B^S / \partial P)_{P=0}$ takes values of 3.88±0.35, 4.97±0.25 and 16.70±2.30 for TiC, TaC and ZrC which have porosities of 8%, 11.7% and 20.4% respectively, i.e. there is an increase of $(\partial B^S / \partial P)_{P=0}$ with porosity. However, measurements have not been made on the same ceramic material with differing porosities, i.e. it is unclear the extent to which the observed trend is an intrinsic property of the ceramic or of its microstructure. In Chapter 7, it will be shown that Fe_3C with a porosity of 29-40% has a value for $(\partial B^S / \partial P)_{P=0}$ of 3.43±1.61 at pressures below 0.06 GPa and of around 25 at higher pressures. This change might at first be attributed to a collapse of the pores with increasing pressure. However, this interpretation may well be too simplistic as discussed in Section 7.4.2.

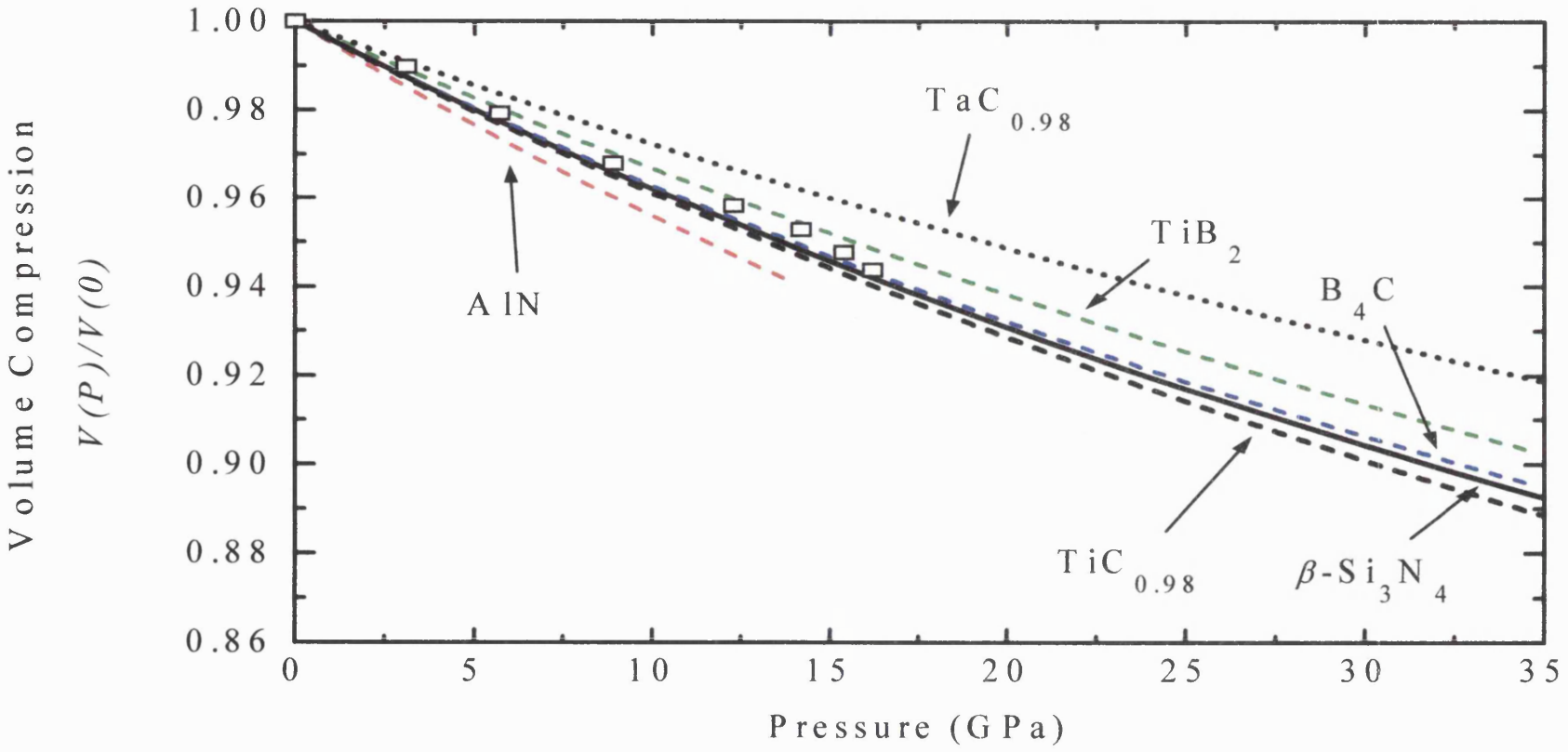

Figure 6.7 Volume compression for $TiC_{0.98}$ and $TaC_{0.98}$ ceramics, compared with high pressure X-ray diffraction data on TiC taken from Dubrovinskaia et al. (1999)-open squares and those ceramic samples studied in Chapters 4 and 5.

Since the pressure derivatives of elastic stiffnesses and bulk modulus for $TiC_{0.98}$ and $TaC_{0.98}$ are not markedly affected by porosity, comparisons of their volume compressions (Figure 6.7), extrapolated to high pressures using Murnaghan's equation of state, are made with the high pressure X-ray powder diffraction measurements on TiC by Dubrovinskaia et al. (1999). Also shown in Figure 6.7 are the volume compression data for the ceramics studied in Chapters 4 and 5. Bulk moduli values for $TiC_{0.98}$ and $TaC_{0.98}$ which are needed to extrapolate to high pressures (using Equation (2.45)) have been taken as the porosity corrected values given in Table 6.6. This volume compression comparison in Figure 6.7 shows that $TaC_{0.98}$ ceramic is the least compressible material for the group of hard ceramics shown, which is due to the high bulk modulus determined for this sample. The $TiC_{0.98}$ ceramic has a comparable compressibility to B_4C and β-Si_3N_4 ceramics, due to the similar bulk moduli values possessed by these three ceramic samples.

6.4.4 Grüneisen Parameters and Acoustic Mode Vibrational Anharmonicity for the Transition-Metal Carbide Ceramics

The elastic stiffnesses and bulk modulus pressure derivatives of both $TiC_{0.98}$ and $TaC_{0.98}$ ceramics do not appear to have been greatly influenced by porosity in the same manner as those calculated for $ZrC_{0.90}$; therefore, the calculated acoustic mode Grüneisen Parameters (γ_L, γ_S and γ^{el}) should produce reasonable estimations for the contribution of the long wavelength acoustic phonon modes to the thermal properties for $TiC_{0.98}$ and $TaC_{0.98}$. These calculations of the Grüneisen Parameters were performed using the elastic stiffness values shown in Table 6.5. Recently, Wolf et al. (1999) estimated a Grüneisen parameter γ(~1.03-1.33) from a theoretical study on the nonlinear acoustic properties of TiC. This Grüneisen parameter was calculated from the derivative of the volume dependence of the Voigt and Reuss averages of a theoretically determined Debye temperature. γ^{el}(=1.11±0.08) determined for $TiC_{0.98}$ in the present pressure study would be equivalent to that value determined by Wolf et al. (1999), which is comparable. The thermal Grüneisen parameter (γ^{th}) quantifies the contributions of both acoustic and optic phonon modes throughout the first Brillioun zone to the thermal properties of a material. An estimation of the room temperature thermal Grüneisen parameter has been made for each carbide using the thermal

expansion data in Table 3.1 and heat capacity results from Krajewski et al. (1998); the calculation of γ^{th} from these data produced 1.88, 2.34 and 1.64 for $TiC_{0.98}$, $TaC_{0.98}$ and $ZrC_{0.90}$, respectively. The larger values obtained for γ^{th} in comparison to γ^{el} for $TiC_{0.98}$ and $TaC_{0.98}$ implies that the optic phonons have the relatively larger Grüneisen parameters. The value of γ^{el}(=2.15±0.21) calculated for $ZrC_{0.90}$ appears not to be solely a consequence of vibrational anharmonicity and therefore cannot be compared with the estimated thermal Grüneisen parameter. Small values for the acoustic mode Grüneisen parameters (Table 6.5) and hence low vibrational anharmonicities are compatible with the low thermal expansions of both $TiC_{0.98}$ and $TaC_{0.98}$, as shown in Table 3.1.

Chapter 7

Ceramic
Iron Carbide (Fe_3C)

7.1 Introduction

Iron carbide (Fe_3C), or cementite, is an important constituent in certain carbon steels and white cast iron because its presence affects their mechanical properties, since Fe_3C is harder than ferrite and quite brittle (Street and Alexander 1998). A number of studies, both theoretical and experimental, have been performed to determine Young's modulus and Poisson's ratio of cementite. The early experimental studies were mainly mechanical tests on Fe_3C embedded in steels or extracted from steels by electrolysis (Kagawa et al. 1987; Webb and Forgeng 1958; Laszlo and Nolle 1959; Drapkin and Fokin 1980). Miodownik (1994) used theoretical calculations to predict Young's modulus for cementite. Recently, Young's modulus and Poisson's ratio of single-phase cementite films, in which the cementite particles were granular with a grain size of about 50 nm, were evaluated using a surface acoustic wave method (Li et al. 1998). A vibrating reed technique was also applied by Mizubayashi et al. (1999) to determine the Young's modulus of single-phase cementite films deposited on silicon reed-substrates. As a result of all these investigations, ranges for room temperature Young's modulus and Poisson's ratio of cementite were 140-200 GPa and 0.26-0.30, respectively. Due to the lack of measurements on bulk cementite samples to determine their technological elastic moduli, it is not surprising that the nine independent elastic stiffness tensor coefficients of single crystal Fe_3C are still unknown.

Cementite is ferromagnetic with a Curie temperature (T_C) of about 465-488 K (Jellinghaus 1966; Jack and Jack 1973; Häglund et al. 1991). Many studies have found that the thermal expansion coefficient of Fe_3C is much smaller for the ferromagnetic state, i.e. below T_C, than for the paramagnetic state (Jellinghaus 1966; Shigematsu 1975; Kagawa and Okamoto 1983; Kagawa et al. 1987; Hartmann and Ruppersberg 1995; Acet et al. 2001). This decrease in the thermal expansion coefficient of cementite below the Curie temperature (T_C) is similar to that found in the iron alloy $Fe_{0.65}Ni_{0.35}$, shown in Figure 7.1. The $Fe_{0.65}Ni_{0.35}$ alloy possesses what has been dubbed "Invar" properties: a small nearly constant (invariant) thermal expansion in a wide region around room temperature, by Guillaume who, in 1897, first discovered the property in that alloy (Mañosa et al. 1992).

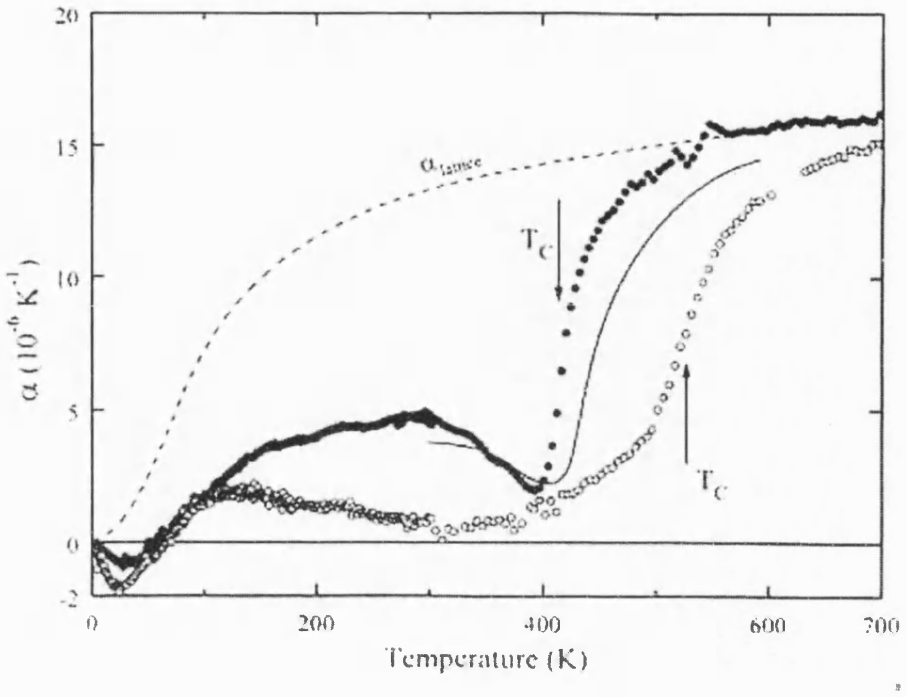

Figure 7.1 The thermal expansion coefficients as a function of temperature for $Fe_{0.65}Ni_{0.35}$ (Invar) and Fe_3C (cementite). Arrows point to the Curie temperatures (T_C) and the dashed line represents a theoretical prediction of a normal lattice thermal expansion of Fe_3C without the influence of a positive spontaneous volume magnetostriction. Solid line is thermal expansion data of cementite measured by Jellinghaus (1966). The graph was taken from Acet et al. (2001).

Ferromagnetic materials generally expand or contract in volume below their Curie temperature; this phenomenon is called the spontaneous volume magnetostriction and is mainly caused by the magnetic exchange interaction (Honda 1978). In ferromagnetic Invar alloys, this decrease in thermal expansion in the ferromagnetic phase is a result of the negative contribution to the expansion from a large positive spontaneous volume magnetostriction (Figure 7.1), which is thought to be a result of magnetic moment-volume instabilities (Wassermann 1990). Cementite has been classed as an Invar material, due to the thermal expansion behaviour below T_C (Acet et al. 2001). Other physical properties of Invar materials, such as molar volume, elastic modulus, heat capacity and magnetization, have also been found to show anomalous behaviour (Dubrovinsky et al. 2001). Invar effects in materials that produce very small temperature coefficients of elastic modulus have been named Elinvar effects (Wassermann 1990). The Elinvar effect in cementite was discovered indirectly in two

independent studies by Kagawa et al. (1987) and Drapkin and Fokin (1980). In these two studies, linear extrapolations from the measurements of the Young's modulus of certain carbon steels and iron-cementite alloy castings as a function of carbon content were used to determine this Elinvar behaviour in Fe_3C. It was found that below the Curie temperature the Young's modulus of cementite softened anomalously, as opposed to the stiffening seen in normal materials.

The elastic properties of Invar iron alloys in their ferromagnetic state have also shown anomalous behaviour under compression. Mañosa et al. (1992) have shown that, due to a magnetoelastic interaction, $Fe_{72}Pt_{28}$ and $Fe_{72}Pt_{25}Ni_3$ single crystals have negative bulk modulus pressure derivatives, which means the crystals become easier to squeeze under compression. In addition, the original Invar alloy $Fe_{65}Ni_{35}$ (or $Fe_{0.65}Ni_{0.35}$) has a very small positive $(\partial B^S / \partial P)_{P=0}$ (Mañosa et al. 1992). No data are available on the hydrostatic pressure dependence of the ultrasonic velocities of cementite, and hence the nonlinear acoustic properties. Only a high pressure (up to 73 GPa) X-ray diffraction study to find the equation of state for cementite has been performed (Scott et al. 2001).

In the present ultrasonic study, the determination of the longitudinal and shear ultrasonic velocities as a function of temperature (75-290K) of a bulk Fe_3C ceramic sample has provided more evidence for the Elinvar behaviour of cementite which was predicted by Kagawa et al. (1987) and Drapkin and Fokin (1980). The implications of this finding are that cementite may be useful for applications in which elastic or dimensional stability is required. In addition, measurements of ultrasonic velocities as a function of hydrostatic pressure (up to 0.2 GPa) have shed light on the nonlinear acoustic properties of cementite, through calculations of the acoustic mode Grüneisen parameters.

7.2 Crystal Structure of Iron Carbide

Fe_3C is a compound, which crystallizes in the orthorhombic structure, with 12 iron and 4 carbon atoms per unit cell. The structure of cementite was established by Lipson and Petch (1940) and since then a number of workers have confirmed the structure (Herbstein and Smuts 1964; Fasiska and Jeffrey 1965). The starting point for this cementite structure, described by Cottrell (1993), is a hypothetical hexagonally close packed (HCP) lattice of iron atoms, the basal planes of which are then distorted by folding to an angle of 112.2°, alternating up and down, along their lines of intersection with $(2\bar{1}\bar{1}0)$ planes (Figure 7.2 (a)). These $(2\bar{1}\bar{1}0)$ planes on which the folding occurs then become the mirror planes of the cementite crystal. Carbon atoms take up interstitial positions along the fold lines with an alternating sequence from one pleated layer to the next. The alternating carbon atom sequence is shown in Figure 7.2 (b) for one pleated layer, where the interstitial carbon sites are shown by open and filled circles. Stacking of the pleated layers in the *a*-axis crystal direction of the cementite crystal is not illustrated in Figure 7.2 (b), but is the same as that for a HCP lattice arrangement.

7.3 Characterisation of Fe_3C Ceramic

In determining the required physical and chemical characteristics of the cementite ceramic used in the present ultrasonic study, as well as the usual methods, one additional method was employed, namely energy dispersive spectroscopy (EPS). The results obtained using this extra technique have been included in the section on the SEM analysis. The cementite (Fe_3C) samples used in the study were prepared elsewhere (Acet el al. 2001) by melting iron (Fe) of purity 99.98% together with 20% excess spectral purity carbon (C) under argon atmosphere in an arc furnace. The resulting ingot Fe_3C+C+Fe was pulverised in a ball mill and chemically separated. Powdered Fe_3C including 1.5 atomic percent chromium, to prevent decomposition at high temperature and pressure, was pressed under 50 MPa at 1050°C. The sample used for ultrasonic studies had a path length of 3.075±0.061 mm.

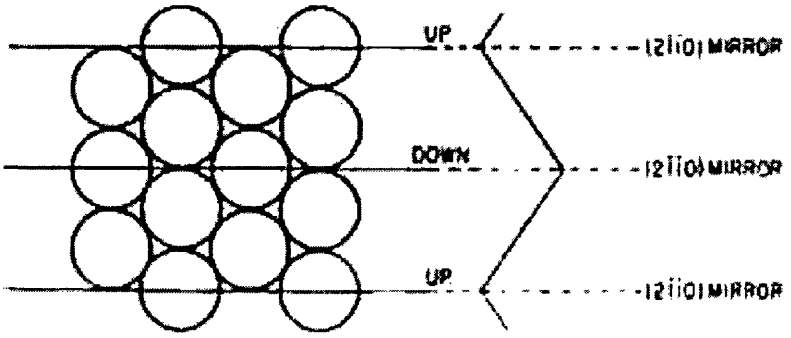

Figure 7.2 (a) The forming of regularly pleated layers from a hypothetical HCP lattice.

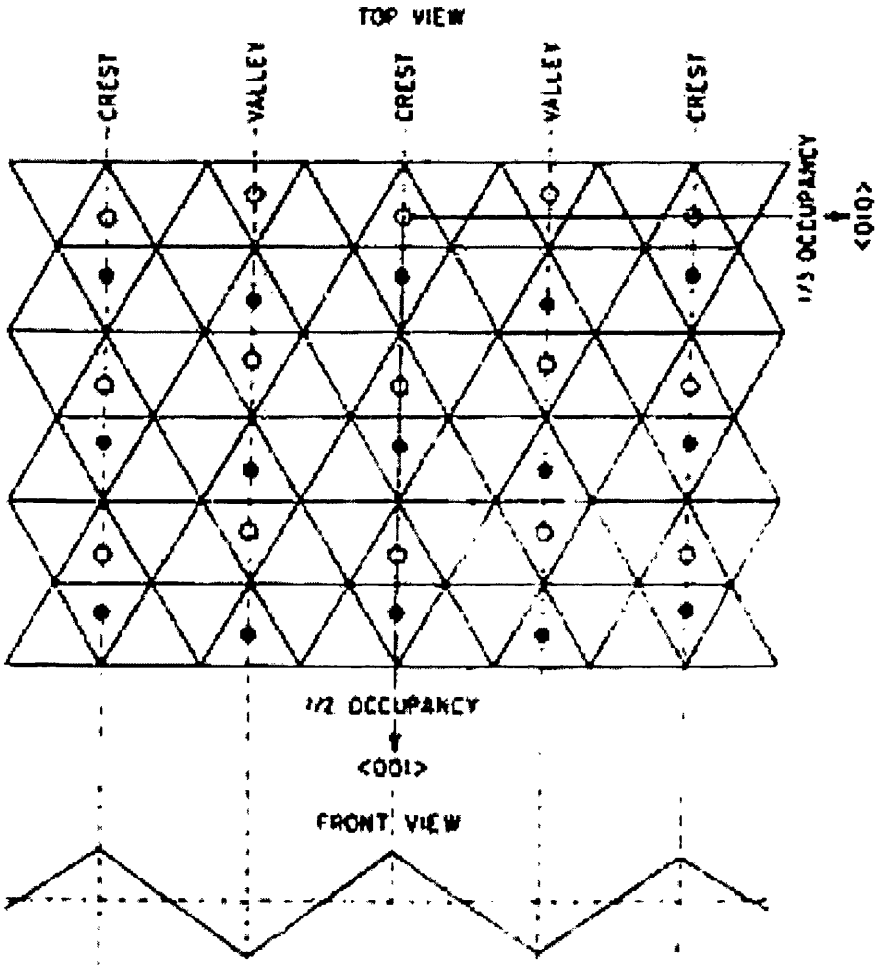

Figure 7.2 (b) Carbon atom positions on a pleated layer: filled and open circles correspond to two atom sites, alternating between site 1 (filled circles) and site 2 (open circles) on successive pleated layers. The "TOP VIEW" shows carbon occupancies of a pleated layer along the *c*-axis (<001> planes) and *b*-axis (<010> planes) of the crystal. The "FRONT VIEW" shows the carbon atom positions in a pleated layer (intersections of dotted lines), looking along the *c*-axis. Illustrations are taken from Fasiska and Jeffrey (1965).

An initial volumetric density measurement produced 4565 kgm^{-3} for the cementite ceramic, which agrees with the estimated density of 4600 kgm^{-3} given by the makers of this ceramic (Acet el al. 2001). Subsequent measurements of the sample density using Archimedes' method produced widely different results to the volumetric method; therefore, the value found by the volumetric measurement was used to represent the density of the ceramic sample. Since the volumetric measurement produced an underestimated density for the porous sample, an upper limit porosity percentage of around 40% was estimated by using a value for the cementite X-ray density of 7680 kgm^{-3}. According to the makers of this ceramic (Acet et al. 2001), the porosity was caused by the air entrapped in the material during hot pressing of the powdered Fe_3C. Measurements of room temperature 5MHz shear mode velocities with polarisations parallel to the *Y*- and *Z*-face of the ultrasonic sample produced values of 2001±10 and 1991±10 ms^{-1}, respectively; the ceramic was elastically isotropic.

7.3.1 X-ray Diffraction Analysis

The X-ray diffraction study on the ultrasonic sample is shown in Figure 7.3 as raw data (counts) and is compared with the cementite diffraction standard. Most spectra lines in Figure 7.3 correspond to cementite with some extra lines being associated with the impurities which were discovered by the EPS study. The lattice parameters (a=5.062±0.01Å, b=6.76±0.02 Å, c=4.53±0.02 Å) of the sample, determined by using certain X-ray diffraction spectra lines: (200) for a-axis; (002) for c-axis; (220) for b-axis, are found to be in good agreement with those of cementite previously reported in the literature (Fasiska and Jeffrey 1965; Stuart and Ridley 1966).

7.3.2 SEM and EPS Analysis

To produce good SEM images and energy dispersive spectroscopy results, the sample of Fe_3C was polished with diamond followed by colloidal silica. The scanning electron microscope image of the grain structure (Figure 7.4 (a)) was analysed over an area of 1585 grains, and, using the method applied in Chapter 4, the average grain size (=4.75±3.08 μm) was calculated. The porosity caused some problems with the grain size measurement leading to a lower cut off of 4.6 μm (true diameter); this cut off can be seen in the histogram for the grain size distribution (Figure 7.4 (b)).

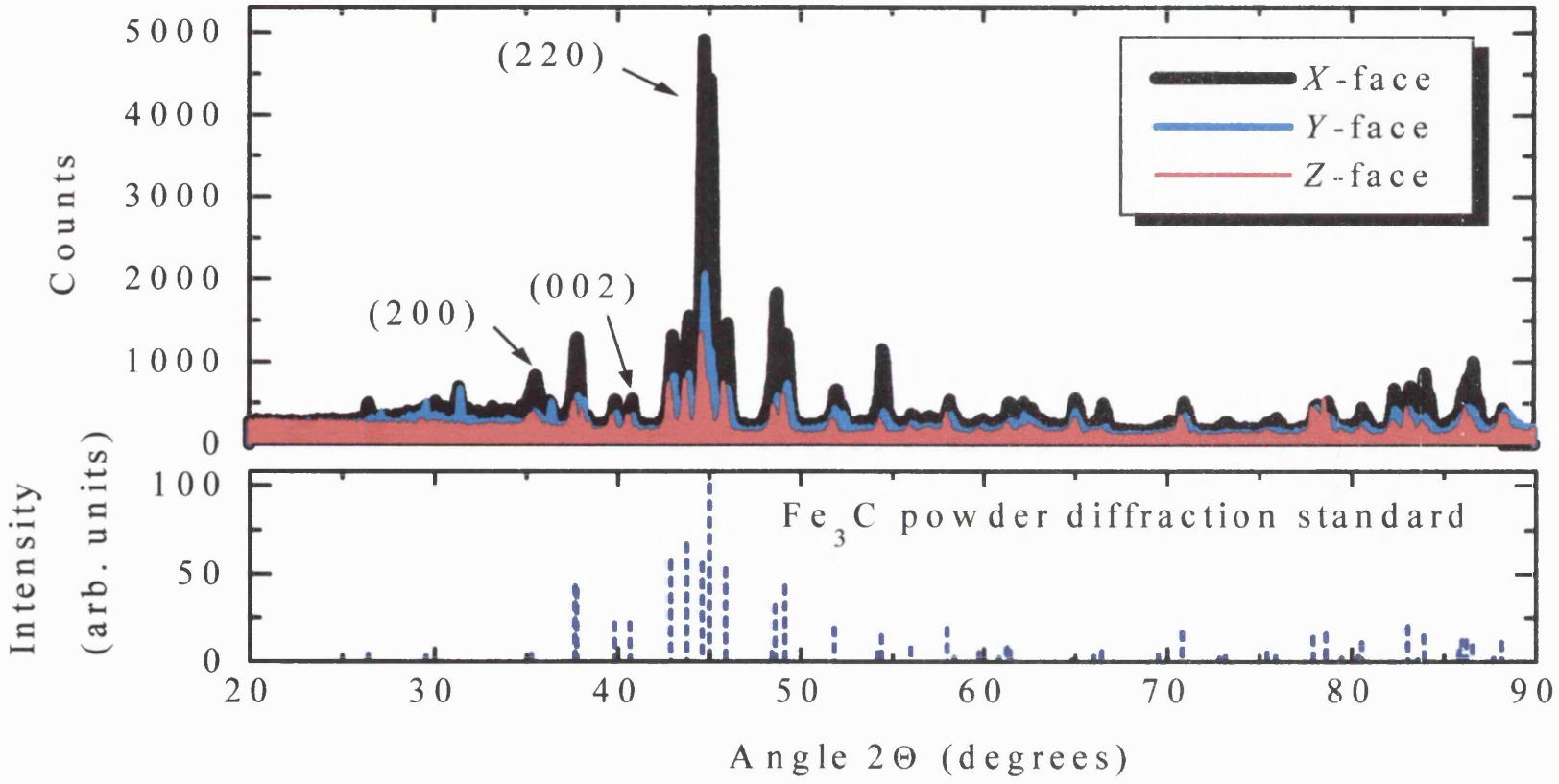

Figure 7.3 X-ray diffraction spectra for three orthogonal faces of cementite ceramic.

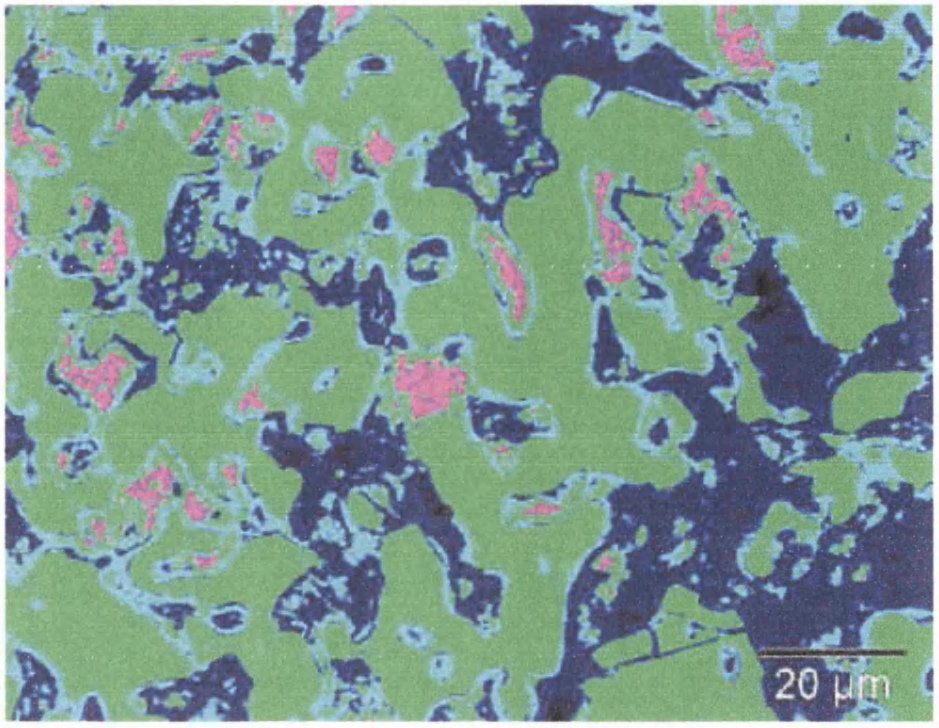

Figure 7.4 (a) Scanning electron microscope image for Fe_3C ceramic. Colours correspond to composition of sample: pink-heavy metals: Pb, Sn; green-cementite; cyan-iron oxide; dark blue-porosity.

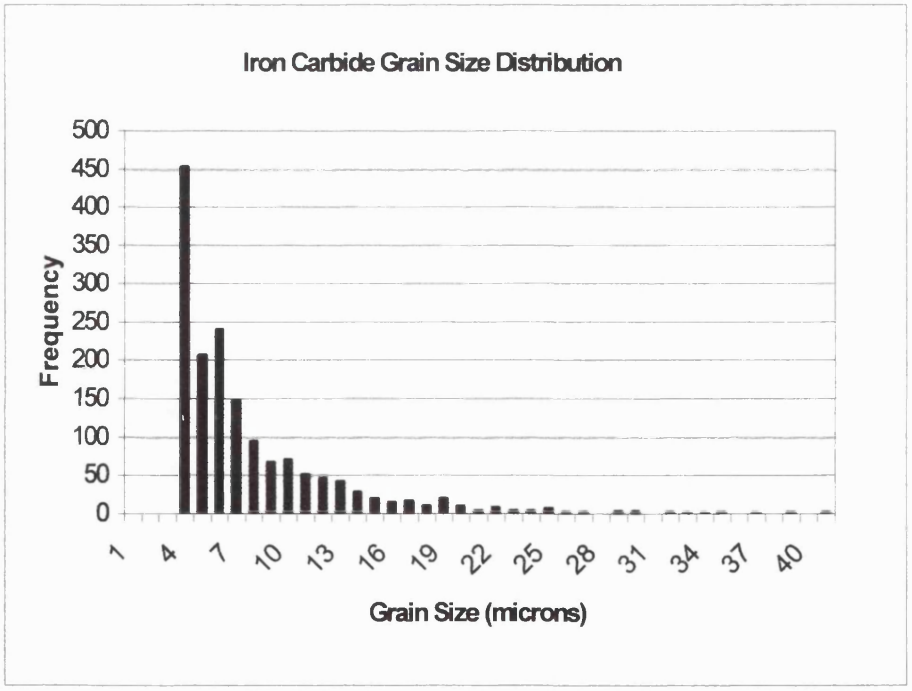

Figure 7.4 (b) Grain size distribution for Fe_3C ceramic.

An electron back scattered diffraction analysis showed that the sample contained a random orientation of grains. The scanning electron microscope image (Figure 7.4 (a)) showed that the Fe_3C grains were coated with a thin film (mean thickness=0.95±0.21 μm) and that some inclusions were present. Energy Dispersive Spectroscopy (EDS) was used to analyse these features and showed that the thin film coating the grains is iron oxide containing silicon, lead, tin and chromium (Figure 7.4 (a)). The inclusions are also iron oxide, rich in silicon, lead and tin and some chromium is present in the iron carbide grains. These phases and impurities are shown as coloured regions in Figure 7.4 (a). An estimate of phase or impurity percentages in the ceramic have been made using an image analysis technique; this was achieved by finding the proportion of each colour present in the SEM image (Figure 7.4 (a)). This image analysis produced area percentages of 3.3, 46.6, 20.6 and 29.1% for heavy metals (lead and tin), cementite, iron oxide and porosity, respectively. Assuming a porosity percentage of 29.1% as a lower limit for the actual value, it is considered reasonable to say the pore fraction in the ultrasonic sample lies between 29% and 40%.

7.3.3 Electrical Resistivity Measurements

Cementite behaves as a metallic electrical conductor: Radcliffe and Rollason (1958) determined the room temperature electrical resistivity ($\rho_{300K}(Fe_3C)$) to be between 24.7-80 μΩcm, from extrapolations of data for steels containing less than 1.5% carbon. Theoretically determined $\rho_{300K}(Fe_3C)$ values were 107 μΩcm (Helsing and Grimvall 1991) and 47 μΩcm (Häglund et al. 1991). So far, it appears that only Lee and Simkovich (1987) have measured the electrical resistivity temperature dependence for a cementite sample (12-15% porous). Their measurements produced $\rho_{300K}(Fe_3C)$=233 μΩcm and showed an "uncharacteristic" linear increase in electrical resistivity as a response to increased temperature (in the range 298-750K), which resulted in a temperature derivative of 823 $n\Omega cmK^{-1}$. This linear temperature behaviour measured by Lee and Simkovich (1987) is classed as "uncharacteristic" when considering the fact that ferromagnetic conductors usually show anomalous electrical resistivity-temperature behaviour around T_C; the lack of an anomaly in the results reported by Lee and Simkovich (1987) was also noted by Helsing and Grimvall (1991). In the present study, a ceramic bar (dimensions: 1.46x1.47x9.8 mm) was cut from a tablet made

using the same process described at the start of this section. A bulk density of 6140±283 kgm^{-3} was determined for this bar, and a porosity value of around 20% was calculated. The electrical behaviour of this small bar has been taken to represent that of the ultrasonic sample. A number of room temperature electrical resistivity measurements performed on this bar produced an average $\rho_{300K}(Fe_3C)$ value of 89±3 μΩcm. By assuming that the main electron scattering mechanism causing the magnitude of $\rho_{300K}(Fe_3C)$ in this bar sample was from pores, a crude approximation given by Toth (1971) for the porosity dependence of electrical resistivity was used to give a value of $\rho_{300K}(Fe_3C)$ for a nonporous cementite sample. This procedure produced 40.5 μΩcm, which falls into the existing range of experimentally determined values of $\rho_{300K}(Fe_3C)$. The linear temperature behaviour of the electrical resistivity of cementite measured in the present study (Figure 7.5) mirrors those results found by Lee and Simkovich (1987), but the temperature derivative determined here is much smaller, having a value of 163±3 $n\Omega cmK^{-1}$. The sample used by Lee and Simkovitch (1987) was not fully characterised. This makes the differences in the resistivity and its temperature derivative between this study and Lee and Simkovitch (1987) difficult to interpret, but they maybe a result of the two samples having different grain sizes or impurities.

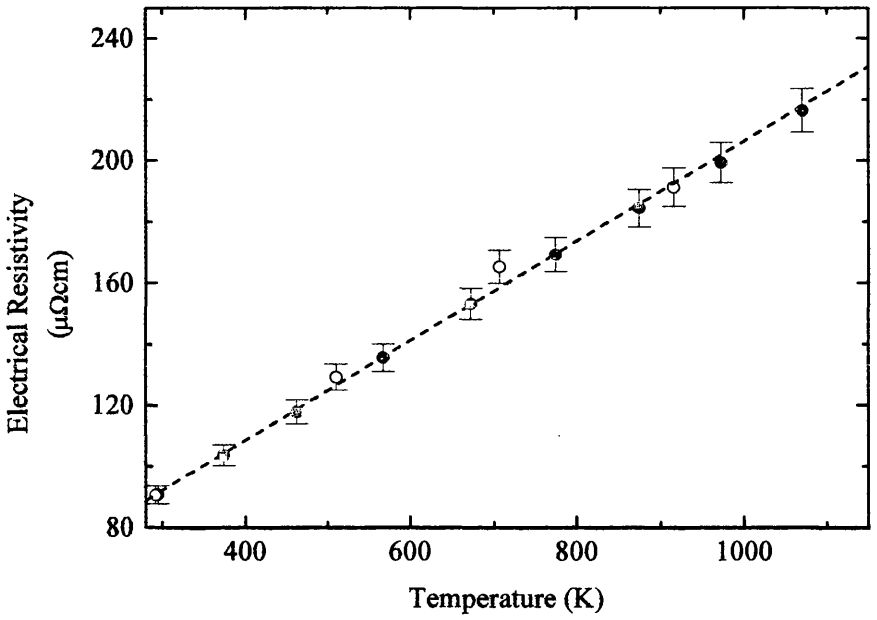

Figure 7.5 The electrical resistivity as a function of temperature for a cementite bar sample fabricated by the same process as the ultrasonic sample. Filled (open) symbols correspond to increasing (decreasing) temperature. Dotted line corresponds to the temperature derivative: 163±3 $n\Omega cmK^{-1}$.

7.4 Ultrasonic Results and Discussion

The absolute magnitudes of the room temperature 5MHz longitudinal and shear mode ultrasonic velocities (and hence elastic moduli) for the cementite sample were substantially reduced by the presence of a large pore fraction; therefore, only their temperature and hydrostatic pressure dependences are considered. However, Poisson's ratio is expected to be less influenced by porosity than the other elastic moduli (Asmani et al. 2001). A value of 0.24±0.01 was determined in the present study for Poisson's ratio of the cementite sample, which is slightly lower than values found previously for cementite by other researchers (Laszlo and Nolle 1959; Li et al. 1998). In Section 7.4.1, the measurements of the elastic moduli temperature dependences for the Fe_3C ceramic will be discussed with reference to other Invar iron alloys. After this, Section 7.4.2 shows the results of the elastic behaviour of this ceramic under hydrostatic compression.

7.4.1 Effects of Temperature on the Elastic Moduli and Ultrasonic Wave Attenuation Coefficients for Fe_3C Ceramic

The changes in the longitudinal and shear stiffnesses calculated from their respective ultrasonic velocities for the Fe_3C sample are shown in Figure 7.6 (a). Temperature cycling between room temperature and 75 K showed no significant thermal hysteresis in the ultrasonic wave velocities and no irreversible effects. The results have been expressed as changes in an elastic property because of the large reductions in absolute velocities and therefore elastic stiffnesses caused by the severe porosity of the sample.

The longitudinal stiffness increases in the normal way, which is expressed as the dotted line in Figure 7.6 (a), with decreasing temperature from 290K down to about 150 K and then decreases anomalously at lower temperatures. The shear stiffness shows pronounced unusual effects: it decreases with decreasing temperature, reaches a minimum at around 110 K and then rises below that temperature. The mismatches between the thermal expansions of the bond, transducer and sample have caused a limiting low temperature value for good measurements of both ultrasonic mode velocities. The temperature range of the attenuation coefficients shown in Figure 7.6 (b) extends to lower temperatures compared with the velocity measurements shown in Figure 7.6 (a) because the data sets were recorded separately. A number of temperature runs were performed and the best data sets for each mode have been shown. These attenuation coefficients also show anomalous temperature behaviour: the shear mode decreases from room temperature to about 110K and then increases at approximately the same rate. This anomalous behaviour can be emphasized by comparing the temperature derivatives of shear mode attenuation coefficients of this cementite sample with that measured for one of the ultrasonic samples in Chapter 4. In the temperature range 250-130K, the approximate gradient of the shear mode attenuation coefficient in Figure 7.6 (b) is 0.03 $dBcm^{-1}K^{-1}$, whereas that for the AlN ceramic, in the temperature range 210-100K (Figure 4.6 (d)), is $6x10^{-4}$ $dBcm^{-1}K^{-1}$; therefore, the changes in attenuation observed in cementite appear not to be indicative of a normal ceramic. For the longitudinal mode, a small decrease in attenuation is observed down to about 150K and then a slight dip, which coincides with the beginning of softening in the longitudinal elastic stiffness, to a minimum at around 110K, and then starts to increase again at a similar rate to the shear mode attenuation.

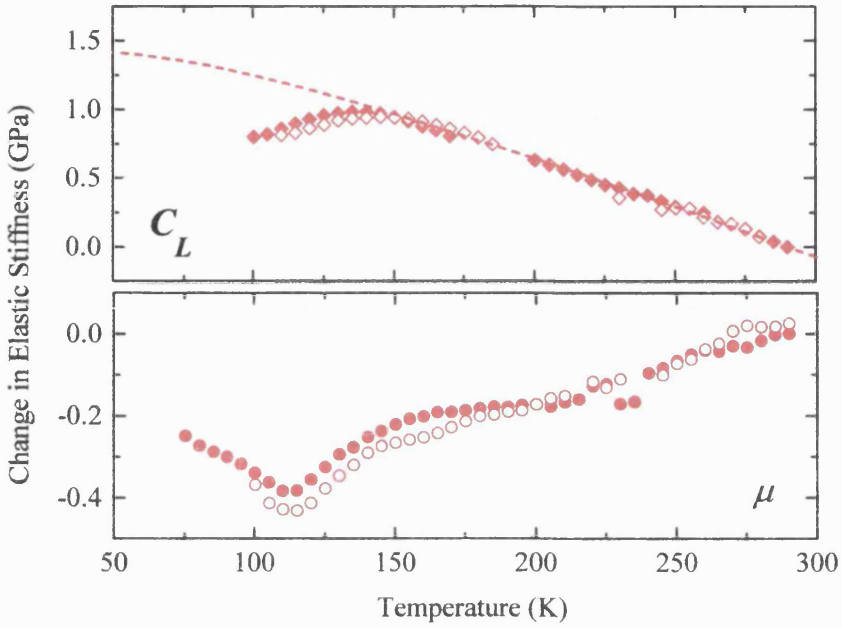

Figure 7.6 (a) Changes in the longitudinal and shear elastic stiffnesses as a function of temperature for Fe_3C ceramic. Filled (open) symbols correspond to decreasing (increasing) temperature. Dotted line is model of conventional lattice vibrational anharmonicity.

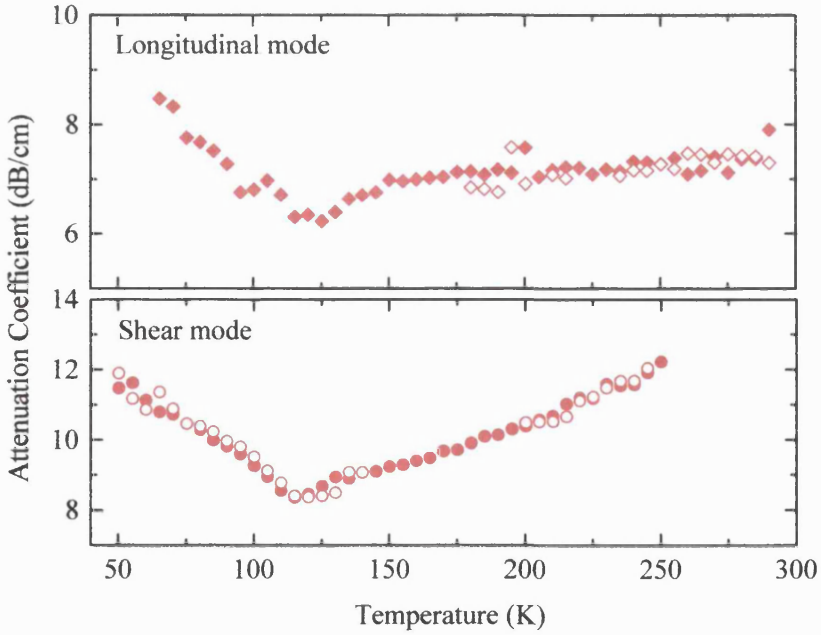

Figure 7.6 (b) Ultrasonic wave attenuation coefficients as a function of temperature for Fe_3C ceramic. Filled and open symbols have the same meaning as Figure 7.6 (a).

The results obtained for the changes in E and B^S with temperature are shown in Figure 7.6 (c). The bulk modulus mirrors the longitudinal elastic stiffness behaviour, i.e. increases as would be expected down to about 110 K, then softening occurs at lower temperatures. Conversely, Young's modulus mirrors the shear stiffness by softening anomalously with decreasing temperature from 295 K to about 110 K and then stiffening on further decrease in temperature; thus indicating that shear modes play an important role in the Young's modulus. The temperature coefficient of Young's modulus (TCYM) estimated from the temperature derivative (red dotted line) in the range 150-295 K of Figure 7.6 (c) has a value of about 4.0×10^{-5} K^{-1}, which is comparable with that ($\sim 6.8 \times 10^{-5}$ K^{-1}) found by Drapkin and Fokin (1980) in the range 300-380 K; this comparison is good considering that the calculation of the TCYM in the present study was performed using a reduced absolute Young's modulus value. It was suggested by Drapkin and Fokin (1980) that one reason for the comparatively low Young's modulus of Fe_3C at room temperature would be the so-called "ΔE-effect", which is domain wall displacement and magnetization rotation caused by an external stress resulting in a reduction in the absolute magnitude of Young's modulus below the Curie point. However, the large softening in the Young's modulus of cementite as it was transformed from the paramagnetic state to the ferromagnetic state was ascribed to

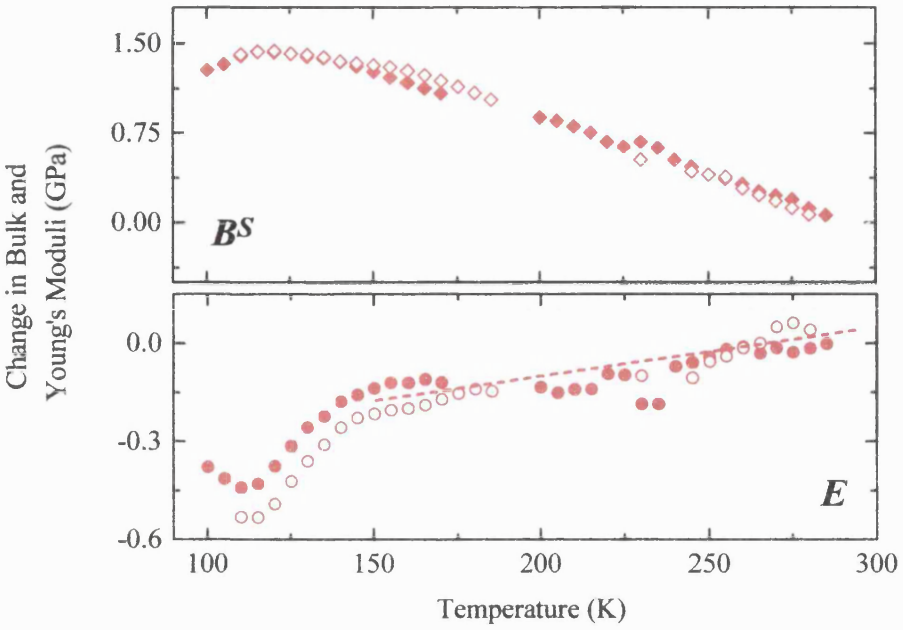

Figure 7.6 (c) Changes in bulk and Young's moduli as a function of temperature for Fe_3C ceramic. Filled (open) symbols correspond to decreasing (increasing) temperature. Dotted line represents an estimate of the temperature derivative.

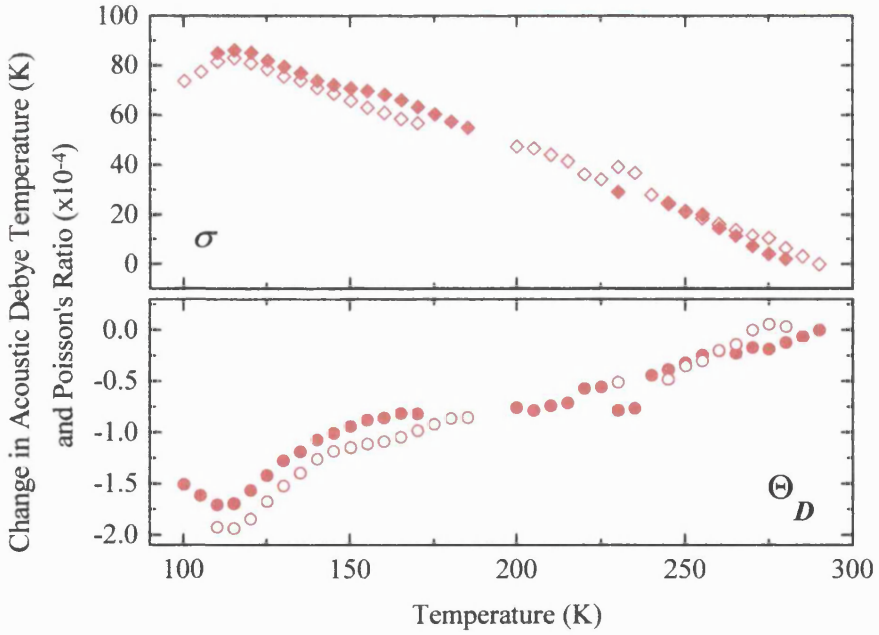

Figure 7.6 (d) Change in acoustic Debye temperature and Poisson's ratio as a function of temperature for Fe_3C ceramic. Filled and open symbols have the same meaning as Figure 7.6 (c).

the Invar properties of cementite by Kagawa et al. (1987) and was confirmed recently from the thermal expansion measurements by Acet et al. (2001). The present results for the temperature dependence of the change in the Young's modulus of cementite (Figure 7.6 (c)) complement those reported previously (Drapkin and Fokin 1980; Kagawa et al. 1987) and confirm the softening of the Young's modulus and hence the elastic Invar property of cementite (i.e. the Elinvar effect).

The Debye temperature, which is an indication of the strength of interatomic forces, has a positive slope above 110K (Figure 7.6 (d)) indicating that on decreasing temperature from 290 to 110K, the forces weaken. The change in Poisson's ratio with decreasing temperature is an order of magnitude larger than those results presented in Chapter 4 over a similar temperature range; thus, indicating that as temperature decreases in cementite there is a decrease in restoring forces associated with shearing of the lattice, which consequently increases Poisson's ratio.

These types of behaviour of the elastic stiffnesses with changing temperature have been found previously for other polycrystalline iron Invar alloys, e.g. Fe-Ni, Fe-Ni-Cr, Fe-Ni-Co alloys (Honda 1978), and more recently for single crystal samples of Fe-Ni and Fe-Pt alloys (Wassermann 1990). The theories behind the effects on elastic properties of spontaneous volume magnetostriction in these Invar alloys are in their infancy, but some common features have been found (Wassermann 1990). One such feature is that the behaviour of the elastic stiffnesses with temperature is not simply a volume effect caused by the magnetostriction, which would in the case of ultrasonic measurements increase the velocities, but is attributed to shear deformation of the lattice arising from a magnetoelastic (coupling) interaction (Honda 1978). This was proven by taking the alloy samples to technical magnetic saturation, which causes a forced volume magnetostriction, and subsequently measuring shear stiffness and Young's modulus as a function of temperature above and below the Curie temperature; the results were the same as for the magnetically unsaturated alloys, i.e. lattice softening below the Curie temperature (Wassermann 1990; Honda 1978). Another general feature is the softening of the longitudinal stiffness around the Curie point and below that an apparent normal stiffening occurs. These features are observed in the ultrasonic measurements on the cementite sample studied here from

290-150K (Figure 7.6 (a)), but at lower temperatures it appears other effects dominate.

There are a number of possible mechanisms that may influence the temperature behaviour in Figure 7.6 (a); since the material is highly inhomogeneous, these mechanisms may be related to both the magnetic properties of cementite and the microstructural properties of the ceramic sample: porosity, secondary phase, impurities. The "magnetic history" of the Fe_3C sample is also an important consideration. In ferromagnets, hysteresis loops are measured when the magnetization is changed by the application of a magnetic field; thus, the magnetic history of the sample determines the magnetization (Jiles 1998). Different states of magnetization in the sample may alter the elastic behaviour under temperature change, since the size of the magnetization is important in magnetoelastic interactions (Chikazuma 1997). However, an experiment which could prove valuable in determining whether these anomalies have a magnetic origin or are a consequence of sample inhomogeneity is to repeat the ultrasonic experiments with the sample magnetically saturated.

7.4.2 Effects of Hydrostatic Pressure on the Ultrasonic Wave Velocities for Fe_3C Ceramic

The effects of hydrostatic pressure on the velocity of ultrasonic waves propagated in the Fe_3C sample are shown in Figure 7.7. The data for the pressure dependence of the velocities of both longitudinal and shear ultrasonic waves are reproducible under pressure cycling and show no measurable hysteresis effects. This observation indicates that the Fe_3C sample does not alter in morphology under pressure cycling up to 0.2 GPa and that there is no relaxation of any residual stress. The velocities of both longitudinal and shear ultrasonic waves increase approximately linearly with pressure to about 0.06GPa, above which the slope of the longitudinal mode increase in magnitude. Although there is a discontinuity in the slope the overall picture indicates normal behaviour: both the long wavelength longitudinal and shear acoustic modes stiffen under pressure.

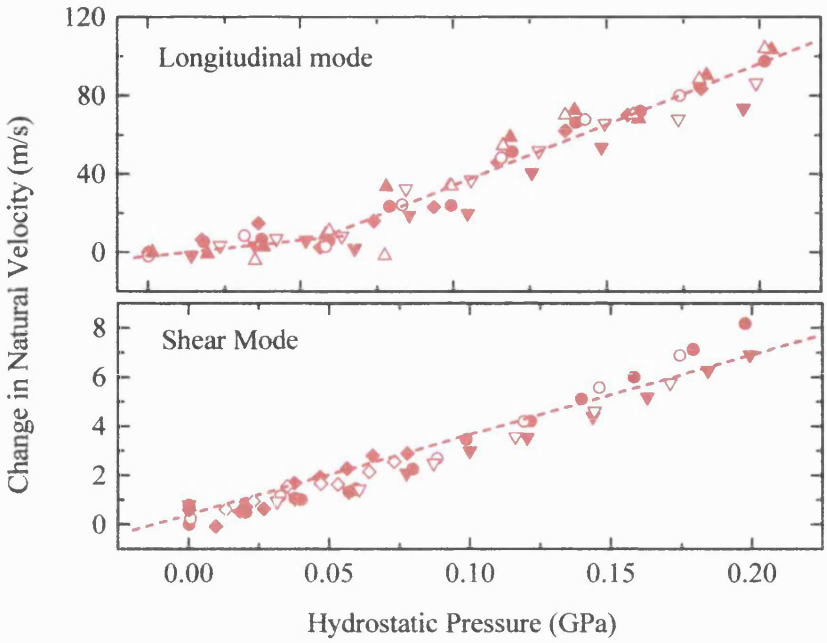

Figure 7.7 Change in longitudinal and shear mode natural velocities as a function of hydrostatic pressure for Fe_3C ceramic. Filled (open) symbols correspond to increasing (decreasing) pressure. Dotted lines are least squares fits to pressure data.

The effect of pressure on the longitudinal mode ultrasonic velocity in cementite (Figure 7.7) can be divided into two regions as according to whether the pressure is above or below 0.06 GPa. No such dependence could be found for the shear velocity. From knowledge of the ultrasonic velocity pressure derivatives, $(\partial B^S / \partial P)_{P=0}$ was calculated to be 3.43±1.61 in the lower pressure region and approximately 25 in the higher pressure region.

The same argument attributed to the large $(\partial B^S / \partial P)_{P=0}$ (=16.7±2.3) value calculated for a porous $ZrC_{0.90}$ ceramic presented in Chapter 6 can be applied here. For pressures above 0.06 GPa, microstructural changes in the cementite sample appear to be dominating the changes in ultrasonic velocity in a similar way to that discovered in the $ZrC_{0.90}$ ceramic, i.e. the density increases owing to pore collapse such that the longitudinal mode velocity increases and hence $(\partial B^S / \partial P)_{P=0}$ takes a large value. In contrast, the value of $(\partial B^S / \partial P)_{P=0}$ for cementite below 0.06 GPa appears to be unusually small for a ceramic material with a pore fraction between 1.5 and 2 times

greater than that in the $ZrC_{0.90}$ ceramic. Also, the pressure dependence of the longitudinal mode velocity is not as marked. This may result from a large positive spontaneous volume magnetostriction, since from the evidence of thermal expansion measurements shown in Figure 7.1, Invar iron alloys resist volume contraction. Wassermann (1990) has stated that in general for ferromagnetic Invar alloys the Curie temperature, and hence the magnetization, is very sensitive to pressure: the pressure derivative of the Curie temperature is linear and negative up to around 20 kbar i.e. the application of hydrostatic pressure reduces the magnetization. Hence if a similar effect occurs in cementite the density changes at low pressures will be small such that the longitudinal mode velocity increases slowly and hence $(\partial B^S / \partial P)_{P=0}$ takes a small value. Eventually, however, microstructural effects will take over when the pressure is sufficiently large. A change in shear mode velocity with pressure is not evident which may result from the fact that the act of applying a shear stress is a volume conserving process. Data with improved statistics are required to verify this point.

The contribution of the acoustic phonon modes to the thermal properties of this Fe_3C ceramic have been quantified by using the elastic stiffness pressure derivatives to calculate the acoustic mode Grüneisen parameters. $(\partial C_L / \partial P)_{P=0}$ and $(\partial \mu / \partial P)_{P=0}$ have been calculated to be 4.87±1.60 and 1.08±0.30, respectively. These values produce longitudinal (γ_L) and shear (γ_S) acoustic mode Grüneisen parameters of 1.16±0.40 and 0.70±0.03, respectively, which result in a mean acoustic mode Grüneisen parameter (γ^{el}) of 0.86±0.20. The calculated acoustic mode Grüneisen parameters apply only to the low pressure region, since it is assumed that microstructural effects are dominant at higher pressures. It must be noted that the room temperature elastic stiffnesses used to calculate $(\partial C_L / \partial P)_{P=0}$ and $(\partial \mu / \partial P)_{P=0}$ are those associated with the porous ceramic sample and hence the Grüneisen parameters will also be affected by using these values. Assuming a balance between the influence of porosity seemingly causing large increases in velocity with pressure, shown in Figure 7.7, and the magnetostriction causing a resistance to this increase, i.e. the slope in the pressure region up to 0.06 GPa due to magnetic interactions is increased by porosity, $(\partial C_L / \partial P)_{P=0}$ of 4.87±1.60 may represent a higher value to that which would be

determined if the influence of porosity was removed. The use of a reduced absolute value of the room temperature shear elastic stiffness to calculate the $(\partial\mu / \partial P)_{P=0}$ effectively lowers the value; coupling this with the slopes in the two defined pressure regions for the shear velocity having similar values, suggests that $(\partial\mu / \partial P)_{P=0}$ may be larger without the influence of porosity. Therefore, $(\partial B^S / \partial P)_{P=0}$, which is calculated using $(\partial C_L / \partial P)_{P=0}$ and $(\partial\mu / \partial P)_{P=0}$, may be smaller if there were no porous microstructure present in the sample.

In the introduction to this chapter, it was stated that Invar iron alloys can have either very small or negative $(\partial B^S / \partial P)_{P=0}$ values. From the evidence presented above concerning the impact of a porous microstructure on the velocity change with pressure, it is possible that $(\partial B^S / \partial P)_{P=0}$ for cementite is less than 3.43, and may even be negative. Thus, very small or negative $(\partial B^S / \partial P)_{P=0}$ values may be indicative of materials possessing Invar and Elinvar properties. Although the mean acoustic mode Grüneisen parameter of 0.86±0.20 may be larger than might be expected for a nonporous cementite ceramic, its small magnitude and hence small vibrational anharmonicity is in accordance with the low thermal expansion measured for this sample, as shown in Figure 7.1.

Chapter 8

Conclusions

Seven refractory hard ceramics and one Invar iron alloy have been characterised by standard non-destructive techniques and their longitudinal and shear mode ultrasonic velocities have been measured as functions of temperature and hydrostatic pressure to determine their elastic and nonlinear acoustic properties.

The velocities of longitudinal and shear ultrasonic waves propagated in the seven refractory hard ceramic samples at room temperature are shown in Table 8.1. Ultrasonic velocities measured for a ceramic cementite sample were significantly reduced by the influence of the porous microstructure, which was determined using the characterisation techniques, so have been omitted from Table 8.1. A porous microstructure was also discovered in each ceramic transition-metal carbide sample, which reduced their absolute ultrasonic velocities. A correction for porosity was performed on the ultrasonic velocity values measured for ceramic $TiC_{0.98}$, $TaC_{0.98}$, $ZrC_{0.90}$ using "theoretical" densities determined in Chapter 6 (velocities shown in brackets in Table 8.1). The high elastic moduli values calculated (or estimated) from the measured (or porosity corrected) velocities shows that the seven ceramics are stiff materials elastically.

With the exception of the ceramic samples of β-Si_3N_4 and Fe_3C, the elastic moduli of these ceramic samples (AlN, TiB_2, B_4C, $TiC_{0.98}$, $TaC_{0.98}$ and $ZrC_{0.90}$) stiffen in the normal way with decreasing temperature from 290K, which is emphasized by fitting the data to a conventional model for vibrational anharmonicity. The porous nature of the microstructures for ceramic $TiC_{0.98}$, $TaC_{0.98}$ and $ZrC_{0.90}$ affected the temperature dependence of their elastic moduli. A comparison between the change in elastic stiffnesses with temperature for each ceramic sample revealed that those samples containing a transition-metal, i.e. TiB_2, $TiC_{0.98}$, $TaC_{0.98}$ and $ZrC_{0.90}$, have the larger temperature dependences.

Anomalous behaviour in the ultrasonic velocities (and hence elastic stiffnesses) with temperature was recorded for the ceramic samples of β-Si_3N_4 and Fe_3C, below 290K. The temperature dependence of the longitudinal elastic stiffness for β-Si_3N_4 shows a

Table 8.1 The sample densities, X-ray and "theoretical" densities, porosity percentages, ultrasonic wave velocities, adiabatic elastic moduli and their hydrostatic pressure derivatives, and the acoustic mode Grüneisen parameters of ceramic AlN, β-Si_3N_4, TiB_2, B_4C, $TiC_{0.98}$, $TaC_{0.98}$ and $ZrC_{0.90}$ at 295 K. The sound velocities and elastic moduli quoted in brackets are those corrected for porosity. The values quoted in brackets for $(\partial\mu / \partial P)_{P=0}$ and γ_S of β-Si_3N_4 refer to the high pressure region, above 0.12 GPa.

Material	AlN	β-Si_3N_4	TiB_2	B_4C	$TiC_{0.98}$	$TaC_{0.98}$	$ZrC_{0.90}$
ρ (kgm^{-3})	3260±10	3290±10	4510±10	2514±15	4495±4	12788±50	5153 ± 20
ρ_{th} (kgm^{-3})	3261	3200	4495	2515	4886±293	14478±1737	6476 ±194
Porosity (%)	-	-	-	-	8.0±0.5	11.7±1.4	20.4±0.6
V_L (ms^{-1})	10700±10	10971±10	11650±10	14086±12	9429±40 (9886±593)	6232±10 (6664±800)	6403±63 (7425±223)
V_S (ms^{-1})	6307±10	6009±120	7470±10	8766±7	5856±24 (6132±367)	3744±13 (4015±481)	3922±42 (4548±136)
C_L (GPa)	373±2	396±7	612±2	498±4	399±3 (477±28)	496±2 (643±77)	211±4 (356±15)
μ (GPa)	130±1	119±3	252±1	193±1	154±1 (184±11)	179±1 (234±27)	79±2 (134±6)
B^S (GPa)	200±2	238±5	276±2	240±3	193±4 (233±14)	257±3 (332±39)	105±5 (178±8)
E (GPa)	320±3	306±6	579±3	456±4	365±5 (436±26)	435±4 (567±68)	189±7 (321±14)
σ	0.234±0.002	0.285±0.005	0.151±0.002	0.180±0.004	0.186±0.006	0.218±0.004	0.201±0.010
Θ_D (K)	952±5	923±20	1190±5	1480±3	862±6 (929±56)	531±2 (593±71)	505±9 (631±26)
$(\partial C_L / \partial P)_{P=0}$	4.64±0.17	4.5±0.10	7.29±0.10	5.63±0.30	6.32±0.26	7.12±0.24	18.9±2.3
$(\partial\mu / \partial P)_{P=0}$	0.28±0.03	0.19±0.04 (-0.040±0.002)	2.54±0.10	0.78±0.03	1.83±0.20	1.61±0.06	1.66±0.08
$(\partial B^S / \partial P)_{P=0}$	4.30±0.18	4.35±0.11	3.91±0.10	4.59±0.17	3.88±0.35	4.97±0.25	16.7±2.3
γ_L	1.08±0.05	1.18±0.03	1.48±0.01	1.19±0.04	1.37±0.07	1.68±0.07	4.56±0.61
γ_S	0.046±0.024	0.018±0.002 (-0.21±0.08)	1.23±0.03	0.32±0.02	0.98±0.11	0.99±0.04	0.94±0.07
γ^{el}	0.39±0.02	0.35±0.02	1.31±0.02	0.61±0.02	1.11±0.08	1.22±0.04	2.15±0.21

decrease in slope at about 235 K, indicating acoustic mode softening. The shear stiffness is practically temperature independent for this β-Si_3N_4 sample. Smallchanges of the elastic stiffnesses with temperature are reflected in the bulk and Young's moduli temperature dependences.

The cementite sample also shows anomalous temperature behaviour in its elastic properties below room temperature. The longitudinal stiffness increases in the normal way with decreasing temperature from 290K down to about 150 K and then decreases anomalously at lower temperatures. The shear stiffness shows pronounced unusual effects: it decreases with decreasing temperature, reaches a minimum at around 110 K and then rises below that temperature. These results for the longitudinal and shear stiffness temperature dependences are in accord with previous temperature studies on the elastic behaviour of other polycrystalline Invar iron alloys, which, in these alloys, was attributed to a shear deformation of the lattice arising from a magnetoelastic interaction. Young's modulus mirrors the shear stiffness by softening anomalously with decreasing temperature from 295 K to about 110 K and then stiffening on further decrease in temperature. This behaviour confirms the softening of the Young's modulus and hence the elastic Invar property of cementite (i.e. the Elinvar effect).

Increases in the ultrasonic velocities as a function of hydrostatic pressure up to 0.2 GPa were measured for the ceramic samples of AlN, TiB_2, B_4C, $TiC_{0.98}$, $TaC_{0.98}$ and $ZrC_{0.90}$, which showed normal temperature behaviour in their ultrasonic velocities; hence, their longitudinal and shear elastic stiffnesses and bulk modulus hydrostatic pressure derivatives are positive and indicate normal behaviour. However, the pressure derivatives of the longitudinal elastic stiffness and bulk modulus for $ZrC_{0.90}$ are much larger than any other ceramic sample measured in this ultrasonic study; this may be due in part to the porous nature of the microstructure in this ceramic.

The longitudinal and shear elastic stiffness hydrostatic pressure derivatives for the cementite sample are positive which indicates normal behaviour, but an increase in the magnitude of the longitudinal stiffness pressure derivative above a pressure of 0.06 GPa is observed. In the high pressure region above 0.06 GPa, the large pressure

derivative maybe due in part to the porous nature of the microstructure. However, inthe low pressure region the positive spontaneous volume magnetostriction, which is a result of the ferromagnetic state of cementite, may be partly responsible for the smaller pressure derivative.

The hydrostatic pressure derivatives of the longitudinal elastic stiffness and bulk modulus for β-Si_3N_4 have positive, normal values. However, the value obtained for the hydrostatic pressure derivative of shear elastic stiffness is very small and positive in the low pressure range, and becomes negative in the pressure range above 0.12 GPa. This behaviour mirrors the effects seen in the shear stiffness temperature dependence: these anomalous temperature and hydrostatic pressure dependences in the shear stiffness are possibly a result of the binding agent present in the sample. This binding agent can produce anelastic behaviour caused by grain boundary sliding.

Similar values were obtained for the adiabatic bulk modulus pressure derivatives of these seven refractory hard ceramics (Table 8.1), with the exception of $ZrC_{0.90}$. The large value found for the $ZrC_{0.90}$ ceramic is due to the large longitudinal stiffness pressure derivative. Comparisons between the volume compression of these ceramic samples extrapolated to pressures of 35 GPa shows that $TaC_{0.98}$ is the least compressible material, followed by TiB_2 and that B_4C, $TiC_{0.98}$ and β-Si_3N_4 ceramics have similar compressibilities. The similar values of the bulk modulus pressure derivatives obtained for these ceramics means that their volume compressions are mainly determined by the different bulk moduli values given in Table 8.1.

A small value was estimated for the adiabatic bulk modulus pressure derivative of the cementite sample in the pressure range 0-0.06 GPa, even though there appeared to be an influence by the porous microstructure of the ceramic. Previously measured bulk modulus pressure derivatives for other Invar iron alloys, which were very small or negative, suggests that there is a correlation between a relatively small value of this pressure derivative and Invar and Elinvar effects.

The long wavelength longitudinal, shear and mean acoustic mode Grüneisen parameters for these samples are positive, with the exception of the β-Si_3N_4 ceramic.A small negative value was determined, above 0.12 GPa, for the shear acoustic modeGrüneisen parameter (see Table 8.1) of β-Si_3N_4; this is due to the small negative shear stiffness pressure derivative. The thermal properties, e.g. thermal expansion and heat capacity, of these ceramic samples are compatible with the low acoustic mode vibrational anharmonicity determined in this ultrasonic study.

As a consequence of a number of factors, several difficulties were encountered in this study. Some of these factors will be highlighted here and the discussion will hopefully aid further ultrasonic investigations. The largest difficulties encountered were in the bulk density and ultrasonic velocity (and hence the elastic moduli) measurements performed on the samples of cementite, TiC, TaC and ZrC. These were mainly a consequence of their porous microstructure which results from the fact that the technology required to fabricate these ceramics into fully dense forms has so far not been fully developed. Obtaining accurate data from chemical characterisation methods, such as electron microprobe quantitative analysis and energy dispersive analysis, is also a problem because of (i) porosity and (ii) the constituent elements in the ceramics having low atomic numbers. In the present study the aforementioned problems were overcome by using an oxidation method. Ideally, extending the ultrasonic velocity measurements on these materials to very low temperatures is desirable as this would give a better picture of their behaviour. However, only intermediate temperatures could be reached owing to bond shearing and no reliable solution could be found for this problem.

Ultimately, these refractory hard ceramic materials will be chosen for engineering and scientific applications on the basis of their desirable chemical, electrical, mechanical, thermal and other physical properties. From the data gathered in this study on the fundamental properties of these materials, it is possible to point out some of the differences between them with respect to applications. The non-transition metal ceramic materials, i.e. the nitrides and boron carbide, would be appealing in areas where a high stiffness (or strength) to weight ratio is required. Conversely, the small

magnitude of the electrical resistivity and its temperature dependence for transition metal ceramics make them suitable for electrical applications where these attributes are utilised (more comments on electrical applications can be found in the review by Williams, 1997). Boron carbide also has appealing electrical properties that areappropriate for use in semiconductor technology. Furthermore, what sets apart the transition metal carbides from the rest of these ceramics is an ability to change their elastic properties, electrical resistivity and the temperature dependence of these parameters by altering the carbon composition. In the future, this behaviour could be utilised in some way. The demand for advanced materials with a number of appealing properties is discussed in a recent perspective on engineering ceramics (Reschke and Bogdanow 2000). In addition, the latest information on the ceramics aluminium nitride, silicon nitride, boron carbide and titanium diboride can be found in a recent article entitled "Advanced Materials and Powders Digest" (Mussler 2001). Similarly, Oyama (1996) gives some useful information relating to the applications of transition metal carbides.

The magnetoelastic properties of cementite could be used in magnetostrictive applications, pending more detailed studies such as those suggested below. Also, the Elinvar effects of cementite could be applicable to situations where dimensional stability is required. De Lacheisserie (1993) gives explanations of the technical aspects of magnetostriction and its industrial applications.

Some anomalous elastic and nonlinear behaviour has been found in this work, which could be further investigated. One great advantage of ultrasonic measurements is that the carrier wave frequency can be varied in addition to the pressure and temperature. This variation could be used, for example, to investigate the anomalous temperature dependence of the elastic moduli of the β-Si_3N_4 ceramic which is reported to be a consequence of anelasticity. Materials that display anelastic processes are sensitive to whether static or dynamic measurements are used to determine their elastic properties; therefore, changing the carrier frequency may alter the absolute elastic properties and their dependence on temperature and pressure. The effects of porosity on the temperature and pressure dependences of the ultrasonic velocities for the transition-

metal carbide samples could also be investigated through changing the carrierfrequency of the propagated ultrasonic wave. By increasing the carrier frequency, the wavelength is shortened and this will cause a greater interaction between pores and the ultrasonic wave. This interaction may give information on the pore size distribution and its dependence on temperature and pressure.

Since the Elinvar effects in cementite are a consequence of magnetoelastic interactions, it would be useful to examine their dependence on an applied magnetic field. Initially, the ferromagnetic hysteresis loop should be determined, i.e. the field dependence of the magnetization. As stated in Chapter 7, repeating the ultrasonic velocity versus temperature experiments as a function of magnetic field up to technical saturation may alter the elastic behaviour in different temperatures regimes, in particular the region around 110 K where anomalous effects occur (see figure 7.6(a)). Since the magnetization of cementite can also be varied by changing the temperature it would be interesting to investigate the pressure dependence of the elastic moduli at temperatures between 295 K and 480 K i.e. up to the Curie temperature of cementite. Hence the nonlinear properties of this material as a function of magnetisation could be studied.

Appendix A: X-ray Diffraction Spectra of Transition Metal Oxide Powders

The process of obtaining a better representation of the carbon-to-metal ratio for each of the transition metal carbide ceramic samples, resulted in oxidised powders. An X-ray diffraction pattern of each oxide powder is given here and compared with the X-ray standard (or standards) of the predicted oxide compounds, which were used in the assumptions leading to the estimated weight gain calculations in Chapter 6. Figures A.1, A.2 and A.3 (a) and (b) show these comparisons for TiO_2, Ta_2O_5 and ZrO_2, respectively.

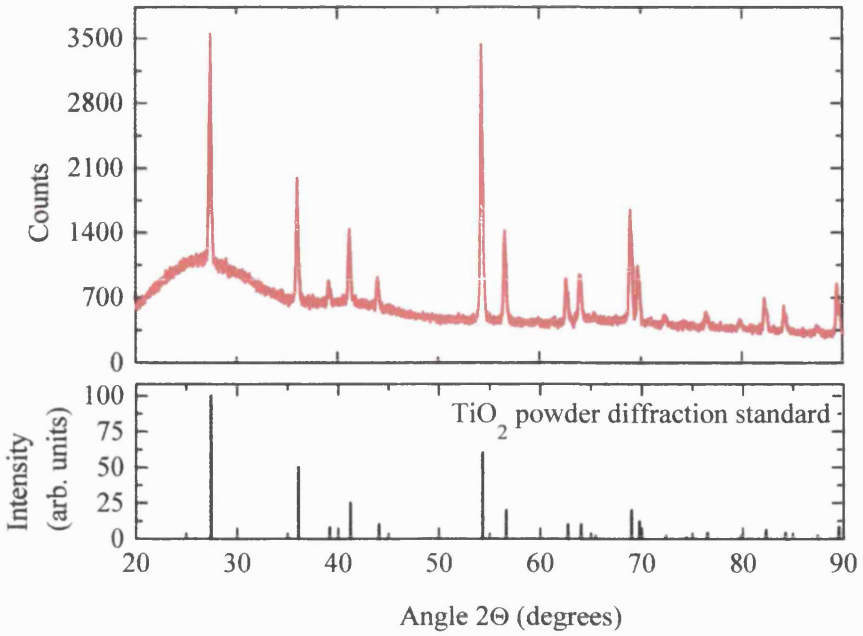

Figure A.1 X-ray diffraction spectrum of oxidised TiC powder (red lines) compared with TiO_2 (Rutile) diffraction standard.

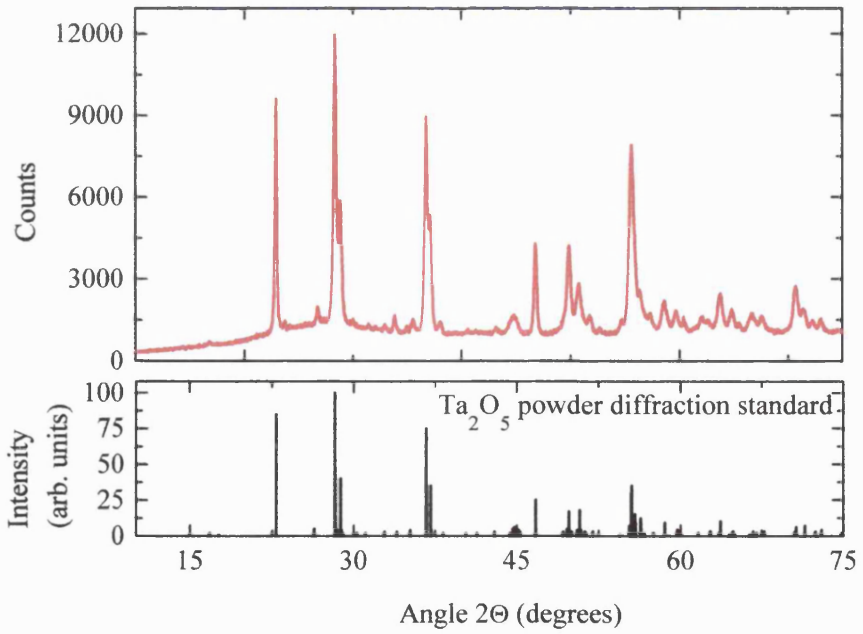

Figure A.2 X-ray diffraction spectrum of oxidised TaC powder compared with Ta_2O_5 diffraction standard.

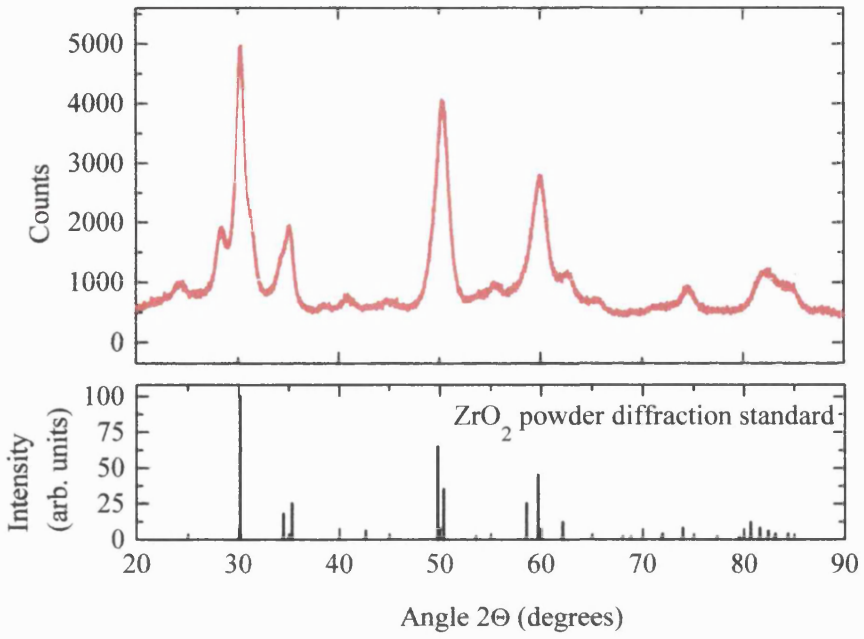

Figure A.3 (a) X-ray diffraction spectrum of oxidised ZrC powder compared with diffraction standard of ZrO_2 in tetraganol form.

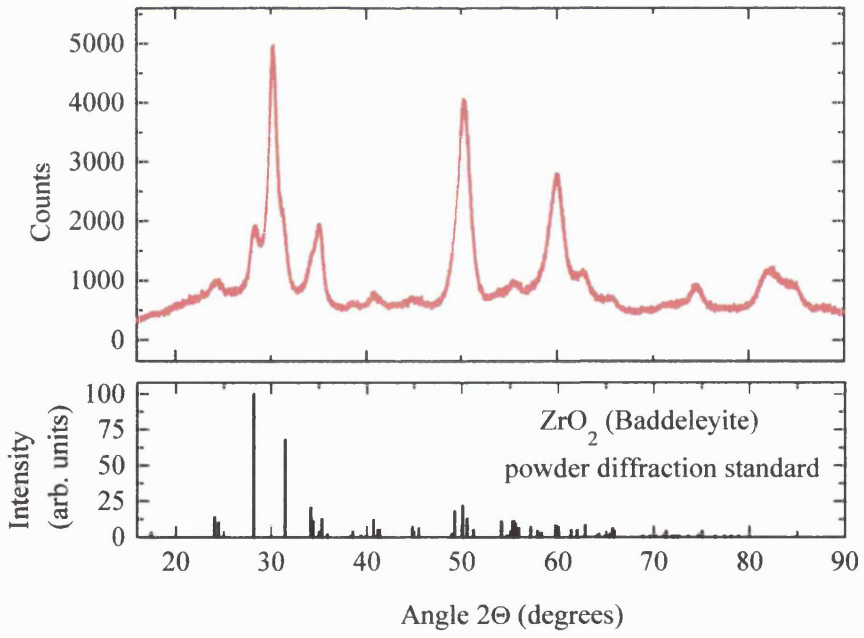

Figure A.3 (b) X-ray diffraction spectrum of oxidised ZrC powder compared to ZrO_2 in monoclinic form (Baddeleyite).

References

Abbate, A., Frankel, J. and Dandekar, D. P., in "Recent Trends in High Pressure Research", edited by Singh, A. K. (Oxford, New Delhi, 1992), p. 881.

Acet, M., Gehrmann, B., Wassermann, E. F., Bach, H. and Pepperhoff, W., J. Magn. Magn. Mater. **232** (2001) 221.

Allison, C. Y., Finch, C. B., Foegelle, M. D. and Modine, F. A., Sol. St. Comm. **68** (1988) 387.

Anderson, O. L., J. Phys. Chem. Solids **24** (1963) 909.

Anderson, O. L., J. Phys. Chem. Solids **27** (1966) 547.

Andrievski, R. A. and Asanov, B. U., J. Mater. Sci. Lett. **10** (1991) 147.

Arenberg, D. L., Final report Contract NONR 734 (00) (1955), tabulated in "Solid State Physics", Volume 7, edited by Seitz, F. and Turnbull, D. (Academic Press Inc., New York, 1958) p. 316.

Aselage, T. L., Emin, D. and McCready, S. S., Phys. Rev. B **64** (2001) 4302.

Aselage, T. L., Emin, D. and McCready, S. S., Phys. St. Sol. B **218** (2000) 255.

Aselage, T. L., Emin, D., Samara, G. A., Tallant, D. R., Van Deusen, S. B., Eatough, M. O., Tardy, H. L., Venturini, E. L. and Johnson, S. M., Phys. Rev. B **48** (1993) 11759.

Aselage, T. L., Tallant, D. R., Gieske, J. H., Van Deusen, S. B. and Tissot, R.G., "The Physics and Chemistry of Carbides; Nitrides and Borides" edited by Freer, R. (Kluwer Academic Publishers, Netherlands, 1990), p. 97.

Asmani, M., Kermel, C., Leriche, A. and Ourak, M., J. Eur. Ceram. Soc. **21** (2001) 1081.

Bairamashvili, I. A., Kalandadze, G. I., Eristavi, A. M., Jobava, J. Sh., Chotulidi, V. V. and Saloev, Yu. I., J. Less-Common Met. **67** (1979) 455.

Barron, T. H. K., Collins, J. G. and White G. K., Adv. Phys. **29** (1980) 609.

Bateman, T. B., J. Acoust. Soc. Am. **41** (1967) 1011.

Baumgartner, H. R. and Steiger, R. A., J. Am. Ceram. Soc. **67** (1984) 207.

Becher, P. F., Finch, C. B. and Ferber, M. K., J. Mater. Sci. Lett. **5** (1986) 195.

Belikov, A. M. and Savinskaya, A. A., Phys. Met. Metall. **14** (1962) 125.

Bellosi, A., Graziani, T., Guicciardi, S. and Tampieri, A., in "Special Ceramics 9", British Ceramic Proceedings, No.49 (Institute of Ceramics, Stoke on Trent, 1992), p. 163.

Bhatia, A. B., "Ultrasonic Absorption: An Introduction to the Theory of Sound Absorption and Dispersion in Gases, Liquids and Solids" (Clarendon Press, Oxford, 1967).

Born, H. and Huang, K., "Dynamic Theory of Crystal Lattices" (Clarendon Press, Oxford, 1954).

Bouchacourt, M. and Thévenot, F., J. Mater. Sci. **20** (1985) 1237.

Brown, H. L. and Kempter, C. P., Phys. St. Sol. **18** (1966) K21.

Brown, H. L., Armstrong, P. E. and Kempter, C. P., J. Chem. Phys. **45** (1966) 547.

Brüesch, P., "Phonons: Theory and Experiments I (Lattice Dynamics and Models of Interatomic Forces)" (Springer-Verlag, Berlin, 1982).

Brugger, K. and Fritz, T. C., Phys. Rev. **157** (1967) 524.

Bruls, R. J., Hintzen, H. T., de With, G. and Metselaar, R., J. Eur. Ceram. Soc. **21** (2001a) 263.

Bruls, R. J., Hintzen, H. T., de With, G., Metselaar, R. and van Miltenburg, J. C., J. Phys. Chem. Solids **62** (2001b) 783.

Bukatov, V. G., Korostin, O. S. and Knyazev, V. I., Inorg. Mater. **11** (1975) 313.

Buljan, S. T., Baldoni, J. G. and Huckabee, M. L., Am. Ceram. Soc. Bull. **66** (1987) 347.

Cankurtaran, M., Saunders, G. A., Ray, P., Wang, Q., Kawald, U., Pelzl, J. and Bach, H., Phys. Rev. B **47** (1993) 3161.

Card H. C., Sol. St. Comm. **16** (1975) 87.

Carlotti, G., Hickernell, F. S., Liaw, H. M., Palmieri, L., Socino, G. and Verona, E., 1995 IEEE Ultrasonics Symposium **1** (1995) 353.

Cartz, L. and Jorgensen, J. D., J. Appl. Phys. **52** (1981) 236.

Case, E. D., Smyth, J. R. and Hunter, O., J. Mater. Sci. **15** (1980) 149.

Castaing, J. and Costa, P., in "Boron and Refractory Borides", edited by Matkovich, V. I. (Springer-Verlag, New York, 1977), p. 390.

Castaing, J., Caudron, R., Toupance, G. and Costa, P., Sol. St. Comm. **7** (1969) 1453.

Champagne, B. and Angers, R., J. Am. Ceram. Soc. **62** (1979) 149.

Chang, R. and Graham, L. J., J. Appl. Phys. **37** (1966) 3778.

Chang, Y. A., Toth, L. E. and Tyan, Y. S., Metall. Trans. **2** (1971) 315.

Chikazumi, S., "Physics of Ferromagnetism" (2nd Edition, Oxford University Press, 1997).

Ching, W. Y. and Harmon, B. N., Phys. Rev. B **34** (1986) 5305.

Ching, W-Y., Xu, Y-N., Gale, J. D. and Rülhe, M., J. Am. Ceram. Soc. **81** (1998) 3189.

Choi, S. R. and Salem, J. A., J. Am. Ceram. Soc. **77** (1994) 1042.

Christensen, N. E. and Gorczyca, I., Phys. Rev. B **47** (1993) 4307.

Cottrell, A. H., Mater. Sci. Technol. **9** (1993) 277.

Dandekar D. P., Abbate, A. and Frankel, J., J. Appl. Phys. **76** (1994) 4077.

Dandekar, D. P. and Benfanti, D. C., J. Appl. Phys. **73** (1993) 673.

Davies, G. F. and O' Connell, R. J., in "High Pressure Research, Applications in Geophysics" Edited by M. H. Manghnani and S.-I. Akimoto (Academic Press Inc., New York, 1977).

De Arellano-Lopez, A. R., Mcmann, M. A., Singh, J. P. and Martinez-Fernandez, J., J. Mater. Sci. **33** (1998) 5803.

De Lacheisserie, E. du T., "Magnetostriction, Theory and Applications of Magnetoelasticity" (CRC Press, London, 1993).

De With, G., J. Mater. Sci. **19** (1984) 457.

Deger, C., Born, E., Angerer, H., Ambacher, O., Stutzmann, M., Hornsteiner, J., Riha, E. and Fischerauer, G., Appl. Phys. Lett. **72** (1998) 2400.

Desmaison-Brut, M., Alexandre, N. and Demaison, J., J. Eur. Ceram. Soc. **17** (1997) 1325.

Dodd, S. P., Saunders, G. A., Cankurtaran, M. and James, B., J. Mater. Sci. **36** (2001) 723.

Drapkin, B. M. and Fokin, B. V., Phys. Met. Metall. **49** (1980) 177.

Dubrovinskaia, N. A., Dubrovinsky, L. S., Saxena, S. K., Ahuja, R. and Johansson, B., J. Alloys Comp. **289** (1999) 24.

Dubrovinsky, L., Dubrovinskaia, N., Abrikosov, I. A., Vennström, M., Westman, F., Carlson, S., Van Schilfgaarde, M. and Johansson, B., Phys. Rev. Lett. **86** (2001) 4851.

Emin, D., Physics Today **40** (1987) 55.

Evans, A. G., Acta Metall. **6** (1978) 1845.

Fasiska, E. J. and Jeffrey, G. A., Acta Cryst. **19** (1965) 463.

Fate, W. A., J. Appl. Phys. **46** (1975) 2375.

Ferber, M. K., Becher, P. F. and Finch, C. B., J. Am. Ceram. Soc. **66** (1983) C-2.

Fisher, E. S., Manghnani, M. H., Wang, J-F. and Routbort, J. L., J. Am. Ceram. Soc. **75** (1992) 908.

Frantsevich, I. N., Zhurakovskii, E. A. and Lyashchenko, A. B., Inorg. Mater. **3** (1967) 6.

Gerlich, D., Dole, S. L. and Slack, G. A., J. Phys. Chem. Solids **47** (1986) 437.

Gieske, J. H., Aselage, T. L. and Emin, D. in "Boron Rich Solids" edited by Emin, D., Aselage, T. L., Beckel, C. L., Switendick, A. C. and Morosin, B., AIP Conf. Proc. No. 231 (American Institute of Physics, New York, 1991), p. 377.

Gitzen, W. H., (Editor) "Alumina as a Ceramic Material" (The American Ceramic Society, USA, 1970).

Goldman, R., "Ultrasonic Technology" (Reinhold Publishing Company, London, 1962).

Goñi, A. R., Siegle, H., Syassen, K., Thomsen, C. and Wagner, J.-M., Phys. Rev. B **64** (2001) 5205.

Green, D. J., Pan, M-J. and Hellmann, J. R., in "Fracture Mechanics of Ceramics, volume 12", edited by Bradt, R. C. et al. (Plenum Press, New York, 1996), p. 333.

Grossman, L. N., J. Am. Ceram. Soc. **48** (1965) 236.

Gubicza, J., Arató, P., Wéber, F. and Juhász, A., Mater. Sci. Eng. A **259** (1999) 65.

Gurin, V. N. and Sinelnikova, V. S. in "Boron and Refractory Borides", edited by Matkovich, V. I. (Springer-Verlag, New York, 1977), p. 390.

Gust, W. H. and Royce, E. B., J. Appl. Phys. **42** (1971) 276.

Gust, W. H., Holt, A. C. and Royce, E. B., J. Appl. Phys. **44** (1973) 550.
Häglund, J., Grimvall, G. and Jarlborg, T., Phys. Rev. B **44** (1991) 2914.

Hannink, R. H. J. and Murray, M. J., J. Mater. Sci. **9** (1974) 223.

Hartmann, S. and Ruppersberg, H., Mater. Sci. Eng. A **190** (1995) 231.

Hay, J. C., Sun, E. Y., Pharr, G. M., Becher, P. F. and Alexander, K. B., J. Am. Ceram. Soc. **81** (1998) 2661.

Helsing, J. and Grimvall, G., J. Appl. Phys. **70** (1991) 1198.

Herbstein, F. H. and Smuts, J., Acta Cryst. **17** (1964) 1331.

Himsolt, G., Knoch, H., Huebner, H. and Kleinlein, F. W., J. Am. Ceram. Soc. **62** (1979) 29.

Hinrichs, C. H., Hinrichs, M. H. and Mackie, W. A., J. Appl. Phys. **68** (1990) 3401.

Hollenberg, G. W. and Walther, G., J. Am. Ceram. Soc. **63** (1980) 610.

Hollenberg, G. W., Am. Ceram. Soc. Bull. **59** (1980) 538-41, 548.

Honda Memorial Series on Materials Science No. 3: The Physics and Applications of Invar Alloys (Marunzen Company, Tokyo, 1978).

Ito, T., Jpn. J. Appl. Phys. **37** (1998) L574.

Jack, D. H. and Jack, K. H., Mater. Sci. Eng. **11** (1973) 1.

Jellinghaus, W., Arch. Eisenhüttenwes. **37** (1966) 181.

Jiles, D., "Introduction to Magnetism and Magnetic Materials" (2nd Edition, Chapman and Hall, London, 1998).

Jun, C. K. and Shaffer, P. T. B., J. Less-Common Met. **23** (1971) 367.

Kagawa, A. and Okamoto, T., J. Mater. Sci. **18** (1983) 225.

Kagawa, A., Okamoto, T. and Matsumoto, H., Acta Metall. **35** (1987) 797.

Kang, E. S. and Kim, C. H., J. Mater. Sci. **25** (1990) 580.

Kato, R. and Hama, J., J. Phys.: Condens. Matter **6** (1994) 7617.

Katz, R. N. and Brantley, W. A., Mater. Sci. Res. **5** (1971) 271.

Kelly, A. and Macmillan, N. H., "Strong Solids" (Oxford University Press, New York, 1986).

Kim, K., Lambrecht, W. R. L. and Segall, B., Phys. Rev. B **53** (1996) 16310.

Kittel, C., "Introduction to Solid State Physics" (5th Edition, John Wiley and Sons, Inc., 1976).

Kittinger, E., Ultrasonics **15** (1977) 30.

Krajewski, A., D'Alessio, L. and De Maria, G., Cryst. Res. Technol. **33** (1998) 341.

Kral, C., Lengauer, W., Rafaja D. and Ettmayer P., J. Alloys Comp. **265** (1998) 215.

Lakkad, S. C., J. Appl. Phys. **42** (1971) 4277.

Lang, S. M., National Bureau of Standards Monograph **6** (1960).

Lange, F. F., J. Am. Ceram. Soc. **56** (1973) 518.

Laszlo, F. and Nolle, H., J. Mech. Phys. Solids **7** (1959) 193.

Lee, F. and Bowman, K. J., J. Am. Ceram. Soc. **75** (1992) 1748.

Lee, M.-C. and Simkovich, G., Metall. Trans. A **18** (1987) 485.

Lee, S., Bylander, D. M. and Kleinman, L., Phys. Rev. B **45** (1992) 3245.

Li, S. J., Ishihara, M., Yumoto, H., Aizawa, T. and Shimotomai, M., Thin Solid Films **316** (1998) 100.

Li, X. Y., Manghnani, M. H., Ming, L. C. and Grady, D. E., J. Appl. Phys. **80** (1996) 3860.

Li, Y. M., Kruger, M. B., Nguyen, J. H., Caldwell, W. A. and Jeanloz, R., Sol. St. Comm. **103** (1997) 107.

Li., D. and Ching, W. Y., Phys. Rev. B **52** (1995) 17073.

Lide, D. R., (editor) "Handbook of Chemistry and Physics" (75th edition, CRC Press, London, 1994).

Lie, K., Brydson, R. and Davock, H., Phys. Rev. B **59** (1999) 5361.

Liebling, R. S., Mater. Res. Bull. **2** (1967) 1035.

Lifshin, E. in "Materials Science and Technology, A Comprehensive Treatment, Volume 2B, Characterization of Materials, Part II", edited by Lifshin, E. (VCH, Cambridge, 1994), p. 351.

Lipatnikov, V. N. and Gusev, A. I., JETP Lett. **70** (1999) 294.

Lipson, H. and Petch, N. J., J. Iron Steel Inst. **142** (1940) 95.
Lundström, T., J. Solid St. Chem. **133** (1997) 88.

Mañosa, Ll., Saunders, G. A., Rahdi, H., Kawald, U., Pelzl, J. and Bach, H., Phys. Rev. B **45** (1992) 2224.

Marsh, S. P., (editor) "LASL Shock Hugoniot Data" (University of California Press, Berkeley, 1980), p. 354.

Mason, W. P., "Physical Acoustics and the Properties of Solids" (D.Van Nostrand company Ltd, 1958).

May, Jr., J. E., IRE. Natl. Conv. Rec. **6** (1958) 134.

McLeod, A. S., Haggerty, J. S. and Sadoway, D.R., J. Am. Ceram. Soc. **67** (1984) 705.

McNeil, L. E., Grimsditch, M. and French, R. H., J. Am. Ceram. Soc. **76** (1993) 1132.

Méçabih, S., Amrane, N., Nabi, Z., Abbar, B. and Aourag, H., Physica A **285** (2000) 392.

Mendelson, M. I., J. Am. Ceram. Soc. **52** (1969) 443.

Miksic, M. G.,"Thermal Vibrations and Bonding Effects in Titanium Diboride", Tech. Repr. Nr. 032-414 (Polytech. Inst. Brooklyn, August 1963) p.12.

Milman, V. and Warren, M. C., J. Phys.: Condens. Matter **13** (2001) 5585.

Miodownik, A. P., Mater. Sci. Technol. **10** (1994) 190.

Mirgorodsky, A. P., Baraton, M. I. and Quintard, P., Phys. Rev. B **48** (1993) 13326.

Miwa, K. and Fukumoto, A., Phys. Rev. B **48** (1993) 7897.

Miyauchi, J. and Kobayashi, Y., SAE Technical Papers Series (Warrendale, Pa., Automotive Engineers, 1985), p. 31.

Mizubayashi, H., Li, S. J., Yumoto, H. and Shimotomai, M., Scripta Materialia **40** (1999) 773.

Mohammad, S. N. and Morkoç, H., Prog. Quant. Electr. **20** (1996) 361.

Monemar, B., J. Mater. Sci.: Mater. El. **10** (1999) 227.

Murgatroyd, R. A. and Kelly, B. T., Atomic Energy Review **15** (1977), p1-74.

Murnaghan, F. D., Proc. N. A. S. **30** (1944) 244.

Murthy, S. R., J. Mater. Sci. Lett. **4** (1985) 603.

Mussler, B. H., Am. Ceram. Soc. Bull. **80** (2001) 61.

Nelmes, R. J., Loveday, J. S., Wilson, R. M., Marshall, W. G., Besson, J. M., Klotz, S., Hamel, G., Aselage, T. L. and Hull, S., Phys. Rev. Lett. **74** (1995) 2268.

Nipko, J. C. and Loong, C.-K., Phys. Rev. B **57** (1998) 10550.

Nye, J. F., "Physical Properties and Crystals and their Representation by Tensors and Matrices" (Clarendon Press, Oxford, 1985).

Okimura, J-F. L. H. and Brittain J. O., Mater. Sci. and Eng. A **123** (1990) 129.

Ordan'yan, S. S. and Fishchev, V. N., Refractories **17** (1976) 111.

Oyama, S. T., (Editor) "The Chemistry of Transition Metal Carbides and Nitrides" (Blackie Acedemic and Professional, London, 1996).

Pan, M-J., Hoffman, P. A., Green, D. J. and Hellman, J. R., J. Am. Ceram. Soc. **80** (1997) 692.

Papadakis, E. P., J. Acoust. Soc. Am. **42** (1967) 1045.

Perlin, P., Polian, A. and Suski, T., Phys. Rev. B **47** (1993) 2874.

Perottoni, C. A., Pereira, A. S. and da Jornada, J. A. H., J. Phys.: Condens. Matter **12** (2000) 7205.

Pezzotti, G., Tanaka, I., Okamoto, T., Koizumi, M. and Miyamoto, Y., J. Am. Ceram. Soc. **72** (1989) 1461.

Pintschovius, L., Reichardt, W. and Scheerer, B., J. Phys. C: Solid State Phys. **11** (1978) 1557.

Radcliffe, S. V. and Rollason, E. C., J. Iron Steel Inst. **189** (1985) 45.

Rahman, M., Wang, C. C., Chen, W. H., Akbar, S. A. and Mroz, C., J. Am. Ceram. Soc. **78** (1995) 1380.

Reed, S. J. B., "Electron Microprobe Analysis" (2nd Edition, Cambridge University Press, 1993).

Reschke, S. and Bogdanow, C., "Engineering Ceramics: Multifunctional Properties – New Perspectives" edited by Šajgalík, P. and Lenčéš, Z. (Trans Tech Publications, Switzerland, 2000) p. 1.

Riley, F. L., "Progress in Nitrogen Ceramics" (Martinus Nijhoff Publishers, Boston, 1983).

Riley, F. L., J. Am. Ceram. Soc. **83** (2000) 245.

Rosenberg, H. M., "The Solid State" (3rd Edition, Oxford University Press, 1988).

Rosenberg, Z., Brar, N. S. and Bless, S. J., J. Appl. Phys. **70** (1991) 167.

Rowcliffe, D J. and Hollox, G. E., J. Mater. Sci. **6** (1971) 1270.

Ruiz, E., Alvarez, S. and Alemany, P., Phys. Rev. B **49** (1994) 7115.

Samara, G. A. and Giardini, A. A., Rev. Sci. Instr. **35** (1964) 989.

Samara, G. A., Emin, D. and Wood, C., Phys. Rev. B **32** (1985) 2315.

Samsonov, G. V. and Kovenskaya, B. A., in "Boron and Refractory Borides", edited by Matkovich, V. I. (Springer-Verlag, New York, 1977), p. 19.

Sato, K., Tanaka, K., Nakano, Y. and Mori, T., J. Am. Ceram. Soc. **76** (1993) 2042.

Sayers, C. M. and Smith, , R. L., Ultrasonics **20** (1982) 201.

Schreiber E., Anderson, O. L. and Soga, N., "Elastic Constants and Their Measurement" (McGraw-Hill Book Company, 1973).

Schwetz, K. A. and Grellner, W., J. Less-Common Met. **82** (1981) 37.

Scott, H. P., Williams, Q. and Knittle, E., Geophys. Research Lett. **28** (2001) 1875.

Serrano, J., Rubio, A., Hernández, E., Muñoz, A. and Mujica, A., Phys. Rev. B **62** (2000) 16612.

Shaffer, P. T. B.,"High Temperature Materials" (Plenum Press, 1964).

Sheard, F. W., Phil. Mag. **3** (1958) 1381.

Shigematsu, T., J. Phys. Soc. Japan **39** (1975) 915.

Shimada, K., Sota, T. and Suzuki, K., J. Appl. Phys. **84** (1998) 4951.

Shirai, K., J. Solid St. Chem. **133** (1997) 215.

Singh, D. and Varshni, Y. P., Phys. Rev. B **24** (1981) 4340.

Singh, J. P., Goretta, K. C., Kupperman, D. S. and Routbort, J. L., Adv. Ceram. Mater. **3** (1988) 357.

Slack, G. A. and Bartram, S. F., J. Appl. Phys. **46** (1975) 89.

Slater, J. C., "Introduction to Chemical Physics" (McGraw-Hill Book Company, Inc., New York, 1939).

Spoor, P. S., Maynard, J. D., Pan, M-J., Green, D. J., Hellman, J. R. and Tanaka, T., Appl. Phys. Lett. **70** (1997) 1959.

Stampfl, C. and Van der Walle, C. G., Phys. Rev. B **59** (1999) 5521.

Steinberg, D. J., J. de Physique IV, Colloque C3, suppl. au J. de Physique III, Volume 1 (1991) C3-837.

Steinitz, R. and Resnick, R., J. Appl. Phys. **37** (1966) 3463.

Storms E. K., "Refractory Carbides" (Academic Press, New York, 1968).

Street, A. and Alexander, W., "Metals in the Service of Man", Eleventh Edition (Penguin Books, London, 1998).

Stuart, H. and Ridley, N., J. Iron Steel Inst. **208** (1970) 1087.

Stuart, H. and Ridley, N., J. Iron Steel Inst. **204** (1966) 711.

Subhash, G. and Ravichandran, G., J. Mater. Sci. **33** (1998) 1933.

Sze, S. M., "Semiconductor Devices, Physics and Technology" (John Wiley and Sons, New York, 1985).

Tanaka, I., Nasu, S., Adachi, H., Miyamoto, Y. and Niihara, K., Acta Metall. Mater. **40** (1992) 1995.

Telle, R., "The Physics and Chemistry of Carbides; Nitrides and Borides", edited by Freer, R. (Kluwer Academic Publishers, Netherlands, 1990), p. 249.

Tennery, V. J., Finch, C. B., Yust, C. S.and Clark, G. W., in "Science of Hard Materials", edited by Viswanadham, R. K. (Plenum Press, New York, 1983), p. 891.

Thévenot, F., J. Eur. Ceram. Soc. **6** (1990) 205.

Thompson, R., "The Physics and Chemistry of Carbides; Nitrides and Borides", edited by Freer, R. (Kluwer Academic Publishers, Netherlands, 1990), p. 113.

Thurston, R. N. and Brugger K., Phys. Rev. **133** (1964) A1604.

Thurston, R. N., Proc. IEEE **53** (1965) 1320.

Toth, L. E., "Transition Metal Carbides and Nitrides" (Academic Press, New York, 1971).

Truell, R., Elbaum, C. and Chick, B. B., "Ultrasonic Methods in Solid State Physics" (Academic Press, New York, 1969).

Tsagareishvili, G. V., Nakashidze, T. G., Jobava, J. Sh., Lomidze, G. P., Khulelidze, D. E., Tsagareishvili, D. Sh. and Tsagareishvili, O. A., J. Less-Common Metals **117** (1986) 159.

Tsubouchi, K., Sugai, K. and Mikoshiba, N., 1981 IEEE Ultrasonics Symposium, Volume 1, (1981) 375.

Tyan, Y. S., Toth, L. E. and Chang, Y. A., J. Phys. Chem. Solids **30** (1969) 785.

Ueno, M., Onodera, A., Shimomura, O. and Takemura, K., Phys. Rev. B **45** (1992) 10123.

Vahldiek, F. W., J. Less-Common Met. **12** (1967) 202.

Vajeeston, P., Ravindran, P., Ravi, C. and Asokamani, R., Phys.Rev. B **63** (2001) 45115.

Van Camp, P. E. and Van Doren, V. E., High Press. Res. **13** (1995) 335.

Van Camp, P. E., Van Doren, V. E. and Devreese, J. T., Phys. Rev. B **44** (1991) 9056.

Vast, N., Besson, J. M., Baroni, S. and Dal Corso, A., Comp. Mater. Sci. **17** (2000) 127.

Wang, C. C., Akbar, S. A., Chen, W. and Patton, V. D., J. Mater. Sci. **30** (1995a) 1627.

Wang, C.-M., Pan, X., Ruhle, M., Riley, F. L. and Mitomo, M., J. Mater. Sci. **31** (1996) 5281.

Wang, L., Wixom, M. R. and Thompson, L. T., J. Mater. Sci. **29** (1994) 534.

Wang, Q., Ph.D. Thesis (University of Bath, 1993).

Wang, Q., Saunders, G. A., Almond, D. P., Cankurtaran, M. and Goretta, K. C., Phys. Rev. B **52** (1995b) 3711.

Wang, Q., Saunders, G. A., Tschaufeser, P., Parker, S. C. and James, B. J., Phys. Rev. B **45** (1992) 10242.

Wassermann, E. F., in "Ferromagnetic Materials", edited by Buschow, K. H. J. and Wohlfarth, E. P. (Volume 5, Elsevier Science Publishing, Holland, 1990), p. 237.

Webb, W. W. and Forgeng, W. D., Acta Metall. **6** (1958) 462.

Wendel, J. A. and Goddard III, W. A., J. Chem. Phys. **97** (1992) 5048.

Wieder, H. H., "Laboratory Notes on Electrical and Galvanomagnetic Measurements" (Elsevier Scientific Publishing Company, Amsterdam, 1979).

Wiley, D. E., Manning, W. R. and Hunter Jr., O., J. Less-Common Met. **18** (1969) 149.

Williams, W. S. and Schaal, R. D., J. Appl. Phys. **33** (1962) 955.

Williams, W. S. in "Science of Hard Materials 3", edited by Sarin V. K. (Elsevier Applied Science Publishing Ltd., London, 1988).

Williams, W. S., Int. J. Refract. Met. & Hard Mater. **17** (1999) 21.

Williams, W. S., J. Min. Met. Mater. Soc. **49** (1997) 38.

Wolf, W., Podloucky, R., Antretter, T. and Fischer, F. D., Phil. Mag. B **79** (1999) 839.

Wood, C. and Emin, D., Phys. Rev. B **29** (1984) 4582.

Wright, A. F., J. Appl. Phys. **82** (1997) 2833.

Xia, Q., Xia, H. and Ruoff, A. L., J. Appl. Phys.**73** (1993) 8198.

Xu, Y. and Ching, W. Y., in "Silicon Dioxide and Its Interface", edited by Pantelides, S. T. and Lucovsky, G. (Materials Research Society, Pittsbhurgh, PA, 1988), p. 181.

Xu, Y. N. and Ching, W. Y., Phys. Rev. B **48** (1993) 4335.

Yamashita, M., J. Phys. E: Sci. Instrum. **20** (1987) 1457.

Yang, Q., Lengauer, W., Koch, T., Schreerer, M. and Smid, I., J. Alloys Comp. **309** (2000) L5.

Yeheskel, O. and Gefen, Y., Mater. Sci. Eng. **71** (1985) 95.

Yeheskel, O., Gefen, Y. and Talianker, M., J. Mater. Sci. **19** (1984) 745.

Publications

Ultrasonic study of the elastic and nonlinear acoustic properties of ceramic aluminium nitride.

Dodd S. P., Saunders, G. A., Cankurtaran, M. and James, B., J. Mater. Sci. **36** (2001) 723.

Ultrasonic study of the temperature and pressure dependences of the elastic properties of β-silicon nitride ceramic.

Dodd S. P., Cankurtaran, M., Saunders, G. A. and James, B., J. Mater. Sci. **36** (2001) 2557.

Ultrasonic determination of the temperature and hydrostatic pressure dependences of the elastic properties of ceramic titanium diboride.

Dodd S. P., Cankurtaran, M., Saunders, G. A. and James, B., J. Mater. Sci. **36** (2001) 3989.

Temperature and pressure dependences of the elastic properties of ceramic boron carbide (B_4C).

Dodd, S. P., Saunders, G. A and James, B., J. Mater. Sci. **37** (2002) 2731.

Submitted to the Journal of Materials Science for publication:

Ultrasonic study of the temperature and hydrostatic-pressure dependences of the elastic properties of cementite (Fe_3C).

Dodd, S. P., Saunders, G. A., Cankurtaran, M., James, B. and Acet, M.